Department of Chemical and Environmental Engineering

STUDY ON THE USE OF REDOX ELECTROLYTES IN SUPERCAPACITORS

By

BAMIDELE AKINWOLEMIWA

Thesis submitted to the University of Nottingham for the degree of Doctor of Philosophy

MARCH 2019

ABSTRACT

Electric double layer (EDL) capacitors (a.k.a. supercapacitors) which are generally characterised by high power and long cycle lives, exploits the electrostatic interaction between electrons and ions within the porous matrix of carbonaceous materials with high specific surface area ranging from 500.00 to over 2,000.00 cm^2/g.

Majority of the research on supercapacitors focuses on developments of the electrodes in order to improve device performance metrics such as: capacitance, power, and cycle stability. The prevailing view on the electrolyte is that it should be chemically inert during the charge-discharge of a supercapacitor. Interestingly, in recent years, the adoption of electrolytes that display redox activity has garnered a lot of attention. This is mainly because redox electrolytes could enhance charge storage capacity.

This research is focused on the use of redox electrolytes to improve the performance of supercapacitors.

We have proposed that the charging of supercapacitors due to dissolved redox species (DRS) incorporates both Nernstian (battery) and EDL capacitance mechanisms, in line with the features of a supercapacitor-battery hybrid i.e. supercapattery. Accordingly, widespread confusion in the literatures regarding the charge storage mechanisms of these devices were critiqued and remedied through basic electrochemical considerations.

Electrochemical analysis of supercapatteries with KI or KBr as redox electrolytes have been studied. Herein, the device characteristics were rigorously analysed from the standpoint of the polarisation of the activated carbon electrodes, the thermodynamics of the DRS, and the adsorption and transport of the charging reaction products. Therefore, the origin of charge

capacity increase at high cell voltages have been fundamentally described. These findings are important to the design of high energy supercapatteries which was exemplified by devices with KBr as redox electrolyte. Additionally, fundamental electrochemical analysis have been used to meticulously assess the relationship between capacitive and non-capacitive storage mechanisms to understand the engineering design of supercapacitors with DRS.

Correspondingly, through the variation of the mass ratio between the activated carbon materials on the positive electrode (positrode) and negative electrode (negatrode), supercapatteries with 1.00 mol/L KBr as redox electrolyte have been operated at energy range of 17.30 to 33.20 Wh/kg with a current load of $\pm$0.25 A/g at 1.60 V. Optimal electrode mass ratio also resulted in high performing devices with specific energy and power of 21.31 Wh/kg and 703.82 W/kg respectively, at a current load of $\pm$1.00 A/g.

The characteristics of three different commercially available carbons which are broadly representative of the porous and surface physico-chemical properties of EDL capacitor electrodes have been rigorously compared and analysed. In this regard, the role of the pore size and surface physico-chemistry of the electrodes have been comprehensively correlated with the redox electrolytes based on the bromide anion, and with various cations such as Li^+, Na^+, K^+ and Mg^{2+}.

Based on these investigations, bromides have been used as DRS in supercapatteries with either a micoroporous or mesoporous and highly graphitised carbon. Herein, it was shown that the cells are operable at 1.8 V and can retain ca. 80.00% of the initial specific energy after 10,000 galvanostatic charge-discharge cycles. Thus, fundamentally relevant and practically important properties of a mesoporous and highly graphitised carbon with bromides as DRS were reported for the first time. Hence, these findings

could serve as useful benchmarks in the design of commercial supercapatteries with DRS.

A redox organic molecule methyl hydroquinone (MH_2Q) has been verified for the first time to be a viable DRS. Through electroanalytical, and spectroscopic comparisons with the more common hydroquinone (H_2Q), it was observed that MH_2Q adsorbs more strongly on the activated carbon electrode compared to H_2Q. Furthermore, the structural basis to the charge storage mechanism of a highly graphitised carbon with MH_2Q have also been revealed. These studies demonstrated that when organic redox molecules are to be selected as DRS, it is important to critically evaluate not just the enhancement of charge capacity, but also the relationship between the structure of the molecules and their interaction within the lattice of the carbon.

Bi-electrolyte cells which are assembled in a manner that allows the positrode and negatrode to operate in two different electrolytes were demonstrated as a versatile means of designing high-performance supercapatteries. Accordingly, a novel bi-electrolyte cell with immiscible electrolytes wherein the positrode is operated in a redox electrolyte was shown to be characterised by slow rate of self-discharge. Also, these cells were operable at 2.00 V, displaying a specific energy of 35.83 Wh/Kg at an applied current load of $\pm$0.50 A/g. This effectively introduces a new class of device engineering strategy with huge promise.

AFFIRMATION

The reports in this thesis have not appeared elsewhere except in the following Peer-reviewed publications.

- Original Research

B. Akinwolemiwa, C. Wei, Q. Yang, L. Yu, D. Hu, L. Xia, C. Peng, and G. Z. Chen. "Optimal Utilization of Combined Double Layer and Nernstian Charging of Activated Carbon Electrodes in Aqueous Halide Supercapattery through Capacitance Unequalisation". ***J. Electrochem. Soc.***, 165, A4067-A4076, (2018).

- Perspectives/Critical-reviews

B. Akinwolemiwa and G. Z. Chen. "Fundamental consideration for electrochemical engineering of supercapattery**". *J. Brazil Chem. Soc.,*** 29, 960-972, (2018).

B. Akinwolemiwa, C. Wei, and G. Z. Chen. "Mechanisms and designs of asymmetrical electrochemical capacitors". ***Electrochim. Acta***, 247, 344-357, (2017).

B. Akinwolemiwa and G. Z. Chen. "Dissolved redox species for the improvement of the performance of supercapacitors". ***Current Topics in Electrochemistry***. 19, 47-65, (2017).

B. Akinwolemiwa, C. Peng, and G. Z. Chen. "Redox electrolytes in supercapacitors". ***J. Electrochem. Soc.,*** 162, A5054-A5059, (2015).

- Conference Presentation

B. Akinwolemiwa, Q. Yang, L. Yu and G. Z. Chen. "Dual-electrolyte supercapattery utilising immiscible aqueous posilyte and ionic liquid negalyte for increased working voltage". (September 2017). [Poster & Abstract] presented at: ***The International Forum on Liquid Salts*** organised by China Automotive Battery Research Institute Co. Ltd and the Royal Society of Chemistry-Molten Salts Discussion Group.

ACKNOWLEDGEMENTS

I sincerely appreciate the International Doctoral Innovation Centre, Ningbo Education Bureau, Ningbo Science and Technology Bureau, and the University of Nottingham, for funding this PhD studentship.

I extend my heartfelt gratitude to my Supervisors: Prof. G. Z. Chen, and Prof. C. Peng, for their guidance and support throughout the duration of this research. Dr. D. Hu is also appreciated for constructive assessments during the progress of this PhD study.

My academic collaborators: Dr. A. Dawodu, Ms. C. Wei, Mr. M. T. Bishop, Mr. Q. Yang, are acknowledged for fruitful discourse and/or experiments.

Staff members: Dr. L. Yu, Dr. L. Xia, Ms. K. Yuan, and student members: Ms. B. Bhattachrya, Mr. A. Dolganov, Ms. M. Ma, and Ms. X. Guo, of the Electrochemical Technology Group, University of Nottingham, Ningbo China (UNNC), are appreciated for useful interactions.

I am also thankful to the technical staffs at the Faculty of Science and Engineering (FoSE) in UNNC, and Ningbo Institute of Materials Technology and Engineering (NIMTE) for their assistance in the course of this research.

To my too numerous to mention friends and colleagues in UNNC and beyond, I extend warm appreciation: academic and social engagements we all shared in, has made this period of my life a memorable one.

To my Dad, Nan, siblings, and extended family: your good wishes and encouragements have been the most endearing aspects of my life.

To my Mom: you are always in my heart. Though you left us unexpectedly, your refreshing brightness, love, and kindness left an undying light in its wake. I am eternally grateful for all you mean to me.

TABLE OF CONTENTS

ABSTRACT.....II

AFFIRMATION.....V

ACKNOWLEDGEMENTS.....VI

TABLE OF CONTENTS.....VII

LIST OF FIGURES.....XIV

ABBREVIATIONS AND SYMBOLS.....XXX

CHAPTER 1: BACKGROUND OF THIS RESEARCH 1

1.1 THE ROLE OF ENERGY STORAGE IN ENVIRONMENTAL SUSTAINABILITY 1

1.2 INTRODUCTION TO ELECTROCHEMICAL ENERGY STORAGE DEVICES 5

1.3 INTRODUCTION TO REDOX ELECTROLYTES FOR ELECTROCHEMICAL CAPACITORS.....7

1.4 MOTIVATION FOR THIS RESEARCH 10

1.5 AIMS AND OBJECTIVES OF THIS RESEARCH.....11

1.6 STRUCTURE OF THIS THESIS AND SUMMARY OF ORIGINAL CONTRIBUTIONS 12

CHAPTER 2: LITERATURE REVIEW.....15

2.1 CHARGE STORAGE MECHANISMS OF ELECTRODES FOR ELECTROCHEMICAL CAPACITORS 15

2.1.1 Non-faradaic capacitive charge storage mechanism 16

2.1.2 Faradaic storage mechanisms 22

2.2 DESIGN OF PRACTICAL SUPERCAPACITORS THROUGH FUNDAMENTAL UNDERSTANDING OF THE CHARGE STORAGE MECHANISMS 27

2.2.1 Asymmetrical electrochemical capacitors with capacitive electrodes 28

2.2.2 Combining Nernstian and capacitive electrodes: Supercapattery 34

2.3 MECHANISM OF CHARGE STORAGE IN SUPERCAPACITORS CONTAINING REDOX ELECTROLYTE 40

2.4 CHARGE STORAGE CAPACITY OF SUPERCAPACITORS CONTAINING REDOX ELECTROLYTES 44
2.5 DISSOLVED ORGANIC MOLECULES FOR ENHANCED INTERFACIAL CHARGE STORAGE 48
2.6 DISSOLVED ANIONIC COMPONENTS FOR ENHANCED INTERFACIAL CHARGE STORAGE 56
2.7 DISSOLVED CATIONIC COMPONENTS FOR ENHANCED INTERFACIAL CHARGE STORAGE 64
2.8 DESIGN OF SUPERCAPACITORS WITH REDOX ELECTROLYTES 66
2.9 CHAPTER SUMMARY 78

CHAPTER 3: METHODOLOGY 79

3.1 RESEARCH APPROACH 79
3.2 MATERIALS AND EQUIPMENT 81
3.3 GENERAL CHARACTERISATION TECHNIQUES 84
3.3.1 Physisorption analysis 84
3.3.2 Thermo-gravimetric analysis 87
3.3.3 Ultraviolet-visible spectroscopy 88
3.3.4 X-ray photoelectron spectroscopy 90
3.3.5 Raman spectroscopy 91
3.3.6 Scanning electron microscopy 93
3.3.7 Transmission electron microscopy 94
3.4 ELECTROCHEMICAL CHARACTERISATION TECHNIQUES 94
3.4.1 Cyclic voltammetry (potential dynamic polarography) 94
3.4.2 Chronopotentiometry (galvanostatic charge-discharge) 99
3.4.3 Electrochemical impedance spectroscopy 102
3.4.4 Electrochemical quartz-crystal microbalance 105
3.5 MATERIAL PREPARATION 107
3.5.1 Electrode and electrolyte preparation 107
3.6 FABRICATION OF CELLS FOR ELECTROCHEMICAL TESTS 110

3.1 CHAPTER SUMMARY 115

CHAPTER 4: COMBINED NERNSTIAN AND DOUBLE LAYER CHARGING OF ACTIVATED CARBON ELECTRODES IN AQUEOUS HALIDE SUPERCAPATTERY.....116

4.1 INTRODUCTION 116

4.2 CARBON ELECTRODE MATERIALS FOR ELECTRIC DOUBLE LAYER CAPACITORS 117

4.2.1 Physisorption analysis of the carbons..... 117

4.2.2 Thermo-gravimetric analysis of carbon electrode materials..... 120

4.2.3 Electrochemical double layer capacitance of devices fabricated with the carbon electrodes..... 122

4.3 ELECTROCHEMICAL CHARACTERISATION OF ACTIVATED CARBON (AC-1) ELECTRODE IN REDOX ELECTROLYTES (KI AND KBR) 124

4.3.1 Background to the investigations of carbon electrodes with redox electrolytes..... 124

4.3.2 Electrochemical characterisation of the carbon | redox-halide interface and supercapatteries with halides as dissolved redox species 126

4.4 NERNSTIAN AND DOUBLE LAYER FEATURES OF SUPERCAPATTERIES WITH REDOX HALIDES..... 129

4.5 FORCED CONFINEMENT OF REDOX ACTIVITY TO ELIMINATE SHUTTLING OF REDOX REACTION PRODUCTS..... 139

4.6 CHAPTER SUMMARY 144

CHAPTER 5: CAPACITANCE UNEQUALISATION AND THE PERFORMANCE OF SUPERCAPATTERIES WITH REDOX ELECTROLYTES 146

5.1 INTRODUCTION 146

5.2 CAPACITANCE UNEQUALISATION OF EDL ELECTRODES 146

5.2.1 Relative polarisations of electrodes and the optimal utilisation of DRS for Nernstian storage 149

5.2.2 Charge and energy efficiencies of UEM cells with $m_- > m_+$ and the effective utilisation of bromide as DRS 152

5.3 ASSESSING THE POWER PERFORMANCE OF UEM CELLS WITH DRS 155

5.4 CHAPTER SUMMARY 159

CHAPTER 6: CARBON ELECTRODE PROPERTIES AND ENERGY CAPACITY OF SUPERCAPATTERIES CONTAINING REDOX ELECTROLYTES.....160

6.1 INTRODUCTION 160

6.2 OVERVIEW OF CARBON ELECTRODE MATERIAL PROPERTIES AND THE BASIS FOR INVESTIGATIONS WITH REDOX ELECTROLYTES 161

6.3 ELECTROANALYSIS OF ACTIVATED CARBON ELECTRODE WITH NEGLIGIBLE SURFACE OXYGEN GROUPS (AC-1) IN ALKALI BROMIDES 162

6.4 PHYSICOCHEMICAL PROPERTIES OF MICOROPOROUS (AC-2) AND MESOPOROUS (GNP) CARBONS WITH SIMILAR EDL CAPACITANCES 164

6.5 UNDERSTANDING EDL CAPACITORS AND SUPERCAPATTERIES ASSEMBLED WITH THE CARBON ELECTRODES AC-2 AND GNP 170

6.6 CORRELATING THE ELECTRODE POROSITY AND SURFACE PROPERTY OF AC-2 AND GNP TO THE ENERGY OF SUPERCAPATTERIES WITH DISSOLVED REDOX SPECIES..... 173

6.6.1 Testing protocols for supercapatteries with DRS..... 174

6.6.2 Charge storage properties of supercapatteries with AC-2 or GNP as electrodes, and varying concentration of LiBr as electrolyte 176

6.7 POROSITY OF CARBON ELECTRODES AND CHARGE STORAGE OF REDOX ELECTROLYTES 181

6.8 CHAPTER SUMMARY 186

CHAPTER 7: ROLE OF CONCENTRATION AND ION DYNAMICS ON THE PERFORMANCE OF SUPERCAPATTERIES WITH REDOX ELECTROLYTES 188

7.1 INTRODUCTION 188

7.2 IMPEDANCE ANALYSIS OF SUPERCAPATTERIES FABRICATED WITH AC-2 OR GNP WITH LIBR AS ELECTROLYTE 188

7.3 CYCLING STABILITY TESTS 199

7.4 CORRELATING THE ELECTRODE PROPERTIES WITH VARYING CATIONS OF DISSOLVED REDOX SPECIES 202

7.5 ROLE OF CATIONS IN THE PERFORMANCE OF GNP ELECTRODES WITH BROMIDES AS REDOX ELECTROLYTES OR REDOX ADDITIVES TO INERT AQUEOUS ELECTROLYTES 205

7.6 CHAPTER SUMMARY 211

CHAPTER 8: DISSOLVED QUINONOIDS AS REDOX ADDITIVES IN SUPERCAPATTERIES 213

8.1 INTRODUCTION 213

8.2 STUDY OF THE CHARGE STORAGE PROPERTIES OF ACTIVATED CARBON (AC-1) WITH QUINONOIDS AS REDOX ADDITIVES 214

8.3 ADSORPTION OF DISSOLVED REDOX QUINONOIDS ON ACTIVATED CARBON (AC-1) AND ITS EFFECTS ON DEVICE PERFORMANCE 217

8.3.1 Performance of supercapatteries with MH_2Q or H_2Q as redox additives in organic electrolyte with AC-1 as electrodes 223

8.3.2 Fabrication of the platinum micro-cavity electrode 224

8.4 STUDIES OF MH_2Q AS REDOX ADDITIVES IN AQUEOUS ELECTROLYTES 230

8.5 CORRELATING THE REDOX REACTION OF MH_2Q WITH THE STRUCTURAL PROPERTIES OF AMORPHOUS (AC-2) AND HIGHLY GRAPHITIZED (GNP) CARBON ELECTRODE MATERIALS 233

8.6 CHAPTER SUMMARY 240

CHAPTER 9: DESIGN OF HIGH PERFORMANCE BI-ELECTROLYTE SUPERCAPATTERIES 241

9.1 INTRODUCTION 241

9.2 FUNDAMENTAL DESIGN OF BI-ELECTROLYTE CELLS 241

9.3 BI-ELECTROLYTE SUPERCAPATTERY COUPLING INERT NEGALYTE WITH REDOX POSILYTE 244

9.3.1 Effects of redox posilyte concentration on the performance of bi-electrolyte cells 246

9.3.2 Redox reaction of the I^- dissolved redox species and the performance of the bi-electrolyte cells 249

9.4 BI-ELECTROLYTE SUPERCAPATTERY COUPLING INERT NEGALYTE WITH IMMISCIBLE REDOX POSILYTE 251

9.5 NOVEL DEVICE ENGINEERING TO IMPROVE THE PERFORMANCE OF METHYL-HYDROQUINONE AS REDOX ADDITIVE 262

9.6 CHAPTER SUMMARY 265

CHAPTER 10: GENERAL CONCLUSIONS AND RECOMMENDATIONS FOR FUTURE WORK 266

10.1 GENERAL CONCLUSIONS 266

10.2 RECOMMENDATIONS FOR FUTURE WORK 272

10.2.1 Porosity matching with solvated geometries of dissolved redox species 272

10.2.2 Investigations of modulated electrolyte permittivity 272

10.2.3 Fundamental studies of the molecular basis of redox reactions at the carbon lattice 273

10.2.4 Life cycle analysis for the environmental impact of dissolved redox species 273

10.2.5 Theoretical simulations of the transport properties of dissolved redox species in carbons 273

10.2.6 Device engineering modifications and improvements..... 274

REFERENCES 275

LIST OF FIGURES

Figure 1.1: Percentage of global energy consumption by source in 2016 (a) Breakdown of global electricity production by source from 1971 to 2016 (b) [4]. 3

Figure 1.2: General energy and power characteristics of electrical energy storage systems and their applications for large-scale electrification [13]. 4

Figure 1.3: General illustration of an electrochemical energy storage device [16]. 6

Figure 1.4: CVs of (a) $KCuFe(CN)_6$ in 0.01M $HNO_3 \cdot$1M KNO_3 (scan rate: 1 mV/s) [22] (b) hydrous RuO_2 in 0.1M H_2SO_4 (scan rate: 50 mV/s) [23]. 8

Figure 1.5: Comparison of the CV of a carbon (EDL) electrode: in an inert electrolyte 1.0 mol/L H_2SO_4 (black curve), and in the inert electrolyte containing 0.1 mol/L $FeSO_4$ redox additive (blue curve). Scan rate: 10 mV/s. 10

Figure 2.1: (a) Charge storage mechanisms for electrochemical energy storage and their possible device classification. **(b)** Schematic representations of the CVs for Nernstian (b1, b2), mixed Nernstian and capacitive (b3) and capacitive (b4) charge storage mechanisms [17]. 15

Figure 2.2: Various models of the electric double-layer based on the proposed theories (a) Helmholtz model (b) Gouy-Chapman model (c) Stern model [28]. 18

Figure 2.3: Structure of the electric double layer, modified from [29]. 20

Figure 2.4: Hypothetical electrical responses of an EDL or capacitive faradaic device (a) CVs at different scan rates (b) GCDs at different applied current [35]. 22

Figure 2.5: Charge storage mechanisms in electrodes (a) non-capacitive Faradaic or Nernstian mechanism of ferrocene containing inactive polymer

COATED ELECTRODE IN AQUEOUS ELECTROLYTE (B) CAPACITIVE FARADAIC MECHANISM OF MnO_x COATED ELECTRODE IN AQUEOUS ELECTROLYTE (C) BAND MODEL FOR THE DESCRIPTION OF CHARGE STORAGE MECHANISMS (ADAPTED FROM REFERENCES [39], [40] AND [41], RESPECTIVELY). 23

FIGURE 2.6: ELECTRICAL RESPONSES OF A NERNSTIAN ELECTRODE (A) CVS AT DIFFERENT SCAN RATES (B) GCDS AT DIFFERENT APPLIED CURRENT. 25

FIGURE 2.7: CVS OF A PAN-CNT FILM IN 1.0 MOL/L HCL SHOWING BOTH THE CAPACITIVE AND MIXED NERNSTIAN AND CAPACITIVE POTENTIAL RANGES [51]. 27

FIGURE 2.8: CMPB (2.5 MG) COATING ON GRAPHITE ELECTRODE IN 0.3 MOL/L K_2SO_4 [55] SHOWING THE DOMINANT CAPACITIVE FEATURES IN THE SCANNED POTENTIAL RANGES. 29

FIGURE 2.9: (A,B) CVS SHOWING THE VARIATION OF CAPACITIVE FEATURE IN DIFFERENT POTENTIAL RANGES OF THE CMPB ELECTRODE IN 0.3 MOL/L K_2SO_4. (C,D) CVS OF AECS WITH CMPB ON BOTH THE POSITRODE AND NEGATRODE AT C_P/C_N = 1 (C) AND 4/3 (D), RESPECTIVELY. (E) PLOTS OF ELECTRODE POTENTIAL AGAINST CELL VOLTAGE OF AN AEC WITH CMPB ON BOTH THE POSITRODE AND NEGATRODE AT C_P/C_N = 1. (F) CYCLIC STABILITY (UP TO 10000 CYCLES) OF AECS AT THE INDICATED C_P/C_N RATIOS AND CELL VOLTAGES [55]. 31

FIGURE 2.10: (A) SCHEMATIC ILLUSTRATION OF CAPACITIVE ELECTRODES IN AECS WITH CPR(−) AND CPR(+) BEING THE CAPACITIVE POTENTIAL RANGE FOR THE NEGATRODE AND POSITRODE, RESPECTIVELY. (B) STABLE CAPACITIVE POTENTIAL RANGE OF SOME CAPACITIVE ELECTRODES IN AQUEOUS ELECTROLYTES. THE COLOURED CIRCULAR DOTS REFER TO THE OPEN CIRCUIT POTENTIALS OF THE RESPECTIVE "ELECTRODE | ELECTROLYTE" INTERFACES AFTER A REST TIME OF 4 H [58]. 32

FIGURE 2.11: AECS WITH EDLC AND PSEUDOCAPACITIVE ELECTRODES. (A) CVS OF (−) CMPB | 1.0 MOL/L H_2SO_4 | PAN-CNT (+) AT INDICATED C_P/C_N RATIOS. (B) ENERGY CHANGE OF THE CELL IN (A) AS A FUNCTION OF THE C_P/C_N RATIO [57].... 33

Figure 2.12: Schematic illustrations of (1,2) CVs of positrode and negatrode in a three electrode cell, and (3) GCDs of the two electrode cell of (a) rechargeable battery, (b) supercapacitor, or (c) supercapattery..... 35

Figure 2.13: GCDs of the positrode, negatrode and cell of (a) the hypothetic supercapattery I with an EDLC positrode and a Li or lithiated carbon negatrode [16], (b) the cell of (–) Li | $LiClO_4$ + IL | AC (+) at 0.4 A/g [93], (c) the hypothetic supercapattery II with a pseudocapacitive positrode and a Li or lithiated carbon negatrode [11], (d) the cell of (–) Li | aqueous electrolyte | solid electrolyte | MnO_2 (+) at 0.255 mA/cm^2 [94], (e) the hypothetic supercabattery with pseudocapacitive positrode and battery material negatrode [16]..... 38

Figure 2.14: Schematic illustration proposed to elucidate the possible charge storage mechanisms in the porous carbon electrode of a SC with a redox electrolyte. 41

Figure 2.15: Illustrative comparison of the galvanostatic charging and discharging plots of a conventional supercapacitor (plot A, linear), and a supercapacitor containing a redox electrolyte (plot B, non-linear). Note that plot B represents very well the characteristics of some SCs containing redox electrolytes as reported in the literature [24, 104-108]. 45

Figure 2.16: GCD plots of cell with (a) 1.0 mol/L H_2SO_4 (b) 0.4 mol/L hydroquinone in 1.0 mol/L H_2SO_4 [98]..... 48

Figure 2.17: CVs of cells showing a comparison between ortho-, meta- and para-hydroquinone as redox additives to 1.0 mol/L H_2SO_4 [96]. 49

Figure 2.18: CVs and corresponding GCD plots of HQ redox additive in H_2SO_4 electrolyte with PEDOT (a) and (b) and PPy (c) and (d) as electrodes [104]. 50

Figure 2.19: CVs of different carbon electrodes in KOH electrolyte incorporated with PPD [120]..... 52

Figure 2.20: CVs of inert and MB incorporated H_2SO_4 with MWCNT as electrode (a) electrode characterisation (b) cell [127]..... 53

Figure 2.21: CVs of pyrocatechol violet as additive in Na_2SO_4 or KOH [128]. 54

Figure 2.22: GCD plots of AQDS in 1.0 mol/L KNO_3 [110]. 55

Figure 2.23: CVs of phenanthroline in organic electrolyte (a) electrode and (b) cell characteristic [131]. 56

Figure 2.24: CVs for redox electrolytes (MI (M = Li, Na, K, Rb or Cs)) with activated carbon (a) electrode and (b) cell, characterisations. 57

Figure 2.25: CVs of supercapacitors with NaI as redox electrolyte (a) different concentration of NaI [107] (b) 2.0 mol/L NaI under floating [96]. 58

Figure 2.26 GCD plot of the cell (-)WO_3-MWCNT | KI in Li_2SO_4 | ZrO_2-MWCNT (+) with varying concentration of KI. 59

Figure 2.27: CV showing cell with AC electrodes and 1.0 mol/L KBr redox electrolyte [137]..... 60

Figure 2.28: GCD plots for (a) cell (b) positrode and negatrode: of the cell with functionalised-CNT as electrodes and 0.5 mol/L KBr as additive in Na_2SO_4 [138]. 61

Figure 2.29: CVs of NiO electrode in KOH with or without the $Fe(CN)_6^{3-}$/ $Fe(CN)_6^{4-}$ DRS [25]..... 63

Figure 2.30: Characterisation of mixed redox cations of Cu^{2+} and Fe^{+} ions in H_2SO_4 (a) CV of electrode characterisation (b) GCD plot of resulting device. 65

Figure 2.31: Generalised diagrams of an electrochemical energy storage device (a) under charging and (b) under discharging conditions. (c) Explanations to symbols in (a) and (b). PEP and NEP are the peak positive and negative electrode potentials, respectively, measured at the maximum

cell voltage (U_L). PZV (point of zero voltage), is the equipotential of the positive and negative electrodes at zero cell voltage. 68

Figure 2.32: Characterisation of the cell (–)AC | $VOSO_4$ || KI | AC(+) (a) CVs (b) GCD plots at different current loads [100]. 69

Figure 2.33: Schematic illustration of the storage mechanism (a) and GCD plot (b) for the cell: (–)Li-metal | organic electrolyte || LiI-KI-I_2 |AC(+) [147]. 70

Figure 2.34: Illustrative comparison of the galvanostatic charging and discharging plots of a conventional SC (plot A, solid line) with a maximum charging voltage, U_{MAX} and a minimum discharging voltage, U_{MIN}, and the same SC containing a redox electrolyte in which the same redox couple can react on both the positrode and negatrode at the same potential (plot B, dot line), or the redox couple is restricted to react only on either the positrode or negatrode, but not both (plot C, bold dotted line). 73

Figure 2.35: Characterisation of the device and interfaces for the cell: (-)AC VO^{2+}/V^{3+}, V^{3+}/V^{5+}, Sn/Sn^{N+} || VO^{2+}/VO_2^{+} | AC(+) (a) CV (b) GCD plot [148]. 74

Figure 2.36: GCD plot for the activated carbon electrodes in a cell comprising of HV^{2+} and Br^- as DRS [112]. 77

Figure 3.1: Approximate formal redox potential of some (a) inorganic and (b) organic redox species that may be used in water. Length of arrow is approximately the relative molar mass of the compounds. 79

Figure 3.2: General research approach 81

Figure 3.3: (a) characteristic physisorption isotherms (b) hysteresis loops for physisorption isotherms [157]. 85

Figure 3.4: Block diagram of the TGA apparatus [158]. 87

Figure 3.5: Schematic illustrations of characteristic TGA curves [159]... 88

Figure 3.6: Energy states showing the transition of electrons from different energy levels due to UV-vis absorption [161]. 90

FIGURE 3.7: ILLUSTRATION OF THE PHOTOELECTRON EMISSION PROCESS FROM THE CORE SHELL OF AN ATOM [162]. 91

FIGURE 3.8: DIFFERENT SCATTERING MODES OF INCIDENT RADIATION DUE TO THE INTERACTION OF THE PHOTONS WITH THE MOLECULES [166]. 93

FIGURE 3.9: SCHEMATIC ILLUSTRATION OF RESULTS FROM A CYCLIC VOLTAMMETRY EXPERIMENT (A) INPUT WAVEFORM (B) RESULTING I-V CYCLIC VOLTAMMOGRAM ... 96

FIGURE 3.10: POTENTIAL STIMULATION, CURRENT RESPONSE AND CORRESPONDING CONCENTRATION PROFILE SHOWING THE THICKNESS/VARIATION OF THE DIFFUSION LAYER (Δ) WITH CHANGE IN CONCENTRATION GRADIENT [172]. 97

FIGURE 3.11: EXAMPLES OF SOME CYCLIC VOLTAMMOGRAMS OBTAINED FROM THIS RESEARCH SHOWING: ELECTRODE (NEGATRODE) (A), CELL (B), WITH CAPACITIVE- AND, CELL WITH NON-CAPACITIVE- (C) FEATURES. 99

FIGURE 3.12: EXCITATION (I VS. T) AND THE CORRESPONDING RESPONSE (V OR E VS. T). 100

FIGURE 3.13: CHARACTERISTIC GCD PLOT FOR A SUPERCAPATTERY (OBTAINED FROM THIS RESEARCH) SHOWING W_C AND W_D AS THE AREA OF THE CHARGING AND DISCHARGING PORTIONS RESPECTIVELY..... 101

FIGURE 3.14: SIMPLE MATHEMATICAL DESCRIPTION OF SINUSOIDAL SIGNAL (A) AND THE CORRESPONDING PHASOR DIAGRAM REPRESENTING THE IMPEDANCE MEASURED (B). 102

FIGURE 3.15: EQUIVALENT ELECTRICAL CIRCUIT MODEL FOR THE INTERFACIAL COMPONENTS OF THE EDL [176]. 103

FIGURE 3.16: SCHEMATIC OF THE NYQUIST PLOT (A) AND MODIFIED RANDLES ELECTRICAL EQUIVALENT CIRCUIT (B) 104

FIGURE 3.17: SCHEMATIC OF THE BODE PLOT. 105

FIGURE 3.18: (A) SCHEMATIC REPRESENTATION OF THE EQCM EXPERIMENTAL SET-UP (B) SHEAR MODULATION OF THE QUARTZ CRYSTAL UNDER AN APPLIED AC FREQUENCY ELECTRIC FIELD [177]. 106

Figure 3.19: Electrode preparation procedure: (a) electrode calendaring (b) electrode rolling (c) electrode punching prior to pressing (d) pressed or punched pellets of specific geometries and mass. 109

Figure 3.20: Degassing of electrolytes (a) vacuum soaking of electrodes inside the electrolytes (b). 109

Figure 3.21: Configurations of electrochemical cells. (a) Schematic illustration of the T-type Swagelok cell (b) actual image of an example of the T-type Swagelok cell arrangement. Schematic of electrode geometry for (c) 3-electrode cell configuration (d) 2-electrode cell (prototype device) configuration. 112

Figure 3.22: (a) Prototype device with Ti current collectors, used for the assembly of 2-electrode cells without electrode potential monitoring (b) Cyclic voltammogram (20.0 mV/s scan rate) of 2.0 mol/L KI with AC electrode in the cell pictured in (a): red solid curve (electrolyte volume in cell filled to the specific constant volume) black dashed curve (cell with unfilled volume). 115

Figure 4.1: N_2 Physisorption graphs showing the adsorption/desorption isotherms and pore size distribution calculated by the DFT method for: AC-1 (a and b), AC-2 (c and d), GNP (e and f) respectively. 119

Figure 4.2: Pore size distribution from the DFT method focusing on the mesoporous characteristics of: AC-1 (a) AC-2 (b) GNP (c). 120

Figure 4.3: TGA profile of AC-1, AC-2 and GNP in N_2. Ramp rate: 10 ^{0}C/min. M_{LOSS} is the loss in mass, and T is temperature. 121

Figure 4.4: CVs of EEM cells fabricated with the three different carbon electrodes using 2.0 mol/L KCl, scan rate: 5 mV/s. 123

Figure 4.5: CVs of the AC electrode in (a) 1.0 mol/L KI, (b) 1.0 mol/L KBr (scan rate: 1 mV/s), and EEM-cells containing 1.0 and 2.0 mol/L of (c) KI, and (d) KBr (scan rate: 5 mV/s). 129

Figure 4.6: Performance of the EEM cell of AC electrodes with 2.0 mol/L KI: (a) CVs recorded at 5.0 mV/s with different upper limits of cell voltage (U_L), (b) plots of the positrode (E_+), negatrode (E_-) and zero voltage (E_{0V}) potentials vs U_L with data extracted from the GCD plots of U, E_+ and E_-, recorded at a current load of 0.1A/g, and (c) GCD plots of U, E_+ and E_-, with U_L = 1.5 and current load = 0.1 A/g. 131

Figure 4.7: GCD plots of EEM cells with 2.0 mol/L KI, at U_L = 1.0, 1.2 and 1.4, current load = 0.1 A/g. 133

Figure 4.8: Performance of the EEM cell of AC electrodes with 2.0 mol/L KBr: (a) CVs recorded at 5.0 mV/s with different upper limits of cell voltage (U_L), and (b) plots of the positrode (E_+), negatrode (E_-) and zero voltage (E_{0V}) potentials vs U_L with data extracted from the GCD plots of U, E_+ and E_-, recorded at a current load of 0.1A/g (c) GCD plots of U, E_+ and E_-, with U_L = 1.5 and current load = 0.1 A/g. 134

Figure 4.9: CVs of the AC electrode in 1.0 mol/L KBr, showing (a) the asymmetry in capacitance in two different potential ranges within the CPR, and (b) the occurrence of the Nernstian process, i.e. oxidation of Br^-, at potentials more positive to the CPR. Scan rate: 1.0 mV/s. (c) CVs of the EEM cell of the AC electrodes in 1.0 mol/L KBr recorded with increasing cell voltage limits from 1.0 to 2.0 V. Scan rate: 5.0 mV/s. 139

Figure 4.10:Performance of the EEM bi-electrolyte cell, (−) AC | 2.0 mol/L KOH || 1.0 mol/L KI | AC (+): (a) CVs recorded at 5.0 mV/s with different upper limits of cell voltage (U_L), (b) plots of the positrode (E_+), negatrode (E_-) and zero voltage (E_{0V}) potentials vs U_L with data extracted from the GCD plots of U, E_+ and E_-, recorded at I = 0.1 A/g, and (c) GCD plots of U, E_+ and E_-, with U_L = 1.5 V and I = 0.1 A/g..... 142

Figure 4.11: GCD plots of U, E_+ and E_-, with U_L = 1.8 V and I = 0.1 A/g for: (a) the EEM bi-electrolyte cell (−) AC | 2.0 mol/L KOH || 1.0 mol/L KI | AC (+) (b) EEM cell (−) AC | 2.0 mol/L KBr | 1.0 mol/L | AC (+). 143

Figure 5.1: Electrode capacitance unequalisation and the relative polarisation of electrodes. CVs of AC-1 electrode in 1.0 mol/L KBr (a1) showing the asymmetry of the capacitance (a2) showing the onset of the oxidation of Br^-. Schematic illustration of the polarisation of electrodes with (b) $M_- > M_+$ (c) $M_- < M_+$. 147

Figure 5.2: UEM cells with different negatrode to positrode mass ratios (note that the total electrode mass on each category of cells are equal), (a) (3:4) and (4:3), (b) (1:2) and (2:1), and (c) (1:2.7) and (2.7:1). Overlay of (4:3), (2:1), and (2.7:1). Scan rate: 10 mV/s. 150

Figure 5.3: CVs at different values of U_L for the UEM cells: (a) (3:4) and (b) (4:3), (c) (1:2) and (d) (2:1), (e) (1:2.7) and (f) (2.7:1). Scan rate: 10 mV/s. 151

Figure 5.4: GCD plots comparing the EEM cell (1:1) with other UEM cells with the indicated negatrode to positrode mass ratios. Current load: 0.25 A/g (normalised to the total dry mass of active materials on both the positrode and negatrode). 153

Figure 5.5: CVs at 1.0 mV/s from 0 to 0.9 V vs SCE, for AC-1 electrode after 1,000 successive cycles at 50 mV/s. 154

Figure 5.6: SEM micrographs of AC-1 (a) fresh electrode (b) electrode after 5000 cycles from 0 – 0.9 V vs SCE at 50 mV/s. 155

Figure 5.7: GCD plot for the UEM cell with (3:1) negatrode to positrode mass ratio at different current load (b) Ragone plot calculated from (a), labelled with the applied current corresponding to the current load. . 156

Figure 5.8: GCD plot for the electrodes of the UEM cell with (3:1) negatrode to positrode mass ratio at different current load. 158

Figure 5.9: (a) CV for the (3:1) UEM cell with 1.0 mol/L KBr, U_L = 1.6 V, scan rate: 5 mV/s (b) AC-1 electrode in 1.0 mol/L KBr scanned at the approximate electrode potential range of the positrode and negatrode at U_L = 1.6V, scan rate: 1 mV/s. 159

Figure 6.1: CVs of EEM cells fabricated with the three different carbon electrodes using 2.0 mol/L KCl, scan rate: 5 mV/s. 162

Figure 6.2: CVs of carbon electrode (AC-1) in 1.0 mol/L solutions of LiBr, NaBr and KBr. Scan rate: 1.0 mV/s. 163

Figure 6.3: Size of the crystal and hydrated radii of some common ions. Cations and anions of some salts used in this work are underlined in blue and red respectively. Adapted from: [202]. 164

Figure 6.4: SEM image of GNP **(a)** and TEM image of GNP **(b1)** further resolution of b1 **(b2)**..... 165

Figure 6.5: High resolution SEM image of AC-2 166

Figure 6.6: Wettability of deionised-water and 2.0 mol/L aqueous solutions of LiBr and LiCl on AC-1 **(a)** and GNP electrodes **(b).** 166

Figure 6.7: X-ray photoelectron spectra for (a) AC-2 (b) GNP; De-convoluted XP spectra for the O 1s core for (c) AC-2 (d) GNP. 168

Figure 6.8: Surface profile of AC-1 **(a)** and GNP **(b)** 169

Figure 6.9: CVs of EEM cells with GNP and AC-2 electrodes using inert 2.0 mol/L KCl (a) and active 2.0 mol/L KBr (b) respectively. Scan rate: 5 mV/s. 171

Figure 6.10: CV of AC-1 and GNP in 1.0 mol/L KBr **(a)** corresponding change in mass of redox species with electrode potential for AC-1 and GNP in 1.0 mol/L KBr **(b)**. Scan rate: 5.0 mV/s..... 173

Figure 6.11: Multiple cells under tests with the multichannel electrochemical workstation..... 176

Figure 6.12: CVs at different upper voltage limits for EEM cells with varying concentration of LiBr assembled with: AC-1 U_L = 1.6 V **(a),** 1.8 V **(b)** 2.0 V **(c)** and GNP U_L = 1.6 V **(d)**, 1.8 V **(e)** 2.0 V **(f)**. Scan rate: 10.0 mV/s. 177

Figure 6.13: GCD plots at different upper voltage limits for EEM cells with varying concentration of LiBr assembled with: AC-1 at U_L = **(a)** 1.6 V **(b)**

1.8 V **(C)** 2.0 V AND GNP AT U_L = **(D)** 1.6 V **(E)** 1.8 V AND **(F)** 2.0 V. CURRENT LOAD: ±0.5 A/G (CA. ± 15 MA OF APPLIED CURRENT)..... 178

FIGURE 6.14: MECHANISM OF CHARGE COMPENSATION WITHIN THE PORE OF CARBONS FOR CHARGE STORAGE SHOWING: COUNTERION ADSORPTION (A) ION SWAPPING (B) CO-ION EXPULSION (C). ADAPTED FROM [222]. 181

FIGURE 6.15: SOLVATION STRUCTURE OF ION-PAIRS (A) HYDRATION SHELL CONTACT TYPE (B) SHARED HYDRATION SHELLS (C) ION CONTACT TYPE [31]. 182

FIGURE 6.16: (A1) CV AT DIFFERENT U_L FOR 1M-LIBR-GNP (A2) THE *U VS.T AND E VS. T* RESPONSE OBTAINED FROM THE CV AT U_L = 1.0 V, SCAN RATE: 10 MV/S. CVS FOR THE CELL: (B) 2M-LIBR-GNP (C) 4M-LIBR-GNP AT DIFFERENT U_L, SCAN RATE: 10 MV/S. 184

FIGURE 6.17: CVS FOR EEM CELLS WITH AC-2 AS ELECTRODES AT DIFFERENT VALUES OF U_L (A) 1M-LIBR-AC-2 (B) 2M-LIBR-AC-2 (C) 4M-LIBR-AC-2. SCAN RATE: 10 MV/S. 185

FIGURE 6.18: GCD OF 2M-LIBR-AC-1 AND 2M-LIBR-GNP AT U_L = 1.6 V AND I = 0.25 A/G..... 186

FIGURE 7.1: SCHEMATIC REPRESENTATION OF THE KINETIC PROPERTIES OF THE IMPEDANCE SPECTRA OF A REPRESENTATIVE (IDEAL) SUPERCAPACITOR. 191

FIGURE 7.2: SCHEMATIC REPRESENTATION OF: SUPERCAPACITOR MADE OF POROUS ELECTRODES **(A)** INNER POROUS STRUCTURE OF THE CARBON ELECTRODE SHOWING THE CONCENTRATION AND POTENTIAL GRADIENT WITHIN THE HELMHOLTZ LAYER OF MICROPORES [63] **(B)** EQUIVALENT CIRCUIT REPRESENTING THE DISTRIBUTED CAPACITANCE WITHIN THE POROUS-MATRIX OF THE CARBON AS A TRANSMISSION LINE **(C)**. 193

FIGURE 7.3: NYQUIST PLOTS AND CORRESPONDING EXPANDED VIEW OF THE HIGH- TO MID-FREQUENCY REGIONS OF SUPERCAPATTERIES WITH DIFFERENT CONCENTRATION OF LIBR FOR EEM CELLS USING **(A)** AC-2 **(B)** GNP. (U) I.E. APPLIED UPPER LIMIT OF CELL VOLTAGE U_L = 1.6 V. 194

FIGURE 7.4: BODE PLOTS OF SUPERCAPATTERIES WITH DIFFERENT CONCENTRATION OF LIBR FOR EEM CELLS USING AC-2 AND GNP AS ELECTRODES **(A)** REAL CAPACITANCE VS. FREQUENCY **(B)** IMAGINARY CAPACITANCE VS. FREQUENCY. (U) I.E. APPLIED UPPER LIMIT OF CELL VOLTAGE U_L = 1.6 V. 194

FIGURE 7.5: PERFORMANCE METRICS OBTAINED FROM IMPEDANCE ANALYSIS OF EEM CELLS WITH EITHER AC-1 OR GNP ELECTRODES, AT VARYING CONCENTRATION OF LIBR; (A) R_{ESR} (EQUIVALENT SERIES RESISTANCE) **(B)** R_{CTR} (CHARGE TRANSFER RESISTANCE) **(C)** T (RESPONSE TIME) **(D)** C_{SURF} (SURFACE CAPACITY EXPRESSED IN F/CM^2). U_L = 1.6 V..... 195

FIGURE 7.6: NYQUIST PLOTS AT DIFFERENT VALUES OF U_{CELL} **(A)** AND VARIATION OF R_{CTR} (CHARGE TRANSFER RESISTANCE) WITH CELL VOLTAGE **(B)** FOR AC-2 AND GNP EEM CELLS USING 2.0 MOL/L LIBR. 199

FIGURE 7.7: CYCLING STABILITY OF EEM CELLS USING 2.0 MOL/L LIBR WITH AC-2 OR GNP ELECTRODES, CURRENT LOAD = 0.5 A/G (± 15 MA OF APPLIED CURRENT) AT UPPER CELL VOLTAGE LIMITS U_L OF: 1.6 V **(A)** 1.8 V **(B)** 2.0 V **(C)**. EOLC: END OF LIFE CRITERION..... 201

FIGURE 7.8: CVS OF DIFFERENT EEM CELLS SHOWING THE EFFECTS OF THE CATIONS: 2M-LIBR-GNP **(A1)**, 2M-LIBR-AC-2 **(A2)**, 2M-NABR-GNP **(B1)**, 2M-NABR-AC-2 **(B2)**, 2M-KBR-GNP **(C1)**, AND 2M-KBR-AC-2 **(C2)**. 203

FIGURE 7.9: ROLE OF CATIONS ON THE RATE PERFORMANCE OF EEM CELLS USING DIFFERENT ALKALI BROMIDES AS DRS WITH AC-2 OR GNP AS ELECTRODES. DATA CALCULATED FROM GCD PLOTS AT DIFFERENT CURRENT LOAD (±I) WITH U_L = 1.6 V. 205

FIGURE 7.10: COMPARISON OF THE PERFORMANCE OF 4M-LIBR-GNP AND 2M-$MGBR_2$- (A) CV WITH U_L = 1.6 V AND SCAN RATE = 10 MV/S (B) NYQUIST PLOT TAKEN AT U_L = 1.6 V (C) CORRESPONDING BODE PLOT TO (B)..... 207

FIGURE 7.11: COMPARISONS BETWEEN EEM CELLS FABRICATED WITH GNP AND USING THE INERT ELECTROLYTES 1.0 MOL/L $MGSO_4$ OR NA_2SO_4 WITH OR WITHOUT 0.15

mol/L KBr as additive (a) CV at U_L = 1.6 V, scan rate: 10 mV/s. (b) C'' vs f (Bode plot) at U_L = 1.6 V. 210

Figure 8.1: CVs of carbon material (AC-1) loaded in a Pt-MC electrode in an electrolyte comprising of 0.1 mol/L MH_2Q or H_2Q in 1.0 mol/L H_2SO_4. Scan rate: 10.0 mV/s. 215

Figure 8.2: CVs of AC-1 EEM cells with equal volumes of inert 1.0 mol/L H_2SO_4 and 1.0 mol/L H_2SO_4 comprising of either 0.25 mol/L H_2Q or MH_2Q. Scan rate: 5.0 mV/s. 216

Figure 8.3: Illustration of the reaction mechanism of H_2Q in: (a) buffered or unbuffered H_2O with $[H^+] > [Q]$ (b) unbuffered media with $[H^+] < [Q]$ (c) aprotic media [114]. 217

Figure 8.4: Illustration of the reaction mechanism of (a) H_2Q and (b) MH_2Q in unbuffered acid electrolyte. 218

Figure 8.5: (a) UV-vis spectra showing the change in absorbance after the adsorption of Q or MQ from the solution by AC-1 electrode sheet (b) calibration curve for the correlation between the measured absorbance and the concentration of analyte solution for Q and MQ. 222

Figure 8.6: CVs of AC-1 EEM cells with equal volumes of inert 1.0 mol/L $TEABF_4$ in acetonitrile (AN) and comprising of either 0.25 mol/L H_2Q or MH_2Q. Scan rate: 10 mV/s. 224

Figure 8.7: Pt-micro-cavity (Pt-MC) electrode (a) schematic illustration (b) and (c) optical micrograph (d) geometric description (e) scanning electron micrograph of the insides of the cavity (f) Pt-MC as the working electrode (WE), SCE as reference electrode (RE) and Pt foil as counter electrode (CE) in a 3-electrode cell which was pictured during electroanalysis as can be seen from the generation of species from the Pt-MC electrode. 227

Figure 8.8: Representative CV at different scan rates of the bare Pt-MC electrode in 4 mmol/L ferrocene dissolved in acetonitrile containing 0.3 mol/L of $TBABF_4$. 228

Figure 8.9: Microbalance (with a measuring range from 1.0 to 2000.0 μg) for direct weighing of the loaded MCE. 228

Figure 8.10: CVs at different scan rates of a Pt-MC electrode loaded with AC-1 powder in 1.0 mol/L Na_2SO_4. 230

Figure 8.11: Pt-MC electrode loaded with AC-1 (a) CV in 1.0 mol/L Na_2SO_4 with or without 0.25 mol/L MH_2Q scan rate: 20 mV/s. (b) CV and (c) GCD in 0.25 mol/L MH_2Q in 1.0 mol/L Na_2SO_4. 232

Figure 8.12: Pt-MC electrode loaded with AC-1 in 0.25 mol/L $MH_2Q \cdot$ 1.0 mol/L H_2SO_4 (a) CV, scan rate: 10 mV/s (b) GCD plot, I = 1.0 A/g. 232

Figure 8.13: CVs of EEM cells containing 0.25 mol/L MH_2Q in (a) 1.0 mol/L Na_2SO_4 (b) 1.0 mol/L H_2SO_4. Scan rate: 10 mV/s. 233

Figure 8.14: CVs showing the *IR* correction procedures of the Pt-MC electrode (a) bare Pt-MC electrode (b) loaded (GNP) and bare Pt-MC electrode and (c) *IR* correction of loaded Pt-MC electrode (scan rate: 10 mV/s). Electrolyte is 0.25 mol/L MH_2Q in 1.0 mol/L H_2SO_4. 235

Figure 8.15: CVs of Pt-MC electrode loaded with (a1) GNP (b1) AC-2 and the 236

Figure 8.16: Comparison of the loaded Pt-MC electrodes (a) CV at 50 mV/s (b) Nyquist plot at 0.4 V vs SCE. 236

Figure 8.17: Raman spectra for: GNP (a) and AC-2 (b). Comparison of the I_D/I_G ratio for both GNP and AC-2 (c). 238

Figure 9.1: CVs showing the maximum possible capacitive potential range of AC electrode in common aqueous electrolytes of different pH. Scan rate: 5 mV/s. 243

Figure 9.2: CVs of the AC electrode in 2.0 mol/L KOH negalyte and 1.0 mol/L KI posilyte. Scan rate: 1 mV/s. 244

Figure 9.3: CVs of (-)AC | 2.0 mol/L KOH || 1.0 mol/L KI | AC(+) bi-electrolyte supercapatteries with different membrane electrolytes. U_L = 1.0 V, scan rate: 5 mV/s. 245

Figure 9.4: CVs showing rate performance for (-)AC | 2.0 mol/L KOH || 1.0 mol/L KI | AC(+) with either 1.0 or 3.0 mol/L KCl as membrane electrolyte: (a) 5 mV/s (b) 10 mV/s (c) 20 mV/s (d) 50 mV/s. 246

Figure 9.5: CVs for the bi-electrolyte cells (-)AC | 2.0 mol/L KOH || 1.0, 2.0 or 3.0 mol/L KI | AC(+). U_L = 1.5 V, scan rate: 5 mV/s..... 247

Figure 9.6: Self-discharge properties of the bi-electrolyte cells (-)AC | 2.0 mol/L KOH || 1.0, 2.0 or 3.0 mol/L KI | AC(+). U_L = 1.5 V. 248

Figure 9.7: Correlating the electrode potential from the CV of the AC in KI (a) with the GCD plots showing the polarisation of the positrode and negatrode (b1) of the bi-electrolyte supercapattery: (-)AC | 2.0 mol/L KOH || 2.0 mol/L KI | AC(+) (b) U_L = 1.5 to 2.0 V, $\pm I$ = 0.1 A/g. 250

Figure 9.8: CV of Pt disc electrode (Φ = 3.0 mm) in 0.5 mol/L $TBAPF_6$ dissolved in CH_2Cl_2. Scan rate: 10 mV/s. 252

Figure 9.9: CVs of the AC electrode in 2.0 mol/L KOH negalyte and 1.0 mol/L TBABr in CH_2Cl_2 water-immiscible posilyte. Scan rate: 5.0 mV/s..... 253

Figure 9.10: Set-up for testing the polarisation of the immiscible electrolyte junction (a) schematic (b) actual experimental layout. 253

Figure 9.11: Impedance spectra across the (3.0 mol/L KCl)-(1.0 mol/L TBABr in CH_2Cl_2) junction. 254

Figure 9.12: GCD plot of the immiscible bi-electrolyte cell: (-)AC | 2.0 mol/L KOH || 1.0 mol/L TBABr in CH_2Cl_2 | AC(+) (a) variation of electrode potential with U (b) variation of electrode potential and cell voltage at U_L = 2.0 V. $\pm I$ = 1.0 A/g. (c) Cycle number vs. Energy retention on GCD cycling at $\pm I$ = 1.0 A/g and U_L = 1.8 V (Inset) GCD plot at 10TH and 6000TH cycle..... 256

Figure 9.13: Illustration of the liquid interface at the junction of two immiscible electrolytes (a) polarisable interface e.g. (KCl in water)-(TBABr in CH_2Cl_2) (b) non-polarisable interface e.g. (TBABr in water)-($TBABF_4$ in CH_2Cl_2) [266, 267]..... 257

Figure 9.14: Self-discharge of the cell: (-)AC | 2.0 mol/L KOH ||• 1.0 mol/L TBABr in CH_2Cl_2 | AC(+), showing the variation of potential of the positrode and negatrode from a U_L of 1.8 V. 259

Figure 9.15: Comparing the rate of SD of the conventional KBr cell, and bi-electrolyte cells with KBr as posilyte, with or without immiscible electrolytes. 260

Figure 9.16: GCD plot of the conventional cell with KBr redox electrolyte and the immiscible electrolyte cell with (TBABr in CH_2Cl_2) as posilyte. U_L = 2.0 V, $\pm I$ = 0.5 A/g. 261

Figure 9.17: Schematic illustration of the modified supercapattery with MH_2Q as DRS, CV from this design is shown in Fig. 9.18b. 263

Figure 9.18: CVs of cells with 0.25 MH_2Q in 1.0 mol/L H_2SO_4 (a) conventional design of cells (b) novel design utilising pre-cycled positrode and negatrode, with Nafion membrane soaked in 1.0 mol/L H_2SO_4. Scan rate: 10 mV/s. 264

Figure 10.1: Schematic illustration of industrial production-line of commercial supercapacitors (grey boxes), point where findings from this research as presented in various chapters of this thesis could be applied in practice (blue boxes). 271

ABBREVIATIONS AND SYMBOLS

AC	Activated carbon
BET	Brunauer-Emmet-Teller
C_{cell}	Specific cell capacitance
C_{dl}	Double layer capacitance
CE	Counter electrode
CF	Capacitive Faradaic
C_Q	Specific cell capacity (expressed in F/g)
C_{sp}	Specific electrode capacitance
CV	Cyclic voltammogram
DFT	Density functional theory
DRS	Dissolved redox species
E	Electrode potential
EC(s)	Electrochemical capacitor(s)
EDL	Electric double layer
EDLC	Electric double layer capacitance
EEM	Equal electrode mass
EES	Electrochemical energy storage
EIS	Electrochemical impedance spectroscopy
EQCM	Electrochemical quartz crystal microbalance
FC	Faradaic capacitive
GCD	Galvanostatic charge-discharge
GNP	Graphene nanoplatelets
H_2Q	Hydroquinone
i	current (in mA or A)
I	mass normalised current (in mA/g or A/g)
j	current density (in mA/cm^2)
ME	Membrane electrolyte
MH_2Q	Methyl hydroquinone

N_0	Concentration
NFC	Non-Faradaic Capacitive
PPD	p-phenyldiamine
PTFE	Poly(tetrafluoroethylene)
Pt-MC	Platinum micro-cavity
Q_{eff} or η_Q	Charge efficiency
RE	Reference electrode
REG	Renewable Energy Generation
SCE	Standard calomel electrode
SD	Self-discharge
SEM	Scanning electron microscopy
SSA	Specific surface area
TBABr	Tetraethylammonium bromide
$TBAPF_6$	Tetraethylammonium hexafluorophosphate
$TEABF_4$	Tetraethylammonium tetrafluoroborate
TEM	Transmission electron microscopy
U	Cell voltage
UEM	Unequal electrode mass
UV-vis	Ultraviolet-visible
VDE	Voltage determining electrode
W	Energy
W_c	Specific charging energy
W_d or W_{sp}	Specific (discharge) energy
WE	Working electrode
W_{eff} or η_{eff}	Energy efficiency
wt.	Weight
XPS	X-ray photoelectron spectroscopy

CHAPTER 1: BACKGROUND OF THIS RESEARCH

1.1 The role of energy storage in environmental sustainability

The gradual implementation of a low- to zero-carbon economy is an important strategy to achieve environmental sustainability. However, attaining this goal is extremely challenging because concerted global efforts are required to reduce human dependence on fossil fuels.

In general, harnessing renewable sources of energy (RSE) is an important means of reducing the oxidation of carbon-based fuels for energy. Nevertheless, the shortcomings resulting from the intermittency of these RSE has to be mitigated. Accordingly, integrating energy storage to renewable energy generation/harvesting (REG) systems is a viable means of optimally utilising RSE. Additionally, optimal energy stores would promote decentralized energy distribution which could aid the reduction of power transmission losses [1], and also encourage the local generation of energy [2]. Indeed, various alternatives to future energy sustainability measures such as the development of the hydrogen economy [3], would also rely largely on optimal energy stores.

Fundamentally, an energy store converts the input energy into another form for storage, and on withdrawal, it delivers energy in the same or different form as the input. For example: in a rechargeable battery, electricity is used to create a chemical change in appropriate materials, and this in turn can then be extracted as electrical energy when needed.

It is important to note that the displayed properties of energy stores i.e. the maximum possible energy, power, or other performance metric is limited by fundamental physical and/or chemical principles as well as design constraints.

For example, the interaction between the polarised electrode and constituents of the dielectric media in capacitors (electrostatic or electrolytic)

and some categories of electrochemical capacitors (aka supercapacitors) is predominantly physical (i.e. electrostatic). Hence, withdrawal of the stored electrical charge is very fast, and can be repeated through many cycles. In line with this, these devices are characterised by high power and long cycle lives. On the other hand, electrochemical storage batteries which store charge through a change in the chemical properties of the materials generally display a comparatively lower rate of energy delivery. Moreover, they can store more charge because some battery materials are characterised by high capacity-to-mass ratios. Therefore, in order to use these energy stores to provide electrical energy, these fundamental principles have to be understood and engineered for optimal performance.

Regarding environmental sustainability, the importance of generating electricity from renewable energy sources cannot be overemphasized. This is because, as shown in Fig. 1.1a, electricity accounted for ca. 18% of the energy consumed as at 2016. Moreover, this has been on a continual rise, because it has been estimated that the global demand for electricity is increasing at a higher rate compared to other forms of energy [4, 5]. Although Fig. 1.1b shows that the share of renewable energy generation (geothermal, solar, wind, pumped hydro etc.) has steadily increased over the years, fossil fuels (coal, oil and natural gas) are still the major primary sources for electrical power generation.

Consequently, in order to increase the proportion of electricity generated from renewable sources, it would be necessary to deploy optimal energy stores in a large scale. This process of scaling up usually involves the connection of large battery or supercapacitor cells/units into the so-called "energy storage banks" [6], or the construction of high volume energy stores like pumped hydropower [7]. To achieve this, the energy stores must be appropriately sized through detailed understanding of their performance metrics e.g.: energy and power.

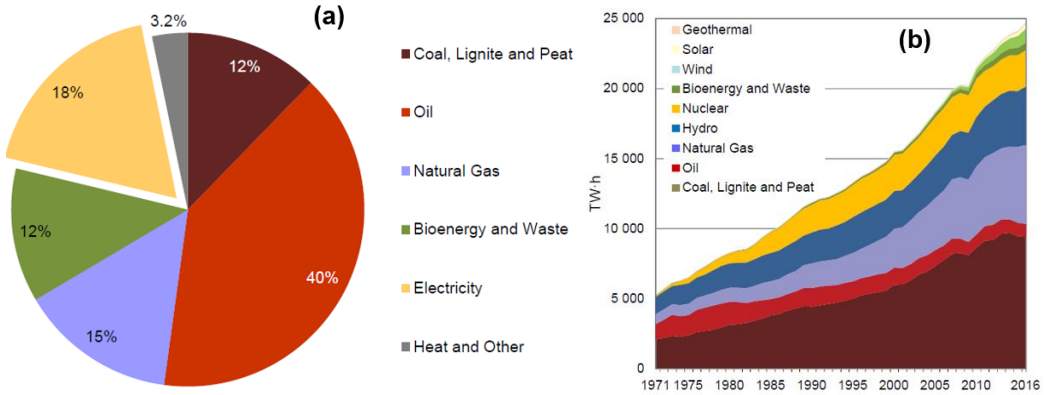

Figure 1.1: Percentage of global energy consumption by source in 2016 (a) Breakdown of global electricity production by source from 1971 to 2016 (b) [4].

Figure 1.2 presents a modified Ragone plot for some major energy storage technologies that can be used to provide electricity. This plot gives the energy of the device (in terms of time of discharge at rated power) on the vertical axis and the power rating on the horizontal axis. Moreover, an additional information that can be obtained from this chart is that the areas of the boxes approximately corresponds to the relative modular size of the technology required to attain the estimated power/energy in the chart. Also, the chart is divided into three broad categories of electricity requirements.

From Fig. 1.2, it is obvious that adequate sizing of mature technologies such as lithium-ion or lead-acid batteries may be designed to service a wide range of electricity requirements. However, there are serious constraints for example over-heating and thermal runaway which could become aggravated especially when the module sizes are very large [8, 9]. On the other hand, practical installations of sodium-sulphur batteries which generally delivers high power and energy, with comparably smaller module sizes than Li-ion batteries, usually require elevated temperatures [10]. It should be highlighted that fuel cells are actually energy conversion devices, moreover, they are useful for grid support or bulk power management.

Generally, high energy supercapacitors can be used for reserve and fast response services, whilst high power supercapacitors can serve the needs of transmission and grid support systems. Pumped hydropower and compressed air storage are very good for bulk power management, however, their construction footprints and possible ecological impacts have to be addressed [7, 10].

In practice, it should be pointed out that various classes of these technologies are in different stages of maturity. For example, cryogenic systems are still in their development phase [11], and although sodium-sulphur batteries are commercially available, its rate of deployment is quite low [12]. Furthermore, the cost and environmental impacts of these energy storage technologies vary widely, and are strongly dependent on the types of materials and the methods used in their processing.

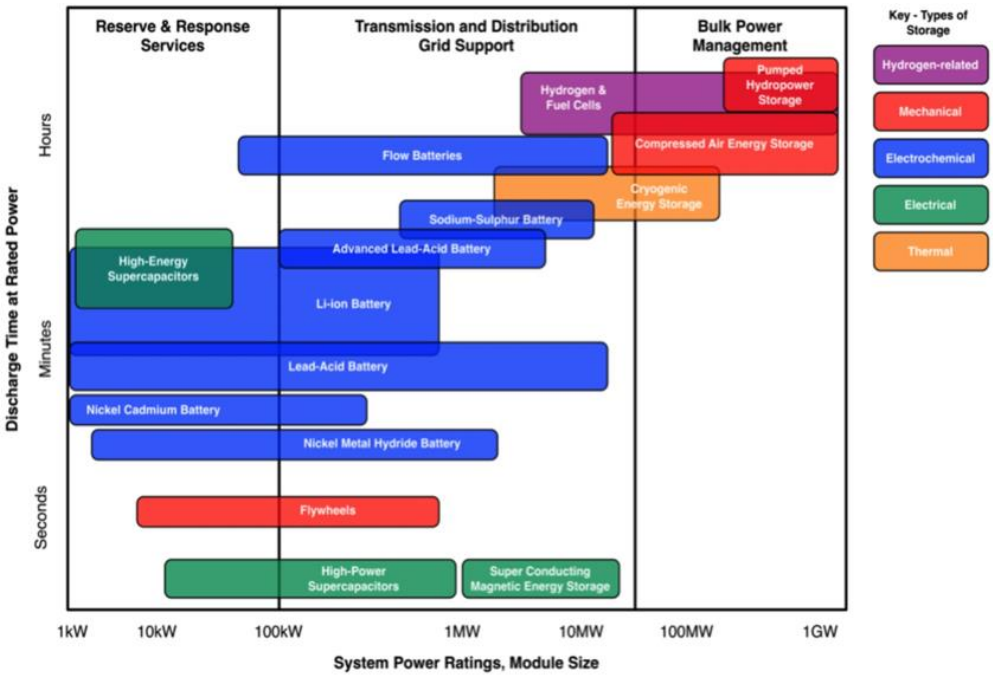

Figure 1.2: General energy and power characteristics of electrical energy storage systems and their applications for large-scale electrification [13].

Moreover, what is of importance to the research community is the continual quest to "push the envelope" in terms of increasing the performance,

and reducing the cost and environmental impacts of these technologies. For instance in the case of supercapacitors, efforts are been made to increase the energy without having adverse effects on the power characteristics.

Accordingly, a number of strategies have been adopted to achieve this. One such method is the integration, into a single unit, of the merits of high power from a supercapacitor and high energy displayed by a battery. This category of device has been variously known as: hybrid capacitors, asymmetric capacitors, etc. Nevertheless, we have always promoted the term supercapattery (SUPERcapacitor-baTTERY) [14-16], to describe these class of devices. This was done in order to adequately capture their characteristics with a self-explanatory nomenclature, and to clearly distinguish it from a "hybrid device or system" which could mean other things such as the external connection between a battery and a supercapacitor in an electrical circuit such as in the power-trains of electric vehicles, etc. Indeed the use of this terminology is gradually gaining acceptance as evident from some recent publications [17].

The focus of this thesis is to study the mechanisms and designs of supercapacitors which displays the properties of supercapatteries on the incorporation of redox electrolytes.

1.2 Introduction to electrochemical energy storage devices

In general, electrochemical energy storage (EES) devices may be represented by the illustration in Fig. 1.3. This generalised schematic shows that the active material on the positive electrode (positrode) and negative electrode (negatrode) can be in contact with, or contain the positive electrolyte (posilyte) and negative electrolyte (negalyte) respectively. Also, these two interfaces are physically separated by the separator which could either be porous, or an ionic conductor.

The current collector is the point of contact between the electrode/electrolyte components and the external connections to the load and/or power supply units. More importantly, the current collector must have very high electronic conductivity.

In general, there are three types of electrode that have been commonly used in EES devices. Firstly, each of the two electrodes can be an electronic conductor which is electrochemically and chemically inert in the range of working potentials. A typical example is the activated carbon electrode in the electric double layer (EDL) capacitor. The second type of electrode is typified by an active metal electrode, e.g. the lead (Pb) metal negative electrode in the lead-acid rechargeable battery, and the zinc (Zn) metal negative electrode in the alkaline zinc-manganese dioxide rechargeable battery.

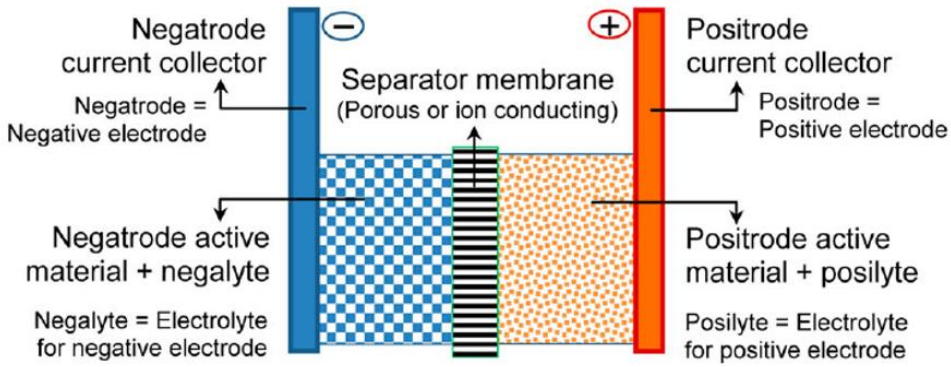

Figure 1.3: General illustration of an electrochemical energy storage device [16].

There is also ongoing effort to directly use lithium (Li) metal and aluminium (Al) metal electrodes to make rechargeable battery with higher energy capacity. It should be pointed out that lithium metal has long been used as the negative electrode in primary battery, but this has not been employed for commercial rechargeable battery [18]. It is also important to note that in a recently reported rechargeable battery, liquid metals were used as both the

negative and positive electrodes [19, 20]. The third type of electrode is composed of two parts, an inert electronic conductor as the current collector on which an electrochemically active material is loaded. This type is most widely used in commercial rechargeable batteries, such as the copper/graphite negative electrode and lithium cobalt oxide/aluminum positive electrode in lithium-ion battery.

This research is focused on improving the performance of electric double layer (EDL) capacitors. Accordingly, the current collectors used were either rods or sheets of graphite or titanium which are inert in the electrolytes investigated, whilst the electrode active materials were carbonaceous.

1.3 Introduction to Redox electrolytes for electrochemical capacitors

Except stated otherwise, throughout this dissertation the electrode is in the solid phase, whilst the electrolyte is in the liquid phase, and the separators are porous membranes.

Generally, charge storage mechanisms at the electrode | electrolyte (E|E) interface can be broadly categorized into two types. One of these involves electron transfer from one state of charge and/or phase to the other (faradaic mechanisms) whilst the other mainly involve electrostatic separation and charge distribution at the electric double layer (EDL), without charge transfer across the interface. For example, consider the generalised faradaic reactions in Equation 1.1:

$$S_1 + ne + nM^{z+} = S_2 \quad (1.1a),$$

$$S_1 + ne = S_3 + nA^{z-} \quad (1.1b).$$

Where in Eq. 1.1, S_I (I = 1, 2 and 3) is a solid phase (electrode), e is the electron, M^{z+} and A^{z-} are ions in the liquid phase (electrolyte) and corresponds to cations and anions respectively [21]. Referring to Eq. 1.1a, there could be

mass transport of M^+ or A^- across the phase boundary within the electrode | electrolyte (E|E) interface.

For example in the practical case of charge storage in copper-hexacyanoferrate $KCuFe(CN)_6$, K^+ in the electrolyte would interact with this active electrode material coated on the inert electrode substrate through mass transport across the phase boundary (Eq. 1.2a) [22]. Considered only from a thermodynamic standpoint, H^+ ions in solution also undergoes similar interactions with hydrous RuO_2 active electrode material (Eq. 1.2b).

$$KCuFe^{III}(CN)_{6(s)} + xe + K^+_{(aq)} = K_{1+x}Cu[Fe^{II}(CN)_6]_x[Fe^{III}(CN)_6]_{1-x(s)} \quad (1.2a),$$

$$RuO_x(OH)_{y(s)} + ze + zH^+ = RuO_{x-z}(OH)_{y+z(s)} \quad (1.2b).$$

However, it should be emphasized that these two faradaic processes which both involve the transfer of charge across the E|E interface are fundamentally different. This is because, whilst the electrical response of the $KCuFe(CN)_6$ electrode material displays peak-shaped cyclic voltammogram (CV) as shown in Fig. 1.4a, the CV of RuO_2 is approximately rectangular. As would be later explained in Ch. 2 (Literature Review), this difference in the electrical response of these electrode materials may be linked to their electronic structures as described with the aid of the band model.

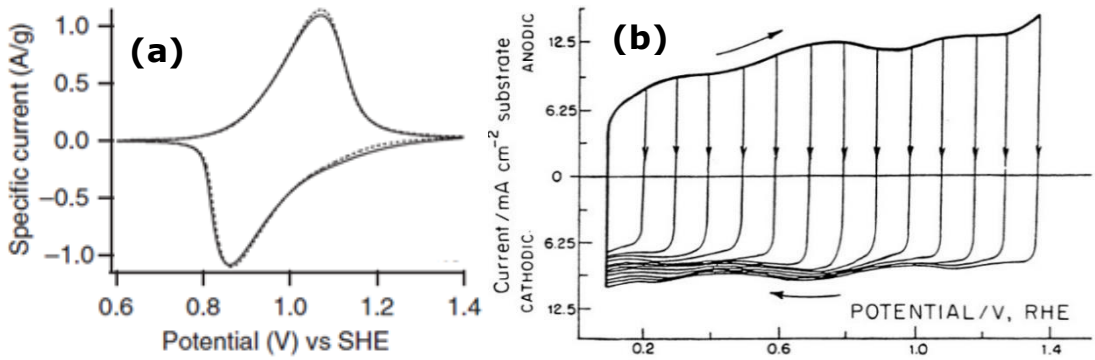

Figure 1.4: CVs of (a) $KCuFe(CN)_6$ in 0.01M HNO_3 ·1M KNO_3 (scan rate: 1 mV/s) [22] (b) hydrous RuO_2 in 0.1M H_2SO_4 (scan rate: 50 mV/s) [23].

For the purpose of the present discussions, what is of importance is that both the non-capacitive faradaic (NCF) mechanism in Fig 1.4a and the capacitive faradaic (CF) mechanism in Fig.1.4b, as described by Eq. 1.2a and 1.2b respectively, took place in inert electrolytes. This means that although the ionic components of the electrolytes for example K^+ in Eq. 1.2a or H^+ in Eq. 1.2b contributed to the charge storage mechanisms, these solution species themselves do not undergo any redox reactions. This is because as explained already, the redox reactions occurred within the lattice of both electrodes.

Now, consider the instance described in Eq. 1.3 in which dissolved species in the electrolyte undergo redox reactions i.e. accept or give out electrons from or to the electrode respectively:

$$O + e = R \qquad (1.3).$$

In Eq. 1.3, O and R are the oxidised and reduced forms of the dissolved species respectively.

In general, from Eq. 1.3, if this redox reaction occurred within the pores of high surface area carbons, the interfacial charge capacity can be enhanced through various processes of electrosorption or chemisorption accompanied by solvation/de-solvation, and adsorption/desorption of the products of the redox reactions. For instance, in equation 1.4a, $FeSO_4$ dissolved in H_2SO_4 undergoes the reaction involving the Fe^{2+}/Fe^{3+} redox couple at the carbon interface, resulting to enhanced interfacial charge capacity (see Fig. 1.5).

Likewise in equation 1.4b the redox active Cu^{2+} ion (from $CuCl_2$ dissolved in HNO_3) can be chemisorbed due to redox reactions of this cation at the carbonyl group on the surface of carbon nanomaterial [24]. Such electrode charging mechanisms due to dissolved redox species (DRS) can also be observed when the interface has a redox reaction from the electrode as well as the electrolyte, such as that given in equation 1.4c [25].

$Fe^{2+} = Fe^{3+} + e$ (1.4a),

$Cu^{2+} = Cu^{+}_{(surface\ adsorbed)} + e$ (1.4b),

$[NiO + OH^{-} = NiOOH + e]_{(electrode\ lattice)}$ | $[Fe(CN)_6^{3-} + e = Fe(CN)_6^{4-}]_{(electrode\ |\ electrolyte\ interface)}$ (1.4c).

As illustrated in Fig. 1.5, the EDL charge storage of the carbon electrode typified by the rectangular CV (i.e. non-faradaic capacitive mechanism) is transformed to a peak shaped CV indicative of the faradaic reaction of the dissolved redox species. This obviously resulted to an enhancement of the charge capacity at the E|E interface. This enhancement in capacity through the use of dissolved redox species is one of the principal factors that underpins the adoption of redox electrolytes in supercapacitors.

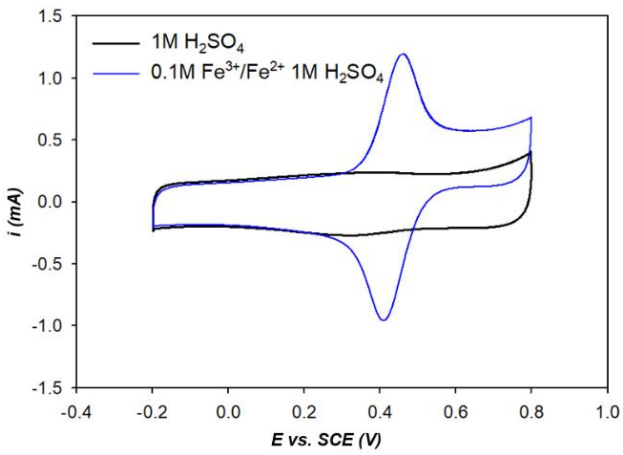

Figure 1.5: Comparison of the CV of a carbon (EDL) electrode: in an inert electrolyte 1.0 mol/L H_2SO_4 (black curve), and in the inert electrolyte containing 0.1 mol/L $FeSO_4$ redox additive (blue curve). Scan rate: 10 mV/s.

1.4 Motivation for this research

The principal motivation to investigate the use of redox electrolytes in supercapacitors is because modification of the electrolyte is a relatively facile approach to improve device performance. Thus, redox species that would otherwise be difficult to graft on electrodes may be incorporated inside the

electrolyte without the need for immense modifications of the device design and/or manufacturing process.

Furthermore, the use of in-electrolyte charging mechanisms could exploit the high conductivity of aqueous electrolytes thereby promoting the commercialisation of supercapacitors with water-based electrolytes – which are more environment friendly than the organic electrolytes currently in use.

1.5 Aims and objectives of this research

The aim of this research is to use fundamental electrochemical device engineering principles to investigate the use of redox electrolytes in electric double layer (EDL) capacitors. Accordingly, the principal objectives of this research are to:

1. Understand the fundamental characteristics of the electrode | redox-electrolyte interface, and utilise these findings to design optimal EDL capacitors with redox electrolytes. Electrode materials investigated are commercial carbons that display different porous and physicochemical properties, whilst redox electrolytes were selected through fundamental considerations of their thermodynamic and interfacial electrochemical properties.
2. Investigate the characteristics of the assembled EDL capacitors with redox electrolytes, and understand various factors that affect their performance metrics. Accordingly, carry out a rigorous correlation between the electrode polarisation, porosity, and surface properties relative to the thermodynamics and solvation characteristics of the dissolved ions.
3. Build prototype devices with various innovative strategies to understand how device-level performance can be improved. Some performance metrics that were investigated and improved included: charge capacity, energy, and self-discharge.

1.6 Structure of this Thesis and summary of original contributions

Chapter 2 of this thesis gives a detailed review of relevant literatures on charge storage mechanisms, and the use of redox electrolytes in supercapacitors. Based on fundamental considerations, a conceptual description for the charge storage mechanisms of redox electrolytes within porous electrode materials was proposed in this chapter. Furthermore, general misconceptions of the charge storage mechanisms which is commonplace in majority of the early and some recent literatures on redox electrolytes were appraised in this chapter.

Chapter 3 presents a description of the research approach together with the experimental procedures and techniques utilised in this research.

The results and discussions of the major findings from this research are presented in Chapters 4 to 9.

Chapter 4 details some fundamental investigations on the electrode | redox-electrolyte interface, and also reports on some properties of the capacitive and Nernstian storage mechanisms of carbon electrodes and their effects on the device features and performance.

In this chapter, conclusive confirmation of the redox shuttling in devices using KI was demonstrated, and for the first time the unequalisation of electrode capacitance was linked to the optimal utilisation of KBr as redox electrolyte. Also, the conjoined role of the thermodynamics and kinetics of the redox reaction and the transport of the redox reaction products coupled with the polarisation of activated carbon electrodes were for the first time, used to rigorously describe the storage features of cells using KI and KBr. Accordingly, this chapter demonstrated the fundamental basis of some important properties of devices with DRS in general.

In Chapter 5, detailed characterisation of the role of unequal electrode capacitance and the increase in energy of supercapacitors with redox

electrolytes were presented. The discussions and analysis in this chapter gave insights to the pros and cons of arbitrary over-sizing of the counter-capacitive electrode in supercapatteries. These findings are thus of significant practical importance for industrial scale-up of these devices.

Chapters 6 and 7 reports on the investigations of the charge storage properties of redox electrolytes on carbons with different porous and surface physicochemical properties. Whilst Ch. 6 focused on energy performance of these devices, Ch.7 further probes the role of the ionic components of the redox electrolytes on the observed charge storage properties.

In chapters 6 and 7, the detailed properties of DRS with a highly graphitised and mesoporous carbon electrode (i.e. graphene nanoplatelets) were provided for the first time, and comparisons between amorphous and graphitised carbon using halides as DRS were also described in detail for the first time. Furthermore, the role of the dissolved alkali metal cations of the bromides used as redox electrolytes coupled with the properties of the electrodes were given rigorous descriptions. In line with this, novel observations which demonstrates the role of ion-ion interactions in the device performance were reported. These findings are relevant to the practical selection and application of redox electrolytes especially with respect to their potential commercialisation.

Quinonoids have been widely used as redox molecules. Accordingly, in Chapter 8, the properties of two quinonoids used as redox additives to inert electrolytes were studied. In line with this, the quinone moiety with the para methyl substituent i.e. p-methyl-hydroquinone (methyl-hydroquinone) was characterised for the first time as a DRS in acid and neutral aqueous electrolytes.

In this vein, the adsorption of these quinonoids on carbon electrodes were used to ascertain the fundamental properties of their charge storage mechanisms. Furthermore, the interaction between methyl-hydroquinone and

carbon materials was described for the first time with respect to the change in the structural properties of the carbons as revealed through Raman spectroscopy. The observation of a structural origin to the charge storage properties displayed by this DRS is of fundamental as well as practical importance to the use of this and possibly other related DRS.

In a bid to extend the operating voltage of cells using aqueous (or organoaqueous) electrolytes, rigorous investigations on the properties of high-performance bi-electrolyte cells were presented in Chapter 9. Accordingly, a novel bi-electrolyte cell with immiscible electrolytes was described and demonstrated as a viable device engineering strategy for assembling supercapatteries with highly improved performance.

A summary of the significant insights together with perspectives on the broader applications of the major findings from this research were presented in Chapter 10. Additionally, recommendations for future work which could be done to further develop some of the findings obtained in the course of this study were briefly enumerated in this chapter.

CHAPTER 2: LITERATURE REVIEW

2.1 Charge storage mechanisms of electrodes for electrochemical capacitors

As was briefly described in Ch.1, charge storage mechanisms in electrochemical energy storage (EES) devices could be fundamentally defined by the electrical response of the electrode | electrolyte (E|E) interface. Thus, in order to understand the properties of supercapacitors with dissolved redox species (DRS), it is pertinent to appraise the fundamentals of these mechanisms and their role in device performance. Accordingly, this review would first describe the properties of supercapacitors from the standpoint of the charge storage mechanisms, after which detailed descriptions of the applications of redox electrolytes in supercapacitors would be given.

Electrochemical energy storage (EES) devices store charge through one or a combination of two or three mechanisms namely: non-faradaic capacitive (EDL capacitance), capacitive faradaic (pseudocapacitance) or non-capacitive faradaic (Nernstian) (see Fig. 2.1a) [26].

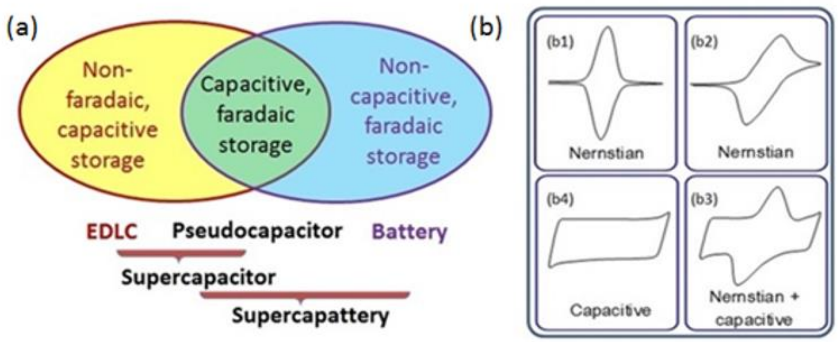

Figure 2.1: (a) Charge storage mechanisms for electrochemical energy storage and their possible device classification. **(b)** Schematic representations of the CVs for Nernstian (b1, b2), mixed Nernstian and capacitive (b3) and capacitive (b4) charge storage mechanisms [17].

Based on these mechanisms, the electrochemical properties of electrodes which could be used in the fabrication of electrochemical capacitors can be categorised under any of the four schematic illustrations given in Fig. 2.1b. The schematic cyclic voltammograms of Fig. 2.1b represents single electrode characterisations (i.e. collected using the three-electrode cell configuration).

2.1.1 Non-faradaic capacitive charge storage mechanism

Figure 2.1(b4) could be used to generally illustrate the electrochemical characteristics of electrodes displaying non-faradaic capacitive storage i.e. EDL capacitance. This is usually due to the electrostatic separation of electrons and ions at the EEI. For example, when ions with an opposite charge to the net-surface charge on a porous carbon electrode (with negligible surface groups) accumulate at the EDL, the electrode is regarded to have stored charge through the NFC mechanism. It is non-faradaic because ideally such an electrostatic interaction between the accumulated ions and the carbon electrode surface does not involve the transfer of electrons crossing the EDL, i,e. the electrode-electrolyte interface. Before the electrical response of this EDL capacitance mechanism is described, a brief discussion of the fundamental principles of charge storage at the EDL is first presented.

It was H. von Helmholtz whom in 1885 provided the first theoretical description of the electric double-layer (EDL) formed on the interface between a conductor and an electrolyte. The ensuing model which was named after him described the EDL as consisting of a layer of charge situated on the surface of the metal and an ionic monolayer formed at the E|E interface (see Fig. 2.2a). In general, these two layers of charge are analogous to an electrostatic capacitor, and the differential capacitance derived from this model is taken to be constant with its value assumed to be independent of the electrolyte concentration and electrode potential:

$$C_{dl} = \frac{\epsilon}{4\pi\delta} \quad (2.1a).$$

In Eq. 2.1 C_{dl} (F), ε (F/m), and δ (m), are the double-layer capacitance, dielectric constant and the separation of the centre of the ion monolayer and the electrode surface.

However, this theory was found to be deficient because it does not take into consideration the dependence of the capacitance on the variation in surface potential. To solve this issue, Gouy and Chapman assumed that the charged species of an electrolyte are point charges. Thus, by invoking the theorems of statistical thermodynamics, they postulated that these point charges are dispersed by thermal fluctuations across the electrolyte side of the E|E interface. Accordingly, the model of the EDL obtained from the Gouy-Chapman theory described it as a charged metal surface and a diffuse layer of charge as shown in Fig. 2.2b. In line with this, the double-layer capacitance from this model was mathematically derived as:

$$C_{dl} = \frac{\varepsilon\kappa}{4\pi} cosh\frac{z}{2} \quad (2.1b),$$

where κ (m), and z are the reciprocal Debye-Huckel length, and the valence of the ion respectively.

Nevertheless, at high electrolyte concentration, the values of the capacitance derived from this model was impractical, hence, Stern-Grahame adjusted this model by suggesting that in conjunction with the Gouy diffuse layer, a compact layer of charge exists near the surface of the electrode as illustrated in Fig. 2.2c.

There have been other modifications of the double layer model, and a notable one was the postulation by Bockris, Devanathan and Muller [27] which adjusted the Stern-Grahame model by including a layer of solvent molecules near the electrode in the so-called inner Helmholtz plane.

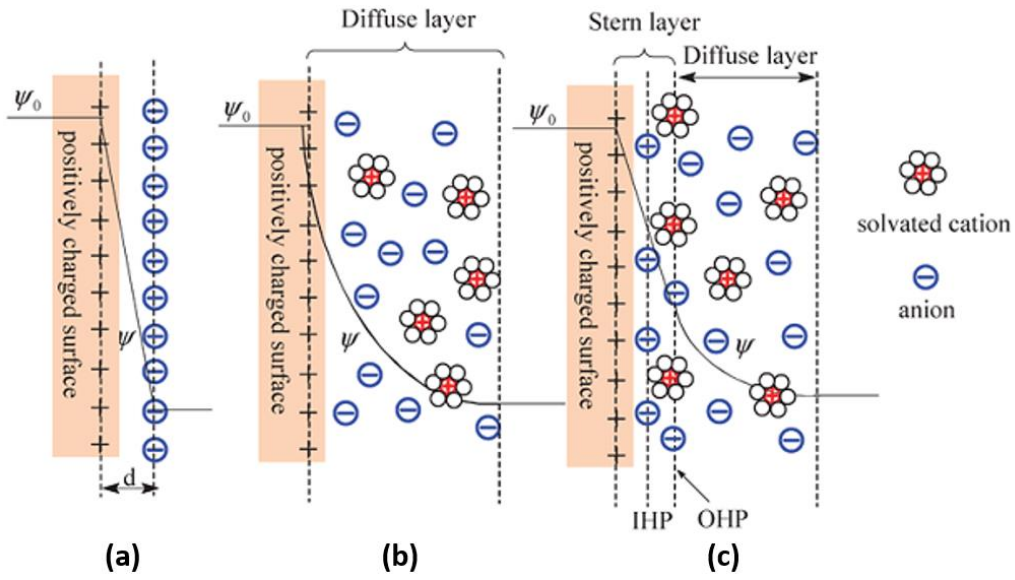

Figure 2.2: Various models of the electric double-layer based on the proposed theories (a) Helmholtz model (b) Gouy-Chapman model (c) Stern model [28].

In line with the aforementioned early models of the EDL, the current model of the double-layer can be illustrated as in Fig. 2.3. This model comprises of an ideally polarizable interface that is divided into two different planes. These are the inner Helmholtz plane (IHP) and the outer Helmholtz plane (OHP). The IHP can be constructed with the locus of points of specifically adsorbed dehydrated ions, whilst the OHP is parallel to the point of closest approach of counter-ions to the double-layer. Ions are strongly bounded or specifically adsorbed to the charged surface in the IHP, and the collection of these immobile ions are collectively assumed to form what is known as the Stern or Helmholtz layer. A diffuse layer (a.k.a. Gouy-Chapman layer) formed outside the OHP comprises of ions which are distributed by a balance between electrostatic interaction and thermal diffusion, and can in principle be mathematically described with Maxwell-Boltzmann statistics [29, 30].

It can be seen from Fig. 2.3 that this charge separation across the interface of the EDL behaves like a capacitor with double layer capacitance C_{dl} which is polarised by the potential drop $\Delta\Phi_{dl} = \Phi_M - \Phi_s$ across the metal-

solution or E|E interface. Assuming if the solution phase and the metal phase are both connected to the same arbitrary point on the diffuse layer, an individual potential drop across the Stern and the diffuse layer can then be established. This in turn would result in the capacitances C_S (Stern layer capacitance) and C_d (diffuse layer capacitance) respectively. In line with this, C_{dl} can be expressed as both these capacitances connected in series as given in Eq. 2.2:

$$\frac{1}{C_{dl}} = \frac{1}{C_s} + \frac{1}{C_d} \tag{2.2}$$

Broadly speaking, the values of C_S and C_d can be used to describe the extreme effects of the ionic concentration at the interface. For example, at low surface charge density and low electrolyte concentration C_{dl} is defined by C_d, however, at high surface charge density and electrolyte concentration the properties of C_{dl} are defined by C_S. Accordingly ascertaining these parameters could help to calculate the value of C_{dl} and the potential of zero charge (PZC) which are parameters that are of fundamental importance in the study of the E|E interface [29, 31]

Generally, for a metal surface, C_{dl} is of the order ca. 10^{-6}F/cm^2. Also, since the Stern layer has a thickness of about 10^{-8} to 10^{-9} m, it follows that at an applied potential of say 1.0 V, the electric field at this interface is around the tremendously high value of ca. 10^8 to 10^9 V/cm^2. Fundamentally, it is this extremely high electric field at the EDL that makes all of electrochemistry possible because such fields are able to transform the properties of materials at an atomic or molecular level [31, 32].

Furthermore, at low ionic concentrations for a 1:1 electrolyte, the thickness of the diffuse layer could be of the order ca. 10×10^{-6} m, and at much dilute concentrations this could increase to over 500×10^{-6} m. However, for the characteristic electrolyte concentrations used in electrochemical capacitor applications for example: > 1.0 mol/L KCl, LiCl, or KOH etc., the

thickness of the diffuse layer is of the order ca. 5 - 10 Å which approximately corresponds to the dimensions of the solvation shell around an ion of the electrolyte [33, 34]

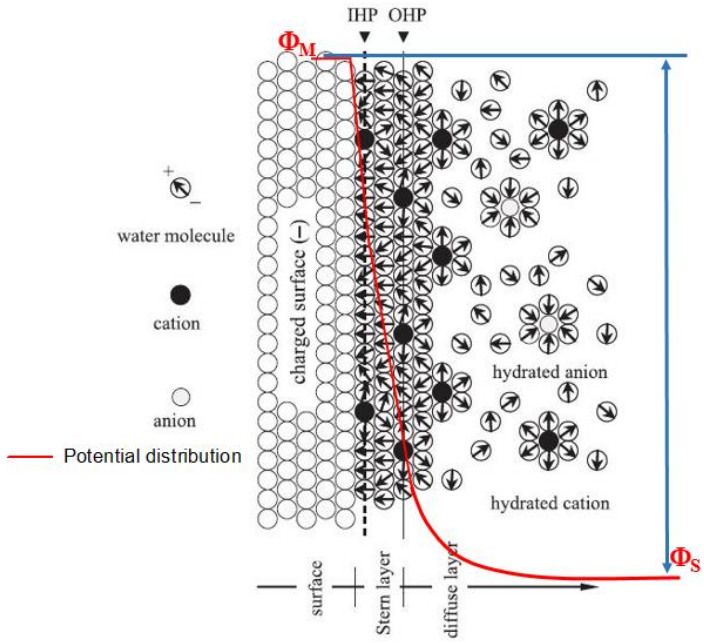

Figure 2.3: Structure of the electric double layer, modified from [29].

With this brief discussion of the fundamental properties of the EDL, the practical case for the storage properties in EDL electrodes in supercapacitors is now appraised. Fundamentally, the amount of interfacial charge storage (*Q*) stored in EDL electrodes can be correlated with the interfacial capacitance (*C*) at a given electrode potential (*E*) by the usual capacitor equation below,

$$C = \frac{dQ}{dE} = \frac{dQ/dt}{dE/dt} = \frac{i}{v} \quad (2.3),$$

where *i* (A) is the current and *v* the potential scan rate (V/s) (for example in cyclic voltammetry) [35].

Note that in practice, Equation (2.3) is correct only when *C* remains constant, at least approximately, in the range of applied potentials. If *C* varies significantly with potential, Equation (2.3) becomes invalid. With a replacement of *E* by the cell voltage, *U*, Eq. 2.4 can be applied in the calculation

of the cell capacitance, C_{cell}, of an EC constructed from two capacitive electrodes (either both EDL or capacitive faradaic). The maximum energy stored in the EC, i.e. W is correlated with C_{cell} and U by Eq. 2.4.

$$\boldsymbol{W = 0.5C_{cell}U^2} \quad (2.4).$$

In Eq. 2.4, C_{cell} results from the serial connection of the positrode capacitance, C_p, and negatrode capacitance, C_n, i.e. $1/C_{cell} = 1/C_p + 1/C_n$. It should be emphasised that C_{cell} in Equation 2.4 should not be replaced by either C_p or C_n because it is practically impossible to store energy in a single electrode without the counter electrode. In other words, energy analysis is only practically meaningful in relation with the cell performance.

As was pointed out already (in Ch. 1) the electrical response of all capacitive electrodes, either the EDL or faradaic kind (i.e. pseudocapacitive), are typified by rectangular cyclic voltammograms (CVs) and triangular galvanostatic charging-discharging curves (GCDs) as shown in Fig. 2.4 a and b respectively. The device of Fig. 2.4 has a hypothetical capacitance of 50 mF, notice the proportionality in the capacitive features of the displayed CVs (Fig. 2.4a) and GCDs (Fig. 2.4b). Also the inset equation in Fig. 2.4b describes the GCD in terms of similar derivations as would be obtained from Eq. 2.3 (note that: $dU/dt = v$).

As is well known, EDL capacitance is the storage mechanism displayed by many carbon-based electrodes such as: activated carbon (AC), carbon nanotubes (CNTs), aerogels, xerogels, carbon onions, graphite, graphene (few-layer graphene), etc. [36, 37].

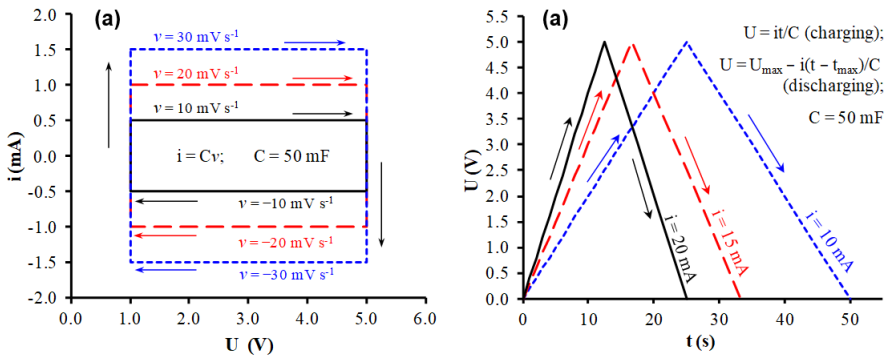

Figure 2.4: Hypothetical electrical responses of an EDL or capacitive faradaic device (a) CVs at different scan rates (b) GCDs at different applied current [35].

2.1.2 Faradaic storage mechanisms

The rectangular CV in Figure 2.1(b4) can be used to describe the electrochemical profile due to either EDL storage or capacitive faradaic storage i.e. pseudocapacitance [38], which are also characterised by linear or triangular GCDs. Materials which display the capacitive faradaic aka pseudocapacitive storage mechanism can be described with the aid of the semiconductor band model (see Figure 1 c and d) [16].

It is well known that reversible electron transfer reactions of redox active molecules or ions in a liquid electrolyte or confined on the electrode surface can be described by the Nernst equation. In these molecules or ions, the valence electrons are localised at a unique and fixed energy level and can therefore be transferred on the electrode at a fixed potential. However, if the valence electrons are delocalised to a certain degree, such as those in semiconductor materials, e.g. many transition metal oxides (TMOs) and electronically conducting polymers (ECPs), the energy levels of these delocalised valence electrons are no longer a single value but spread over an energy band.

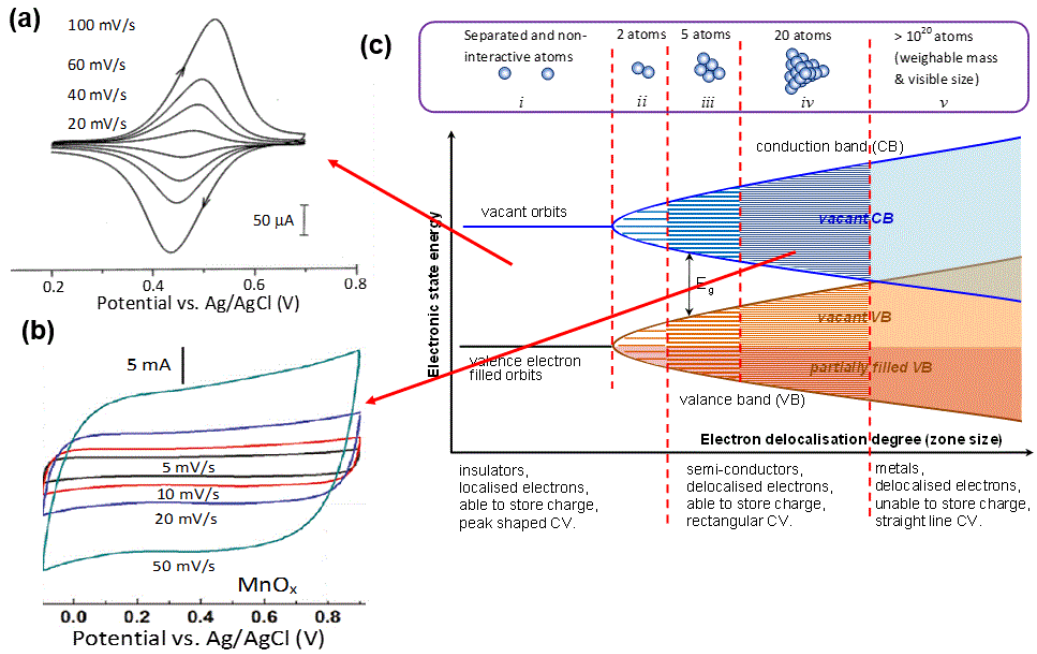

Figure 2.5: Charge storage mechanisms in electrodes (a) non-capacitive Faradaic or Nernstian mechanism of ferrocene containing inactive polymer coated electrode in aqueous electrolyte (b) capacitive Faradaic mechanism of MnO_x coated electrode in aqueous electrolyte (c) Band model for the description of charge storage mechanisms (adapted from references [39], [40] and [41], respectively).

Note that for Fig. 2.5 c(i), are for metal atoms that are separated and non-interactive, and forming clusters of 2 (ii), 5 (iii), 20 (iv) and 10^{20} (v) atoms. Additionally, these regions are represented with the corresponding energy levels of the valence electrons as a function of the degree (or zone size) of delocalisation of valence electrons in the respective clusters of metal atoms [16].

In line with this, the transfer of these delocalised valence electrons occurs in a continuous range of potentials, instead of a fixed single potential. This energetic feature of delocalised valence electrons is responsible for the flow of the capacitive current over a relatively wide potential range [16]. TMOs, such as RuO_2 (as described in Ch.1 see Fig. 1.4b), MnO_2, SnO_2 and their composites with nanostructured carbon materials [23, 42-45] are important examples of electrodes which store charge by the pseudocapacitance

mechanism. Additionally, ECPs such as Poly(pyyrole) (PPy), Poly(aniline) (PAn) and Poly(3,4-ethylenedioxythiophene) (PEDOT) and their composites with nanostructured carbon materials [46-49] also store charge via pseudocapacitance. Other classes of electrode materials for pseudocapacitive storage such as transition metal dichalcogenides (TMDs) e.g. MoS_2, WS_2, TiS_2 have also been investigated [50]. It should be pointed out that although the band model has been used to describe the possible current response of different charge storage mechanisms, it cannot be used to ascertain the rate kinetics of the electron transfer reactions.

The two remaining types of faradaic storage described below are non-capacitive and mixed capacitive plus non-capacitive.

Electrodes giving rise to peaked shaped CVs without any significant capacitive contribution (see Fig. 2.1 (b2) or 2.5a) are in general referred to as Nernstian electrodes and they display the faradaic non-capacitive mechanism of storage. In these electrodes the exchange of electrons across the EEI occurs at a fixed electrode potential which can be described by the Nernst equation with respect to the mole fraction, x, of the reduced sites on the electrode surface.

$$E = E^{o} + \frac{nF}{RT} ln\left(\frac{1-x}{x}\right) \quad (2.5).$$

If the process is reversible i.e. occurring under Nernstian conditions, and assuming that the entire bulk of the material on the electrode undergoes the same redox reaction, the theoretical value of Q_M (C) of the electrode material can be expressed by the Faraday equation [41], where n, F (F/g) and M (g/mol) are the number of electrons, faraday's constant and molar mass of respectively.

$$Q_M = \frac{nF}{M} \quad (2.6).$$

The CVs of a Nernstian electrode are typically peak shaped and hence cannot be analysed using any capacitor equations. Instead, the material

property of a Nernstian electrode is analysed in terms of Q_M. What is not always clearly referenced in the literature is that Q_M is always associated with a fixed potential, E^o (or potentials for reactions involving the transfer of multiple electrons) as defined by Equation (2.5). This is in contrast to C_M for a capacitive electrode which is associated with a potential range, ΔE. This property of the electrical response of Nernstian electrodes is seen in the CVs displaying current peaks, and the corresponding GCDs with potential plateaus around the fixed potential E^o which indicates the potential of the localised electron transfer. The peak current can thus be mathematically derived as in Eq. 2.6.

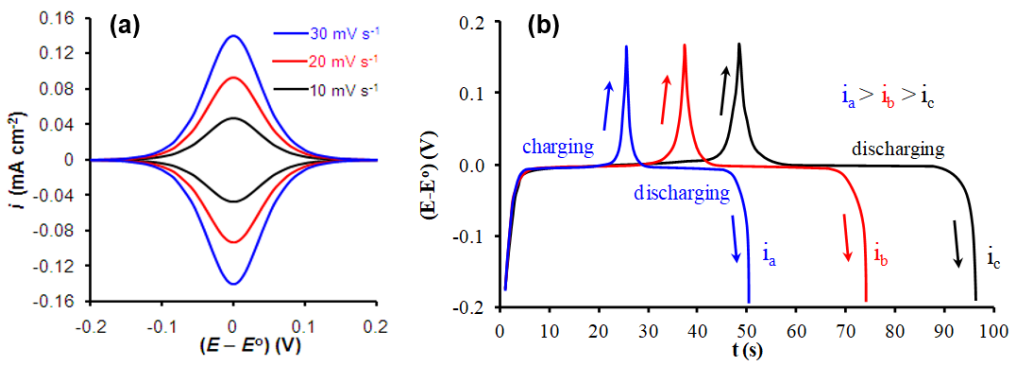

Figure 2.6: Electrical responses of a Nernstian electrode (a) CVs at different scan rates (b) GCDs at different applied current.

$$i = \frac{n^2 F^2 A \Gamma_t v \exp\left[\left(E - E^o\right)\frac{nF}{RT}\right]}{RT\left\{1 + \exp\left[\left(E - E^o\right)\frac{nF}{RT}\right]\right\}} \qquad (2.6).$$

Accordingly, it would be noticed that such Nernstian electrodes with narrow potentials around E^o are reflective of non-interactive redox centres as was explained for the case of $KCuFe(CN)_6$ electrode in Ch. 1 (see Fig. 1.4a), or in the case of Fig. 2.5a the redox centres of the ferrocene are isolated by the insulating polymeric monolayer.

In this vein, two Nernstian electrodes with different E^o values can form a battery whose theoretical cell voltage equals to the difference between the positrode and negatrode potentials, i.e. $U = E^o_p - E^o_n$. If the specific charges

and masses of the positrode and negatrode are $Q_{m,p}$ and m_p, and $Q_{m,n}$ and m_n, respectively, then $Q_{m,p} \times m_p = Q_{m,n} \times m_n = Q_{cell}$. The energy stored in the battery, *W,* can then be calculated by Eq. 2.7:

$$W = Q_{\mathrm{cell}}U \quad (2.7).$$

Electrodes which store charge via a mixed Nernstian and capacitive mechanism are those that conjointly display marked capacitive and Nernstian features as illustrated in Figure 2.1(b3). For example PAn nanofibrils typify this property when it is scanned from –0.1 to 1.0 V vs Ag/AgCl (see Fig. 2.7) [51]. As seen from Fig. 2.7, within the potential range 0.2 to 0.7 V vs Ag/AgCl, this material displays a capacitive storage mechanism (in this case, pseudocapacitance dominates). Lithiated carbon materials, particularly those with nanostructures accessible by the electrolyte, would also display such properties with the capacitive storage being largely due to EDL capacitance from the carbon electrodes [16].

Accordingly, in calculation of the specific charge of such an electrode (Q_M), the contributions from both the Nernstian and capacitive storage mechanisms must be considered. This could be achieved by using expressions such as that in Eq. 2.8, which describes the stored charge as due to the faradaic storage and the EDL capacitance storage mechanisms:

$$Q_{\mathrm{M}} = \frac{Q}{M} = \frac{nF}{M} + AC_{\mathrm{dl}}\Delta E \quad (2.8),$$

where Q is the faradaic charge transferred over the applied potential range, ΔE, n the number of electrons participating in the Faradaic reaction, M the molar mass of the electrode material, A the specific area of the electrode (m^2/g), C_{dl} the capacitance per unit specific area of the electrode material (F/m^2). If the faradaic charge transfer is capacitive, Equation (2.8) can be re-written as Eq. 2.9 below for calculation of the specific capacitance of the electrode material, C_M:

$$C_{\mathrm{M}} = \frac{Q}{M\Delta E} = \frac{nF}{M\Delta E} + AC_{\mathrm{dl}} \quad (2.9).$$

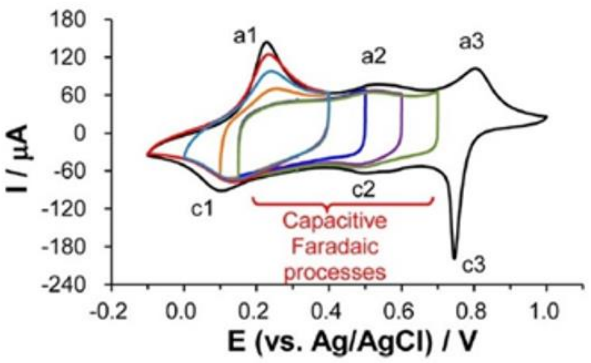

Figure 2.7: CVs of a PAn-CNT film in 1.0 mol/L HCl showing both the capacitive and mixed Nernstian and capacitive potential ranges [51].

2.2 Design of practical supercapacitors through fundamental understanding of the charge storage mechanisms

In order to properly design cells that would optimally utilise the mechanisms of charge storage of these electrodes, it is necessary to fundamentally understand how these storage mechanisms can be translated into optimal device performance metrics when the electrodes are coupled. This is very important because there are numerous publications that have misconstrued Nernstian mechanisms for pseudocapacitance through considering the ratio *Q*/*U* of a Nernstian electrode as capacitance. This inevitably results in claims of unrealistically large capacitance values for produced electrode materials. However, there have been recent attempts at drawing attention to this confusion [15, 35, 38], and some fundamental theoretical calculations have been utilized to reveal the basis of the charge storage mechanisms displayed by electrode materials [52-54]. In line with this, the subsequent part of this section would critically describe procedures that can be used to optimally couple electrodes in the design of practical supercapacitors.

2.2.1 Asymmetrical electrochemical capacitors with capacitive electrodes

The possible configurations of this class of asymmetrical electrochemical capacitors (AECs) are the use of two electrodes with EDL capacitance (i.e. EDLC electrodes), two pseudocapacitive electrodes, or the use of an EDLC electrode and a pseudocapacitive electrode. Moreover, in this section, the method of critically understanding the asymmetry of electrode capacitances and strategies that have been used to design optimal devices particularly with carbon electrodes would be appraised.

Of particular importance to the fabrication of AECs is the determination of the capacitive potential range (CPR) of each electrode. Within the CPR, all processes on the electrode are electrochemically reversible and capacitive in nature. That is the potential range (window) before the onset of any irreversible reaction of the electrode and/or decomposition of the electrolyte, see Fig. 2.8 [55]. The CPR can be determined from the CV of a given "electrode | electrolyte" combination using the following equation,

$$\boldsymbol{CPR = E_{p,max} - E_{n,max}} \tag{2.10}$$

where $E_{p,max}$ and $E_{n,max}$ are the experimentally determined maximum positive and negative potentials of the capacitive CV.

Figure 2.8 shows the CVs of an AC electrode in different potential ranges recorded in a three-electrode cell containing the aqueous electrolyte of 0.3 mol/L K_2SO_4. The AC used was Cabot Monarch 1300 pigment black (CMPB) and it was coated on the surface of a graphite disc electrode (0.6 cm in diameter) [55]. In Fig. 2.8, it can be seen that $E_{p,max}$ and $E_{n,max}$ are 0.9 V and −1.3 V, respectively. Referring to Fig. 2.8 and using Eq. 2.10, the CPR of the CMPB electrode in K_2SO_4 can be calculated as 0.9 − (−1.3) = 2.2 V. It is worth mentioning that for using the CMPB to make both the positrode and negatrode in a cell, i.e. the so called symmetrical supercapacitor. The CPR is in principle the same as the maximum capacitive voltage (MCV). In such a case, the

specific energy of the cell, W_M, can be derived from the C_M of the CMPB according to Equation (2) and $C_{cell}/(2m) = C_M/4$ where m is the mass of each electrode,

$$W_M = \frac{W}{2m} = \frac{C_{cell}U^2/2}{2m} = \frac{C_M U^2}{8} \quad (2.11).$$

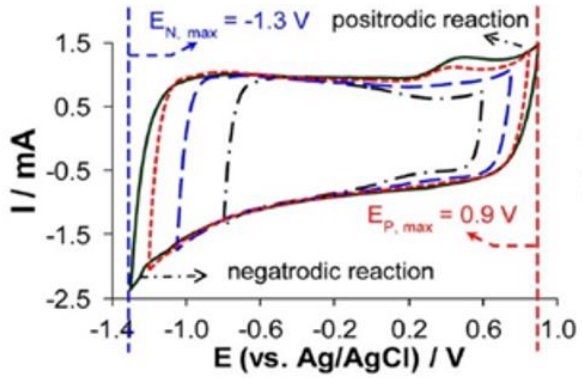

Figure 2.8: CMPB (2.5 mg) coating on graphite electrode in 0.3 mol/L K_2SO_4 [55] showing the dominant capacitive features in the scanned potential ranges.

It is common knowledge that a carbon electrode (e.g. activated carbon) could show different interfacial capacitive profiles depending on if it is used on the negatrode or positrode. In other words, the electrostatic attraction of anions to the positrode and that of cations to the negatrode have different capacitances (or capacitive profiles) as can be clearly observed in Figure 2.9b. This implies that even if the two electrodes of the same material in a given EC have equal masses, such a device is inherently asymmetrical. In fact, it has been explained that ECs with similar electrode material assembled with equal electrode capacitances (e.g. with equal masses), would exhibit different capacitances after extensive cycling [56].

Figure 2.9a and 2.9b show CVs collected from the same "electrode | electrolyte" that was used to record the CVs in Figure 2.8. The solid curves correspond to a whole range of the potential scan of the single carbon electrode and the whole range can eventually increase to the CPR. The dashed curves

correspond to positive (red curve) and negative (blue curve) polarisations of the electrode i.e. the charge profiles of the positrode (with capacitance C_p) and negatrode (with capacitance C_n), respectively. E_{V0} is the equal potential of both the positrode and negatrode when the cell voltage of the device (two-electrode cell) is 0.0 V. It is also known as the potential of zero voltage (PZV). By defining $U_P = (E_p - E_{V0})$ and $U_N = (E_{V0} - E_n)$ where E_p and E_n are the positrode and negatrode potentials, respectively, the capacitance equation based on the principle of conservation of charge (Q) can be expressed by Eq. 2.11. Also, since the electrodes in the device are connected in series the cell capacitance, C_{cell}, can be given by Eq. 2.12 whilst the cell voltage, U, can be expressed by Eq. 2.13 [57].

$$\boldsymbol{Q = C_p U_P = C_N U_N \quad \text{or} \quad U_N = U_P \frac{C_P}{C_N}} \qquad (2.11),$$

$$\boldsymbol{C_{cell} = \frac{C_P C_N}{(C_P + C_N)} = \frac{C_P}{(1 + C_P/C_N)}} \qquad (2.12),$$

$$\boldsymbol{U = U_P + U_N = U_P \left(1 + \frac{C_P}{C_N}\right)} \qquad (2.13).$$

From Eq. 2.11 – 2.13, it is obvious that an adequate adjustment of the C_p/C_n ratio can extend U of the AEC, but decrease C_{cell}. Because $W = 0.5C_{cell}U^2$, the loss in C_{cell} would be compensated by the gain in W. Indeed, it was shown that with the CMPB as both the positrode and negatrode, at $C_p/C_n = 4/3$, the AEC gave the optimal performance at a cell voltage, i.e. the MCV, as high as 1.9 V in aqueous K_2SO_4 [55]. In essence, by raising C_p/C_n, the negatrode potential as shown in Fig. 2.9b was extended to recover what is termed as the "wasted potential" in Fig. 2.9a.

It was also shown that the performance of the AEC depended strongly on the C_P/C_N ratio [55]. For example as shown in Fig. 2.9c, with $C_p/C_n = 1$, the CV starts showing an additional current near the high voltage end when the cell voltage is greater than 1.6 V, indicating unwanted reactions at the electrodes. The same behaviour is not seen on the CVs in Fig. 2.9d with C_p/C_n

= 4/3. Fig. 2.9e plots the electrode potential against the cell voltage and indicates the maximum positrode potential to be 0.91 V (vs. Ag/AgCl). At C_p/C_n = 1, it can be seen that the positrode potential increased beyond 0.91 V, leading to inevitable unwanted anodic reaction. Furthermore, as shown in Fig. 2.9f, the device exhibited the optimal capacitance ratio of C_p/C_n = 4/3, optimal cell voltage of 1.9 V, and good stability in 10000 cycles. At other values of C_p/C_n and U, e.g. 3:1 and 2.0 V, or 1:1 and 1.9 V, the cell showed obvious degradation in cycle stability. More importantly, data analysis confirmed that at C_p/C_n = 4/3, the cell capacitance decreased by only 2% whereas the specific energy of the cell increased by 38% [55].

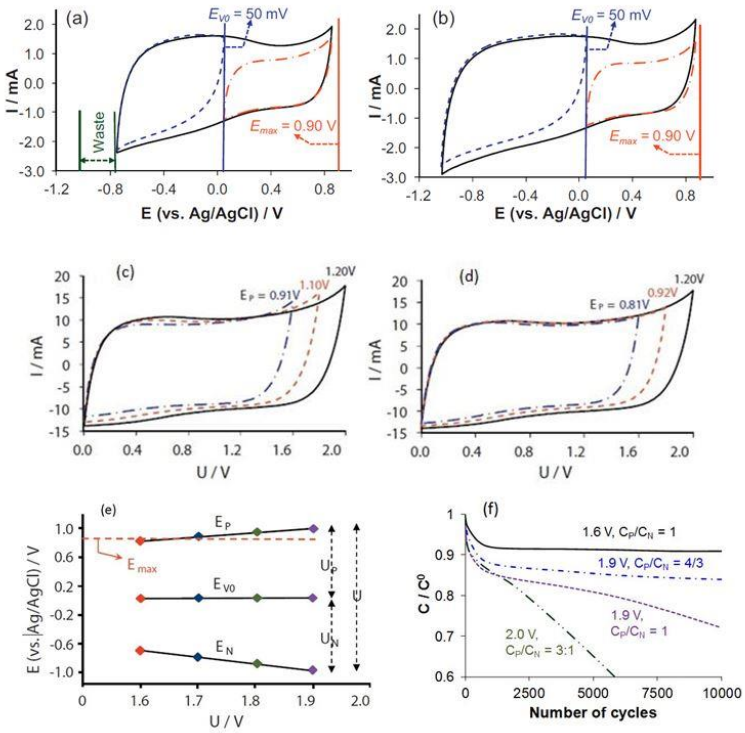

Figure 2.9: (a,b) CVs showing the variation of capacitive feature in different potential ranges of the CMPB electrode in 0.3 mol/L K_2SO_4. (c,d) CVs of AECs with CMPB on both the positrode and negatrode at C_p/C_n = 1 (c) and 4/3 (d), respectively. (e) Plots of electrode potential against cell voltage of an AEC with CMPB on both the positrode and negatrode at C_p/C_n = 1. (f) Cyclic stability (up to 10000 cycles) of AECs at the indicated C_p/C_n ratios and cell voltages [55].

In Eq. 2.13, U_p can extend to the CPR of the positrode. In the case of the AEC with CMPB electrodes in 0.3 mol/L K_2SO_4, the positrode is the so-called "cell voltage limiting electrode" or the "voltage determining electrode" (VDE). In other words, the MCV of the AEC is limited by the CPR of the positrode [57]. If the negatrode is VDE, Eq. 2.13 which applies to all AECs can be rearranged as $U = U_n(1 + C_n/C_p)$. This generalisation is best appreciated from Fig. 2.10a, which illustrates these concepts for capacitive electrodes. From 2.10a, with $E_{n2} > E_{p1}$, the positrode is the VDE. However, if $E_{p1} > E_{n2}$, then the negatrode is the VDE [57, 58].

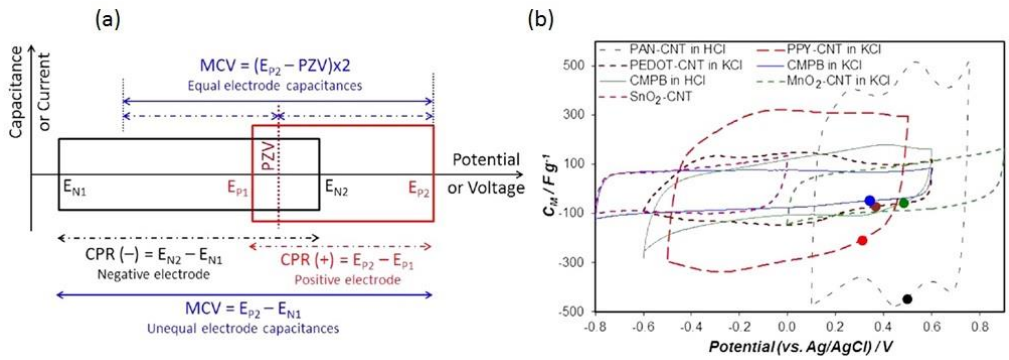

Figure 2.10: (a) Schematic illustration of capacitive electrodes in AECs with CPR(–) and CPR(+) being the capacitive potential range for the negatrode and positrode, respectively. (b) Stable capacitive potential range of some capacitive electrodes in aqueous electrolytes. The coloured circular dots refer to the open circuit potentials of the respective "electrode | electrolyte" interfaces after a rest time of 4 h [58].

Combining a non-Faradaic capacitive electrode (e.g. an EDLC electrode) and a Faradaic capacitive or pseudocapacitive electrode into an AEC is a well-known design [59]. This is mostly due to the improved cell capacitance and increased energy (increased voltage) which might be obtained from such devices particularly in aqueous electrolytes. Due to their high polarisability, carbon materials are usually used as the EDLC electrode of choice in such AECs [60].

Electronically conducting polymers (ECPs) as pseudocapacitive materials have been combined with EDLC materials such as CNTs or AC to

fabricate AECs. As was demonstrated in [57], the performances of this class of AECs are also sensitive to the C_p/C_n ratio. Fig. 2.11a shows the CVs of an AEC of (–) AC | HCl (1.0 mol/L) | PAn-CNT (+). The PAn-CNT positrode was prepared from the co-deposition of CNT and polyaniline. The total deposition charge which is proportional to the mass of film deposited is also shown in Fig. 2.11a, together with the electrode capacitance ratio C_p/C_n. The bar chart in Fig. 2.11b shows the percentage change in the specific energy of the AEC as a function of C_p/C_n. It should be pointed out that the capacitance (C_P) of the PAn-CNT positrode was calculated from rectangular CVs recorded within the CPR, i.e. the potential region for capacitive Faradaic process as shown in Figure 3a [57].

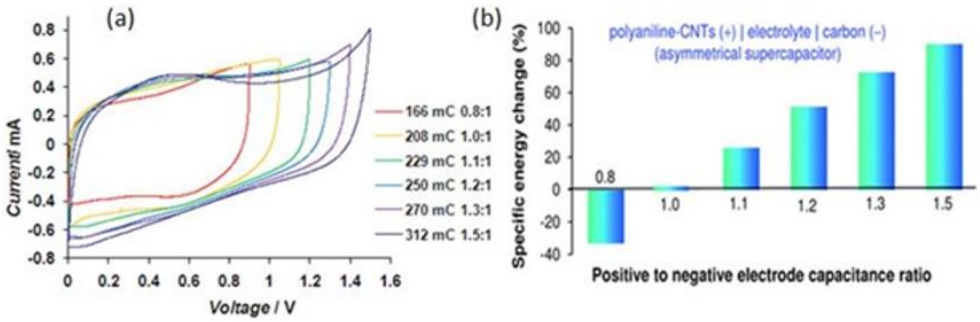

Figure 2.11: AECs with EDLC and pseudocapacitive electrodes. (a) CVs of (–) CMPB | 1.0 mol/L H_2SO_4 | PAn-CNT (+) at indicated C_p/C_N ratios. (b) Energy change of the cell in (a) as a function of the C_P/C_N ratio [57].

In general, the systematic determination of the capacitive stability limits of EDLC and pseudocapacitive electrodes with respect to their performance in AECs is of immense design importance. Therefore, experimental data such as those provided in Fig. 2.10b which shows the CPR of some common capacitive electrodes, could aid in the correct selection of electrodes and electrolytes in the fabrication of optimal AECs.

2.2.2 Combining Nernstian and capacitive electrodes: Supercapattery

To achieve improved energy densities in AECs, there have been numerous reports on the pairing of EDLC or pseudocapacitive electrodes with electrodes displaying non-capacitive Faradaic or Nernstian storage mechanisms [61-63]. Since Nernstian and capacitive electrodes are generally characterised by their peak-shaped (Figure 2.1b1 to 2.1b3) and rectangular (Figure 2.1b4) CVs, respectively, it is necessary to make general descriptions of the cells made from these paired electrodes.

Figure 2.12 illustrates schematically the CVs of the negatrode and positrode, and the two-electrode cell of differently paired electrodes. The devices shown are battery (Fig. 2.12a), supercapacitor (Fig. 2.12b) and what has been termed as the supercapattery (Fig. 2.12c) [16].

Note that in Fig. 2.12, U_{max} and U_{min}: maximum and minimum cell voltages that can be reached during charging and discharging, respectively, without causing irreversible changes in the cell. U_{dis}: average discharging voltage. τ and t: end times of the first charging and discharging cycle, $\tau \geq (t-\tau)$. 2τ and 2t: end times of the second charging and discharging cycle, but not necessarily twice of τ and t [15, 16].

In theory, either the capacitive or Nernstian electrode can be used as a positrode or negatrode. Moreover, selection of the positrode or negatrode is usually done with knowledge of the stable potential window of the electrode relative to the electrolyte adopted.

Accordingly, the redox potential of the Nernstian electrode, and the CPR of capacitive electrodes are used to help such selections. It is also important to point out that various attempts have been made to devise a nomenclature that clearly describes these broad range of so-called hybrid "supercapacitor-battery" devices [64] which makes use of a Nernstian and a capacitive electrode.

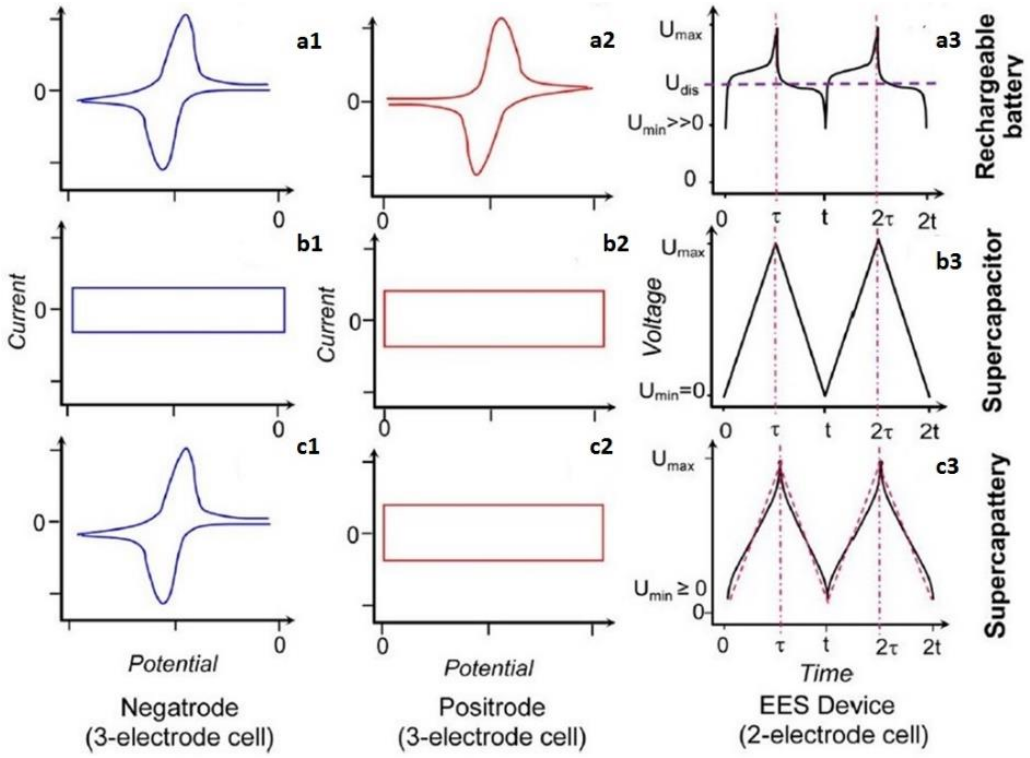

Figure 2.12: Schematic illustrations of (1,2) CVs of positrode and negatrode in a three electrode cell, and (3) GCDs of the two electrode cell of (a) rechargeable battery, (b) supercapacitor, or (c) supercapattery.

For example, in trying to describe various classes of device configurations for practical applications, three different types of hybrids were itemised: (a) discrete supercapacitors externally connected with batteries for load-levelling, (b) use of an internal combustion engine with a battery or supercapacitor for automotive drivetrains, and (c) the incorporation of a faradaic and EDL type electrode materials into a single device: which was referred to as asymmetric capacitor devices [56].

Also, in order to clearly elucidate the nomenclature, devices which could be classed under (a) and (b) above were called external hybrids, whilst asymmetric capacitor devices were termed as internal serial hybrids [60]. A recent attempt has also been made to classify these devices into "asymmetric devices with or without hybrid behaviour" [65]. The terms pseudocapacitors

have also been used to describe some of these devices, particularly those ones employing new Nernstian electrodes [66-76].

In this thesis, the terms "supercapattery" which have been used to describe the properties of devices incorporating Nernstian and capacitive electrodes [37, 61, 77-92], would be adopted as a concise term to describe such devices from the standpoint of their electrochemical performances. With this noted, a brief description of some devices with Nernstian and capacitive electrodes are presented. For these examples, the negatrode and positrode are Nernstian and capacitive respectively.

In combining a capacitive and a Nernstian electrode together in one cell, the conservation of charge equation can be written as:

$$Q_{-} = m_{-}Q_{sp-} = m_{+}C_{sp+}\Delta E_{+} = Q_{+} \quad (2.14).$$

Where m_{-} and Q_{-}, m_{+} and Q_{+}, are the mass and total charge stored in the negatrode and positrode respectively. Q_{sp-} is the specific charge of the negatrode i.e. ($Q_{sp-} = nF/M$).

The important factor to note for these cells illustrated in Fig. 2.13 a and c is that the capacitive features are dominant, accordingly, their approximate specific cell capacitance may be estimated. Moreover, this is done by understanding that the polarisation of the positrode ΔE_p, determines the maximum cell voltage (MCV), because the polarisation of the Nernstian negatrode is negligible. Also, the Nernstian negatrode in this case displays an infinitely large "capacitance (i.e. Q/V ratio)", accordingly, the energy of the supercapattery can then be expressed as:

$$W_{sp} = \frac{C_{cell}\Delta E^2}{2(m_{+}+m_{-})} = \frac{C_{sp}\Delta E^2}{8} \quad (2.15).$$

Note that it is possible to express the specific energy of the cell by the specific capacitance of the positrode (C_{sp}) because in practice, $m_{-} >> m_{+}$. Accordingly, for such supercapattery, the entire capacitance of the positrode is utilised: this is a significant improvement to a normal supercapacitor

because as shown already, for normal supercapacitors, the cell capacitance is effectively 1/4th the specific capacitance. In line with this, the cell: (-)Li | Li^+ | IL + $LiClO_4$ | AC(+), (where IL is an ionic liquid), as illustrated in Fig. 2.13b was able to display a high W_{sp} of 230 Wh/kg at 1 mA/cm^2 [93]. In another supercapattery related to the illustration in Fig. 2.13c with actual data in Fig. 2.13d, and with configuration: (-) Li/Li^+ | buffer-layer | solid-electrolyte | aqueous-electrolyte | RuO_2-nanosheet (+), the pseudocapacitive positrode RuO_2-nanosheet was employed, thus displaying a high specific cell capacitance, with a maximum cell voltage of 3.8 V. Another related cell with the positrode replaced by MnO_2 displayed a voltage of 4.0 V [94]. It is important to point out that some configurations of these cells with improved practicality employed lithiated carbons as the negatrode, thus in such a case, the m_- in Eq. 2.15 would become significant. Moreover, since the capacitance of the positrode is greatly increased, the displayed energy of these cells were still impressive as shown in Fig. 2.13d. An important point to note in these class of cells described in Fig. 2.13d is that they are bi-electrolyte cells in which the negatrode operates in the organic negalyte and the positrode in the aqueous posilyte which makes the redox mechanism of the pseudocapacitive electrode possible. Coupling these two interfaces was made possible by the use of an ion-conducting layer with elevated temperature required for its operation [94]. Accordingly, these and other related cell configurations which were adopted for use with redox electrolytes (as described later) are characterised by very complex designs. In line with this, it should be stated that designing simpler bi-electrolyte cells for use with redox electrolytes, was an important aspect covered in this dissertation (i.e. in Ch. 9).

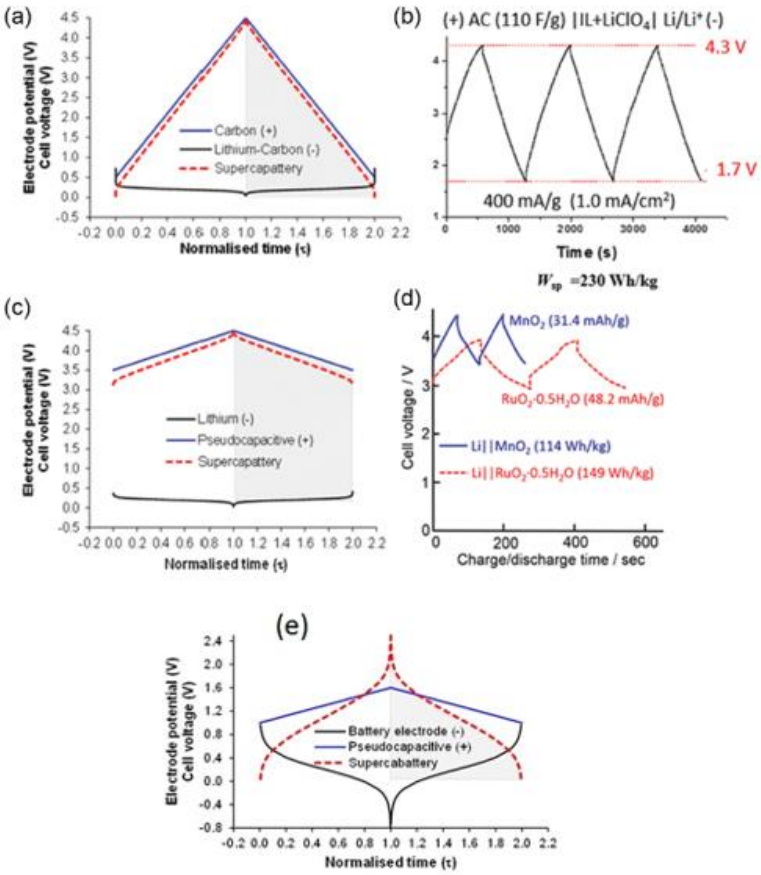

Figure 2.13: GCDs of the positrode, negatrode and cell of (a) the hypothetic supercapattery I with an EDLC positrode and a Li or lithiated carbon negatrode [16], (b) the cell of (–) Li | $LiClO_4$ + IL | AC (+) at 0.4 A/g [93], (c) the hypothetic supercapattery II with a pseudocapacitive positrode and a Li or lithiated carbon negatrode [11], (d) the cell of (–) Li | aqueous electrolyte | solid electrolyte | MnO_2 (+) at 0.255 mA/cm^2 [94], (e) the hypothetic supercabattery with pseudocapacitive positrode and battery material negatrode [16].

Note that in the supercapatteries explained in the preceding paragraphs, lithium metal or lithiated carbon were used as the Nernstian electrode, and as such were characterised by very little slope in their potential plateau, and also had more negative electrode potentials. However, in practice, many battery electrode materials, particularly nanostructured, behave quite differently from the electrochemical performance of Li metal or lithiated carbons. The difference is typically reflected by these materials having redox

potentials more positive than that of Li | Li^+, and a highly sloped potential plateau over a potential range, $\Delta E_{plateau}$, that can be as wide as hundreds of mV or wider. Consequently, combining a pseudocapacitive material and a battery material whose capacitive potential range (CPR) and $\Delta E_{plateau}$, respectively, are comparable would result in GCD profiles similar to the one shown in Fig. 4.13e (red GCD curve for device). U_{min} in this case could be close to zero.

Fundamentally, such devices would behave like batteries and their performances should be expressed as charge capacity, instead of capacitance. In essence, the capacitor concept and equations cannot be used in analysing such devices whose energy capacity should be calculated using Equation (2.16).

$$W = i \int U dt \tag{2.16}$$

The cells with configuration (–) $Li_4Ti_5O_{12}$ | Li^+ | AC (+) and (–) AC | Li^+ | $LiMn_2O_4$ (+) [95] displayed features similar to the illustration in Fig. 2.13 e.

With these charge storage mechanisms rigorously reviewed and analysed, the applications of redox electrolytes in supercapacitors are now presented. It is important to highlight that the electrical response features such as those displayed in Fig. 2.12a and 2.12b or even 2.16e, are generally some characteristic device signatures that may be expected from the use of redox electrolytes in ECs. This is because, as would be further described in the succeeding sections, the use of redox electrolytes introduces Nernstian mechanisms at the E|E interface. However, although this may seem obvious against the backdrop of the electrode storage mechanisms that have been described, most early and even recent literatures on redox electrolytes made some confusing assertions relating to the actual features of these devices. This and other related issues would be addressed in subsequent sections of this chapter.

2.3 Mechanism of charge storage in supercapacitors containing redox electrolyte

The reactions of various redox active species on the surfaces of activated carbon (AC), functionalized carbon, or materials that display pseudocapacitance are the basis for the applications of redox electrolytes in supercapacitors. Here, redox species refer to those capable of undergoing electrochemical reactions with good charging and discharging performances. In general, the properties of ECs with dissolved redox species (DRS) can be described from the standpoint of the mechanism of storage displayed by the electrode at the interface were the redox reaction occurs. The generalised expression for the mechanism of charge storage from a dissolved redox specie can be expressed as:

$$O + e = R \qquad (2.17).$$

In reality, the enhancement in the mechanism of charge storage obtained by introducing a redox electrolyte into the supercapacitor is complex and may be explained by the illustration in Fig. 2.14. In Figure 2.14, O and R are the oxidized and reduced states of the redox species in the electrolyte, and their interaction were schematically described as occurring within the pore of an electrode material. To participate in the charge storage process, the redox species in the bulk solution (either O_{bulk} or R_{bulk}) need to firstly enter the pores of the electrode, accompanied likely by process (1) or (1′) which represents the equilibria of de-solvation and solvation of the species when entering or exiting the pores. Before electron transfer reactions, redox species in the pore (O_{pore} and R_{pore}) must reach the transition state (O* or R*) via (2) or (2′) as in a conventional electrode reaction. Processes (3) and (3′) show the conversion from the transition states to the adsorbed states (O_{ads} and R_{ads}) which may not present in a conventional electrode reaction, but is a necessity for application in supercapacitors. Electron transfer via (4) causes the conversion between the adsorbed redox species on the internal and external surfaces of the

electrode, which is directly responsible for the enhanced charge storage capacity.

Note that once in the transition state, the redox species (O* and R*) may also undergo electron transfer reaction via (5) or (5′) without invoking adsorption. Further, it is possible that upon electron transfer, the adsorbed species (O_{ads} or R_{ads}) is converted via (5) or (5′) to a soluble product (O_{pore} or R_{pore}) that can diffuse through the pore and enter the bulk electrolyte. In both cases, if the electron transfer reaction corresponds to the charging process, the soluble product means that charge storage would be short-lived or not occur because the product of the charging process may diffuse into the bulk electrolyte, and is not fully recoverable electrochemically.

On the other hand, the electron transfer reaction can take place not only inside the pores, but also on the outer surface of the electrode via (6) or (6′). However, because the outer surface area is usually much smaller than the internal surface area of a porous electrode, the contribution from either (6) or (6′) should be insignificant.

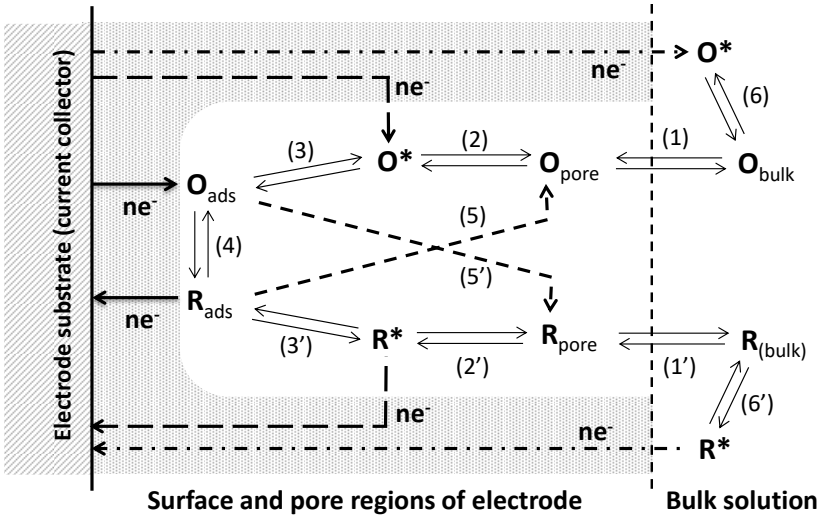

Figure 2.14: Schematic illustration proposed to elucidate the possible charge storage mechanisms in the porous carbon electrode of a SC with a redox electrolyte.

The above analysis and discussion warrant some conclusions. To enable a meaningful application of redox electrolytes in supercapacitors, the electrode material must be sufficiently porous and be able to retain the redox species, particularly the product from the charging reaction, inside the pores of the electrode. Adsorption of the redox species on the internal and external surfaces of the porous electrode is a good way towards retention.

However, there are other retention mechanisms, such as entrapment of the redox species in the pores of the electrode, or simply deposition of only the product from the charging reaction.

There is another important aspect worth mentioning. A redox reaction is determined by the thermodynamic stability of the redox species with respect to the electrode potential and the supporting electrolyte. When involving simple or complex metal ions, redox reactions may be identified from the Pourbaix diagram [96]. However, thermodynamic data do not usually consider the influence of the environment in the pores on the redox reaction, such as de-solvation and adsorption.

Therefore, the thermodynamically predicted electrode potential for a redox reaction may be altered when the reaction occurs inside the porous structure of the electrode. Depending on the surface properties of the electrode material, redox species could either be electro-adsorbed in the electrode material (porous carbon electrodes) [97, 98], or interact with the reactive edge sites and functional groups on the surface of the carbon material for example carbonyl groups (surface functionalized carbon materials) [24, 99, 100]. Also, if the electrode material displays pseudocapacitance or non-capacitive activity, the electron transfer reactions occurring in the lattice of the electrode could be shuttled by the redox specie of the electrolyte [25, 101].

In order for the supercapacitor with a redox electrolyte to display satisfactory stability in repeated charging-discharging cycles, it is important for the redox specie to show fast and reversible electrochemical activity in the

supporting electrolyte. It could be ensured by matching the concentration of the redox species to the supporting electrolyte. For example, the charge storage obtained from the redox activity of the $Fe(CN)_6^{3-}/Fe(CN)_6^{4-}$ couple in KOH, has been shown to be highly dependent on the concentrations of both the added $K_3Fe(CN)_6$ and $K_4Fe(CN)_6$, and the supporting electrolyte KOH [101, 102].

Furthermore, the effect of the substituent location of the hydroxyl groups on the electrochemical performance of redox electrolytes of hydroquinone was explained form the standpoint of the rate kinetics, for example para-hydroquinone was found to be more kinetically effective than ortho-hydroquinone [96]. As expected, the wettability of the electrolyte on the electrode surface is very important in ensuring effective electro-sorption and transport of the redox species from the electrolytes.

The roles of the pores of the carbon electrode in promoting the charge storage of the redox species has also been highlighted, because the various redox species from the electrolyte require optimal pore sizes to ensure effective electro- or chemisorption.

For instance, favourable capacitive behaviour of the AC | iodide interface has been shown to be dependent on the porosity of the carbon electrode [97, 103]. Likewise, the surface property of the carbon materials which determines important characteristics such as the location of active sites, has been linked to the charge storage capabilities offered by the redox species [99]. Accordingly, electrode material properties like highly improved conductivity, increased electron mass transport, and low charge transfer resistance are also desirable.

In line with the preceding discussions, the mechanisms of charge storage of supercapacitors with redox electrolytes could be described based on three broad categories in relation with the general properties of the dissolved redox species (DRS):

1. Dissolved organic molecules
2. Dissolved redox anionic components
3. Dissolved redox cationic components

Before discussing the use of DRS based on the categories listed above, it is pertinent to briefly address some common confusions about the proper means of characterising supercapacitors incorporated with dissolved redox species.

2.4 Charge storage capacity of supercapacitors containing redox electrolytes

This section would draw on some of the concepts already addressed in the previous sections on electrode charge storage mechanisms. In relation with the application of Eq. (2.18) which was earlier described:

$$C = \Delta Q/\Delta U \qquad (2.18),$$

Fig. 2.15 gives a comparative illustration between the GCDs of a conventional SC (plot A, linear) and a SC with redox electrolytes (plot B, non-linear). Clearly, under galvanostatic conditions (*i.e.* constant current), these two curves have the same amount of charge, ΔQ, and the same voltage range, ΔU, for either charging or discharging, and hence the same ΔQ/ΔU ratio. However, if this ΔQ/ΔU ratio is the capacitance for the linear plot A, it cannot be the same for the non-linear plot B. In other words, for the non-linear plot B, the capacitance concept should not be applied, although the ΔQ/ΔU ratio can always be expressed in the units of farad (F).

The above analysis and conclusion on the linear and non-linear GCDs in Fig. 2.15 are valid against Eq. (2.18). However, these GCDs are important for measurement of the amount of energy, W, stored in or released from the device. Eq. (2.19) below is the general form for the energy stored in the charging process under a constant current, I, whilst a similar equation can be written for discharging [35].

$$W = \int_{U_{min}}^{U_{max}} I dU = I \int_{t=0}^{t=t} U(t) dt \qquad (2.19).$$

For a supercapacitor, U(t) is a linear function, and Eq. 2.19 simplifies to Eq. 2.20.

$$W = \frac{CU_{max}^2}{2} \qquad (2.20).$$

For a nonlinear GCD plot, Eq. 2.20 is invalid and one has to apply (2.19) for calculation of the energy stored in the device.

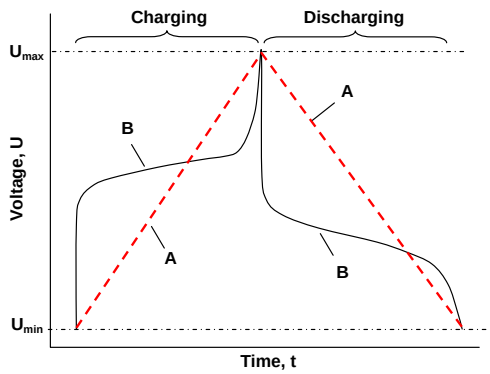

Figure 2.15: Illustrative comparison of the galvanostatic charging and discharging plots of a conventional supercapacitor (plot A, linear), and a supercapacitor containing a redox electrolyte (plot B, non-linear). Note that plot B represents very well the characteristics of some SCs containing redox electrolytes as reported in the literature [24, 104-108].

For supercapacitors, the area under the linear plot A (in Fig. 2.15) is the same as that represented by Eq. (2.20), in which C is calculated from the ΔQ/ΔU ratio. For the non-linear GCD plot B in Fig. 2.15, the same ΔQ/ΔU ratio can be derived as from the linear plot A. Therefore, if one applies this ΔQ/ΔU ratio in Eq. (2.20) for calculation of the amount of energy stored, the value will be different from that calculated using Eq. (2.19) for the non-linear plot B. Specifically for Fig. 2.15, the linear plot A gives a smaller amount of energy for the charging process than the non-linear plot B. For discharging, the non-linear plot B corresponds to a smaller amount of energy than the linear plot A. Such differences indicate that charging up the SC with redox electrolyte

requires a greater amount of energy than it can discharge, which is indication of lower energy efficiency than the conventional SC. Because the non-linear plot B in Figure 2 corresponds to a lot of literature reports, the analysis provided here argues strongly why it is inappropriate to use the ΔQ/ΔU ratio as the capacitance. Similarly, Eq. (2.20) should not be applied for analysis of non-linear GCDs, which is unfortunately contradictory to some literatures.

In the literature, other approaches have been proposed to by-pass the above discussed problems in analysis of non-linear GCD plots. For example, Eq. (2.21) below was proposed [24, 109] to define and calculate the ΔQ/ΔU ratio and hence the "claimed capacitance", C_{claim}, for a device that exhibited non-linear GCD plots.

$$C_{claim} = \frac{2i_m \int V dt}{V^2 \Big|_{V_i}^{V_f}} \qquad (2.21).$$

The term on the right side of Eq. (2.21) have been used in some literatures [24, 109] in which i_m (A g^{-1}) is the mass normalised current, t the time, and V the applied potential (or voltage) with V_i and V_f being the initial and final values, respectively. While this equation is valid for calculation of the ΔQ/ΔU ratio from a non-linear GCD plot as that in Figure 2, it is important to note that this ratio is not capacitance [41]. There is no doubt that using such a "claimed capacitance" derived from Eq. (2.21) and a non-linear GCD plot will lead to incorrect calculation of energy stored in the relevant device as discussed above.

Another interesting attempt was reported to conceal the above mentioned mistakes on deriving the "claimed capacitance" from non-linear GCD plots. This was presented by correlating the charge *capacity* with the unit of F/g [24]. The consequence was that specific capacitance values as high as 4700 F/g [24], or 477 F/g [65] has been ascribed to carbon-electrode / redox-electrolyte electrical features that are similar to or identical to the battery

features illustrated by Curve B in Fig. 2.15. Furthermore, such claimed capacitance for these curved GCDs were then used to calculate the energy stored according to Eq. 2.18, leading to a misleading claim of 163 Wh/kg for an electrode [24]. As would be pointed out in Ch. 3 and have been discussed in preceding sections, energy values cannot be calculated for "single" electrode characterisations, but only makes sense when a device is been considered.

In fact, the generally high "claimed capacitance" values ascribed to some supercapacitors with redox electrolytes are a result of the incorrect use of the capacitance concept and its relation with the ΔQ/ΔU ratio under well-defined conditions for description of battery-like performances. It must have been very tempting to report large ΔQ/ΔU ratios as capacitance values against properly measured literature data, which is a historically known [31] and re-emphasized source of great confusion [35].

In line with this, it is relatively difficult to critically compare the quantitative values of the performance metrics claimed for a lot of these supercapacitors with redox electrolytes. Nevertheless, in spite of the above mentioned misleading claims of capacitance values in some literature, supercapacitors with redox electrolytes are still promising electrochemical energy storage devices. Also, in the specific case of trying to compare performance metrics, easily verifiable properties like the percentage improvement in capacity [110], maximum operating cell voltages [111], cycle stability [112], rate of self-discharge [113], etc., are still important means of appraising the impressive improvements that could be obtained from the use of redox electrolytes in supercapacitors.

In Chapter 3, the steps taken to rigorously quantify the performance metrics of the devices developed in this thesis would be presented.

The broad categories of dissolved redox species, their properties, and performance are now presented.

2.5 Dissolved organic molecules for enhanced interfacial charge storage

The electrochemical properties of quinonoids are of immense interests in the general literature [114, 115], and the versatility of these organic molecules have been put into use for applications in supercapacitors [98]. It is generally accepted that the redox reactions of some simple quinonoids, for example hydroquinone (HQ), in aqueous media involve a single step two-electron and two-proton transfer reaction at the electrode [116]. The reversible redox reaction of hydroquinone/benzoquinone in the porous matrix of activated carbon electrodes have been used for enhanced storage [98]. As shown in Fig. 2.16, the redox reaction occurs in the positrode, by transforming the EDL capacitance of the activated carbon (AC) positrode in the cell without HQ into Nernstian feature with the positrode in the solution containing the DRS (Fig. 2.16) [98].

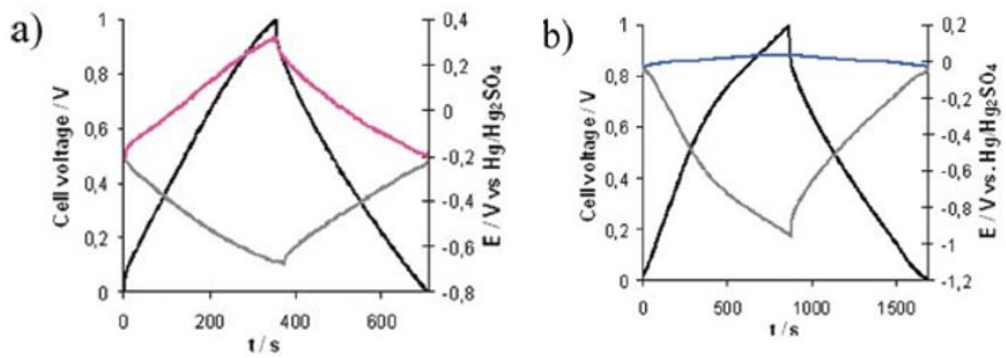

Figure 2.16: GCD plots of cell with (a) 1.0 mol/L H_2SO_4 (b) 0.4 mol/L hydroquinone in 1.0 mol/L H_2SO_4 [98].

Along these lines, the property of the substituents of hydroquinone i.e. ortho-, meta-, and para-hydroquinone has been studied in acidic media [96]. The poor redox activity of both the *ortho-* and *meta-* substituted hydroquinones at the carbon electrodes observed through three-electrode tests was used to explain their relatively low contribution to charge storage

when they were used as redox additives to fabricate supercapacitors (SCs) with 1.0 mol/L H_2SO_4 as the electrolyte. This implies that substituent effects could play an important role in the selection of some organic molecules as redox additives.

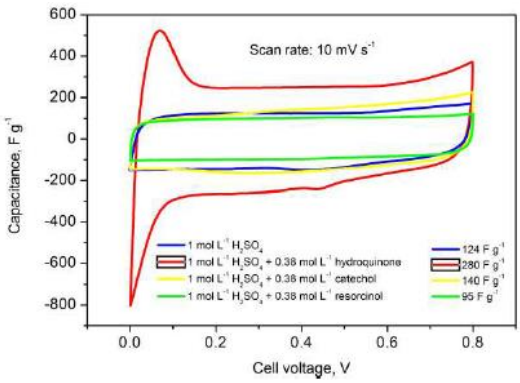

Figure 2.17: CVs of cells showing a comparison between ortho-, meta- and para-hydroquinone as redox additives to 1.0 mol/L H_2SO_4 [96].

It has also been shown that interfacial charge at carbon electrodes can be increased by addition of quinones with substituted halides e.g. di-bromo-hydroquinone (DBHQ) in a KOH electrolyte [117]. Experimental findings indicated that the interfacial charge stored was dependent on both the concentrations of the redox additive and the supporting electrolyte. It was also observed that the optimal performance of this redox additive was obtained from an electrolyte of 0.2 mol/L DBHQ and 2.0 mol/L KOH. HQ in acidic media has also been used to enhance the charge storage property of a polyaniline-coated curved-graphene oxide (PAn-G) composite. Generally, the recorded increase in interfacial charge was attributed to the redox activity at the electrode surface. However, through impedance measurements it was observed that the charge transfer resistance for the PAn-G in an electrolyte mixed with HQ is greater than the normal H_2SO_4 electrolyte. It was also shown that the charge retention after 10,000 cycles was about 64% (with final capacity values still appreciably greater than the SCs without redox additives),

although the electrolyte without additive had over 90% charge retention on comparable cycling. This was attributed to surface-induced effects due to the ionic activities of the redox electrolytes [118].

These investigations involving the use of HQ as redox additive to 1 mol/L H_2SO_4 were extended to include a broad range of electronically conducting polymer (ECP) electrodes such as polyaniline (PAn), polypyrrole (PPy) and poly(3, 4–ethylenedioxythiophene) (PEDOT) [104]. When tested in the two-electrode cell, the most notable performance feature was the appearance of peak-shaped CVs for the PAn cell, but relatively rectangular CVs for the cell of PPy with an electrolyte containing HQ. Since in all cases capacitive properties were assumed for these ECPs, this marked difference in the charge storage profiles of these ECPs operating in electrolytes with redox additives was not clearly elucidated (see Fig. 2.18).

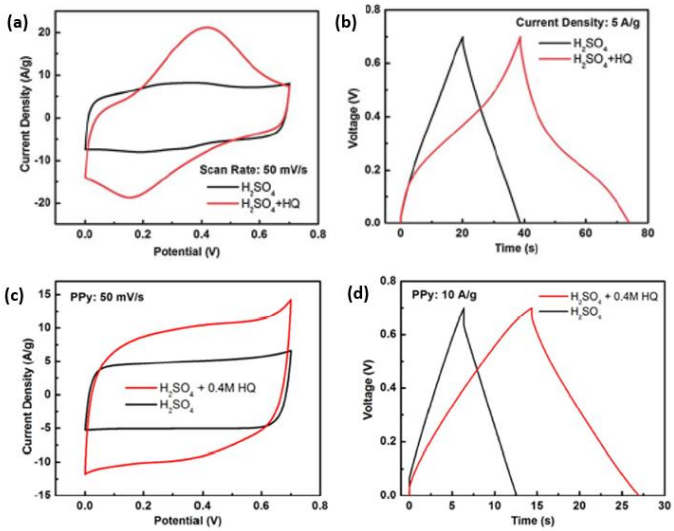

Figure 2.18: CVs and corresponding GCD plots of HQ redox additive in H_2SO_4 electrolyte with PEDOT (a) and (b) and PPy (c) and (d) as electrodes [104].

Moreover, it was shown that the addition of HQ with optimal molarities of 0.3 to 0.4 mol/L in the electrolyte reduces the charge transfer resistance of the devices [104]. Other reports have also described the use of HQ in acidic media with ECP-metal oxide composites. Notably, using a PPy-SnO_2 electrode,

the charge storage profile of the HQ/BQ (hydroquinone/benzoquinone) redox couple at the electrode | electrolyte (E|E) interface was described as a surface-controlled process, leading to an increase in interfacial charge. The charge-discharge profile of the "PPy-SnO_2 electrode/HQ electrolyte" combination also displayed good coulombic efficiency, implying good interfacial kinetics [119].

The redox reaction of the *p*-phenyldiamine/*p*-phenyldiimine couple is a two-electron mechanism in alkaline media (e.g. KOH), and this has been matched to various properties such as the porosity [106, 120], and surface property [121, 122] of the electrode. The use of *p*-phenyldiamine (PPD) could serve as a good example to highlight some properties of redox additives in practical SCs. Firstly, when dissolved in solutions of neutral aqueous salts, PPD displays relatively slow kinetics [123], whilst in acidic media, it tends to form the protonated salt which on oxidation could lead to an electro-polymerisation reaction [124]. Although, this has been adopted for use in co-polymerisation, for example preparation of conducting polymers for energy storage applications, or in the preparation of the polymers of *p*-phenylenediamines [124], such electrochemical properties in acidic media might preclude them from use as dissolved redox species in SCs with acidic electrolytes. This is because reversibility and stability of the dissolved redox species is a vital aspect of their use in practical devices [15].

Accordingly most of all the reports using PPD as the redox additive in SCs have utilised it in either alkaline solutions, particularly KOH [25, 101, 121] or in aprotic organic electrolytes [125]. Moreover, the solubility of PPD in KOH decreases with increasing concentration of the supporting KOH electrolyte. Accordingly, 2.0 mol/L KOH has been found to be the optimum supporting electrolyte concentration when PPD is used as the redox additive [120].

Contrastingly, in the application of PPD as redox additive for low-temperature charge capacity enhancement in SCs with MnO_2 electrodes, KOH

concentration was increased to 4 mol/L, in order to be able to increase the freezing point of the electrolyte [101].

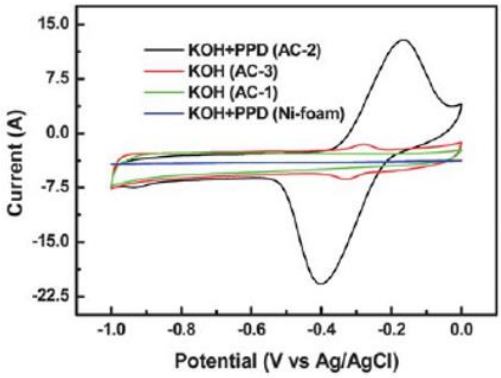

Figure 2.19: CVs of different carbon electrodes in KOH electrolyte incorporated with PPD [120].

In general, the electrochemical properties of PPD, particularly its fast redox activity and relatively strong surface adsorption of the product of charging implies that when used with mesoporous carbon electrodes, e.g. single-walled carbon-nanotubes (SWCNTs), it displays a large increase in the interfacial charge. Moreover, the devices fabricated with the SWCNT/PPD in the KOH electrolyte displays high charge capacities at relatively high cell voltages [126].

It is also important to state that the use of PPD dissolved in KOH as electrolytes for MnO_2 electrodes [101, 120] reveals how two redox mechanisms (faradaic capacitive in the lattice of the electrode and faradaic non-capacitive from the electrolyte) can provide the increase in interfacial charge storage for SCs and other related hybrids [26].

Interestingly, in contrast to the meta-hydroquinone additive which displayed a poor interfacial property owing to difficulty in electrochemically oxidising it at the carbon surface, meta-phenyldiamine displayed highly reversible charge transfer kinetics with greatly enhanced interfacial charge storage [106].

The organic dye methylene blue (MB) has also been adopted as redox additive to 1.0 M H_2SO_4 with MWCNTs as electrodes with a high increase in capacity (Fig. 2.20a). However, in the two-electrode SC test (Fig. 2.20b), this increase in charge capacity was obtained at low cell voltage values (< ca. 0.1 V) [127].

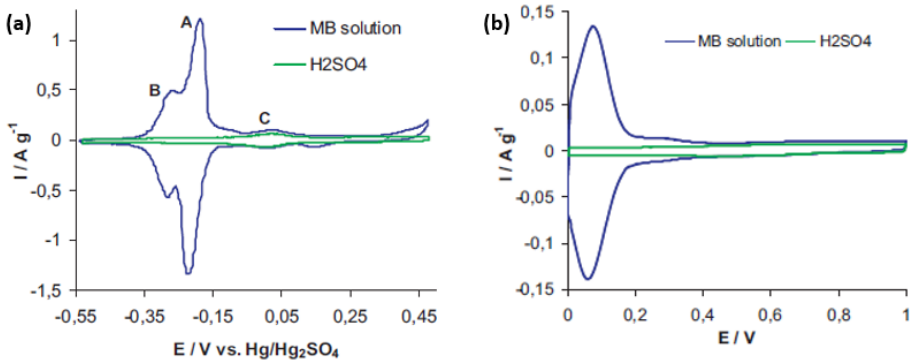

Figure 2.20: CVs of inert and MB incorporated H_2SO_4 with MWCNT as electrode (a) electrode characterisation (b) cell [127].

Also, by adopting the two-electron, two-proton redox reaction of its functional hydroxyl groups, pyrocatechol violet has been used to enhance the charge capacity of AC electrodes [128]. This was carried out by testing pyrocatechol violet as the redox additive in different electrolytes, i.e. 1.0 mol/L Na_2SO_4, 1.0 mol/L H_2SO_4, and 6.0 mol/L KOH. Notably, whilst tests in the 3-electrode configuration showed redox peaks in the 1.0 mol/L Na_2SO_4 and 1.0 mol/L H_2SO_4 electrolytes, in 6.0 mol/L KOH there were no identifiable redox peaks, but rather redox waves corresponding to surface-controlled redox reactions at the carbon surface. However, in the two electrode (device) configuration, the CVs for the pyrocatechol violet redox additive in both 1.0 mol/L Na_2SO_4 and 6.0 mol/L KOH were rectangular i.e. EDL capacitance dominates in the voltage range 0 to 1.0 V.

Whereas, for the 1.0 mol/L Na_2SO_4 supporting electrolyte, two-electrode tests revealed broad peaks [128]. This points out that the charge

storage mechanisms in different electrolytes can lead to differences in how the charge capacity of these devices may be characterised in practice (Fig. 2.21). However, no details of the actual mechanism of the reaction was given with respect to the cell performance in this work, and the Nernstian mechanism of the electrode was not clearly elucidated.

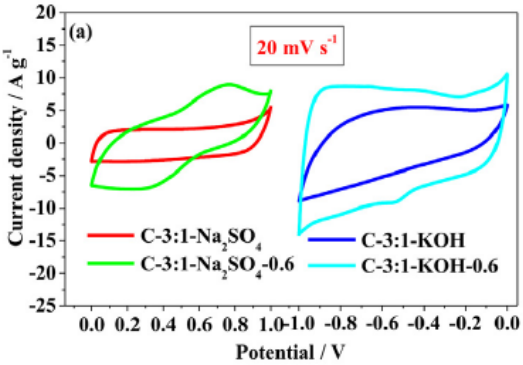

Figure 2.21: CVs of pyrocatechol violet as additive in Na_2SO_4 or KOH [128].

In KOH solutions, *p*-aminobenzenesulfonate [129] and *p*-nitroaniline [129], both of which can undergo a single proton and single electron transfer reaction, have been used as DRS. Furthermore, a comparison of the substituent site of the *ortho-, meta-, and para*-nitroaniline substituents has also shown that in KOH solutions, the redox reaction of *p*-nitrophenol is more effective in acquiring improved interfacial charge storage [130]. Although these reports described the comparative improvement in interfacial capacity obtained from various redox additive, still most of the investigations were on electrode characterisation with only few attempts at understanding how these electrodes would behave in devices. Furthermore, due to the relatively low efficiencies of some of the electrode/redox-electrolyte combination, and the more negative redox potentials of these DRS, the claims of capacitance values for the curved GCD plots were generally misleading (as has been addressed already) and the reported electrode | redox-electrolyte features may not be adequately transferred into a full-range device performance.

Anthraquinone-2,7-disulphonate (AQDS) which undergoes a two-proton, two-electron redox reaction has also been applied to 1.0 mol/L KNO_3, and it was shown that the ESR reduced with increasing concentration of the DRS. For example 27.1 ohms for the blank KNO_3 and 15.3 ohms for 0.1 mol/L AQDS in 1 mol/L KNO_3. Moreover, the energy efficiency was less than 90%, although the charge capacity increase was over 60% compared to the inert KNO_3 electrolyte (see Fig. 2.22) [110].

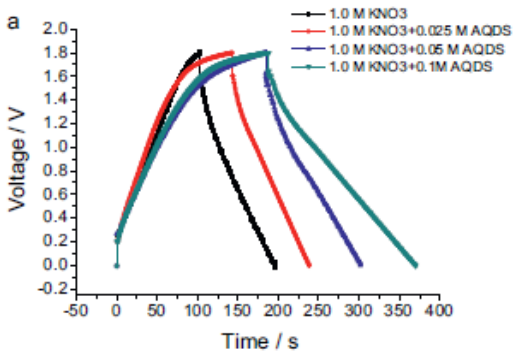

Figure 2.22: GCD plots of AQDS in 1.0 mol/L KNO_3 [110].

Organic electrolytes are known to be stable over a wide potential range. Thus, they can be used to fabricate high voltage devices [31]. As such, the charge capacity of SCs using organic electrolytes has also been increased with the use of some organic DRS. Recently, 1,10 phenanthroline was used as DRS in 1.8 mol/L tetraethylammonium tetrafluoroborate ($TEABF_4$) in polycarbonate. The redox reactions of 1,10 phenanthroline gave a rectangular profile with broad waves corresponding to the oxidation and reduction of phenanthroline, and in 2-electrode device tests the SC containing the phenanthroline showed a rectangular cyclic voltammogram, enhanced by increase in the interfacial charge transfer. This device gave over 40% (see Fig. 2.23) increase in capacity, although its decrease in capacitance with current density (during galvanostatic charging/discharging) was more rapid than that of the SC without the DRS; still it displayed much higher mass normalised energy and power than the SC without the DRS. More importantly, the device using the DRS displays better

cycle stability at higher cell voltages than the device using only the supporting electrolyte [131].

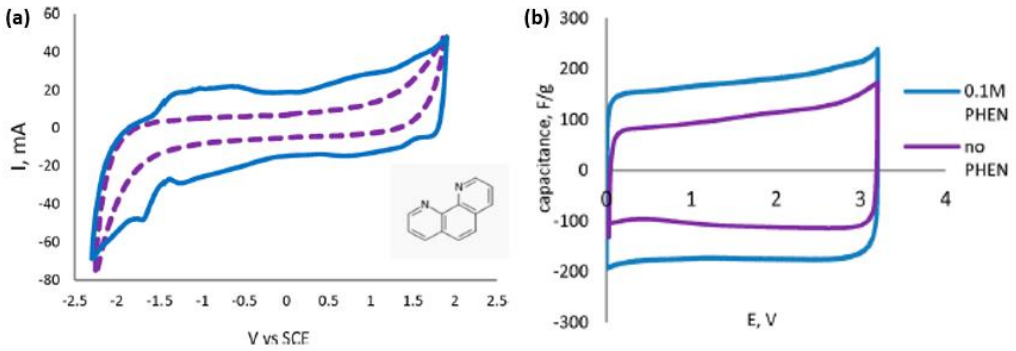

Figure 2.23: CVs of phenanthroline in organic electrolyte (a) electrode and (b) cell characteristic [131].

Successful application of *p*-phenyldiamine in 1.0 mol/L $LiClO_4$ in acetonitrile has also been achieved, confirming a marked improvement in interfacial charge storage with non-peak-shaped CVs. This is understandable since in aprotic media the electron transfer mechanisms of these organic redox molecules are different from that in aqueous media [125].

2.6 Dissolved anionic components for enhanced interfacial charge storage

Ever since the earlier reports on iodides as DRS [97], they have become one of the most widely used dissolved redox anionic species for charge capacity enhancement in supercapacitors.

Basically, on oxidation of the MI (M = Li, Na, K, Rb or Cs), both the reactant and products involving mainly the I_3^- /I^- couple and possibly higher polyiodides would be adsorbed on the electrode, leading to a non-capacitive faradaic (battery-like) charge storage mechanism on the positive electrode. Moreover, the iodides as anions themselves could also contribute to charging the EDLC at the positive electrode.

The interfacial charge stored in the positive electrodes which can be translated to the observed device capacitance also shows some important features that could be linked to the type of metal alkali used. Notably, the electrode capacitance was found to be 203 F/g for NaI and 220 F/g for RbI. This difference was ascribed to the higher polarisation power of Na^+ compared to the larger Rb^+. Since the same AC was used as positive and negative electrodes in both cases, the larger device capacitance indicates a greater ΔQ/ΔU ratio of the positive AC electrode in the RbI electrolyte, considering that $C_{device} = C_+C_-/(C_+ + C_-) = C_-/(1 + C_-/C_+)$ (see Fig. 2.24) [15, 97].

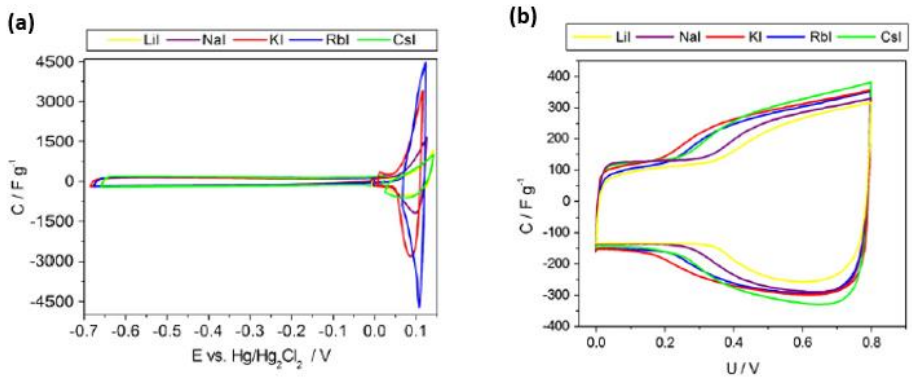

Figure 2.24: CVs for redox electrolytes (MI (M = Li, Na, K, Rb or Cs)) with activated carbon (a) electrode and (b) cell, characterisations.

It is worth mentioning that the claimed capacitance variation of porous carbon electrodes in different iodide containing electrolytes was mainly based on the ΔQ/ΔU ratios, disregarding if the CVs or GCDs were capacitive. As was also stated earlier on, it is necessary to express these storage mechanism in terms of capacity. The concentration effects of NaI in SCs have also been used to elucidate the properties of metal halides as DRS for practical applications [107]. Although no linear correlation was found between an increase in NaI concentration and the performance of the devices (see Fig. 2.25a), 2.0 mol/L performed better than 5 mol/L [107]. However, since the U_L tested in this research i.e. (0.8 V) is rather low, the actual role of possible diffusion, role of

concntration and polarisation were left unaddressed in this report. Furthermore, these current peaks at low cell voltage values which characterises most of these DRS such as I^- or even hydroquinone as earlier addressed in Section 2.5, is an important feature that has only been explained limitedly, and as such, has affected the rigorous understanding of the use of DRS in general. Moreover, as shown in Fig. 2.25b, on floating, it was observed that this current peak also increases.

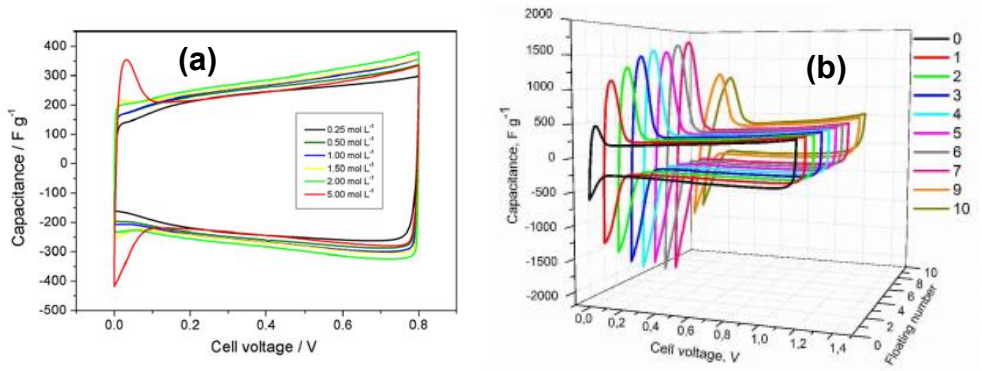

Figure 2.25: CVs of supercapacitors with NaI as redox electrolyte (a) different concentration of NaI [107] (b) 2.0 mol/L NaI under floating [96].

The influence of the concentration of KI as additives to a 1.0 mol/L Li_2SO_4 electrolyte used in fabricating asymmetric SCs comprising of the composite of ZrO_2-MWCNT as positive electrode and WO_3-MWCNT as negative electrode has also been reported [132]. It was shown that increasing the concentration of KI from 7.5 to 30 × 10^{-3} mol/L dramatically affects the charge storage profile of the device. For example at 7.5 and 15 × 10^{-3} mol/L KI the CV of the device was rectangular; however at 30 × 10^{-3} mol/L KI, the CV of the device develops sharp peaks. Moreover, the capacitance of the device tested at a current load of 1 A/g was 198 F/g for the device with 7.5 × 10^{-3} mol/L KI and 96 F/g for the device using Li_2SO_4 without the redox additive, and the cell operated at an optimal voltage of 2.2 V (Fig. 2.26). This essentially shows that paying close attention to the concentration of the redox electrolytes

as additives can indeed lead to improved devices, particularly in asymmetrical SC designs [132]. It is important to point out that although capacitance was not normalised for the amount of redox additive, the capacitance increase at such small addition of DRS is appreciable.

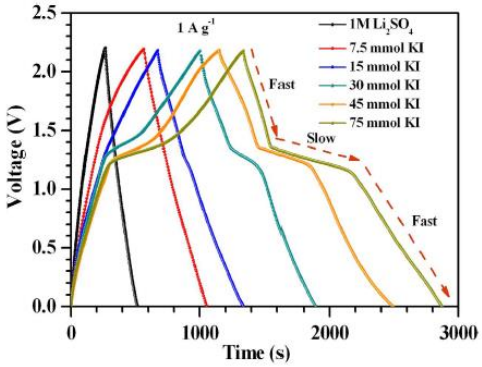

Figure 2.26 GCD plot of the cell (-)WO_3-MWCNT | KI in Li_2SO_4 | ZrO_2-MWCNT (+) with varying concentration of KI.

However, the fundamental reason for this, for example the role of the redox electrode on this observed feature were not explained. Neither was the origin of the increased diffusion due to the increase in concentration correlated with factors such as adsorption, or nanostructure of the electrodes, which were all stated in the report, and clearly had some impact on the observed features.

Using LiI as additive to a solution of Li_2SO_4 and methanol in a symmetric SC with AC electrodes, the self-discharge properties and the low temperature properties were investigated. It was observed that the presence of LiI in the electrolyte helped improve the charge capacity at a low temperature of –40 ^{0}C [133]. The advantageous properties of the mesoporous structure of MWCNTs when they were used as additives to AC electrodes were also described when 1.0 mol/L KI was used as DRS in SCs. This improvement in charge storage properties was attributed to the improved ionic conductivity due to the presence of mesopores which can be of benefit to the transport of the iodide and polyiodide anions [134].

Compared to iodides, bromides have been employed to a lesser extent as DRS: it is important to point out that fundamental findings from this PhD research conclusively confirmed some of these reasons, whilst also extending the broader applications of bromides as viable DRS. An early report showed the enhancement of the capacity of activated carbon electrodes, through the application of an initial long-duration floating step in NaBr solution, however, the capacity increase demonstrated was obtained within a cell voltage of only 1.0 V [135]. Also, another report utilised 1-ethyl-3 methylimidazolium bromide as redox additive to the ionic liquid 1-ethyl-3-methylimidazolium tetrafluoroborate, resulting to a highly stable device with enhanced capacity and good cycling stability [136].

More recently, a report using KBr as electrolyte for AC electrodes was demonstrated to describe the concept of pre-cycling at a higher voltage to enhance capacity [137], which was somewhat similar to the report in [135]. However, the cell voltage profile showed the contribution from the bromide redox activity only at high cell voltage values, i.e. very low utilisation of the bromide DRS for charging (see Fig. 2.27).

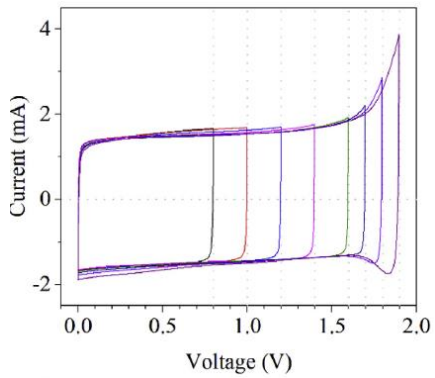

Figure 2.27: CV showing cell with AC electrodes and 1.0 mol/L KBr redox electrolyte [137].

Also, another report on the use of KBr as additive to Na_2SO_4 showed an enhancement in capacity, however, despite using a cation exchange membrane, the demonstrated cell had low voltage current plateaus (Fig. 2.28a)

[138] similar to what was obtainable for KI cells. As was demonstrated by the electrode GCD of this cell (Fig. 2.28b), there also seem to be under-utilisation of the bromide DRS, although in this case, its origin seem to be different from what was described in Fig. 2.27. Generally, the results from these two cells may have been dependent on the design of the cells, which for example may be characterised by cells with poor penetration of redox electrolytes into the porous matrix of the thin (100 μm) electrode in [137] or very-thin and low mass-loading electrode coupled with some effects from the ion-exchange membrane used in [138].

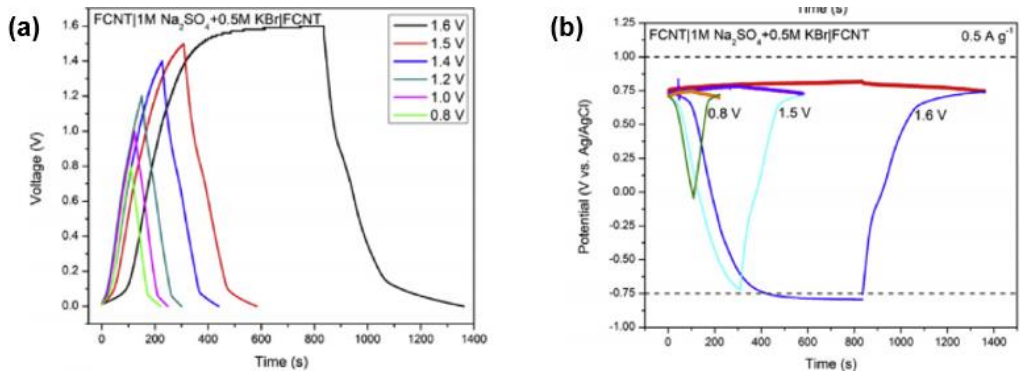

Figure 2.28: GCD plots for (a) cell (b) positrode and negatrode: of the cell with functionalised-CNT as electrodes and 0.5 mol/L KBr as additive in Na_2SO_4 [138].

The $Fe(CN)_6^{3-}/Fe(CN)_6^{4-}$ couple is a typical example for describing redox reactions in the literature. Accordingly, the exemplary electrochemical property of this couple has been adopted as DRS for SC applications. Carbon electrodes that have been used to test the suitability of this couple for improving charge storage in SCs include graphene paper [139], vertically aligned carbon nanotubes (VACNTs) [140], and AC [64]. Since the desirable reversibility of the $Fe(CN)_6^{3-}/Fe(CN)_6^{4-}$ redox reaction is well known, another important property that should be considered is the adsorption of these redox anions at the positive electrode. In practice, it has been shown that although

the electrostatic attraction of these redox anions to the positive carbon electrode interface is relatively strong, the adsorption of these anions at the interface is still quite low.

A recent spectroscopic investigation of the adsorption of the $Fe(CN)_6^{3-}/Fe(CN)_6^{4-}$ couple at AC showed low adsorption for the oxidation product. This property was used to explain the high rate of self-discharge in devices using $Fe(CN)_6^{3-}/Fe(CN)_6^{4-}$ as DRS. In contrast, devices using the I_3^-/I^- couple which showed high adsorption at the carbon surface displayed self-discharge properties that were 100 times slower than that of devices using the $Fe(CN)_6^{3-}/Fe(CN)_6^{4-}$ as DRS [141]. This high rate of self-discharge is the reason why ion-selective separator membrane was used to improve the practical device performance of SCs using the $Fe(CN)_6^{3-}/Fe(CN)_6^{4-}$ couple as DRS [64]. A detailed description of the general design of practical devices using DRS is given in section 2.9.

Despite the low adsorption leading to high rate of self-discharge of the $Fe(CN)_6^{3-}/Fe(CN)_6^{4-}$ couple as DRS, a large improvement in the interfacial charge of graphene paper has been reported, and this charge capacity enhancement showed a strong dependence on the concentration of the $K_3Fe(CN)_6^{3-}$ redox additive in 1.0 mol/L Na_2SO_4 [139]. Also, by using vertically aligned carbon nanotube (VACNT) as the electrode material, it was shown that the redox activity of the $Fe(CN)_6^{3-}/Fe(CN)_6^{4-}$ couple was confined in the macropores of the VACNT, leading to an electrode-confined thin-layer effect characterised by high-rate and low-diffusion charge storage in the porous structure of the electrode material. This E|E interface displayed high stability after 5000 cycles [139]. In another investigation, equimolar proportions of the $K_4Fe(CN)_6$ and $K_3Fe(CN)_6$ redox additives in alkaline KOH electrolyte were used to increase the interfacial charge of a NiO electrode. Due to the increase in charge capacity, the electrode also showed improved charge storage properties at a low temperature of –20 °C [25].

Additionally, the $Fe(CN)_6^{3-}/Fe(CN)_6^{4-}$ couple has been applied to improve the interfacial charge storage of transition metal hydroxide electrodes such as $Co(OH)_2$-graphene nanosheet [102], Co-Al double hydroxide [142], and ECP electrodes, for example polyaniline [143]. It should be pointed out that the use of redox electrolytes with redox electrodes exemplifies dual interfacial redox mechanisms occurring in the lattice of the electrode and in the electrolyte. This was briefly described in Ch.1, and herein reproduced in Eq. 2.22, with the accompanying illustration of the electrode characterisation shown in Fig. 2.29 [25].

In electrode: $NiO + OH^- = NiOOH + e$ (2.22a),

At E|E interface: $Fe(CN)_6^{3-} + e = Fe(CN)_6^{4-}$ (2.22b).

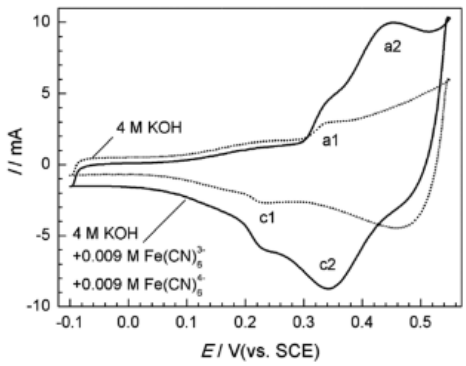

Figure 2.29: CVs of NiO electrode in KOH with or without the $Fe(CN)_6^{3-}$/ $Fe(CN)_6^{4-}$ DRS [25].

Moreover, only interfacial properties (electrode | electrolyte characterisation) of these combinations of transition metal hydroxide electrode and DRS have been described thus far, and the performance of practical devices using such combined storage mechanisms has not yet been given detailed treatments. However, the strategies that would be described in general, and with specific design examples in Section 2.9, may be applied to enhance the practical performance of these redox-electrode | redox-electrolyte combinations.

It is also important to point out that the MoO_2^- anion obtained from using Na_2MoO_4 as DRS was shown to improve the capacitance of a symmetric EDL capacitor with AC electrode from 51 F/g in 1 mol/L Li_2SO_4 to 65 F/g in 1.0 mol/L Li_2SO_4 + 0.1 mol/L Na_2MoO_4 (calculated based on rectangular CVs). The optimal cell voltage of this device was 1.6 V. The Na_2MoO_4 redox additive also increased the passivation of the stainless steel current collector, thereby reducing its susceptibility to pitting corrosion due to attack from the SO_4^{2-} ion [144].

2.7 Dissolved cationic components for enhanced interfacial charge storage

When a positive electrode is functionalised with cation affinitive groups, electroactive cations from the electrolyte could be chemically adsorbed at these positive electrodes, even though cations are not electrostatically attractive to positive electrodes. Since carbon atoms at the edge sites are more reactive than the internal carbon atoms, these edge sites could readily become oxidised (or stabilised) thereby forming oxygen-containing groups, e.g. –OH and –COOH, etc. These functional groups which can be deprotonated to become negatively charged would then have a high cation affinity. On the other hand, irrespective of deprotonation, the highly electronegative oxygen (and also nitrogen, sulphur and halogen) atoms can still offer some affinity to metal cations [15].

Examples of this mechanism include "(+)AC | $CuSO_4$ – $FeSO_4$-H_2SO_4" [99], "(+)functionalised carbon surface | $CuCl_2$-HNO_3" [24], and "(+)Graphene-felt | Ce^{3+}-H_2SO_4" [105]. Brief descriptions of these mechanisms for charge storage at the stated interfaces are presented forthwith.

In an earlier report, it was demonstrated that when CuSO4 and FeSO4 were used as mixed redox additives in H_2SO4, the charge storage property was observed to be related to the concentrations of the Fe^{2+} and Cu^{2+} ions, and

also with the porosity of the carbon electrode. It was thus shown that using the $CuSO_4$ electrolyte alone as additive gave a poor reversibility. However, on mixing with $FeSO_4$, improved charge storage properties was observed. In general, the reaction mechanism for this enhanced charge storage is mainly due to the accessibility of the Cu^{2+} and Fe^{+} ions to the surface oxy-groups of the carbon electrode [99]. The mixture of $CuCl_2$ and HNO_3 as electrolyte for porous carbon microsphere (PCM) electrode resulted in large interfacial charge storage.

This was attributed to the adsorption of Cu^{2+} on the surface carbonyl groups to form a reversibly adsorbed layer of $CuCl_2$ on the surface of the PCM electrode. It was also important to locate an optimal potential range across the interface in order to prevent the irreversible deposition of Cu [24].

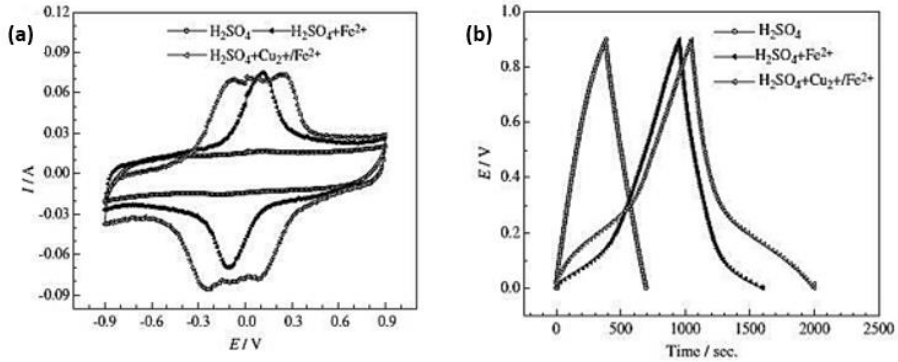

Figure 2.30: Characterisation of mixed redox cations of Cu^{2+} and Fe^{+} ions in H_2SO_4 (a) CV of electrode characterisation (b) GCD plot of resulting device.

The use of an electrode material that provides a high overpotential for the redox reaction of the Ce^{4+}/Ce^{3+} in aqueous (acidic) media has been shown to be greatly dependent on the surface property of the graphene-felt electrode used [105]**.** This is because when the reaction in Eq. (2.23) takes place in acidic media, e.g. 1.0 mol/L H_2SO4, the standard electrode potential E_N for the reaction is 1.44 V vs NHE.

Thus if an electrolyte, e.g. $Ce_2(SO_4)_3$ dissolved in 1.0 mol/L H_2SO_4 is used as the source of the Ce^{4+}/Ce^{3+} couple, the redox reaction cannot occur within the stable operating potential of water. However, if an electrode with a higher overpotential for the evolution of oxygen is employed, then this redox reaction can be accommodated without electrolyte decomposition thus leading to improved charge storage at more positive potentials. This reasoning has been used to develop an asymmetric SC with AC as the negative electrode, and modified graphite felt as the positive electrode. The resulting device was operated at an optimal cell voltage of 1.5 V (with specific energy of about 13.8 Wh/kg) [105].

$$Ce^{3+} = Ce^{4+} + e \qquad (2.22).$$

It is also important to mention that the Fe^{3+}/Fe^{2+} couple (in 1.0 mol/L H_2SO_4) has been used to enhance the interfacial charge properties of the polyaniline-SnO_2 composite electrode, and the enhanced interfacial charge was relatively stable after 2000 galvanostatic charge-discharge cycles at 1.0 A/g [145]. Also, the Cu^{2+}/Cu^{+} couple (in 1.0 mol/L H_2SO_4) was used to enhance the interfacial charge of the PAn electrode, giving rise to improved charge capacity. However, due to the well-known complicated heterogeneous reaction kinetics involving the reduction caused by Cu deposit on the electrode surface, the rate property of the electrode was relatively poor [146].

2.8 Design of supercapacitors with redox electrolytes

It is important to point out that although the use of redox electrolytes have been demonstrated as also been suitable for adoption with redox-electrode such as TMOs or ECPs, still, the main focus of this dissertation is on the specific use of redox electrolytes in EDL capacitors especially with carbonaceous electrodes.

Based on the preceding discussions on the applications of redox electrolytes, a detailed exposition on the design of practical devices with DRS would be given in this section. Although all the examples used to explain these designs utilised carbon electrodes, it would be easily appreciated that the designs described herein, can be extended to include other class of electrodes which may be coupled with DRS.

Figure 2.31 (a and b) gives a generalised and schematic description of the design of an electrochemical energy store, for instance a supercapacitor or battery. Notice that the illustrations in Fig. 2.31 are more detailed representations of Fig. 1.3 which was briefly described in Ch. 1.

Figure 2.31 a and b corresponds to the device in the charging and discharging modes respectively. In the most general case, this charge storage device can comprise of two non-mixing electrolytes namely the negalyte which is the electrolyte at the negative electrode (negatrode) and the posilyte which is the electrolyte at the positive electrode (positrode). It would be noticed that these terms have been used throughout the earlier parts of this dissertation to represent the electrodes and electrolyte(s) in an electrochemical storage device.

Specifically, the terms positrode, negatrode, posilyte, and negalyte are used in place of the terms of cathode, anode, catholyte and anolyte, respectively. The former terms were recently introduced as a means of avoiding the confusion that inevitably arises when the latter terms are used in fundamentally describing the components of electrochemical energy stores [16]. For example, it is a fact that a positrode is a cathode in discharging but an anode in charging. Similar situations apply to the use of negatrode, posilyte and negalyte. In Fig. 2.29, S is a separator membrane, and it could either be an ion-exchange membrane (IEM) (or more generally an ion-conductor or solid electrolyte) which allows the passage of specific ions, whilst blocking the passage of others, e.g. Nafion membrane. Or it could be a porous separator

membrane, e.g. glass-fibre paper, cellulose-based separators etc. Also, note that the DRS may either be in one or both compartments. A number of scenarios would now be used to describe various features of this configuration in practice.

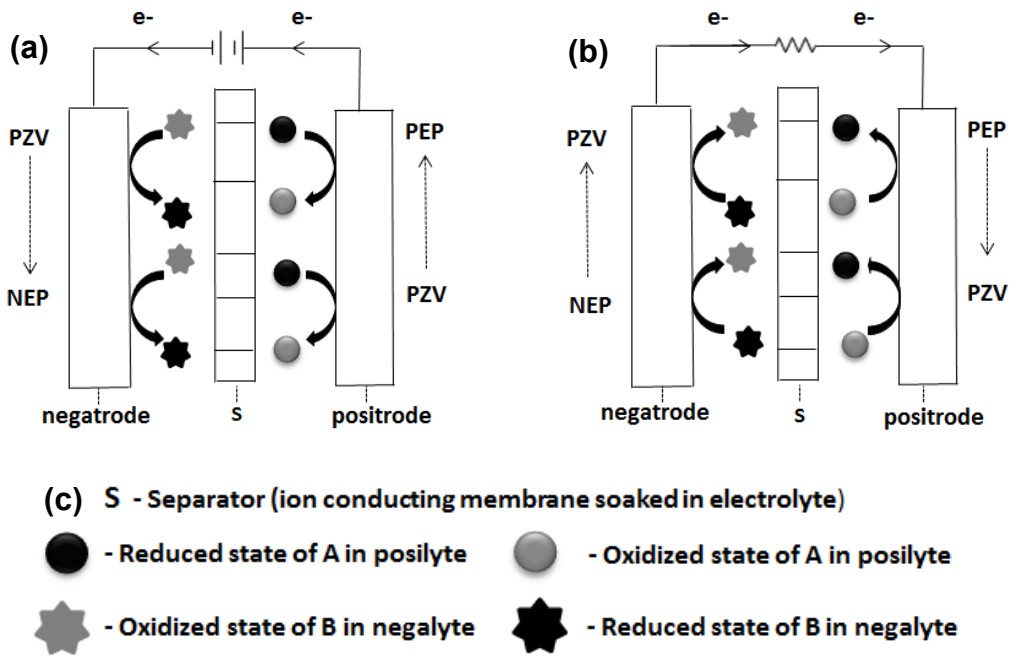

Figure 2.31: Generalised diagrams of an electrochemical energy storage device (a) under charging and (b) under discharging conditions. (c) Explanations to symbols in (a) and (b). PEP and NEP are the peak positive and negative electrode potentials, respectively, measured at the maximum cell voltage (U_L). PZV (point of zero voltage), is the equipotential of the positive and negative electrodes at zero cell voltage.

When this device is adopted exactly as is shown (i.e. the separator membrane is able to prevent electrolyte mixing), on charging, the DRS in the posilyte is oxidised whilst the DRS in the negalyte is reduced (Fig.2.31a). On discharging the DRS in the posilyte is reduced and the DRS in the negalyte is oxidised (Fig. 2.31b). If the separator completely compartmentalises these redox species but allows ionic conduction of protons, cations or anions, whilst been able to stop the cross-diffusion of the products of the electrode reactions, there would be limited self-discharge of such a cell under open circuit

conditions. (Note that open circuit conditions correspond to a removal of the load in Fig. 2.29b). Such a design strategy could result in optimum devices.

Such a configuration was applied in a device comprising of (–)AC | $VOSO_4$ || KI | AC(+), which makes use of the redox reactions of the VO_2^{2+}/VO_2^{+} couple in the negalyte and the I_3^-/I^- couple in the posilyte. The separator denoted by || was a proton exchange membrane (Nafion 117). This device showed improved charge capacity, with the positrode being characterised by the reaction mechanism resulting in strong adsorption of the I_3^-/I^- couple, whilst the VO^{2+} can transfer electrons to the negatrode along the –$COOVO^+$ bond between the oxy-group and VO^{2+} ion in the negatrode [100].

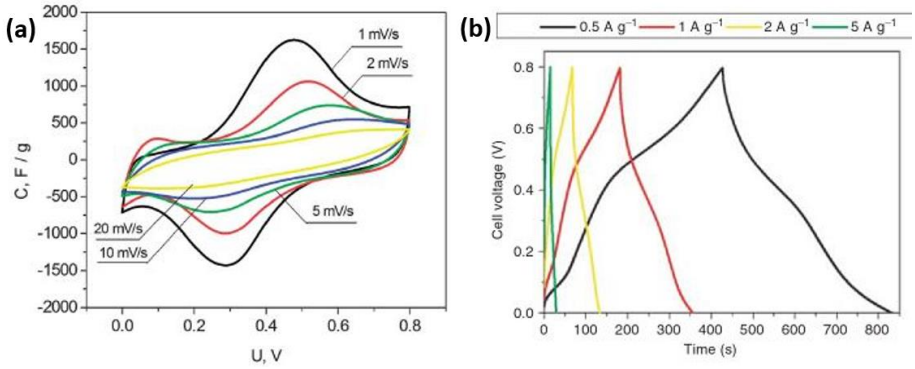

Figure 2.32: Characterisation of the cell (–)AC | $VOSO_4$ || KI | AC(+) (a) CVs (b) GCD plots at different current loads [100].

It is interesting to note that a related adaptation of this concept has been applied to Li-ion battery research. In this case the configuration was: (–)Li-metal | organic electrolyte || LiI-KI-I_2 |AC(+), where the organic electrolyte (negalyte) is 1.0 mol/L $LiPF_6$ in ethylene carbonate/dimethyl carbonate, and the separator (||) is the glass ceramic separator LATP (i.e. Li_2O-Al_2O_3-P_2O_5) which allows the passage of only Li^+, but blocks the passage of other solution components. The resulting device displayed charge capacity approaching 98% of the theoretical capacity of the aqueous posilyte (although

the current loads are relatively low at ca. 2.5 mA/cm^2). It should be noted that the charge capacity reported was normalised to the total mass of the active species in the posilyte since the investigators could measure the mass of posilyte confined in the positive electrode portion of their cylindrical cell design. Also, the theoretical electrode capacity was normalised based on all active components, leading to reliably calculated performance metrics. Furthermore, in the design of this hybrid device which uses an aqueous DRS/carbon positrode, it should be noted that the mechanism of charge storage is due to the Li^+/Li redox mechanism of the negatrode/negalyte and the I_3^-/I^- redox mechanism of the DRS in the posilyte. As such it made use of the good interfacial properties of the "I_3^-/I^- | AC" interface, leading to a high-energy prototype device with a charge efficiency of over 97% [147].

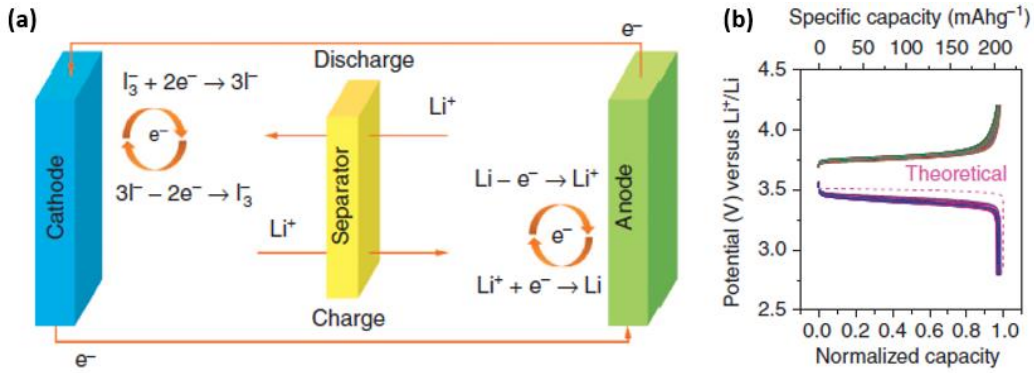

Figure 2.33: Schematic illustration of the storage mechanism (a) and GCD plot (b) for the cell: (–)Li-metal | organic electrolyte || LiI-KI-I_2 |AC(+) [147].

In the configuration where the posilyte and the negalyte are the same as in a conventional cell, but with the electrolyte consisting of a DRS, for example hydroquinone dissolved in H_2SO_4 [98, 113], or $K_3Fe(CN)_6$ dissolved in Na_2SO_4 [64], then one can visualise the main redox mechanism as the one occurring at the positrode | posilyte interface. Accordingly, if the DRS is assumed to be hydroquinone, then the reaction would involve the oxidation of

hydroquinone into benzoquinone at the positrode according to Eq. (2.23) (where HQ is hydroquinone and BQ is benzoquinone):

$$HQ = BQ + 2e \quad (2.23).$$

From Eq. (2.23), it can be appreciated that although the product of the charged species, i.e. BQ, could adsorb on the AC positrode, it may still diffuse into the electrolyte and then migrate to the negatrode. Accordingly, if in Fig. 2.29 we assume that there is no load across the terminals (i.e. at open circuit state) then the BQ that diffuses into the negalyte portion of the cell can then be reduced at the negatrode, and this would in turn positively shift the potential of the negatrode, thus reducing the overall voltage of the cell.

This mechanism, known as redox shuttling, accounts for the high rate of self-discharge that some practical supercapacitors with DRS suffer from, as has been rigorously described in [113]. Thus, if the separator S is an ion-exchange membrane (e.g. a proton exchange membrane) which could impede the movement of BQ into the negalyte compartment of the cell, whilst allowing the transport of the H^+ ions, then the self-discharge rate can be reduced. This strategy has been adopted to mitigate the self-discharge of SCs using graphene-hydrogel electrodes with a DRS of 0.4 mol/L HQ dissolved in 1.0 mol/L H_2SO_4. The self-discharge rate was markedly reduced in the device using the Nafion membrane in comparison with the device that used conventional porous separators [113]. Accordingly, by making use of an ion-exchange membrane, a SC with AC electrodes using $K_3Fe(CN)_6$ as DRS in 1.0 mol/L Na_2SO_4 showed improved charge capacity. A high cell voltage of 1.8 V was recorded for this cell. Also, the performance of EDLCs (without the DRS) using either the glass-fibre paper or IEM was similar, although the ESR of the device using the IEM increased with increasing the IEM thickness. Furthermore, after 15,000 cycles this report also demonstrated that there was no marked degradation of the IEM. Thus, apart from the slight difference in power response (ion transport in IEMs is slower compared to the conventional glass-

fibre or filter paper), the charge storage profile of these two types of separators were identical. Moreover, the use of the IEM greatly improved the charge storage properties of the device with the DRS, whilst DRS-containing devices using conventional porous separators showed a comparatively poor performance due to redox shuttling [64].

Another important property for consideration in the selection of DRS for practical applications is the standard electrode potential of the redox reaction of the DRS. This is important because in certain cases when the positrode potential of the redox reaction is relatively less positive, the charge capacity increase of the resulting device would occur at low cell voltage values, which is of little use in terms of energy storage capacity. The features of the cells with hydroquinone/benzoquinone (see Fig. 2.16 and 2.17) or I^-/ I_3^- (see Fig. 2.24 and 2.25) as the redox additive can be used to explain this point.

Figure 2.32 gives an illustration of the GCD plots that could be displayed by some supercapacitors with DRS. From Fig. 2.32, curve A corresponds to the supercapacitor without DRS, and as could be observed, curve B clearly represents the GCD plots when couples with less positive electrode potentials e.g. I_3^-/I^- or hydroquinone/benzoquinone are used as the positrode in SCs.

Moreover, the selection of DRS in practice is constrained by the appropriate pH at which the thermodynamics and kinetics of the redox reaction would be favourable, and also by the stability of aqueous solutions at different pH values. Consequently, most of the reports using DRS have actually made use of the common redox additives, for example H_2Q [98] and also $FeSO_4$ and $CuSO_4$ [99] in acidic electrolytes, PPD in alkaline media [120], and KI in neutral solutions [97], within the bounds of the thermodynamic restrictions. This is one of the reasons why device engineering principles as generalised and rigorously explained in Fig. 2.29, is of immense importance to the practical applications of DRS.

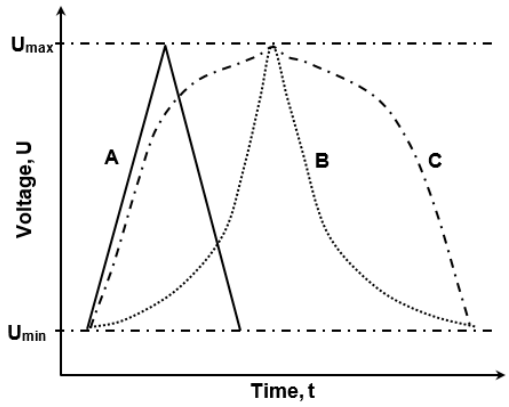

Figure 2.34: Illustrative comparison of the galvanostatic charging and discharging plots of a conventional SC (plot A, solid line) with a maximum charging voltage, U_{max} and a minimum discharging voltage, U_{min}, and the same SC containing a redox electrolyte in which the same redox couple can react on both the positrode and negatrode at the same potential (plot B, dot line), or the redox couple is restricted to react only on either the positrode or negatrode, but not both (plot C, bold dotted line).

In a recently reported approach, the electrolyte comprising mixed $VOSO_4$ and $SnSO_4$ in 0.1 mol/L H_2SO_4 was used as the DRS [148]. In this investigation, the electrolyte composition was not separated into negalyte or posilyte, although an anion-exchange membrane was used as the separator to prevent the redox shuttling of the active species. Accordingly, the designed cell was able to confine the redox reaction of VO^{2+}/VO_2^{+} to the positrode. Also, the redox reactions of VO^{2+}/V^{3+}, V^{3+}/V^{5+} and Sn/Sn^{n+} (i.e. deposition of tin on the surface of the AC during charging of the cell, and the dissolution of the deposited tin into mainly Sn^{2+} and possibly Sn^{4+} during the discharging of the cell) were confined to the negatrode. Post-mortem analyses of the electrodes used in these cells also pointed out the possibility that these redox reactions mainly occurred within the porous structure of the AC electrodes utilised. This arrangement resulted in a battery-like storage which operated at an optimal

cell voltage of 1.4 V and displayed relatively good power performance during galvanostatic charge-discharge cycles (see Fig. 2.33) [148].

The ability of well-chosen membranes (ion-exchange or otherwise) to physically separate the two different electrolytes i.e. the negalyte and posilyte, in addition to being used to confine the redox mechanism occurring at both electrodes without shuttling, can also be applied in practice to increase the maximum cell voltage of devices using DRS. It has been explained that using the KI DRS in an unseparated cell can result in devices with high charge capacity at low cell voltage (see curve B in Fig. 2.34, or specifically Fig. 2.24 and 2.25)

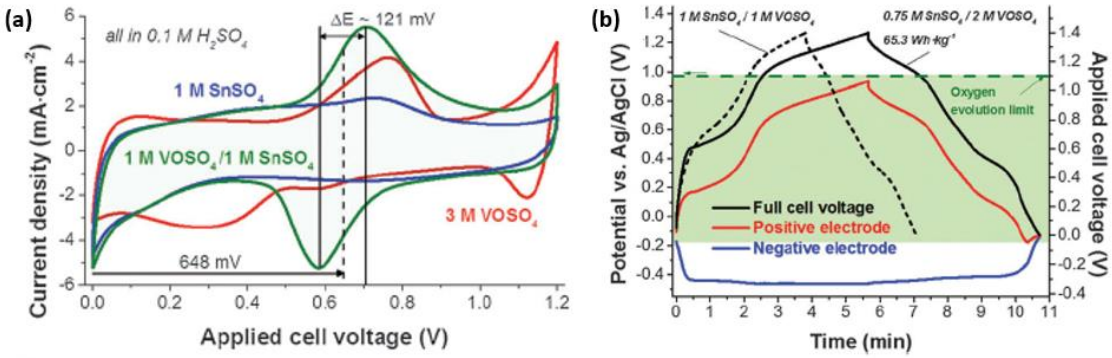

Figure 2.35: Characterisation of the device and interfaces for the cell: (-)AC VO^{2+}/V^{3+}, V^{3+}/V^{5+}, Sn/Sn^{n+} || VO^{2+}/VO_2^{+} | AC(+) (a) CV (b) GCD plot [148].

However, by separating KI in the posilyte from KOH in the negalyte, it has been shown that the cell voltage of these devices can be extended from about 1.0 V in the case of the unseparated symmetric cell using KI, to 1.5 V for the cell with the configuration of "(–)AC| KOH || KI | AC(+)". This cell arrangement makes use of the high overpotential for hydrogen evolution on the AC negatrode in alkaline media, to extend the capacitive potential range of the negatrode (without DRS in the negalyte), thus increasing the maximum cell voltage of the device [14]. The resulting performance from such a cell is similar to the illustration in (Fig. 2.34, curve C) (Note that curves B and C are features of devices which have been described as supercabattery, because the

battery-like properties of the devices dominate over the inherent capacitive properties of one or both of the electrodes used [15]). However, for simplicity sake, the more general term supercapattery would be adopted throughout this thesis.

Also, it is important to state that the use of these terms to describe these devices are non-trivial. This is because important findings from this PhD research actually showed that these deviations of the features of devices from predominantly capacitive to battery behaviour can be fundamentally linked to the properties of the electrode | electrolyte interface resulting in important characteristics that are pertinent to the design of these devices.

It should also be pointed out that for the cell (–)AC| KOH || KI | AC(+), the separator (||) does not need to be an ion exchange membrane. Moreover, it must be able to prevent the intermixing of the electrolytes to some degree. Accordingly, devices of this sort are designed in such a way that the positrode and negatrode do not have excess posilyte or negalyte, respectively [111]. Similarly, by designing a cell comprising of a high pH negalyte and acidic posilyte i.e. "(–)AC | $MgSO_4$ + KOH || KI + H_2SO_4 | AC(+)", devices with maximum voltage of about 1.8 V have been demonstrated. It was shown that their performance exceeded that of the cell with mixed $MgSO_4$/KI electrolyte [149].

It is also important to point out that this use of dual electrolytes in cells which are termed as bi-electrolyte cells in this research, has been adopted as a means of increasing the maximum cell voltage of conventional SC devices (i.e. without any dissolved redox species). Notably, the configuration "(–)AC | KOH || $LiNO_3$ | AC(+)" has been used to design cells with maximum operating voltages of 2.2 V [59]. This implies that by confining the electrolytes to particular electrodes, the full stable potential window of the E|E interface can be reached, leading to increased maximum cell voltage for the device. These

aforementioned device engineering approaches are indeed promising, but it should be pointed out that their commercial adoption might be challenging.

In a bid to design devices displaying relatively high specific energy values using DRS but circumventing the use of (relatively expensive) ion-exchange membranes, the mixed electrolyte comprising of KBr and methyl-viologen-dichloride ($MVCl_2$) was used in an SC device with carbon electrodes. This device exploited the strong adsorption of the product of the reduction of the methyl-viologen cation and oxidation of Br^- at the negatrode and positrode, respectively. The resulting device operated at a maximum cell voltage of 1.4 V with relatively high specific energy [41]. Note that this design concept actually utilises a cationic and anionic DRS in one cell, thus the resulting device actually displayed predominantly battery characteristics. In this case, such devices are good analogues with batteries based on the mechanism of storage coming from the electrodes, and as such these resulting devices are strictly supercabatteries due to their very marked battery features (see Fig. 2.13e). It should be pointed out that this PhD research only used the general term supercapattery as described already.

It has also been shown that some redox electrolytes which undergo interfacial chemical reactions leading to strongly adsorbed complexes on the carbon surface can result in devices that display improved charge capacity and reduced rate of self-discharge. This has been applied when the electrolyte of mixed heptyl-viologen and NaBr was used with AC electrodes. This device made use of the surface-adsorbed complexes reversibly formed and dissolved during charging and discharging, respectively. On the positrode Br^- was oxidised to Br_3^- which then reacted with the HV^{2+} to form the adsorbed $[HV^{2+} . 2Br_3^-]_{ads}$ complex. On the negatrode HV^{2+} was reduced to HV^+ which then reacted with the Br^- to produce the adsorbed $[HV^+ . Br^-]_{ads}$ complex. The reverse of this reaction occurred during discharging when the surface-adsorbed complexes both dissolved.

Equation 2.23 (a and b) describes this process, where the forward reaction corresponds to charging, and the reverse reaction to discharging the cell [112].

At the negatrode: $HV^{2+} + Br^{-} = [HV^{+} . Br^{-}]_{ads}$ (2.23a),

At the positrode: $2Br_3^{-} + HV = [HV^{2+} . 2Br_3^{-}]_{ads}$ (2.23b).

With increasing attempts at developing flexible supercapacitors, the use of polymer electrolytes has been on a rise. Briefly, the polymer electrolyte comprises of the binder material (e.g. PVA) and the electrolyte (H_2SO_4), and it is placed in between the positrode and negatrode, making the polymeric electrolyte both separator and electrolyte [150]. Essentially, with the redox electrolyte added into the polymer electrolyte composition, the so-called redox-polymer electrolyte is formed. Some examples include PVA-H_2SO_4-hydroquinone [150], PVA-H_2SO_4-alizarine red S [151], KOH-PVA-KI [152]. In general, some of these investigations have shown that the conductivity of the gel-polymer electrolyte increases with increase in concentration of the redox additive. This is mainly attributed to improved charge transport on the application of the ionic additive. However at much higher concentrations, conductivity reduces due to migration effects or phase separation [151].

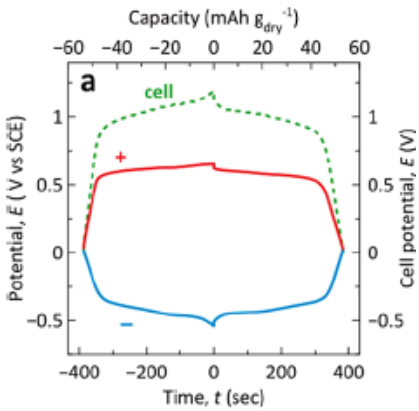

Figure 2.36: GCD plot for the activated carbon electrodes in a cell comprising of HV^{2+} and Br^{-} as DRS [112].

In general, this increase in conductivity of gel polymer electrolyte with the incorporation of redox additives have been linked to improved rate kinetics from impedance spectroscopic investigations [153]. Due to the inherent properties of these redox polymer electrolytes, the energy efficiency is usually low [154], although some of these devices are promising [151].

2.9 Chapter Summary

Electrode charge storage mechanisms have been critically reviewed. Against this backdrop the mechanism of charge storage in supercapacitors with redox electrolytes have been rigorously analysed.

The confusions inherent in the characterisation and quantification of charge storage due to charging by DRS have been comprehensively assessed with detailed examples.

Organic molecules, cationic, and anionic components that are used as DRS have been critically reviewed. Also, the features, and general characteristics of the electrode | electrolyte interface and corresponding devices were discussed.

It was shown that some redox-electrode | redox-electrolyte configurations have only been characterised at the interface level only, with only few significant demonstration of devices.

Designs of supercapacitors with DRS were critically assessed and a number of peculiarities were identified. For example it was generally observed that the features of cells assembled with DRS with narrow electrode potential within the stability window of water usually display current peaks at low cell voltage values.

General device engineering strategies were also reviewed, accordingly, detailed and insightful descriptions of their storage mechanisms were provided.

CHAPTER 3: METHODOLOGY

3.1 Research Approach

The main aim of this research was to apply fundamental electrochemical device engineering principles to investigate the use of dissolved redox species in EDL capacitors with aqueous electrolytes. Based on the review of relevant literatures, and the corresponding identification of some gaps and opportunities for improvement to the fundamental understanding of these devices: the first series of tasks undertaken were to critically survey the theoretical reduction potentials of candidate redox electrolytes. Accordingly, the solubility, theoretical capacity and conductivity of some selected dissolved redox species were appraised.

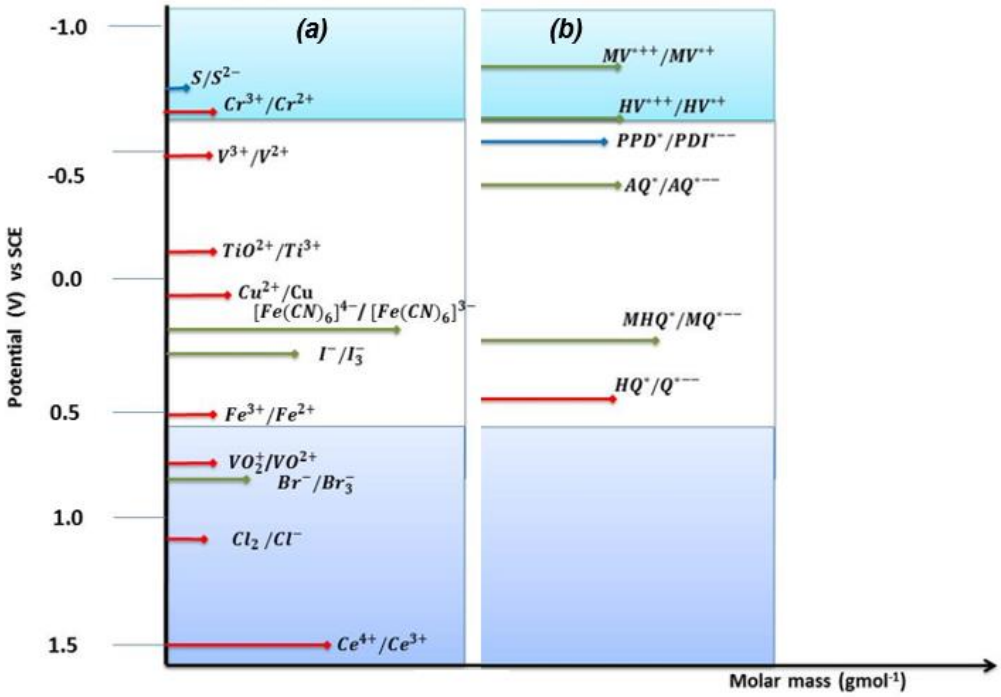

Figure 3.1: Approximate formal redox potential of some (a) inorganic and (b) organic redox species that may be used in water. Length of arrow is approximately the relative molar mass of the compounds.

For the organic molecules, MV: methyl-viologen, HV: heptyl-viologen, PPD: p-phenyldiamine, AQ: anthraquinone disulfonate, MHQ: methyl hydroquinone,

HQ: hydroquinone. The colour of the arrows represents the pH of the solution which these species have been used for based on the available literatures. Blue: alkaline, red: acidic, green: neutral. Note that the organic DRS MHQ (which was investigated for the first time in this research, can also be used in acid electrolytes).

For electrode suitability, representative commercial electrodes that display varying porous and surface characteristics were screened, and subsequent selections were made. In line with this, two different activated carbons were chosen. Furthermore, with the aim of understanding the fundamental effects of the structural properties of the electrode on the redox kinetics, a highly graphitized (few-layer graphene nanoplatelets) was also selected for investigation.

Accordingly, as seen from the generic structure of the experiments carried out in this research (Fig. 3.2), fundamental electroanalysis were used to understand the effects of the redox and thermodynamic properties of the dissolved redox species (DRS) at inert electrodes, whilst basic interfacial electroanalysis of the carbons in inert electrolytes were also carried out. Through electrochemical device design principles, the electrode – redox electrolytes were then coupled to investigate both their fundamental characteristics and applications in practical devices.

In Fig. 3.2, the abbreviations for the analytical techniques are: BET: Brunauer-Emmet-Teller and DFT: density functional theoretical analysis of physisorption properties. CV: cyclic voltammetry, GCD: galvanostatic charge-discharge, EIS: electrochemical impedance spectroscopy, EQCM: electrochemical quartz crystal microbalance. XPS: x-ray photoelectron spectroscopy, Raman spectroscopy, UV-vis (ultraviolet-visible spectroscopy). Imaging includes SEM (scanning electron microscope), TEM (transmission electron microscopy) and Atomic force microscopy (AFM).

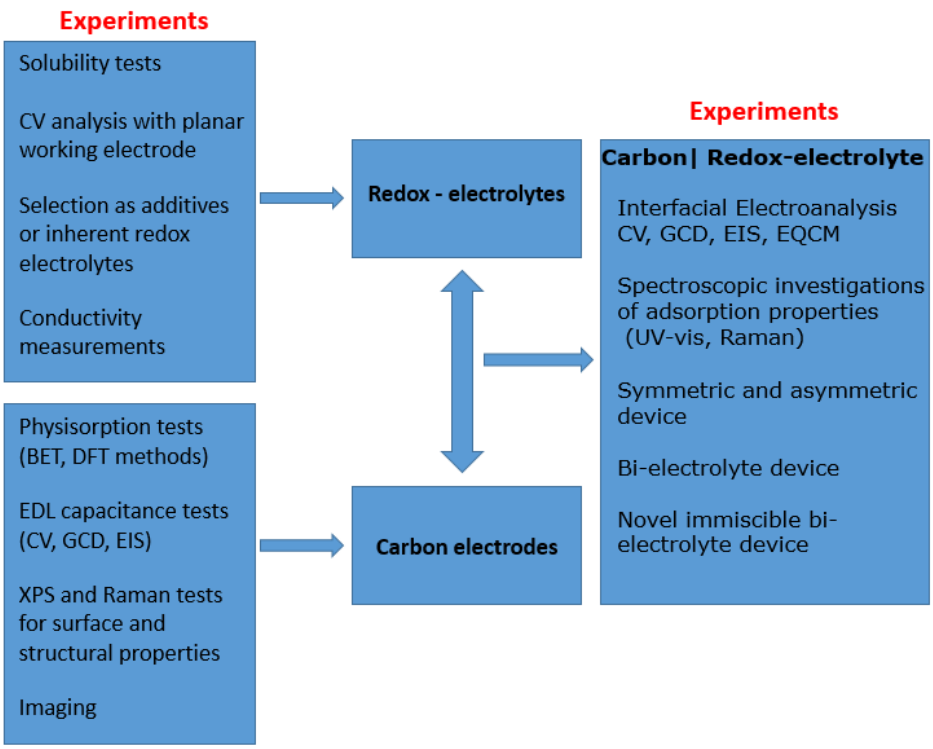

Figure 3.2: General research approach

3.2 Materials and equipment

Table 3.1 and 3.2 lists the materials and chemicals used in this research respectively, whilst Table 3.3 itemises the equipment used.

Table 3.1: List of materials

Material	Designation	Vendor
Graphite rod (99% carbon)	High Purity, High Density Graphite	Henan Huaxi, Co., China
Titanium rod (99% Ti)	High Strength ASTM	Shaanxi, Non-ferrous Metal Co., China
Titanium foil (0.2 mm thickness)	High purity Ti	Goodfellow, UK
Platinum foil (0.2 mm thickness)	High purity Pt	CH Instruments, China
Platinum wire (0.25 mm diameter)	High purity Pt	CH Instruments, China
Standard calomel electrode	CHI 150 SCE	CH Instruments, China

Activated carbon	YEC-8A	Fuzhou Yihuan Carbon Co., China.
Activated carbon	HCE 202	Haycarb, USA
Graphene nanoplatelets	Grade – C750	XGSciences, USA
Carbon black	BP 2000	Cabot, USA
Poly(tetrafluoroethylene) (PTFE)	PTFE 60% wt. in water	Sigma Aldrich
Glass microfiber filters	GF/D	Whatman, USA
Cation exchange membrane	Nafion 117	DuPont
PTFE Swagelok Fittings	PTFE high pressure fittings	Yangzhong Gongzheng Fluid Controls Co., China

Table 3.2: List of chemicals

Chemical name	Formula (Purity or % wt.)	Vendor
Potassium chloride	KCl (> 99.8%)	CS,
Sodium sulphate	Na_2SO_4 (> 99.0%)	CS,
Magnesium sulphate	$MgSO_4$ (> 99.0%)	CS,
Potassium hydroxide	KOH (>98.0%)	SA
Sulphuric acid	H_2SO_4 (96 – 98% wt.)	CS,
Nitric acid	HNO_3 (64 – 67% wt.)	CS,
Hydrochloric acid	HCl (36.5 – 38% wt.)	CS,
Hydrogen peroxide	H_2O_2 (30.0% wt.)	CS,
Lithium bromide	LiBr (>99.0%)	CS,
Sodium bromide	NaBr (>99.0%)	CS,
Potassium bromide	KBr (>99.0%)	CS,

Magnesium bromide	$MgBr_2$ (>99.0%)	CS,
Potassium iodide	KI (>99.0%)	CS,
Iron (II) sulphate	$FeSO_4$ (>99.0%)	CS,
Alcohol	C_2H_5OH (> 98.0% wt.)	CS,
Ferrocene	$Fe(C_5H_5)_2$ (98.0%)	Fisher, UK
Hydroquinone	$C_6H_6O_2$ (99.0%)	SA
Methyl-hydroquinone	$C_6H_6O_2(CH_3)$ (99.0%)	SA
Tetrabutylammonium bromide	$C_{16}H_{36}BrN$ (99.0%)	SA
Tetraethylammonium tetrafluoroborate	$C_8H_{20}BF_4N$ (99.0%)	SA
Tetrabutylammonium hexafluorophosphate	$C_{16}H_{36}F_6NP$ (99.0%)	SA
Acetonitrile	CH_3CN (99.0% wt.)	CS,
Dichloromethane	CH_2Cl_2 (99.8% wt.)	CS,

In Table 3.2: CS: China Sinopharm Co., China. SA: Sigma Aldrich.

Table 3.3: List of equipment

Equipment	**Model**	**Vendor**
Electrochemical Workstation	PARSTAT 1000, 2000	Princeton Advanced Instruments, USA
Electrochemical Quartz Crystal Microbalance	CHI 440C	CH Instruments, China
Battery Cycler	Land CT2001A	Landt Instruments, China
Physisorption Analyser	ASAP Micrometrics 2020	Micrometrics Instruments

Thermogravimetric Analyser	TG/DTA 6300	SII Nano Technology Inc., Japan
Raman Spectrometer	inVia Reflex (with confocal microscopy)	Renishaw, UK
X-ray Photoelectron Spectroscope	AXIS Ultra DLD spectrometer	Kratos Analytical
UV-vis Spectrophotometer	Evolution 201	Thermo Scientific
Field Emission Scanning Electron Microscope	Sigma VP	Zeiss, Germany
Transmission Electron Microscope	Tecnai F20	FEI, USA
Atomic Force Microscope	Multimode AFM	Being Nano-Instruments Ltd.
Digital optical microscope	5X-500X 2MP 8-LED Zoom Digital USB Microscope	AmScope, USA
Contact Angle Measurement	OCA-20 integrated with CCD and Image Analyser	DataPhysics Instruments
Ultrasonic Cleaner	Fisherbrand Ultrasonic	Fisher Scientific, Co.
Microbalance	Sartorius microbalance	Sartorius
Roller	DG 200L Roll Press	MAX China

3.3 General Characterisation Techniques

3.3.1 Physisorption analysis

The Brunauer-Emmet-Teller (BET) is widely used as the standard for the determination of the surface area of materials with finely-divided and porous characteristics [155]. The BET theory is an extension of the Langmuir theory which describes the isothermal monolayer adsorption of gasses on a solid surface in order to account for multi-molecular adsorption. By assuming that gas molecules physically adsorb on a solid in infinite layers and that there

is no interaction between these layers, the well-known BET equation was derived as [156]:

$$\frac{p}{n^{a}.(p^{o}-p)} = \frac{1}{n_{m}^{a}.Cp^{o}} + \frac{(G-1)}{n_{m}^{a}.G}.\frac{p}{p^{o}} \quad (3.1).$$

In Eq. 3.1, n^{a} is the amount of gas adsorbed at the relative pressure p/p^{o} and n^{a}_{m} is the monolayer capacity, G has an exponential relationship with the enthalpy of adsorption) [156]. When surface analysis tests such as the BET is used, characteristic structural information of the material can be obtained from the physisorption isotherms as given in Fig. 3.3a. These characteristic isotherms are briefly described in Table 3.3.

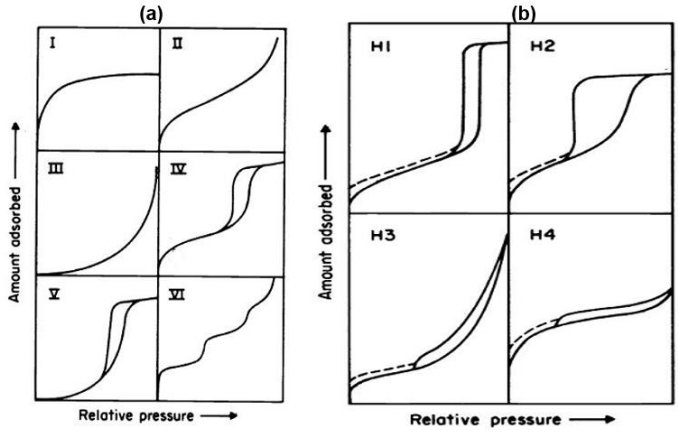

Figure 3.3: (a) characteristic physisorption isotherms (b) hysteresis loops for physisorption isotherms [157].

When analysing such physisorption isotherms, there could be the presence of hysteresis loops (see figure 3.3b) which are usually associated with capillary condensation in mesoporous structures.

In figure 3.3b, H1 is usually assumed to denote porous materials that consist of agglomerates, or compact uniform spheres in a regular array with narrow pore size. H2 loop corresponds to some porous adsorbents e.g. porous glasses. H3 loops are associated with aggregates of plate-like structures which are characterized by slit-shaped pores, and the H4 loop is usually taken to connote slit-like pores, and when it occurs in a Type I isotherm it clearly

indicates microporosity [156, 157]. It is important to note that these interpretations are not necessarily conclusive of the material structure, and hence other methods such as BJH (Barret-Joyner-Hallender), BDDT (Braunner-Deming-Deming-Teller), DFT (density functional theory) etc. are adopted to give detailed physisorption classifications of the material.

Table 3.4: Classification of physisorption isotherms [157]

Isotherm category	**Brief Description of material characteristic**
Reversible Type I	Microporous solids with relatively small external surfaces e.g.: activated carbon materials, some porous oxides
Reversible Type II	Non-porous or macroporous adsorbent
Reversible Type III	Uncommon systems in which the role of adsorbent-adsorbate is important
Reversible Type IV	Mesoporous high adsorption capacity adsorbents
Reversible Type V	Uncommon system, but weak adsorbent-adsorbate interaction, exhibited by certain porous adsorbents
Reversible Type VI	Typically exhibited by graphitized carbon black

Information obtained from the DFT structural analysis have been shown to give detailed descriptions of the porous properties of carbon materials. This is because, the various available DFT methods such as the original DFT, non-local DFT, are able to account for the complexities of the pores, particularly the effects of variable in-pore condensation of the adsorption gas.

In this research, the carbon materials were analysed with nitrogen adsorption-desorption isotherms at temperature of 77K. Furthermore, detailed pore analysis was obtained using the original density functional theory analysis of the porous carbons from the in-built software of the equipment (ASAP Micrometrics 2020).

3.3.2 Thermo-gravimetric analysis

When materials are heated in a controlled atmosphere (comprising of air, N_2, or He), the mass change (or lack thereof) as a function of temperature and/or time can be used to make inferences regarding the properties of the materials. For example, various compounds have varying degrees of volatility, as such their presence in a given material can be correlated to the change in mass with temperature. Thermo-gravimetric analysis (TGA) is used to analytically characterise the change in the properties of materials under controlled heating.

Since these materials could undergo an increase or decrease in mass due to decomposition or oxidation, the chemical and thermal stability of materials can also be inferred from thermogravimetry. Accordingly, the composition of the materials can be assessed through inferences made from the decomposition rates of the materials which displays the volatility of its constituents. In general, TGA can be used to assess the thermal properties of materials up to 1000 ^{0}C. Figure 3.4 shows the block diagram of the TGA apparatus, whilst Fig. 3.5 gives an illustration of typical results obtained from TGA [158, 159].

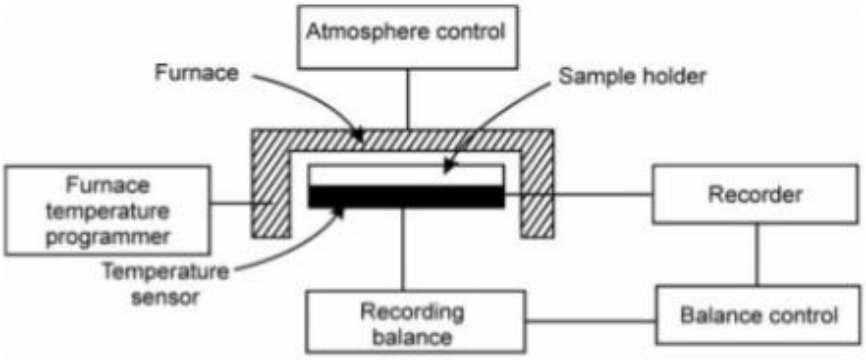

Figure 3.4: Block diagram of the TGA apparatus [158].

From Fig. 3.5, curve 1: corresponds to no mass change on increase in temperature, which indicates that the change in temperature at this range does

not involve any decomposition. Curve 2 indicates the evaporation of volatiles followed by a constant mass with increase in temperature. Curve 3 denotes a single stage decomposition between the initial and final plateau temperatures, curve 4 shows multi-stage decomposition between different plateau temperatures, whilst curve 5 is analogous to curve 4, but the inexistences of marked plateaus denotes the absence of intermediates, or too fast a temperature ramp rate. Curve 6 which denotes a mass increase corresponds surface reactions due to the atmosphere been reacting. In contrast curve 7 corresponds to a mass increase accompanied by decomposition for example oxidation of the material's surface accompanied by the decomposition of the oxidation product.

In this research, the thermal properties of the carbon electrode materials used were analysed with the TGA specifically to understand the nature of the surface groups on these carbons. Typically, the tests were carried out in N_2 atmosphere at a temperature ramp rate of 10 ^{0}C/min.

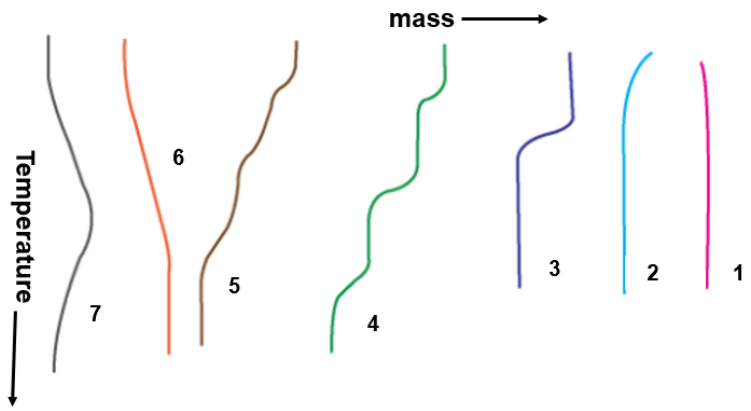

Figure 3.5: Schematic illustrations of characteristic TGA curves [159].

3.3.3 Ultraviolet-visible spectroscopy

Light absorption by solutions can be used to describe the nature and amount of its constituents. Spectrophotometry involves the use of a spectrometer to generate light within a range of wavelength that is used to

irradiate a cuvette (with well-defined optical properties) containing the liquid sample. The light then passes through the cuvette to the photometer which records the intensity. The beam of light in a UV-visible spectrophotometer comprises of ultraviolet (200~400 nm) or visible light (400~800 nm) which is scattered or absorbed by the atom or molecules of the substance present in the solution [160].

Generally, the light in the UV-vis portion of the electromagnetic (EM) spectrum promotes the electrons in the constituent molecules of the solution into different excited states. Accordingly, the chromophore which are the light absorbing species of the solutions, absorbs light at characteristic frequencies which are influenced by their structures and surrounding chemical environment. Figure 3.6 shows the excitations of the electrons within molecules or elements from the energy levels that correlate to the UV-vis portion of the EM spectrum.

This characteristic absorption peak(s) can thus be used to identify the constituents of the solutions, moreover, the intensity of the absorption at a given frequency is also indicative of the concentration of the absorbing constituents [160, 161]. In line with this, the Beer–Lambert law which gives a quantitative relationship between the intensity of the background solvent, and solvent comprising of the compounds to be tested can be used to derive a logarithmic relationship between the transmittance *T* and the absorbance:

$$-logT = \log\left(\frac{1}{T}\right) = kN_0 = absorbance \qquad (3.2).$$

Where k a constant of proportionality, and N_0 is the concentration of the species in the background solution.

In this research, UV-vis was used to study the change in concentration of dissolved redox species after adsorption by different carbon electrode materials. This information was used to understand the role of surface interactivity of the redox species with the carbon electrodes, and how this can be used to understand their resulting electrochemical properties.

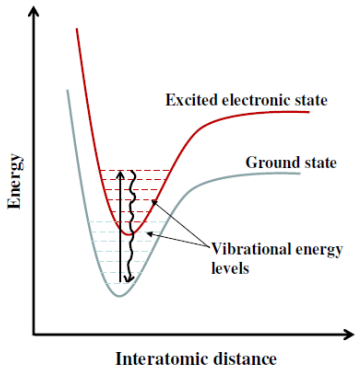

Figure 3.6: Energy states showing the transition of electrons from different energy levels due to UV-vis absorption [161].

3.3.4 X-ray photoelectron spectroscopy

The photoelectric effect describes the emission of an electron when a photon is incident on the surface of an electronically conducting material. As a quantitative technique, X-ray photoelectron spectroscopy (XPS) utilises photons from soft x-rays with energy ranging from 200 to 2000 eV to irradiate the surface of the material. Thus, by measuring the kinetic energy and number of electrons emitted from the top-layer (between 1 to 10 nm) of the material a photoelectron spectrum is plotted [162]. This photoelectron spectrum is characterised by peaks which are generated by atoms emitting electrons of a specific characteristic energy. Accordingly, the recorded energies and intensities of these peaks can be used to identify and quantify all the elements (except hydrogen) on the surface of the material.

Generally, the determination of the binding energy E_{BE} can be obtained from the expression:

$$E_{KE} = hv - (E_{BE} + \Phi) \qquad (3.3),$$

where E_{KE}, hv, and E_{BE}, and Φ are the kinetic energy of the emitted electrons, energy of the incident radiation, binding energy of the emitted electron, and work function of the material respectively.

The determination of the characteristic binding energy (E_{BE}) from a distribution of the electrons emitted can be used to ascertain the surface

composition of the material. This is because E_{BE} is dependent on: the element which emits the electron, the orbital from which the electron was ejected, and the chemical environment around the atom which emits the electron [163]. Figure 3.7 illustrates the emission of a photoelectron from the core-shell energy level to higher energy states, due to the interaction with an x-ray photon.

In practice, computational techniques are used to de-convolute the X-ray spectra through procedures such as smoothing/filtering, background and satellite subtraction, which are used for refining and resolving overlapping intensity peaks.

In this research XPS was used to ascertain the surface groups on the carbon electrodes, and the analysis of the spectrograms were carried out with the aid of the CASP software.

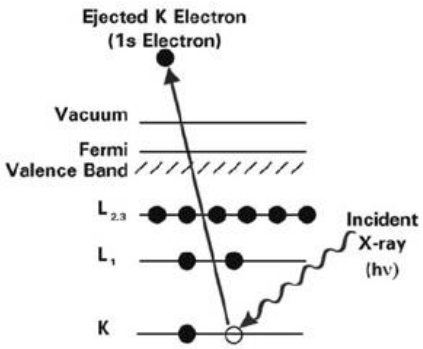

Figure 3.7: Illustration of the photoelectron emission process from the core shell of an atom [162].

3.3.5 **Raman spectroscopy**

Fundamentally, the Raman Effect refers to a situation in which photons that are scattered by a molecule or crystal have different energy (or frequency) from the incident photons which are usually scattered elastically. Accordingly, this change in the energy of the scattered photons is indicative of a change in the vibrational, rotational or electronic energy of the molecule. Generally the

elastic scattering which has the same output energy as the incident photon (i.e. hv) is known as Rayleigh scattering, whilst inelastic scattering with energy shifts of $h(v_0 - v_s)$ and $h(v_0 + v_s)$ are known as Raman-Stokes and Raman anti-Stokes shifts respectively (Fig. 3.8). Both frequency shifts from inelastic scattering are thus due to the interaction of the radiation with the molecules, however, the intensity peaks due to the Stokes scattering is markedly higher than that of anti-Stokes scattering. This is because the earlier is due to vibrational modes from molecules that are at ground state prior to irradiation. Thus the Raman spectra utilised for the characterisation of complex molecules is due to its interaction with photons which excites it to higher vibrational states [164]. Moreover, since these energies are quantized (i.e. $E_N = nhv$) where n is the mode and E_N is the given energy level, the vibrational states can be described by degrees of freedoms that are dependent on specific vibrational modes. For instance, a linear molecule with N atoms would have 3N-5 normal modes, whilst a non-linear molecule has 3N-6 normal modes. These motions which characterises the normal mode (i.e. the degrees of freedom) could be either: bending motion between three atoms with two bonds, stretching motion between two atoms that are bonded, or the transformation of a planar structure to a non-planar one due to out-of-plane deformation [164, 165].

In this vein, the Raman spectrum is a versatile tool that is used to elucidate the molecular structure of a given material because the vibrational spectrum of different molecules are characteristic properties dependent on the chemical composition and electronic structure.

In this research, Raman analysis was used to investigate the change in structural properties of carbon electrodes when they interact with dissolved redox species.

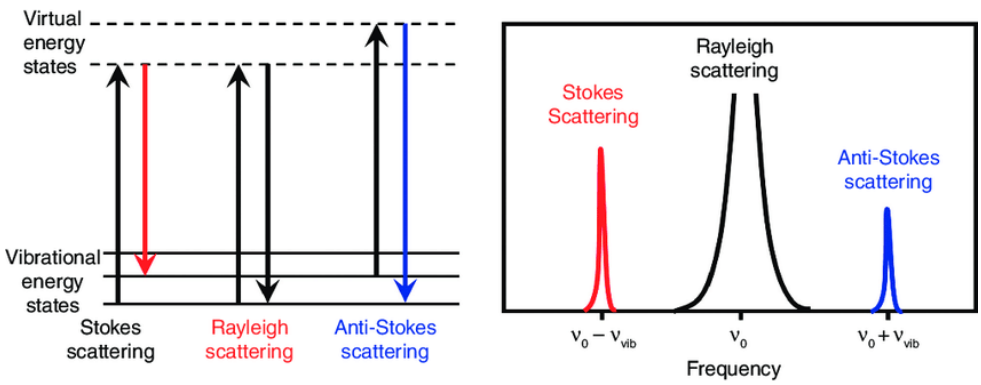

Figure 3.8: Different scattering modes of incident radiation due to the interaction of the photons with the molecules [166].

3.3.6 Scanning electron microscopy

By focusing a beam of high-energy electrons on the surface of a solid specimen, the scanning electron microscope (SEM) induces electronic signals at the surface of the material. Accordingly, the resulting signal from the interaction of the specimen and the electron beam reveals characteristic information such as the texture, crystalline structure, chemical composition and the orientation of the constituent components of the sample [167]. The scanning mode of conventional scanning electron microscopy is capable of providing magnification from 20X to about 30,000X, with a spatial resolution of 50 to 100 nm [168]. The high kinetic energy of the accelerated electrons in an SEM dissipates into different types of signals when it interacts with the sample, these signals include: secondary electrons, backscattered electrons, diffracted backscattered electrons, x-rays etc. The SEM use secondary electrons for revealing the morphology and topology on the samples.

In this research, SEM is utilized to study the surface morphology of the carbon materials utilised, thus all SEM images presented are due to secondary electrons.

3.3.7 Transmission electron microscopy

Transmission electron microscopy (TEM) involves focusing a beam of electrons generated either through thermionic emission or field effect on an ultrathin specimen. The interaction between the beam and the specimen creates an image of the specimen which is then magnified and focused on an imaging device such as charged coupled device cameras. The resolution of images obtained from TEM is extremely high owing to the short de-Broglie wavelengths of electrons, as such detailed structural aspects of specimens can be studied using this technique [169].

TEM is used in this thesis for further study of the surface characteristics of the nanoparticles of the activated carbon and graphene nanoplatelets.

3.4 Electrochemical characterisation techniques

The main focus of this research was to understand the electrochemical properties of the materials and devices. The main equipment utilised for electroanalysis were the Princeton Multichannel and CHI 440C (EQCM) electrochemical workstations. The inbuilt software i.e. the PARSTAT (Versa Studio) and CHI analysis software in the earlier and latter equipment are used to quantitatively assess the results from the experiments. Moreover, graphing software (e.g. Origin) or simple programs with MATLAB were also used to quantitatively analyse the results from the raw output data. The following are the electrochemical techniques used in this research.

3.4.1 Cyclic voltammetry (potential dynamic polarography)

Cyclic voltammetry is a useful electroanalytical technique that can be used to study the redox properties of complex chemical reactions which occurs in chemicals or interfacial structures [170]. Due to its rapid analytical capabilities for instance fast location of redox potentials of electroactive species, it has

become the most widely adopted electroanalytical technique for acquiring qualitative information about electrochemical reactions [171].

The cell configuration to describe the conventional cyclic voltammetry experiment comprises of three electrodes, namely:

(i) The working electrode (WE) which is inert and it is the electrode whose current response is measured. This electrode can also be modified by other active materials whose electrochemical properties are of interests. Generally, the dissolved species and/or the electrode active material are usually of interest in electroanalysis.

(ii) The counter electrode (CE) is also an inert electrode and its area must be larger than that of the WE in order for its change in potential to be as low as possible. This would ensure that all the potential variation is occurring at the WE which is of interest.

(iii) The reference electrode (RE) is used to precisely control the potential between the WE and CE, and it is an ideally polarisable electrode with very high (in principle infinite) impedance.

In a conventional cyclic voltammetry experiment, the input waveform is usually triangular and the slope of this waveform is the scan rate i.e. the rate of change of the potential with time. Thus, assuming O (oxidised species) was initially present in solution, and also that there is no kinetic control at the interface. On the application of the square waveform potential gradient, the diffusion of O to the electrode surface and its reduction to R (reduced species) would result in the feature given in Fig. 3.5a. This feature of the cyclic voltammogram thus represents the change in the concentration of the species as they diffuse to or from the electrode in the course of oxidation/reduction.

As seen from Fig. 3.5b, some important parameters are the: anodic peak, cathodic peak, anodic and cathodic peak potentials, which all describe important information of the redox reaction occurring at the WE.

In general, a reversible electrode process is usually defined for electrodes with rapid kinetics, such that a Nernstian relation can be used to express the relationship between the current and potential:

$$E = E_0 + \frac{RT}{nF} ln \frac{[O]_{(0,t)}}{[R]_{(0,t)}} \quad (3.4)$$

Accordingly, a reversible process in which all the resulting species are stable is said to have occurred when $i_{p,c}/i_{p,a}$ is unity.

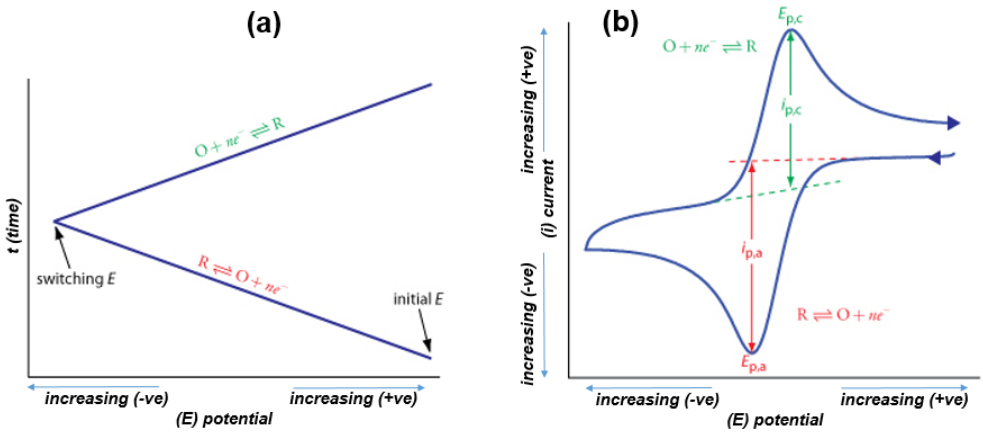

Figure 3.9: Schematic illustration of results from a cyclic voltammetry experiment (a) Input waveform (b) Resulting i-V cyclic voltammogram

From fundamental considerations, the formal reduction potential (E^0) for a reversible couple may be determined from:

$$E^0 = \frac{E_{pa}+E_{pc}}{2} \quad (3.5).$$

It is also important to note that current profile obtained from the cyclic voltammogram fundamentally describes the concentration profile within the EDL as described by the features shown in Fig. 3.10. In line with this, for a diffusion controlled process, the variation of the peak current with scan rate may be expressed with the Randles-Sevick equation which is useful in visualising the profile of the electrode kinetics:

$$i_p = (2.69 \times 10^5) n^{3/2} A D^{1/2} N_0 v^{1/2} \quad (3.6).$$

Where in Eq. 3.6, i_p is the peak current (A), n the stoichiometric number of the electrons, A the area of the working electrode (cm^2), D the diffusion coefficient (cm^2/s), N_0 the concentration (mol/cm^3), and v is the scan rate (V/s).

In general for a capacitive process at the EDL in which C (the EDL capacitance) is constant (or does not change significantly), C can be expressed as:

$$C = \frac{\Delta q}{\Delta E} = \frac{dq/dt}{dE/dt} = \frac{i}{v} \quad (3.7).$$

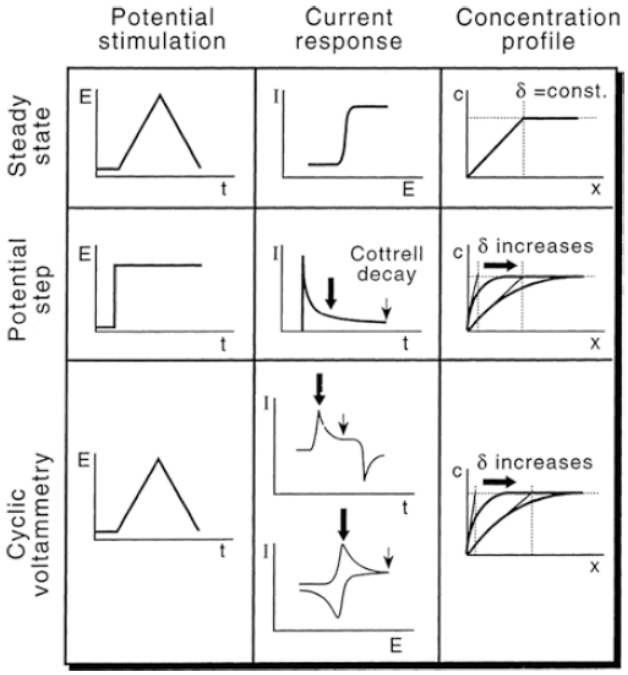

Figure 3.10: Potential stimulation, current response and corresponding concentration profile showing the thickness/variation of the diffusion layer (δ) with change in concentration gradient [172].

In this research, cyclic voltammetry was used for the fundamental analysis of the E|E interface. Also, cyclic voltammetry was used in the characterisation of the features of the devices that were investigated. Accordingly, equations used for calculation of the charge efficiency (η_Q) or (Q_e), and capacitance (C) for a rectangular cyclic voltammogram (see Fig. 3.11 a and b) are:

$$\eta_Q = \frac{Q_d}{Q_c} \times 100\% \quad (3.8),$$

and

$$C = \frac{Q_+ + Q_-}{2\Delta E} \quad (3.9),$$

respectively.

Herein: Q_d and Q_c are the passing charges when recording the Galvanostatic discharging and charging plot (GCD) (see section 3.4.2), Q_+ and Q_- are those during the positive and negative potential scans for recording a cyclic voltammogram (CV), respectively, and ΔE is the maximum potential range for recording a rectangular CV, i.e. the capacitive potential range (CPR). It is worth noting that, in principle, $Q_d = Q_-$ and $Q_c = Q_+$ for the positrode, but $Q_d = Q_+$ and $Q_c = Q_-$ for the negatrode (see Fig. 3.11a).

It is important to note that both Eqs. (3.8 and 3.9) can also be applied for similar calculations of a two-electrode cell (supercapacitor or supercapattery) by replacing ΔE in Eq. (3.9) with the maximum charging voltage (MCV) of the cell, U_{max} or (U_L). Also, for a cell, there is always $Q_d = Q_-$ and $Q_c = Q_+$ because charging or discharging a cell always, respectively, increases or decreases the cell voltage, U (this is shown in Fig. 3.13 b and c).

Furthermore, it should be emphasized that although the Q/U ratio (expressed in F) can be derived for the non-capacitive cell (supercapattery) in Fig. 3.11c, in this research, this was only done for the sake of discussions, for example when the scan rates are varied. Accordingly, the value of $C/(m_+ + m_-)$ (expressed in F/g with respect to the mass of the active materials on the two electrodes in the cells) calculated from Eq. 3.9 are denoted as C_{cell} and C_Q for cells with features similar to the representations in Figs. 3.11b and 3.1c respectively. This is to strictly emphasise that the F/g value calculated for the cell in Fig. 3.11c was obtained from a non-capacitive cell. The significance of this strict distinctions in characterising these features particularly for research

into energy storage in general was discussed at length in Ch.2 (Literature Review).

More importantly, throughout this research, the energy of the device is always calculated from the galvanostatic charge-discharge plots obtained from cells, as will be explained in Section 3.4.2.

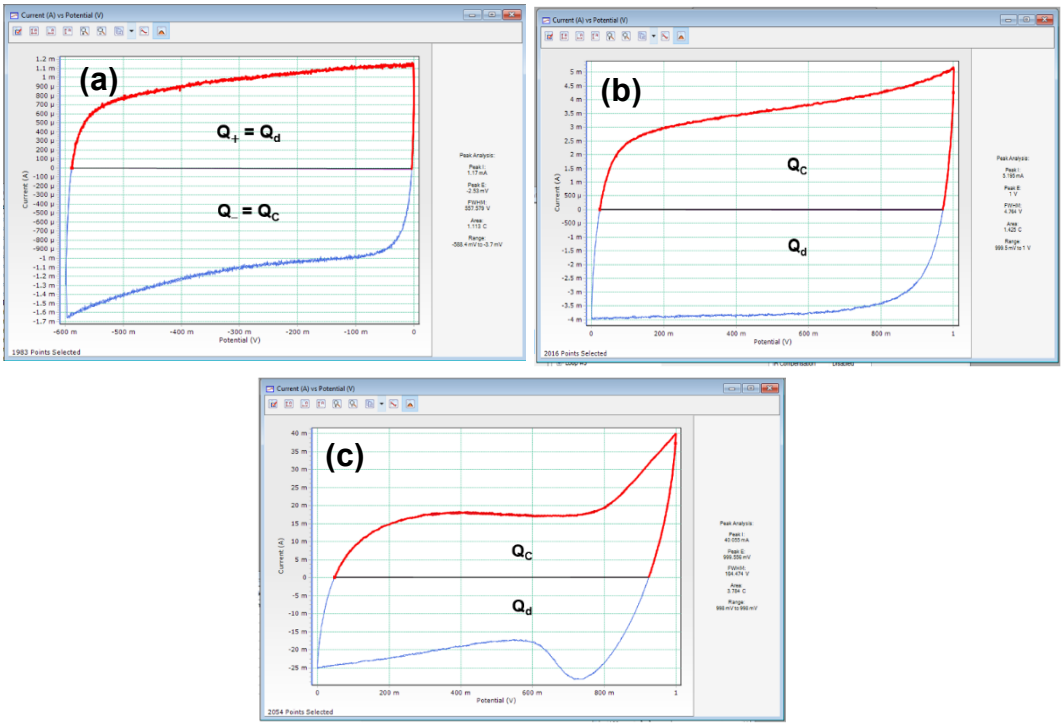

Figure 3.11: Examples of some cyclic voltammograms obtained from this research showing: electrode (negatrode) (a), cell (b), with capacitive- and, cell with non-capacitive- (c) features.

3.4.2 Chronopotentiometry (galvanostatic charge-discharge)

Chronopotentiometry records the potential response as a function of time, with a current stimulation as the input. Some controlled current excitations that can be applied are shown in Fig. 3.12 [41].

Fundamentally, for a diffusion-controlled redox reaction, the current-time (i-t) curve is described by the Cottrell equation below:

$$i = nFAN_0D^{1/2}\pi^{-1/2}t^{-1/2} \quad (3.10).$$

Where n is the number of electrons, F (faraday's constant), A is the area, N_0 the concentration of analyte (bulk concentration) and t is time. In general, the diffusion coefficient D with units of (cm^2/s) may be ascertained from the chronopotentiomery experiment through the use of Eq. (3.10).

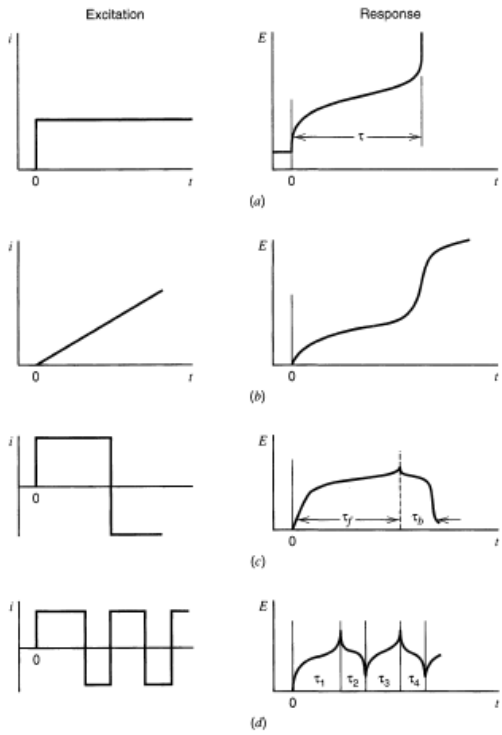

Figure 3.12: Excitation (i vs. t) and the corresponding response (V or E vs. t).

In this research, chronopotentiomery was used in ascertaining the energy, and power of the devices fabricated. Also, the signal excitation used throughout this research corresponds to that shown in Fig. 3.12a. Furthermore, for self-discharge tests (i.e. voltage recorded as a function of time at open circuit conditions), chronopotentiometry at a low applied current is used to raise the cell voltage of the device to the U_L (upper limit of cell voltage), prior to the open-circuit cell voltage measurements.

Also, repeating the charge-discharge cycles from the chronopotentiometry experiment (≥ 5000 cycles) was used in ascertaining the stability of assembled devices (this was mainly done with the aid of a high current battery cycler).

In line with the discussions presented in Section 3.4.1, the following equations are only applicable to GCDs recorded from a cell. The specific energy (W_{sp}) (or W_d as obtained from Fig. 3.13) can be obtained as:

$$W_{sp} = \int_{U_{min}}^{U_{max}} IdU = I\int_{t=0}^{t=t} U_d(t)dt \qquad (3.11),$$

and the energy efficiency (η_W) or (W_e) could thus be expressed as in Eq. 3.12 below:

$$\eta_W = \frac{\int U_d(t)dt}{\int U_c(t)dt} \times 100\% \qquad (3.12).$$

Where $U_d(t)$ and $U_c(t)$ are the cell voltage as a function of the time, t, of discharging and charging, respectively, in the GCD measurement of the cell, and I is the mass normalised current (or specific current or current load) against the total mass of active materials on both the positrode and negatrode (i.e. $m_+ + m_-$) in the cell with the unit in A/g (or mA/g).

Also, with I expressed in (A/g), $U_d(t)$ in (V) and dt in (s), $W_{sp}/3.6$ gives the energy in the units of (Wh/kg). Accordingly the specific power P_{sp} can then be obtained from: $(W_{sp}/3.6) \times (\Delta t_d)^{-1}$ in the units of (W/kg). Herein Δt_d is the duration for the discharging of the cell (see Fig. 3.13).

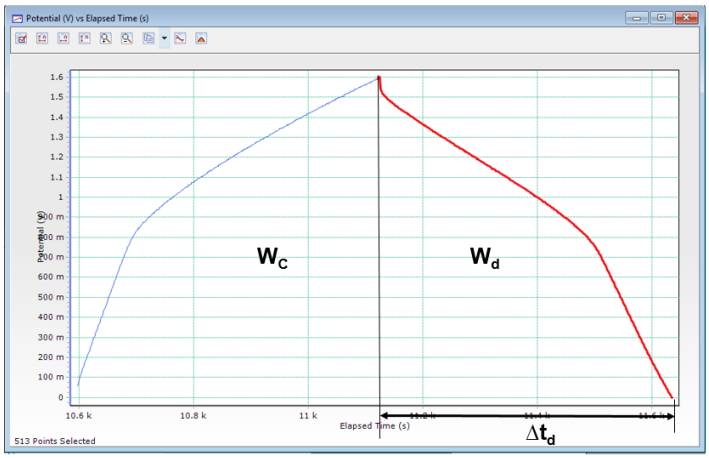

Figure 3.13: Characteristic GCD plot for a supercapattery (obtained from this research) showing W_c and W_d as the area of the charging and discharging portions respectively.

3.4.3 **Electrochemical impedance spectroscopy**

Electrochemical impedance spectroscopy (EIS) is a well-established and powerful tool for investigating the mechanisms of electrochemical reactions, measuring the dielectric and transport properties of materials, investigating passive surfaces and for exploring the properties of porous electrodes [173]. EIS involves the measurement of the current response of an electrochemical system when an alternating current (ac) potential is applied to it, and in order to attain a pseudo-linear system (i.e. a well behaved system that would suit the theory of linear systems on which the theoretical background of EIS is based) the applied ac potential is usually small [174]. The response of the system to a sinusoidal potential *E* is a sinusoidal current I at the same frequency, but with a phase shift (ϕ) [175] (see Fig. 3.14a); the resulting impedance *Z* is thus a complex number which can be expressed as given in Eq. 3.11 and visualized as shown in Fig. 3.14b:

$$Z = \frac{E}{I} = Z_o \exp(j\Phi) = |Z|(cos\Phi + jsin\Phi) \qquad (3.11).$$

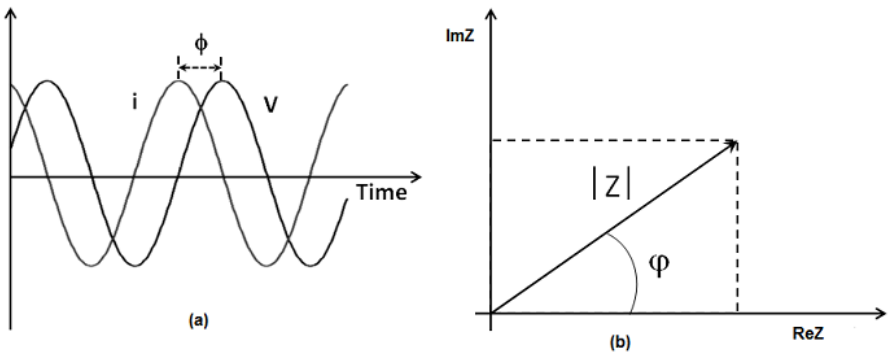

Figure 3.14: Simple mathematical description of sinusoidal signal (a) and the corresponding phasor diagram representing the impedance measured (b).

A frequently used concept of EIS measurements for electrochemical systems is based on the principle that slow electrode kinetics, chemical reaction mechanisms, and chemical species diffusion can all impede the flow of charges, and as such it is possible to assume that these mechanisms are

analogous to conventional circuit elements such as resistors, capacitors and inductors that impede the flow of electrons in an ac circuit. Hence, analysing the mechanism of the electrochemical double-layer (EDL) can be done by defining corresponding circuit analogues (capacitors, resistors etc.) to represent different interfacial components of the EDL (see Fig. 3.15).

From such a circuit analogue (as shown in Fig. 3.15), EIS measurements can thus be used to ascertain important properties such as the impedance and capacitance of an electrochemical system. Data obtained from carrying EIS measurements can be presented in different forms, some of which includes the Nyquist plot, Bode plot, and equivalent circuit models.

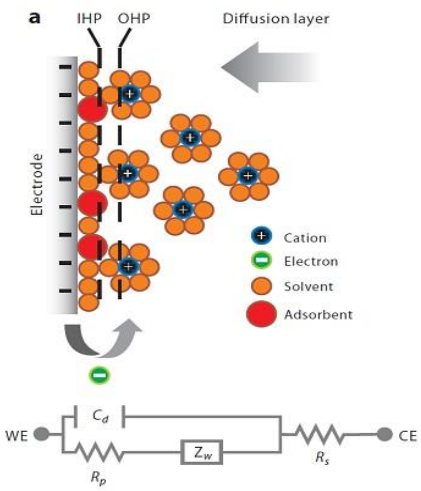

Figure 3.15: Equivalent electrical circuit model for the interfacial components of the EDL [176].

The Nyquist plot (see Fig. 3.16a) represents the impedance as a vector of length |Z| (that is a plot of the imaginary impedance versus the real impedance), and the angle between this vector and the horizontal-axis is the phase angle. For EIS data used in describing EDLs represented by the simple Randles circuit (see Fig. 3.16b). The Nyquist plot makes it easy to ascertain important electrochemical processes occurring in the interface for example; reaction kinetics and mass transfer. The Nyquist plot also facilitates the

calculation of ohmic and faradaic resistances, double-layer capacitance (if the frequency is known) and other important elements of the EDL interface. However, one obvious shortcoming of the Nyquist plot is that it does not explicitly show the frequency that corresponds to the various impedance points which it presents [176]. This limitation can be mitigated by visualizing EIS data in the Bode plot.

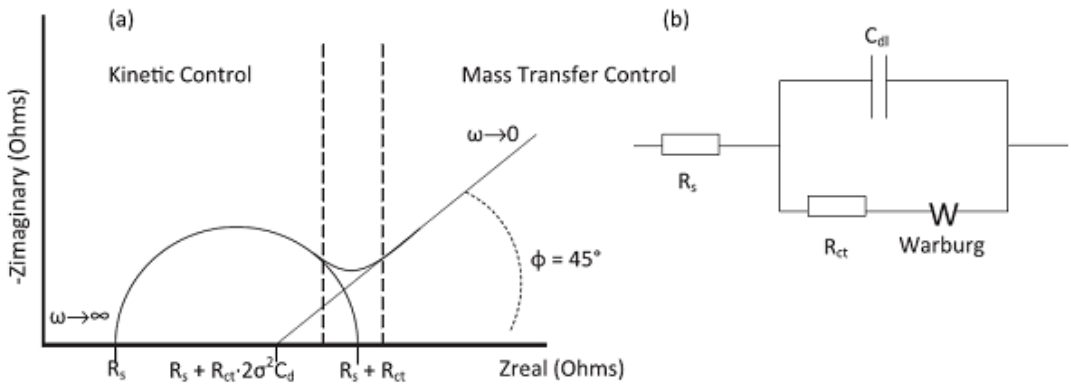

Figure 3.16: Schematic of the Nyquist plot (a) and modified Randles electrical equivalent circuit (b)

The Bode plot explicitly show frequency information, it comprises of the absolute value of both the impedance and phase-shift plotted on the vertical axis, against the frequency on the horizontal axis. Since it is essentially a log-log plot, it gives wide values of impedances at wide frequency values, also values of ohmic and faradaic resistances can be ascertained directly from the plot. The Bode plot (see Fig. 3.17) is also very important for systems with more than one time constant making it very useful for systems with different rate determining steps [173]. However, one major drawback of the Bode plot is that the ohmic resistance influences the characteristic of the phase angle plot, this could affect the accuracy of the parameters (for example capacitance) calculated from it [174].

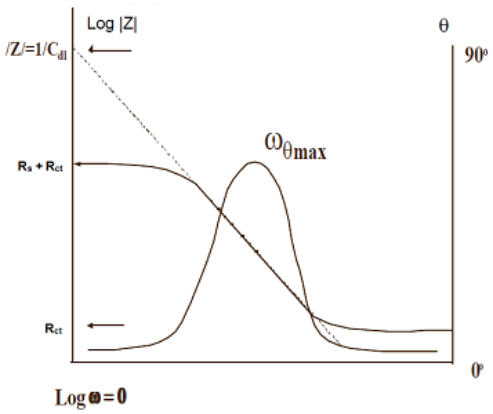

Figure 3.17: Schematic of the Bode plot.

This thesis utilizes EIS measurements conducted in the frequency range 0.01 Hz to 100 × 10^3 Hz, at amplitude of 0.01 V around the U_L (cell voltage) or E_L (electrode potential) of interest. EIS characterization undertaken in this thesis was done to:

1. Understand the mechanism of charge storage of the electrode | redox-electrolyte interface, or of supercapacitors using redox electrolytes
2. Rigorously study the ion dynamics and correlation between electrode porosities and the DRS.

The impedance matching software ZView accompanying the PARSTAT software of the electrochemical workstation was also used in ascertaining some of the parameters that were directly obtained from the read-out, simple circuits e.g. Fig. 3.16b (or other related variations) were thus used in simulating some aspects of the impedance calculations.

3.4.4 Electrochemical quartz-crystal microbalance

The electrochemical quartz crystal microbalance (EQCM) is an ultrasensitive technique used to carry out mass measurements corresponding to changes obtained from electroanalysis. In practice, typical EQCM can ascertain mass changes in the range 0.1-1 ng/cm^2. A schematic illustration of the experimental set-up for the EQCM is given in Fig. 3.18a. Fundamentally,

when a high frequency AC electric field is applied across the thickness of the crystal, the QCM oscillates in a mechanically resonant shear as shown by the edge view of a QCM crystal undergoing oscillatory shear distortion (Fig. 3.18b).

In practice, the main sections of the top and bottom of the quartz-crystal are coated with a typically disk-shaped thin metal film such as gold. This gold-surface then acts as the substrate on which the material is coated on. Fundamentally, the mass sensitivity of the QCM originates from the relationship between the oscillation frequency on the total mass of the metal-coated crystal, or any ad-layers of deposited materials, and this change in mass with frequency is in turn given by the Sauerbrey equation:

$$\Delta f = -2f_0^2 \, \Delta m / (A \sqrt{\mu\rho}) \qquad (3.12).$$

Where: f_0 is the resonant frequency of crystal's fundamental mode (Hz), A, area of the gold disk coated onto the crystal (cm^2), ρ = quartz crystal's density (= 2.684 g/cm^3) μ = shear modulus of quartz (= 2.947×10^{11} $g/cm.s^2$). Generally, for the crystal employed for the CHI 440C EQCM workstation, the fundamental frequency is: 7.995-MHz. In line with this, a net change of 1 Hz corresponds to 1.34 ng of mass adsorbed or desorbed on the crystal surface which has an area of area of 0.196 cm^2.

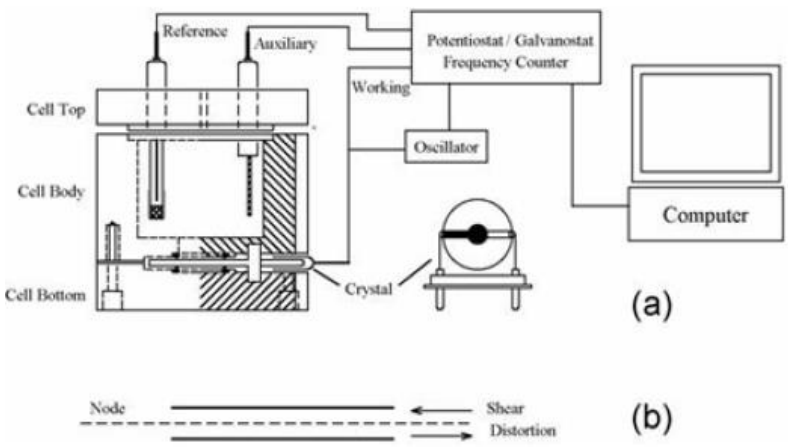

Figure 3.18: (a) schematic representation of the EQCM experimental set-up (b) shear modulation of the quartz crystal under an applied AC frequency electric field [177].

In this research, EQCM was used for confirming the mass change of dissolved redox species on oxidation/reduction at the carbon electrode. This was done mostly to confirm and to understand some fundamental electrode processes (as a general routine for DRS selection). However, an example of this was also presented in the current dissertation.

It should be pointed out that other materials characterisation tools as itemised in Table 3.3, for example scanning probe microscope, digital optical microscope, contact angle measurement device, conductivity meter, pH meter, were also employed for other fundamental and/or routine tests in the course of this research.

3.5 Material preparation

In this research the two main materials of interest are the electrodes and electrolytes. The following procedures were followed to prepare these materials.

3.5.1 Electrode and electrolyte preparation

In a typical procedure for the electrode preparation, the electrode material powder of mass ca. 4.50 g and carbon black (conductive-additive) ca. 0.25 mg were weighed. A dispersion (60% wt in water) of PTFE (i.e. Poly(tetrafluoroethylene)) of mass ca. 0.42 g (corresponding to ca. 0.25 g of PTFE) was weighed and poured into about 50 mL of ethanol. The electrode material powder was then poured into the mixture of ethanol and binder, giving the mass ratio of electrode material : conductive-additive : binder as 90:5:5.

This slurry was then stirred at 70 ^{0}C to evaporate ethanol, producing a paste that was roll-pressed into a blanket which was dried at 120 ^{0}C for 12 hours. The dried blanket was then cut or punched and weighed in the microbalance (with accuracy of ± 0.01 mg). The electrode material was then die pressed under a force of 2 tonnes (aided by little drops of ethanol to

enhance lubrication) into cylindrical pellets (diameter: 6.0 or 13.0 mm). The pressed pellets were further dried at 80 ^{o}C in air for at least 10 hours.

Figure 3.19 a to c, shows an outline of the electrode material preparation procedure, i.e.: calendaring of electrode slurry (Fig. 13.19a); roll pressing of the electrode (Fig. 13.19b); and punching or cutting electrode before been die pressed (Fig. 13.19c). Figure 13.19d shows the different diameters of electrode materials that were prepared in this research. As would be described in Section 3.6, various cell configurations make use of electrodes with appropriate mass and geometry. Generally, electrode pellets used in this research had an areal mass loading of at least 11.30 mg/cm^2 and a thickness ranging from 240 to 280 μm, depending on the mass. It is important to point out that these electrode thickness adopted in the design of devices aim to simulate as much as possible commercial electrode materials, in order that the results obtained from this research could be used as reliable benchmarks for further development purposes [178]. This is because, as has been described already [179], majority of the electrodes used for research purposes do not adequately reflect industrial scale electrodes for high energy applications. Moreover, it is well-known, that high energy supercapacitor electrodes are meant to be of the order 200 micron to hundreds of microns thick, whilst the conventional high power but low energy electrodes such as those ones adopted for filters and RC microelectronic-circuits may be thinner [178, 180, 181]. In our opinion, supercapatteries with DRS are envisaged for high energy applications which requires the high power properties of supercapacitors.

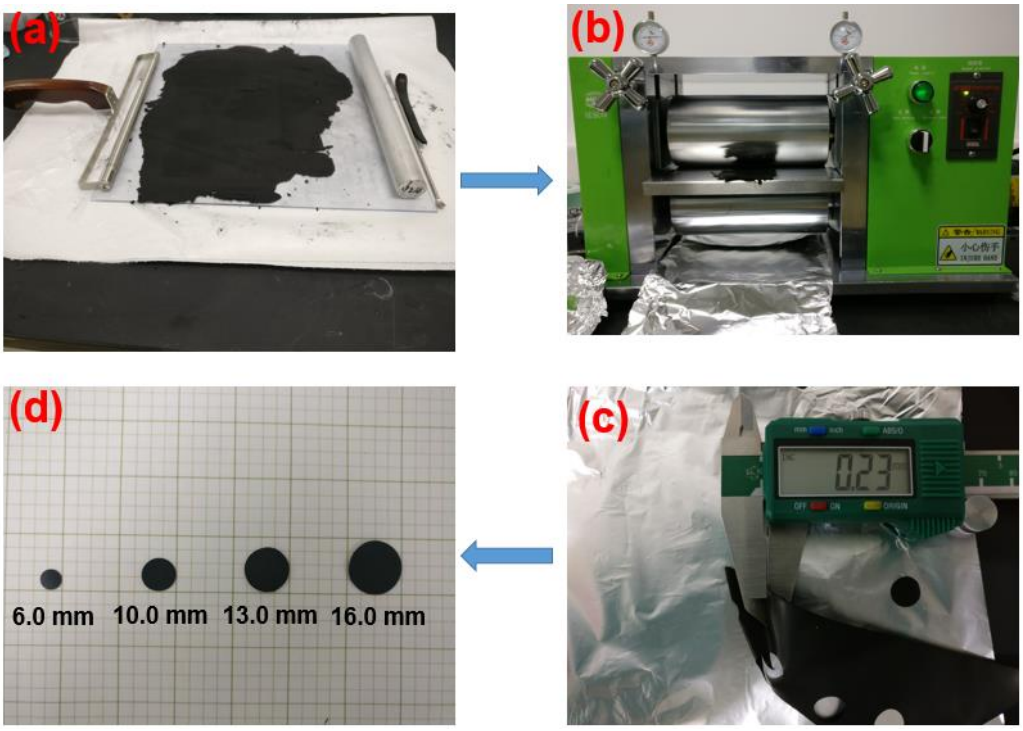

Figure 3.19: Electrode preparation procedure: (a) electrode calendaring (b) electrode rolling (c) electrode punching prior to pressing (d) pressed or punched pellets of specific geometries and mass.

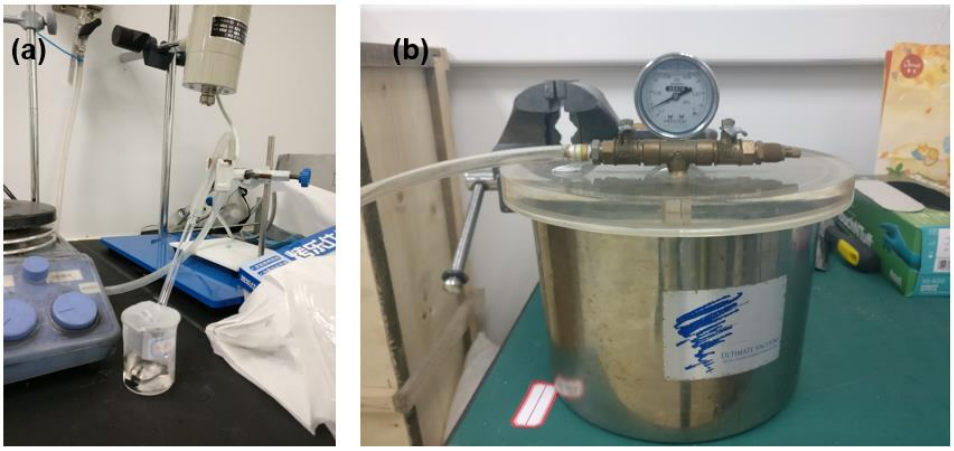

Figure 3.20: Degassing of electrolytes (a) vacuum soaking of electrodes inside the electrolytes (b).

3.6 Fabrication of cells for electrochemical tests

In this research, cells in the three-electrode or two-electrode configurations were fabricated, the earlier was used to ascertain the electrochemical properties of the electrode | electrolyte (E|E) interface, whilst the latter was used to assess the characteristics of prototype devices.

Two kinds of 3-electrode cell configurations were used in this research. The first kind is a flooded cell (with total electrolyte volume of ca. 5.0 mL), platinum micro-cavity (Pt-MC) loaded with electrode material powder as the working electrode (WE), and a large area Pt-foil was used as the counter electrode (CE). The reference electrode was either a standard calomel electrode (SCE) or Ag wire coated with AgCl (Ag/AgCl). The full details of the fabrication and use of the Pt-MC electrode in this research was fully described in Ch. 8. The other type of 3-electrode cell configuration (which was adopted in the majority of this research) is a T-type Swagelok cell with either Ti or graphite rods as current collectors. The T-type Swagelok cell is illustrated and shown in Figs 3.21. Note that in this configuration, the counter electrode chosen has a larger diameter (16.00 mm) and mass (ca. 30.00 mg) than the working electrode which has a diameter and mass of 6.00 mm and ca. 5.00 mg respectively.

The 2-electrode cell (prototype device) design used in this research is a fixed-volume Swagelok cell. Moreover, there are two categories of devices that were investigated in this research. These are: conventional devices with the configuration: (−) negatrode | electrolyte | positrode (+) or bi-electrolyte cells with the configuration: (−) negatrode | negalyte || posilyte | positrode (+).

For the fabrication of the Swagelok cells, a PTFE based T-shaped Swagelok cell with a reference electrode (SCE or silver and silver chloride electrode, Ag/AgCl) and titanium or graphite current collectors was used both

for electrode characterisation in the 3-electrode cell (as described in Section 3.5.1), and also for monitoring the potential of the electrodes in the 2-electrode cell. The only difference between the 3-electrode cell and 2-electrode cell with reference electrode, is that the areas of electrode are similar for the 2-electrode cells (with equal or different mass of electrodes). Whereas the 3-electrode Swagelok cell follows the configuration of the WE, and CE explained in Section 3.5.1. The schematic illustrations of these cells are given in Fig 3.21 c and d.

In all the cells fabricated, the electrolyte volume was controlled so that the contribution from the DRS in the electrolyte to the electrode and cell performance metrics could be quantitatively evaluated.

This control of electrolyte volume was done by weighing the mass of the soaked electrodes and separator to ascertain the volumes absorbed, and then a digital micropipette was used to add a specific volume of electrolyte to obtain equal volumes of electrolytes in the cells. The approximate volume of electrolyte in the Swagelok cell is ca. 1.10 mL.

Table 3.5 gives the apparent density of solutions of some electrolytes used in this research. This information was used to ascertain the volumes corresponding to the mass absorbed by the electrodes and separator. It should be noted that this attempt at having similar volumes of electrolytes in the cells is because, when the species are dissolved in solution the charge is given by $Q = nFN_0V$. n: number of electrons, *F:* Faraday's constant, N_0 concentration, V is the volume of the electrolyte.

Table 3.5: Measured apparent densities (ρ_{app}) of some electrolytes used in this research

Redox Electrolyte	1.0 mol/L ρ_{app} g/mL	2.0 mol/L ρ_{app} g/mL	4.0 mol/L ρ_{app} g/mL
LiBr	1.03	1.08	1.22
NaBr	1.05	1.07	1.22
KBr	1.02	1.06	1.15

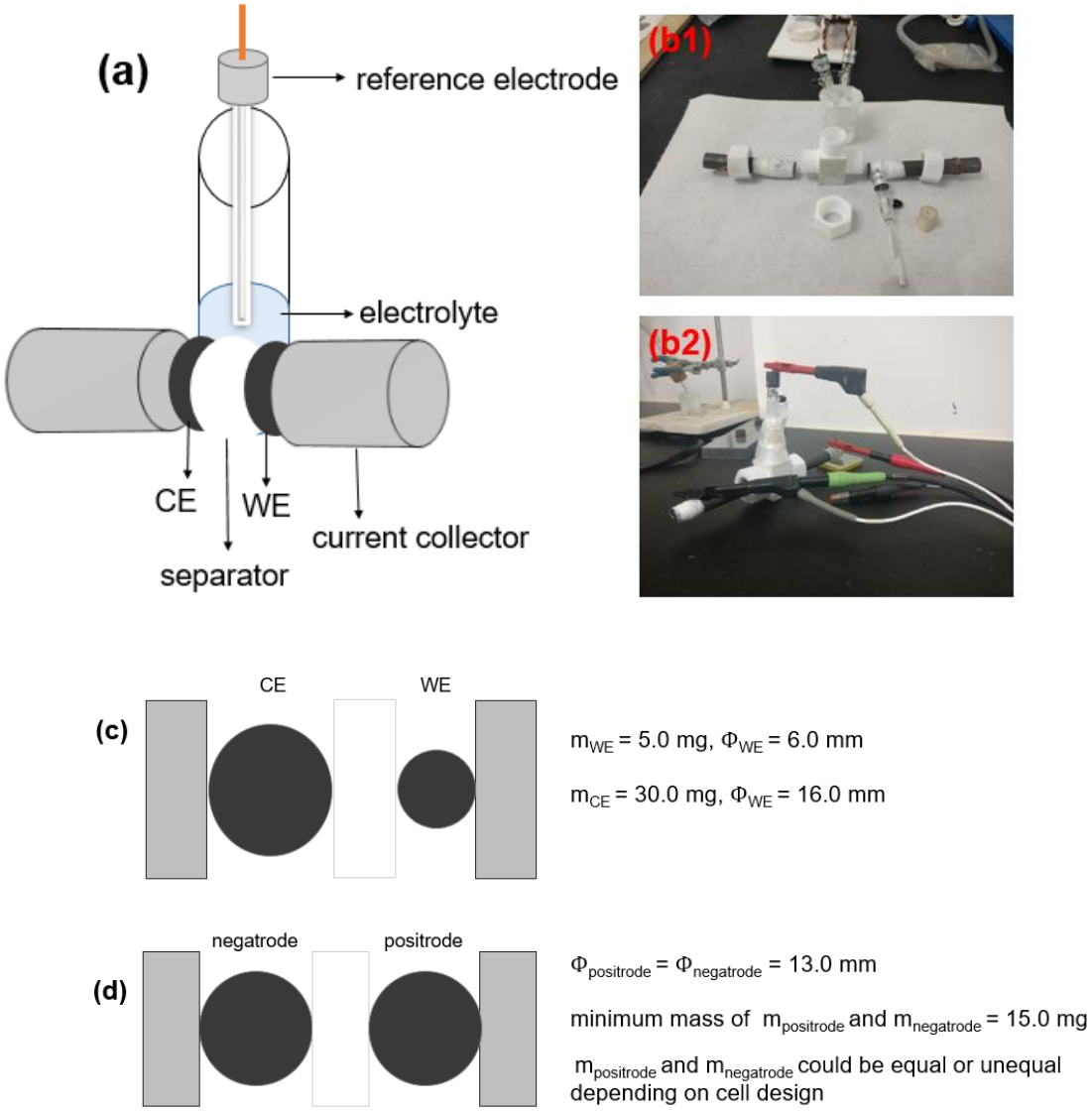

Figure 3.21: Configurations of electrochemical cells. (a) Schematic illustration of the T-type Swagelok cell (b) actual image of an example of the T-type Swagelok cell arrangement. Schematic of electrode geometry for (c) 3-electrode cell configuration (d) 2-electrode cell (prototype device) configuration.

Generally, the 2-electrode cell configuration for both conventional and bi-electrolyte cells were prepared in a similar manner. The separator membrane used was one layer of glassy paper (GF/D, Whatman) in the conventional cell, but two layers for making the bi-electrolyte cell. The

membranes were soaked in the electrolyte before use. However, in the bi-electrolyte cell, the electrodes and the separators were soaked in different electrolytes, i.e.: positrode and negatrode soaked in the posilyte and negalyte respectively, whilst the separators denoted by (||**)** was soaked in a solution known as the membrane electrolyte (ME). The two-electrode cell (without electrode potential monitoring) i.e. the prototype device reported in this dissertation is shown in Fig. 3.22.

For the fabrication of the bi-electrolyte cell, after soaking the membranes and the electrodes in the electrolytes, the excess electrolyte in the membranes were gently squeezed out and wiped away, and the two membranes were placed between the positrode and negatrode. The entire cell was assembled without any excess electrolyte following procedures already described in [111].

For monitoring the potential of each electrode in the bi-electrolyte cell, the Ag/AgCl reference electrode (a Ag wire coated with AgCl) was placed in-between the two layers of glassy paper. For consistence of discussion throughout this thesis, the potential of the Ag/AgCl reference was calibrated against a commercial SCE (at ca. 0.06V). In this dissertation, except stated otherwise, all potential data would be reported with reference to the SCE. Also, all electrolytes were bubbled by Ar (99.8%) for at least 20 minutes before use for soaking the electrodes or membranes under vacuum for an hour, followed by further Ar bubbling for another 10 min (see Fig. 3.20).

Figure 3.22b shows the CVs of a cell fabricated with just the absorbed electrolyte (black dashed curve) and the electrolyte volume topped up to the specific volume used in the cells (red curve). As was observed from Fig. 3.22b, the difference in the features are not marked, although as expected the cell with topped up fixed electrolyte volume displays a slightly reduced polarisation resistance as might be observed from the low voltage (around ca. 0 to 0.1 V) current peaks. Accordingly, in addition to allowing the quantitative

comparisons of the cells to be accurate, the fixed electrolyte volume also reduces experimental artefacts that might be introduced in the characterisations of the cells. Note that although the bi-electrolyte cell as described earlier do not possess excess electrolyte, nevertheless, the ionic conductivity between membranes and absorbed electrolyte allows these cells to display satisfactory performance.

Furthermore, from fundamental considerations, it should be pointed out that the electrochemical properties of the electrodes or devices as revealed through electroanalysis are due to the interaction within the porous matrix of the carbon materials. In this regard, the bulk electrolyte solution (in this case referring to excess electrolytes not absorbed by the electrodes) been carefully modulated for similar experiments generally helps to reduce experimental artefacts. This was the main reason why careful attention was paid to the geometry of the electrodes and the electrolyte volumes used for all the tests undertaken in this research.

When necessary, other specific details of the cells and/or experimental designs would be described in the relevant result chapters, and reference would also be made to the general descriptions given in this chapter.

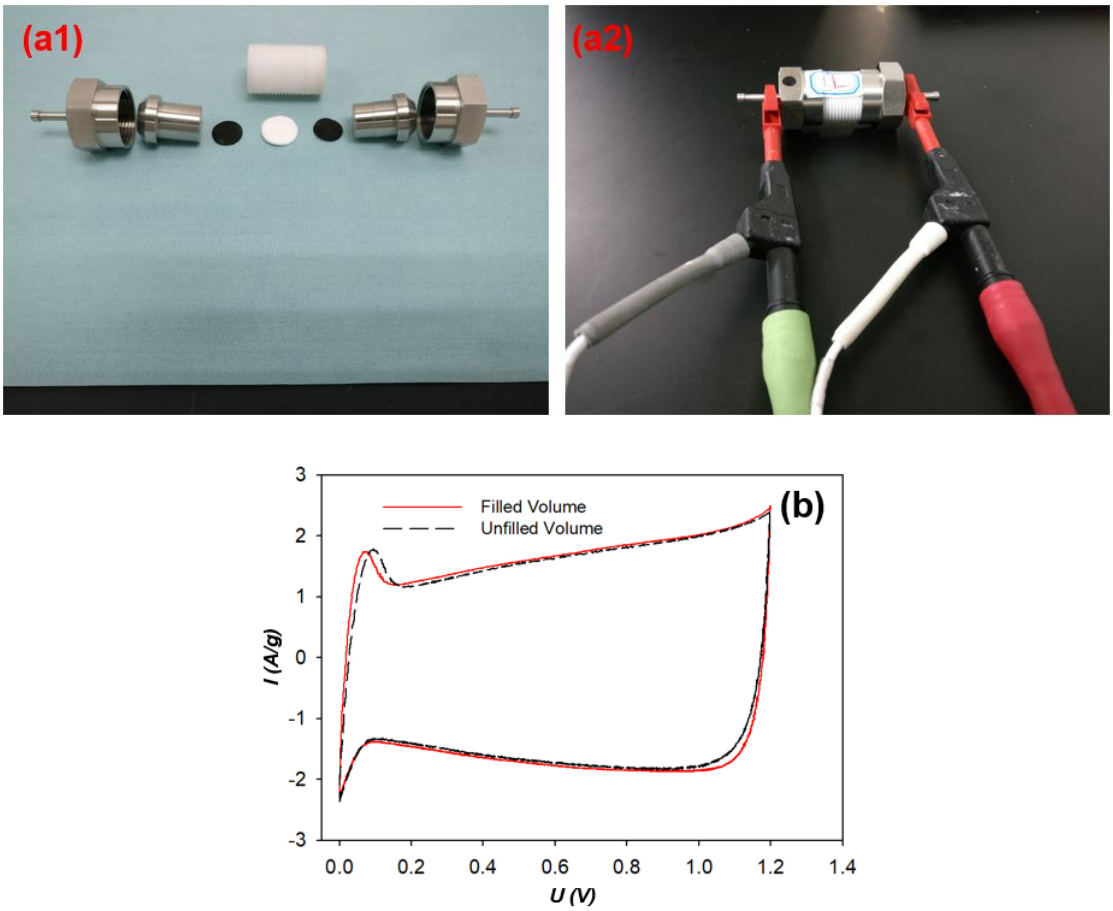

Figure 3.22: (a) Prototype device with Ti current collectors, used for the assembly of 2-electrode cells without electrode potential monitoring (b) Cyclic voltammogram (20.0 mV/s scan rate) of 2.0 mol/L KI with AC electrode in the cell pictured in (a): red solid curve (electrolyte volume in cell filled to the specific constant volume) black dashed curve (cell with unfilled volume).

3.1 Chapter summary

The experimental techniques and methodologies adopted in this research has been described. The numerical basis to the quantification of the electrochemical properties were also presented. The attention to careful ascertainment of the geometry of electrodes and volume of electrolytes tested in this research were also emphasised in order to showcase the procedures adopted to attain accurate volumetric and gravimetric analysis of the performance metrics investigated in this research.

CHAPTER 4: COMBINED NERNSTIAN AND DOUBLE LAYER CHARGING OF ACTIVATED CARBON ELECTRODES IN AQUEOUS HALIDE SUPERCAPATTERY

4.1 Introduction

As was discussed in Ch. 2 (Literature Review), when dissolved redox species (DRS) contribute to charge storage in electric double layer (EDL) electrodes, the mechanism of storage could result in peak-shaped CVs comprising of: non-faradaic capacitive (EDL capacitance) and Nernstian (or battery) mechanisms. Accordingly, these devices have been generally classified as the so-called supercapattery [15]. In line with this, critically characterising these storage mechanisms at the E|E interface can be used to design devices with improved performance, particularly with regards to charge capacity and energy enhancement.

In this chapter, cyclic voltammetry and galvanostatic charging-discharging (GCD) was used to understand the features and performance of supercapatteries with DRS. This was appraised from the standpoint of: electrode polarisation, the thermodynamics of the redox reaction, and shuttling of the redox reaction products between the electrodes.

The halides (KI and KBr) were selected as DRS because of their thermodynamic properties and redox chemistries. A high surface area, low-oxygen content activated carbon was used as active material for the electrodes. Prior to the analysis of the electrochemical findings, this chapter also provided detailed analysis of the porous, and thermo-gravimetric properties, together with the elemental composition of the three different types of carbons used as active electrode materials in this research.

4.2 Carbon electrode materials for electric double layer capacitors

In this research, commercially available carbons with broadly representative properties of common active electrode materials for EDL capacitors were used in the study of redox electrolytes. Some general properties of the three types of carbons are outlined in Table 4.1. The N_2 physisorption properties of these materials are described in detail in Section 4.2.1.

Table 4.1: General description of commercial carbons used as the active electrode material in this research

Carbon Type / Designation	Commercial name / vendor	General property
Activated carbon / (AC-1)	YEC / Fuzhou Yihuan Carbon Co. China.	Highly microporous, amorphous.
Activated carbon / (AC-2)	HCE 202 / Haycarb activated carbon solutions, U.S.A.	Microporous, amorphous.
Graphene nanoplatelets (few layer stacks of platelets) / (GNP)	Graphene nanoplatelets Grade C-750 / XGSciences, U.S.A.	Mesoporous, highly graphitised.

4.2.1 Physisorption analysis of the carbons

Figure 4.1 shows the BET ad-/desorption isotherms and pore size distribution for the three carbons itemised in Table 4.1. Table 4.2 enumerates some of the porous characteristics of the carbons. AC-1 and AC-2 are microporous carbons, as can be seen from their isotherms which is characterised by a high volume of adsorption at low values of relative pressure [182].

Since the isotherm of GNP possesses an increase in the adsorption at high values of p/p^o, its characteristics is indicative of an H3 hysteresis loop [157]. In line with this, AC-1 and AC-2 both display type H4 hysteresis loop, which together with the type H3 could be assumed to represent slit-like pores,

but with the earlier been predominantly microporous whilst the latter comprises mainly of mesopores [182, 183].

Thus, as presented in Table 4.2 mesopores contribute to ca. 35.81% of the total pore volume of AC-2, but accounts for only ca. 22.33% of the total pore volume of AC-1. The average pore width of AC-1 is 1.97 nm whilst that of AC-2 is 2.23 nm. The pore volume of GNP comprises of ca. 18.54% of micropores, 81.46% of mesopores, and it has an average pore width of 6.22 nm.

It is important to point out that these hysteresis loops and pore structures for carbons are generally based on different models of gas-phase condensation in pores. These models approximately assumes specific pore geometries to describe the filling and emptying of pores during N_2 adsorption and desorption respectively [183, 184]. As such, slit-like pores are assumed for capillary condensation which may be suggested for AC-1 and AC-2. Relatedly, the so-called "bottle-neck" pores have been proposed for the case of the hysteresis features displayed by GNP [185, 186]. Moreover it should be highlighted that the N_2 adsorption features of GNP accurately matches porous materials with plate-like structures [182, 186].

The limitations in analysing N_2 physisorption with the BET model, particularly its ineffectiveness in identifying sub-nanometre pores, or inability to offer detailed information on the pore geometries [182, 187] should also be emphasised. Also, it should be acknowledged that the calculated BET-SSA does not necessarily reflect a direct correlation with ion adsorption in the pores [31].

However, the detailed DFT models of the pore size distribution, provides good information of the physisorption properties of these materials which could be used as a basis to generally understand their properties as electrode materials [31, 187, 188]. For example, Fig. 4.2 shows an enlargement of the DFT pore size volume information presented in Fig 4.1 (b, d and f). This difference in the pore size distribution of the materials, could be

used to approximately understand the electrical response of the EDL properties of these carbons, especially with respect to the complementary role between the mesopores and micropores.

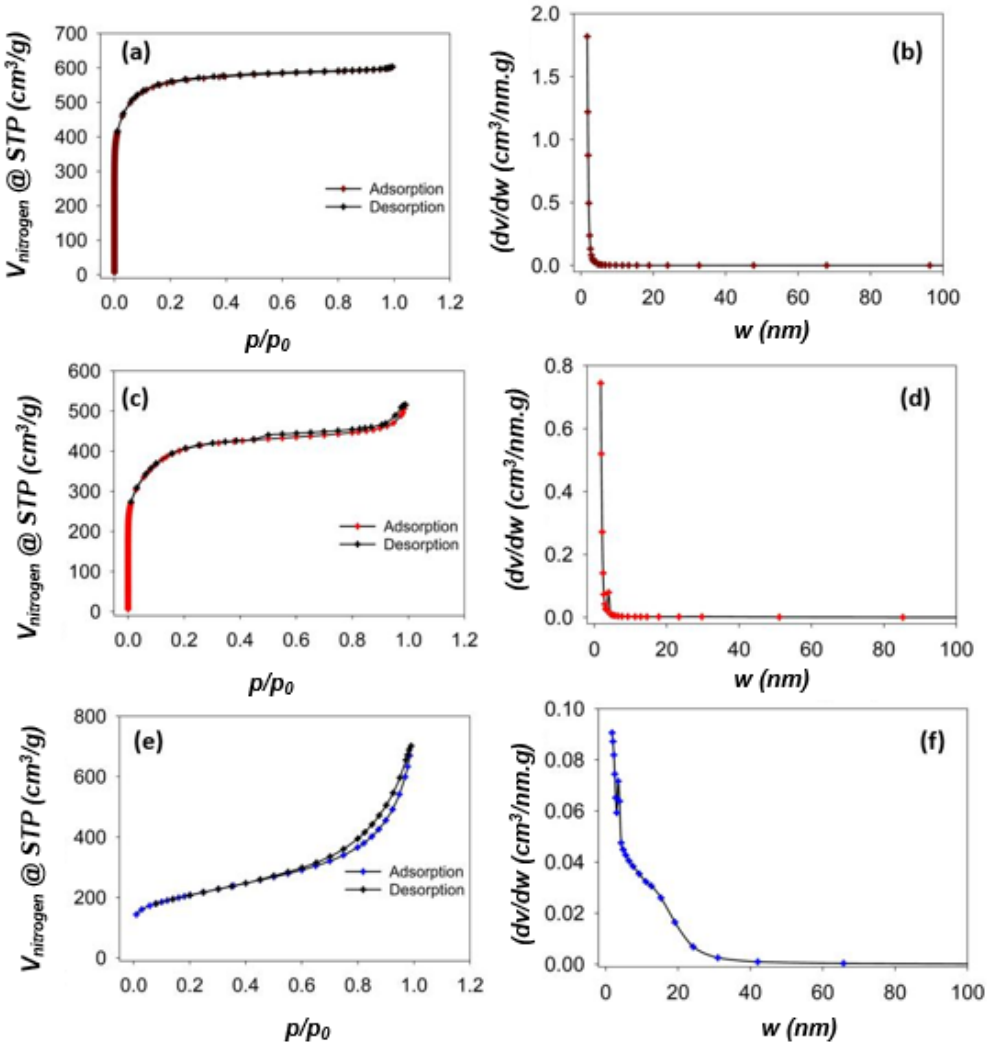

Figure 4.1: N_2 Physisorption graphs showing the adsorption/desorption isotherms and pore size distribution calculated by the DFT method for: AC-1 (a and b), AC-2 (c and d), GNP (e and f) respectively.

Table 4.2: Porous characteristics of carbons from N_2 physisorption analysis

Carbon	S_{BET} (m^2/g)	V_T (m^3/g)	V_{mi}/V_T (%)	V_{me}/V (%)	w_{avg} (nm)
AC-1	1897.63	0.93	77.67	22.33	1.97
AC-2	1487.18	0.80	64.19	35.81	2.23
GNP	698.53	1.09	18.54	81.46	6.22

From Table 4.2, S_{BET} is the specific surface area obtained from the BET method, V_T is the total pore volume, whilst V_{mi}/V_T and V_{me}/V_T are the ratios of the micropores and mesopores to the total pore volume respectively.

Accordingly, in this research, the important information from this physisorption analysis is the knowledge that both AC-1 and AC-2 though micoroporous, possesses different pore size features, particularly the significant presence of mesopores in AC-2. Also, for the purposes of comparison, it would be noticed that the pore size distribution and average pore size of AC-2 (2.2 nm) and GNP (6.2 nm) represents good models for small (micropore) and large (mesopore) pores respectively.

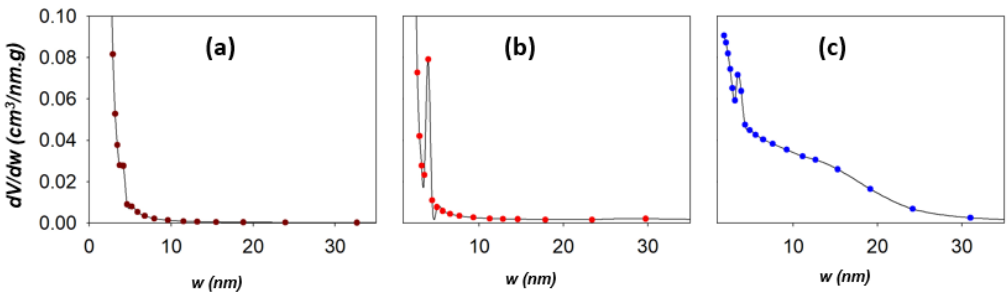

Figure 4.2: Pore size distribution from the DFT method focusing on the mesoporous characteristics of: AC-1 (a) AC-2 (b) GNP (c).

Note that according to the IUPAC Classification the average dimensions for the pores are: micropores (< 2nm), mesopores (2nm to 50 nm), macropores (> 50 nm) [156].

4.2.2 Thermo-gravimetric analysis of carbon electrode materials

The profile obtained from the thermo-gravimetric analysis (TGA) of the carbons showed that some of the surface (carboxyl and quinone) groups in AC-2 and GNP are similar.

This is because from ca. 100.35 to 493.57 ^{0}C AC-2 lost about 13.8% of its mass, which is comparable to the mass loss of 15.06% in GNP from a similar temperature range of 100.31 to 494.23 ^{0}C. This temperature range

corresponds broadly to the decomposition of C-O surface groups [188, 189], implying that both AC-2 and GNP comprises of these groups.

It was observed from the thermo-gravimetric analysis (TGA) of the carbons shown in Fig. 4.2 that some of the surface (quinone or ether) groups in AC-2 and GNP are similar.

This is because from ca. 100.35 to 493.57 ^{0}C AC-2 lost about 13.8% of its mass, which is comparable to the mass loss of 15.06% in GNP from a similar temperature range of 100.31 to 494.23 ^{0}C. This temperature range corresponds broadly to the decomposition of C-O surface groups [188, 190], implying that both AC-2 and GNP comprises of these groups.

However, majority of the mass of AC-2 decomposed from 493.57 to 578.46 ^{0}C, and this is indicative of a higher proportion of carboxyl groups (see Fig. 6.7c for the corresponding x-ray spectrogram) [188, 190, 191]. On the other hand, the thermal stability of AC-1 is markedly higher than that of both AC-2 and GNP, since it displays majority of its mass loss at the temperature range from 566.07 to 668.87 ^{0}C. This indicates that the surface groups or volatile constituents in AC-1 are significantly lower in comparison to that of either GNP or AC-2.

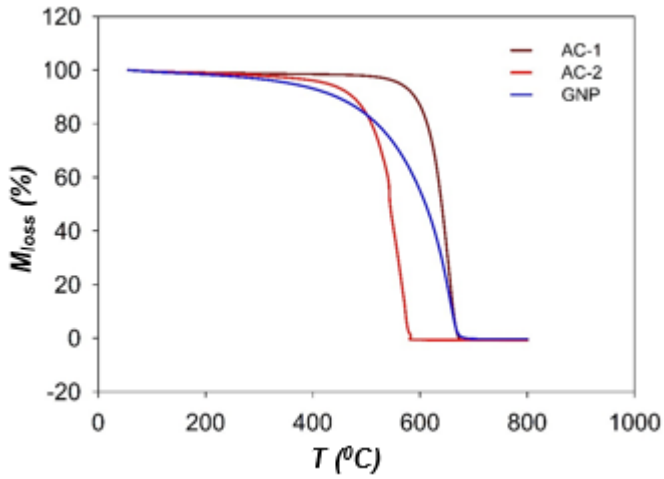

Figure 4.3: TGA profile of AC-1, AC-2 and GNP in N_2. Ramp rate: 10 ^{0}C/min. M_{loss} is the loss in mass, and T is temperature.

The information obtained from the TGA analysis, can also be confirmed from the elemental analysis of the carbons as shown in Table 4.3. Note that Table 4.3 only presents the major elements in the carbon and all other trace components (for example silicon and aluminium which are the major constituents of the ash content) were less than 0.01% to 0.05% for all the carbons, and thus are not presented). From Table 4.3 it was observed that AC-1 has the highest composition of carbon with only a comparatively small amount of oxygen (or oxygen containing surface groups in general). Although, AC-2 is composed of a higher amount of oxygen (18.51%) of all the carbons investigated, nevertheless, its oxygen content is only slightly higher than that of GNP (15.27%).

Table 4.3: Elemental composition of carbonaceous electrode materials

Carbon	**C (%)**	**O (%)**	**H (%)**	**N (%)**
AC-1	94.28	4.32	0.52	0.54
AC-2	79.60	18.51	1.52	0.28
GNP	82.75	15.27	1.30	0.65

4.2.3 Electrochemical double layer capacitance of devices fabricated with the carbon electrodes

With knowledge of the physisorption and elemental composition of the carbon electrode materials, equal electrode mass (EEM) cells with 2.0 mol/L of KCl were fabricated with the carbon electrodes. Fig. 4.4 shows the CVs of the EDL cells.

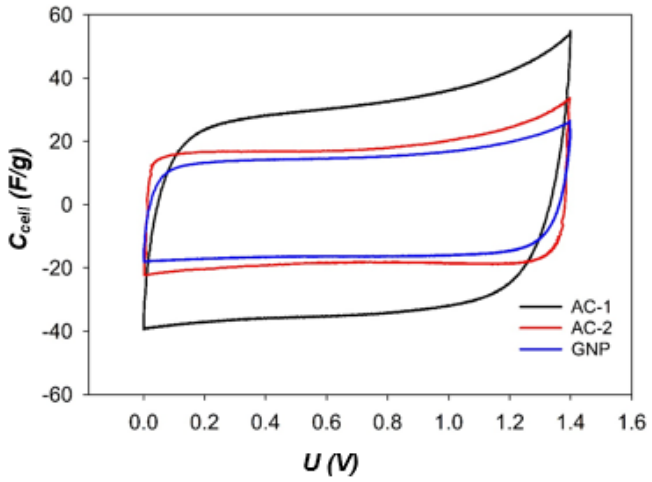

Figure 4.4: CVs of EEM cells fabricated with the three different carbon electrodes using 2.0 mol/L KCl, scan rate: 5 mV/s.

From Fig. 4.4, it was noticed that there was only a small difference between the specific cell capacitance (C_{cell}) of AC-2 (ca. 17.94 F/g) and GNP (ca. 14.29 F/g). However, the C_{cell} of AC-1 of ca. 35.26 F/g is approximately twice that of either AC-2 or GNP.

Generally, the comparatively optimal ratio between the micropores/mesopores of AC-1 coupled with its high surface area may be identified as the reason why its specific electrode capacitance (C_{sp}) in 2.0 mol/L KCl (ca. 141.04 F/g) is significantly larger than that of AC-2 and GNP which are: ca. 71.76 and 57.16 F/g respectively. Accordingly, in this research, AC-1 is used as a typical EDL electrode to probe the general enhancement in capacity and energy provided by DRS. Moreover, the uniquely similar EDL properties of AC-2 and GNP, makes them very useful in gaining further understanding of the role of the texture of these carbons on the performance of supercapatteries with redox electrolytes. Texture herein refers to the porous and surface physicochemical properties of the carbons. Furthermore, the highly-graphitised and porous property of GNP (which was analysed in detail in Ch. 6) was also of particular interest, because there have been very few studies focused on the properties of DRS with this class of carbons. To the best of the author's knowledge: all the results from the studies of DRS in supercapacitors

with GNP electrodes as reported in this dissertation, were the first of their kind, especially the studies carried out for high voltage applications of DRS.

AC-1 is the electrode used throughout the remainder of this chapter. It should also be pointed out that in subsequent chapters, the electrode used would be explicitly stated. This is because for every experiment carried out to investigate the properties of DRS in this research, it was necessary to always understand the property of the electrode utilised. Moreover, the fundamental testing of redox electrolytes with these typical (commercial) EDL electrodes, is a practical means of ascertaining the promise of industrial scale-up of DRS in general.

4.3 Electrochemical characterisation of activated carbon (AC-1) electrode in redox electrolytes (KI and KBr)

4.3.1 Background to the investigations of carbon electrodes with redox electrolytes

Some beneficial properties of the DRS as listed and explained below are crucial for effective and efficient coupling with an EDL electrode, and these properties in general were the basis for the selection of the dissolved redox species investigated in this research:

(1) Reversibility of the redox reaction is of great importance because a more reversible reaction can lead to higher charge and energy efficiency of the device.

(2) Solubility of the DRS in the electrolyte should be as large as possible to maximise the storage capacity from the additional charge obtainable.

(3) Potential of the DRS should be as close as possible to the limit of the potential window of the electrolyte so that the working voltage and hence energy capacity of the cell can be maximised.

(4) Specific interactions of the product of the charging reaction of the DRS with the EDL electrode (e.g. chemical and electrostatic

adsorption, or coating or deposition due to poor solubility) may help retain the product in the electrode, minimising energy loss and self-discharge of the cells due to the redox shuttling between the positive electrode (positrode) and negative electrode (negatrode) [15].

(5) The signs of charge on an ionic DRS and its electrode reaction product should better be the same, e.g. I^- and I_3^-, and opposite to that of the electrode, i.e. cations for negatrode and anions for positrode, to ensure favourable electrostatic interactions.

A commonly expected issue related with using redox electrolyte in supercapacitors is the shuttling of the redox couple between the positrode and negatrode, which can in principle be mitigated by using an ion-selective membrane. Generally, as was described in Ch. 2 (Section 2.8) such membranes (specifically ion-exchange membranes) have been shown to be effective in reducing self-discharge in supercapacitors using redox electrolytes [113]. The use of a membrane helps compartmentalise the cell, thus enabling each E|E interface of the positrode and negatrode to operate within their capacitive potential ranges (CPRs) [111]. Such bi-electrolyte cells can also incorporate DRS at one [192], or both [100] the E|E interface(s) to further enhance the charge capacity.

An important point that has not been addressed in most of the research on redox electrolytes is that although the presence of DRS in the electrolyte of a supercapacitor can increase the charge storage capacity, this does not always mean an increase in the energy storage capacity. For example, some DRS have electrode potentials that are located in the middle range of the electrochemical window of water. Consequently, aqueous supercapacitors using such DRS tend to have an increased amount of charge stored at low cell voltages, which is of little benefit to increasing the energy capacity [193].

In line with this, the remaining sections of this chapter would rigorously study the features of EEM cells using KI, KBr and the bi-electrolyte cell (−)AC | 2.0 mol/L KOH || 2.0 mol/L KI | AC(+). In this chapter, the property of these cells would be used to:

i. Thoroughly explain the shuttling of products of the redox reaction from the standpoint of the thermodynamics of the DRS.
ii. Assess the role of electrode polarization in determining: the features of the cell, and the utilisation of the DRS.
iii. Briefly, explain the role played by membranes when used in the design of bi-electrolyte supercapatteries with DRS. In Ch. 9, details of the practical applications of bi-electrolyte cells would be extensively covered.

4.3.2 Electrochemical characterisation of the carbon | redox-halide interface and supercapatteries with halides as dissolved redox species

Cyclic voltammograms (CVs) of the AC electrode in the electrolytes of 1.0 mol/L KI and 1.0 mol/L KBr are shown in Fig 4.5 a and b, respectively. The CVs of AC in 1.0 mol/L KI from −1.40 to 0.90 V vs. SCE shows the expected full feature of the anodic oxidation of I^- into I_2 + I_3^- and their further oxidation [194]. However, within the same potential range, the CVs recorded in 1.0 mol/L KBr indicated only the oxidation of Br^- to Br_2 + Br_3^-, but their further oxidation did not occur. This difference is actually expected because the oxidation potentials of Br^- and Br_2 + Br_3^- are more positive than those of I^- and I_2 + I_3^-. It should be mentioned that this potential window from −1.40 to 0.90 V was selected to enable the Faradaic reactions from the dissolved halide anions, but to avoid those from carbon and/or water.

According to both Fig. 4.5a and 4.5b, from 0 to −1.40 V, the charge storage mechanism at the carbon | halide interface is due to the EDL capacitance. The CVs indicate I^- ion oxidation starting at potentials slightly

above ca. 0.03 V. This is in contrast with the CVs of Br^- ion showing dominantly EDL storage until ca. 0.60 V, before commencing Br^- oxidation.

The oxidation of halide ions at potentials of the current peaks on the CVs are in line with thermodynamic expectation. However, the contribution of these halide ions, (particularly Br^- at positive potentials up to ca. 0.50 V as shown in Fig. 4.5b), to EDL charging of the AC electrode before the occurrence of halide oxidation, is also significant.

The highly potential dependent behaviour of the Br^- and I^- ions as revealed by the CVs in Fig. 4.5a and 4.5b should affect the charge storage performance of the supercapacitor with two AC electrodes. Thus, two electrode cells with equal electrode mass (EEM) were fabricated and studied. Fig. 4.5c and 4.5d show the CVs of the EEM cell with KI and KBr, respectively. It was observed that the cell with 1.0 mol/L KI exhibited small current peaks whilst the cell with 2.0 mol/L KI displays marked peaks at low cell voltages near 0 V. On the contrary, the cell with KBr showed large currents at cell voltages higher than 0.70 V.

In the literature on supercapacitors with I^- containing electrolytes, the low voltage peaks were reported to be linked to the type of current collector used [134], and could even increase after continuous cycling/floating of the cells (see Fig. 2.25b) [96]. However, no clear and convincing explanation has been given on how the low cell voltage peaks form, and their correlation with the experimental conditions, such as the upper cell voltage limit of charging and the concentration of I^-. It should also be emphasized that the importance of such an analysis is because, critical understanding of this feature is of importance to the rigorous characterisation of supercapatteries with DRS in general.

As shown in Fig. 4.5c, the low voltage peaks are merely visible on the CV recorded in 1.0 mol/L KI, but quite marked on that in 2.0 mol/L KI. In Fig. 4.6a, the CVs recorded in 2.0 mol/L KI show a clear trend of the low voltage

peaks becoming more prominent with increasing the upper limit of the cell voltage.

These observations indicate that at higher I^- concentrations and charging voltages, the charging reactions were promoted, and more products from charging reactions were accumulated in the cell before discharging. However, both Figs. 4.5a and 4.6a suggest that in KI, the conversion between the reactant (I^-) and products (I_2 + I_3^-) could only occur at low or near zero cell voltages at which the positrode and negatrode potentials, E_+ and E_-, must be approaching E_{0V}. Note that E_{0V} is the potential of zero voltage (PZV) at which the cell is fully discharged. In other words, PZV is the equal potential of the positrode and negatrode when the cell is fully discharged to 0 V, however, it is not necessarily the same as the better known PZC i.e. (potential of zero charge).

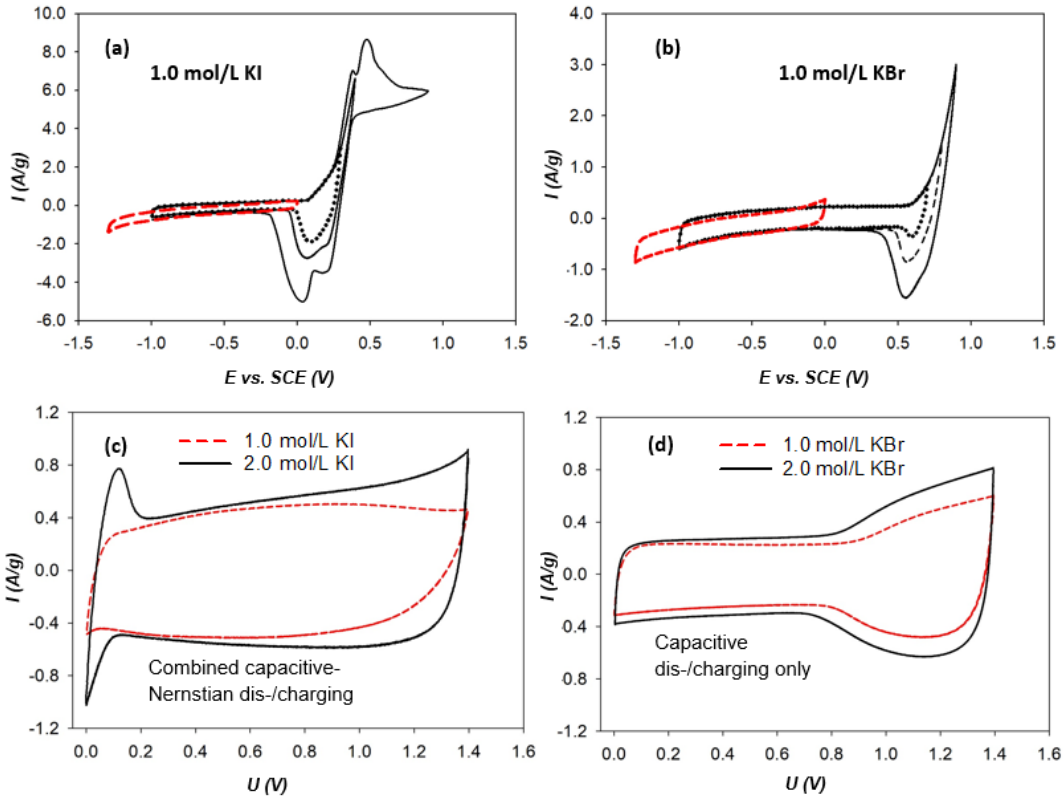

Figure 4.5: CVs of the AC electrode in (a) 1.0 mol/L KI, (b) 1.0 mol/L KBr (scan rate: 1 mV/s), and EEM-cells containing 1.0 and 2.0 mol/L of (c) KI, and (d) KBr (scan rate: 5 mV/s).

4.4 Nernstian and double layer features of supercapatteries with redox halides

Figure 4.6b plots the measured E_{0V}, and peak E_+ and E_-, against the upper cell voltage limit, U_L, with the data being extracted from GCD experiments as exemplified in Fig. 4.6b. Comparing Fig. 4.6b with Fig. 4.5a, it can be certain that E_{0V} coincides with the oxidation potential of the I^- ion. Thus, the fact that E_+ varied only slightly in parallel with E_{0V} as shown in both Fig. 4.6b and 4.6c confirms that charging and discharging the positrode were dominantly undertaken by Nernstian reactions, i.e. the oxidation of I^- and the reduction of $I_2 + I_3^-$, respectively. On the other hand, the small variation of E_+ is strong evidence of very little contribution, if any, resulting from EDL charging and discharging in the positrode because $Q = C\Delta E$ for a capacitive electrode.

On the negatrode, as shown in Fig. 4.6c, both charging and discharging processes involved EDL (the linear portion at more negative potentials) and Nernstian (the small potential plateaus near E_{0V}) contributions. This behaviour of the negatrode can be explained starting from discharging the negatrode at the negative potential limit (ca. −1.32 V in Fig. 4.5c, blue line) where the negatrode could not oxidise the I^- ion, but underwent EDL discharging. When continued discharging caused E_- to approach E_{0V}, I^- oxidation became feasible to produce $I_2 + I_3^-$, leading to the discharging potential plateau (DPP). Upon charging the cell, E_- moved negatively away from E_{0V}, and enabled the reduction of $I_2 + I_3^-$ that were generated from I^- oxidation, corresponding to the charging potential plateau (CPP).

Without considering the influence from the positrode, it is expected that the total amount of $I_2 + I_3^-$ in the negatrode available for charging should be

the same as or less than that generated from I^- oxidation at the immediate last stage of discharging the negatrode. (Note that to consider this earlier statement, the diffusion of $I_2 + I_3^-$ into the bulk electrolyte and the electrostatic repulsion between the negatrode and anions must be noted). This expectation seems to agree with the fact that the length (charge) ratio of DPP/CPP on the GCD plot of the negatrode in Fig. 4.6c is ca. 1.24. Similar DPP/CPP ratios were obtained from other GCD plots recorded on the negatrode in the KI electrolytes.

The DPP/CPP ratio being larger than 1 is an interesting finding because it seems to agree with that the majority, if not all, of $I_2 + I_3^-$ in the negatrode were generated in the negatrode, instead of coming from the positrode via the so called redox shuttling. If so, it is then expected that on the positrode the charges, Q_c and Q_d, passed in the charging (oxidation of I^-) and discharging (reduction of $I_2 + I_3^-$) processes, respectively, should be the same or very close. In other words, the charge efficiency of the positrode, Q_d/Q_c, should be close to 100%.

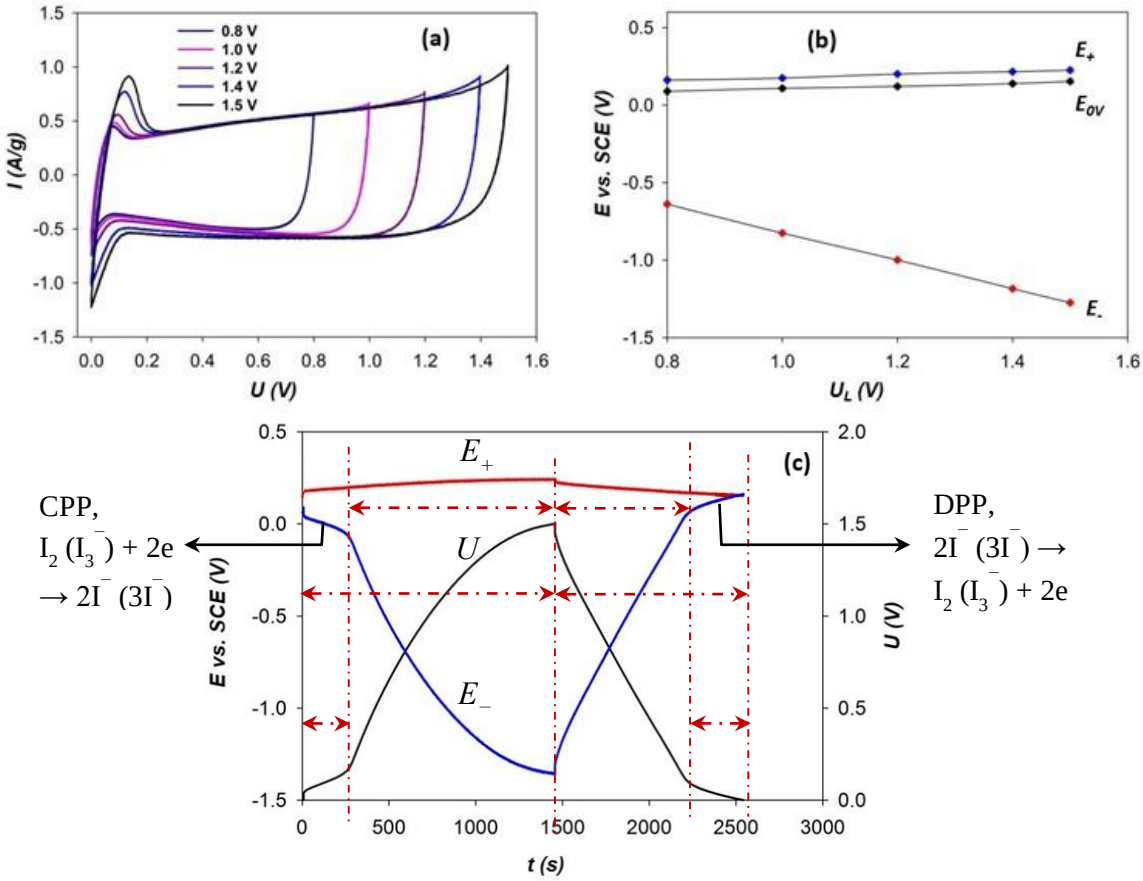

Figure 4.6: Performance of the EEM cell of AC electrodes with 2.0 mol/L KI: (a) CVs recorded at 5.0 mV/s with different upper limits of cell voltage (U_L), (b) plots of the positrode (E_+), negatrode (E_-) and zero voltage (E_{0V}) potentials vs U_L with data extracted from the GCD plots of U, E_+ and E_-, recorded at a current load of 0.1A/g, and (c) GCD plots of U, E_+ and E_-, with U_L = 1.5 and current load = 0.1 A/g.

However, the charge efficiency derived from the GCD of the positrode in Fig. 4.6c is only 73.1%, which is evidence of a significant part of $I_2 + I_3^-$ generated in the positrode during charging was not recovered during discharging. A possible fate for the lost $I_2 + I_3^-$ from the positrode was that they diffused into the electrolyte, and then were reduced on the negatrode as discussed below.

The above mentioned experimental finding and analysis of the charging and discharging reactions on both the positrode and negatrode suggest that the conversion between I^- and $I_2 + I_3^-$ occur in both electrodes. A particular

point to note is that the reduction of $I_2 + I_3^-$, if present in the electrolyte, should have continued on the negatrode at potentials more negative than that of the DPP, i.e. approximately between 0 and – 1.4 V in Fig. 4.6c. The reason why this portion of the negatrode GCD plot is apparently capacitive is because at such negative potentials, reduction of $I_2 + I_3^-$ must be under diffusion control, giving rise to a current that could be constant if the $I_2 + I_3^-$ concentration in the electrolyte remains approximately the same. This understanding agrees well with the fact that the charge efficiency as derived from the apparent capacitive portions of the negatrode GCD plot is as low as 65.1%, which is obviously the main cause for the fairly low overall charge efficiency of 74.1% as derived from all the GCD plots in Fig. 4.6c.

It was also found that the overall cell charge efficiency decreased with increasing the charging cell voltage. For example, the overall charge efficiency was > 90%, 83.3%, 74.1% when the charging cell voltage was 1.0, 1.2 and 1.4 V, respectively (see Fig. 4.7). This is understandable because at higher charging cell voltages, more $I_2 + I_3^-$ were produced in the positrode, and hence more diffused to and underwent reduction at the negatrode, leading to lower charge efficiency.

While the above discussion leads to a conclusive confirmation of the occurrence of redox shuttling of $I_2 + I_3^-$ between the positrode (charging) and negatrode (discharging), the question is why $I_2 + I_3^-$ did not all remain in the positrode, but part of $I_2 + I_3^-$ diffused into the electrolyte? Generally, this could be due to some causes such as pore size and chemical interactions that may affect the retention of $I_2 + I_3^-$ [141, 195]. Still, it is worth noting that the positrode potential did not increase significantly during charging and discharging, as shown in Fig. 4.6b and 4.6c. It suggests that electrostatic interaction did not help retain $I_2 + I_3^-$ in the positrode, even at high cell voltages. This means two possibilities.

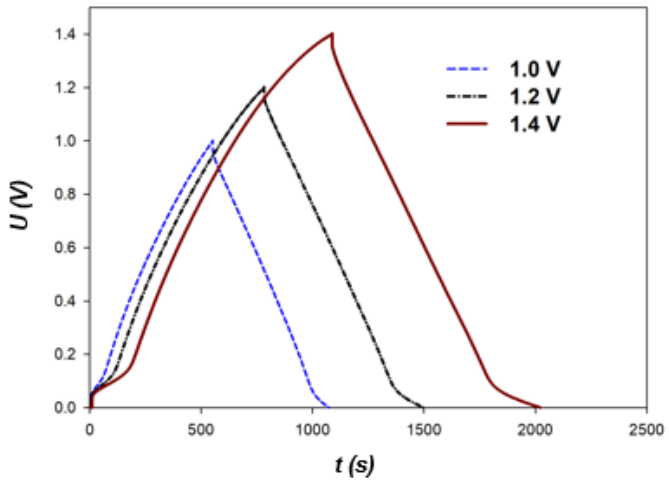

Figure 4.7: GCD plots of EEM cells with 2.0 mol/L KI, at U_L = 1.0, 1.2 and 1.4, current load = 0.1 A/g.

Firstly, because I_2 is neutral in terms of charge, its retention in the positrode could not be affected by the potential change but more controlled by chemical potential, particularly concentration gradient that is responsible for diffusion. Secondly, as shown in Fig. 4.6b and 4.6c, the positrode potential and its increase during charging were too small to enhance the retention of I_3^- in the positrode. Thus, diffusion of I_3^- away from the positrode could also occur. More results and discussion on the shuttling of I_2 + I_3^- will be given later.

Unlike in KI, the cell CVs and GCDs recorded in KBr presented very different shapes as shown in Figs. 4.8a, 4.8b and 4.8c.

The first difference is the absence of the low cell voltage peaks on the CVs. This observation is reflected by the absence of low voltage plateaus on the GCD of the negatrode in Fig. 4.8c. According to the analysis and discussion above on the CV and GCD of KI, these features are indicative of little or no redox shuttling of Br_2 + Br_3^- as generated from oxidation of Br^- in the positrode.

The other difference is the appearance of broad current waves at high voltages, i.e. 0.80 to 1.50 V, on the CVs as expected from oxidation of Br^- to Br_2 + Br_3^- and the reversed process during the forward and backward voltage scans, respectively. The corresponding positrode GCD also showed clearly the

potential plateaus of the Nernstian feature above the capacitive slopes, which were absent on the positrode GCD of KI. The negatrode GCD in KBr showed only the capacitive slopes. These GCD features are in agreement with those of the CVs, and support the claim of oxidation of Br^- to Br_2 + Br_3^-, but little or no redox shuttling of Br_2 + Br_3^-.

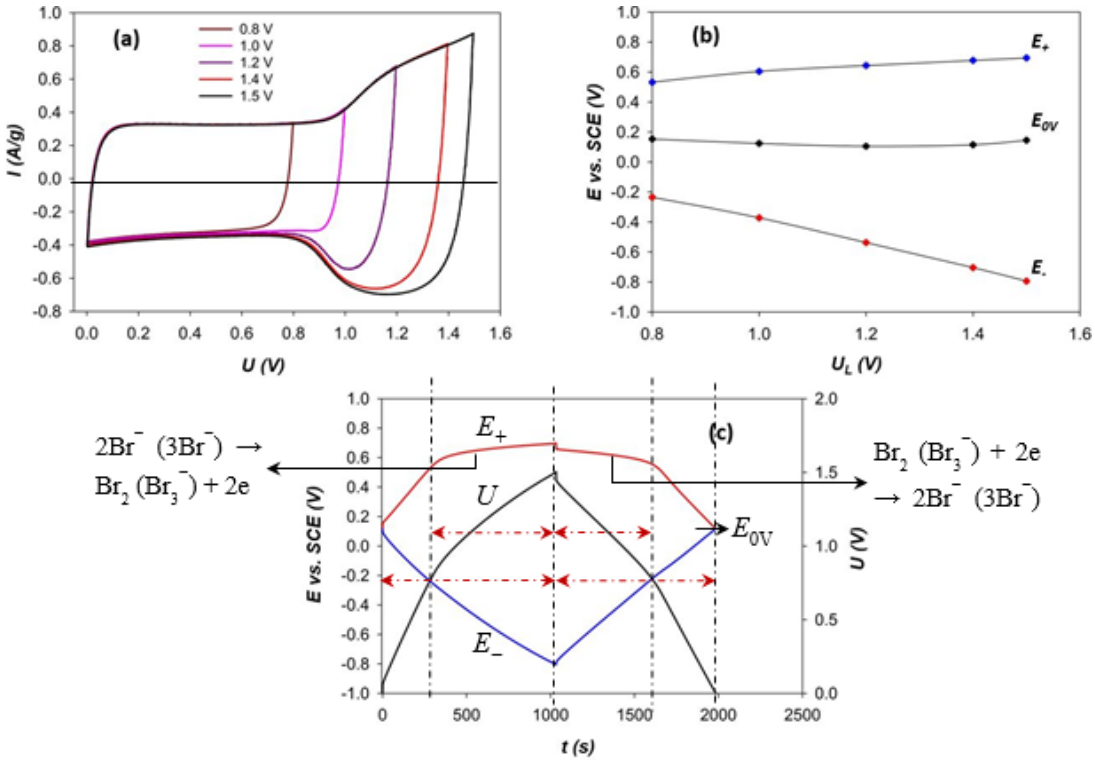

Figure 4.8: Performance of the EEM cell of AC electrodes with 2.0 mol/L KBr: (a) CVs recorded at 5.0 mV/s with different upper limits of cell voltage (U_L), and (b) plots of the positrode (E_+), negatrode (E_-) and zero voltage (E_{0V}) potentials vs U_L with data extracted from the GCD plots of U, E_+ and E_-, recorded at a current load of 0.1A/g (c) GCD plots of U, E_+ and E_-, with U_L = 1.5 and current load = 0.1 A/g.

A third difference can be seen by comparing between Fig. 4.5c and 4.5d, and also between Fig. 4.6a and 4.8a. The capacitive currents (< 0.40 A/g in Fig. 4.8a) on the CVs of KBr between 0 and 0.80 V are notably smaller than

those (> 0.50 A/g in Fig. 4.6a) on the CVs of KI between 0.20 and 1.40 V. The larger capacitive currents in KI can be explained by the cell voltage variation being undertaken dominantly by the potential change of the negatrode in KI because the positrode potential varied only slightly under Nernstian control as shown in Fig. 4.6b and 4.6c. On the same time scale, the wider and hence faster potential change (versus those of both the positrode and negatrode in KBr) means a larger current for a dominantly capacitive negatrode.

In fact, the apparently larger capacitive currents in KI could be also partly due to redox shuttling of $I_2 + I_3^-$. The negatrode in KBr was only capable of EDL charging and discharging, but in KI underwent both EDL and Nernstian charging (reduction of $I_2 + I_3^-$, partly shuttled from the positrode under diffusion control), contributing to larger charging currents. Upon discharging the negatrode, however, oxidation of I^- could not occur until the potential reached near E_{0V}. The consequence was a lower charge efficiency. Indeed, the overall charge efficiency was 94.2% in KBr as derived from Fig. 4.8c, in contrast to 74.1% in KI from Fig. 4.6c. This analysis again suggests insignificant, if any, redox shuttling in KBr.

The CVs and GCDs of the cell deserve more discussion in terms of whether the cell voltage (not the electrode potential) at which the redox reaction occurs may be increased so that redox shuttling can be avoided or minimised, whilst energy capacity can be increased. For the cell containing 2.0 mol/L KBr (cf. Fig. 4.8), it was noticed that in the course of increasing the cell voltage (U) to the upper limit (U_L = 1.5 V), the positrode potential also increased from 0.13 V (= E_{0V}) to 0.72 V vs. SCE, experiencing EDL charging only (0.13 to 0.62 V), and then mainly Nernstian charging as indicated by the potential plateaus (0.62 to 0.72 V). However, for the cell with 2.0 mol/L KI, at all cell voltages applied, the positrode exhibited dominant Nernstian charging in a narrow potential range (0.16 to 0.23 V vs SCE, cf. Fig. 4.6c). In line with the behaviour of the positrode, Fig. 4.8 shows also obviously and

understandably that at $U < 0.90$ V, the cell containing KBr displayed capacitive features, and the contribution from the redox charging of the electrode only set in when U > 0.90 V. This observation can be explained from the concept of the unequal electrode capacitance of the cell.

For charge conservation, the amounts of charge passing through the positrode and negatrode must be equal and can be expressed as follows, if both electrodes are capacitive,

$$Q_n = C_n \Delta E_n = C_p \Delta E_p = Q_p \quad (4.1).$$

Where Q, C and ΔE (= $E - E_{0V}$) are the total charge, capacitance and applied potential range that is within or the same as the capacitive potential range (CPR) of the electrode, and the subscripts *n* and *p* indicate the negatrode and positrode respectively. Note that E is the potential of the negatrode or positrode at an applied cell voltage U, and E_{0V} is the equipotential of the positrode and negatrode at $U = 0$ V, i.e. the potential of zero voltage (PZV).

Accordingly, provided that E_{0V}, E_n and E_p are within the CPR of the respective electrodes, the maximum charging voltage (MCV) of the cell can be extended through unequalisation of electrode capacitances by utilising the following Eq. (4.1).

$$\text{MCV } (U_{max}) = \Delta E_p(1 + C_p / C_n) \quad (4.2).$$

In Eq. (4.2), the choice of ΔE_p is based on the assumption that of the two electrodes, the positrode has the narrower CPR and hence is the voltage determining electrode [57]. It is also important to point out that Eq. (4.2) simply means that the polarisation of one electrode relative to the other can be adjusted by changing the capacitance ratio of the two electrodes. This reasoning is very important to understand the operation of the EEM cells using KBr, and this would be addressed later.

Referring to Eq. (4.1), if a redox reaction occurs at the positrode, then Q_p would have two components, namely, $Q_p = Q_{p1} + Q_{p2}$, where Q_{p1} and Q_{p2} refer to the EDL and Nernstian contributions, respectively. Obviously, Q_{p1} =

$m_pC_{sp}\Delta E_p$, whilst it would be generally correct for $Q_{p2} = nFN_0V_0$, where N_0 and V_0 are the concentration and volume of the redox electrolyte in the porous positrode, respectively, n is the number of electron(s) participating in the reaction, and F the Faraday constant (96,485.33 C/mol). Thus, the following expression can be established.

$$Q_p = Q_{p1} + Q_{p2} = m_pC_{sp}\Delta E_p + nFN_0V_0 \quad (4.3).$$

As a first approximation, V_0 in Eq. 4.3 can be considered to be the total volume of electrolyte absorbed into the saturated porous positrode (excluding any excess electrolyte). However, from a practical perspective, because some pores may not be accessible electrochemically, V_0 could be larger than the volume of accessible pores of the positrode, V_{pore}. Furthermore, V_{pore} should be fundamentally expressed as a function of the pore size distribution, for example, as obtained from DFT analysis of the physisorption properties of the electrode material.

By substituting Eq. (4.3) into Eq. (4.1), and dividing through by ΔE_p, one can then obtain the following expression,

$$\frac{Q_p}{\Delta E_p} = m_pC_{sp} + \frac{nFN_0V_0}{\Delta E_p} \quad (4.4).$$

Eq. (4.4) implies that the Faradaic component of the charge stored would provide a given amount of charge stored per unit increase in the positrode potential. Of course for this Faradaic component to set in, there should be $\Delta E_p \geq E_N - E_{0V}$, where E_N is the electrode potential of the redox couple determined by the Nernst equation. For example, in the KBr solution, the oxidation of Br^- to $Br_2 + Br_3^-$ can be expressed as

$$(2 + \beta)\ Br^- = \alpha\ Br_2 + \beta\ Br_3^- + 2\ e \quad (4.5),$$

where $\alpha + \beta = 1$.

Then, the Nernst equation is given below:

$$E_{\mathrm{N}} = E^{\mathrm{o}} + \frac{RT}{2F}\ln\left(\frac{a_{Br_2}^{\alpha} a_{Br_3^-}^{\beta}}{a_{Br^-}^{2+\beta}}\right) \quad (4.6),$$

where E^0 is the standard potential for the oxidation of Br^- to Br_2 + Br_3^-, and *a* the activity of the respective redox species in the electrolyte.

The above descriptions of the electrode properties can now be used to explain in detail the properties of supercapacitors with DRS. Figure 4.8a shows the CVs of the AC electrode in 1.0 mol/L KBr recorded respectively in the potential range from 0 to 0.5 V and from 0 to −0.5 V vs. SCE. The capacitance of the AC was 124.6 F/g when measured between 0 and 0.5 V, but 165.2 F/g between 0 and −0.5 V. This finding implies that in the EEM cell with KBr, as the cell voltage limit is gradually increased, the positrode would be slightly more polarised relative to the negatrode according to Eq. (4.1), which also agrees with the *E* vs. *U* plot in Fig. 4.8b. For example from Fig. 4.8b, within the capacitive range of both electrodes at U_L = 0.8 V, ΔE_p = (0.57 – 0.15) = 0.42 V, whilst ΔE_n = (0.53 – 0.15) = 0.38 V. Subsequently, when the potential of the positrode reached the value at which the Br^- is active, its charge storage mechanism attains the Nernstian component, and thus takes on the expression given in Eq. (4.4).

It is also important to point out that Eq. (4.2) can be used to approximately predict the cell voltage, U_{redox} at which the Nernstian contribution could be observed in the EEM cell with KBr. From Fig. 4.8c, ΔE_{p} can be taken as 0.49 V, i.e. from 0.13 V (= $E_{0\mathrm{V}}$) to 0.62 V vs. SCE, and by taking C_{p} = 124.6 F/g, and C_{n} = 165.2 F/g from Fig. 4.9a, and substituting these data into Eq. (4.2), it can be obtained that U_{redox} = 0.49 (1 + 124.6/165.2) = 0.86 V at which the Nernstian contribution to the cell with KBr would commence. This agrees well with that of 0.90 V shown in Fig. 4.4c, or as labelled in the CV of Fig. 4.9c. Also from the CVs in Fig. 4.5b, it can be seen that it is possible to extend the voltage of the EEM cell with KBr to 2.0 V

as shown in Fig. 4.9c. Such analysis and calculation demonstrates that the electrode thermodynamics of the DRS, and the nature and extent of the electrode polarisation determine the observed performance features of the cells.

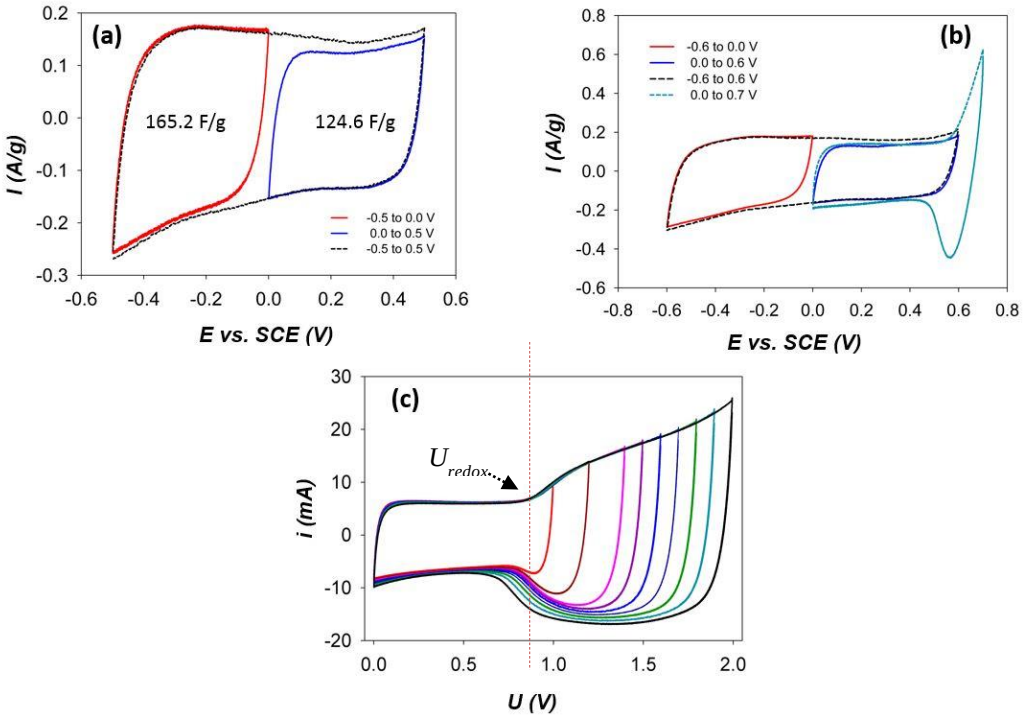

Figure 4.9: CVs of the AC electrode in 1.0 mol/L KBr, showing (a) the asymmetry in capacitance in two different potential ranges within the CPR, and (b) the occurrence of the Nernstian process, i.e. oxidation of Br^-, at potentials more positive to the CPR. Scan rate: 1.0 mV/s. (c) CVs of the EEM cell of the AC electrodes in 1.0 mol/L KBr recorded with increasing cell voltage limits from 1.0 to 2.0 V. Scan rate: 5.0 mV/s.

4.5 Forced confinement of redox activity to eliminate shuttling of redox reaction products

To describe the occurrence of the current peaks on the CVs at low voltages for the KI cells, it is necessary to assess the position of the E_{0V} of the electrodes in any given supercapacitor with or without DRS. In principle, at an applied U on a given cell, E_{0V} may be linked to the properties of the E|E interface, but it can still vary considerably from one supercapacitor to another,

or even between similar devices with different histories. Also, at E_{0V}, there may still be excess charges on the surfaces of the positrode and negatrode, and under open-circuit conditions, the electrode potentials would readily proceed to assume their respective equilibrium states through a redistribution of these surface charges.

In the situation of the KI cell, what is most striking is that E_{0V} varied between ca. 0.09 and 0.15 V vs SCE, and was very close to E_p (0.16 to 0.23 V vs SCE) of the positrode where I^- and I_2 + I_3^- are all active (see Fig. 4.5b). However, for the KBr cell, E_{0V} varied from 0.15 to 0.13 V vs SCE, and was farther from E_p (0.44 to 0.72 V vs SCE, cf. Fig. 4.8b and 4.8c). Consequently, in the KI cell, the oxidation of I^- to I_2 + I_3^- could contribute to the charge storage in both the positrode and negatrode, resulting in the current peaks at low cell voltages. Regarding the KBr cell, there was absence of the current peaks because E_{0V} was separated far away from the potential range where the Br^- to Br_2 + Br^-_3 conversion would occur.

The above findings, analyses and discussions demonstrate that the occurrence of low voltage peaks in KI is largely due to the negatrode working at potentials near the redox potential for the I^- to I_2 + I_3^- conversion, instead of being indicative of the extent of adsorption of the generated redox species. For instance, it was demonstrated that the products of I^- oxidation could strongly adsorb on or interact with an AC positrode [196]. It was also shown that iodides could adsorb on the carbon electrode more readily than bromides [141]. Further, a recent report on cells with functionalised carbon nanotubes in an aqueous electrolyte comprising of 0.5 mol/L KBr and 1.0 mol/L Na_2SO_4, presented high currents at low cell voltages, despite a cation exchange membrane was used in the cell. However, as shown in Fig. 2.28 (see Ch. 2), which presents this cell from the literature, it could be observed that the cell allowed the negatrode to operate at potentials where the redox activity of halide (bromide) ions could have been invoked [138]. In such a situation, it is

then unclear what the ion-exchange membrane was used for, or why the bromide activity was not fully utilised in this cell. Such adoption of ion exchange membranes, without a critical understanding of the electrode polarisation is essentially one of the main reasons why cells that do not fully utilise the activity of the DRS are constantly been reported. In line with this, the cell reported in Fig. 4.8 is the first conclusive demonstration of an equal electrode mass cell using KBr which exhibits the property of a full utilisation of the DRS.

To gain further understanding on the origin of these low voltage peaks, the performance of a bi-electrolyte cell with different posilyte and negalyte, (−) AC | 2 mol/L KOH || 1 mol/L KI | AC (+), was assembled and analysed. From Fig. 4.10a, it can be observed that despite I^- and I_2 + I_3^- are active at the positrode in this cell, its current increase occurred at higher cell voltages. Also, Fig. 4.10b which shows the *E* vs *U* plot of this cell suggests that the presence of the membrane kinetically adjusted E_{0V} to a range (−0.17 to -0.24 V vs SCE) where I^- and I_2 + I_3^- could not contribute to the charge storage in the negatrode. Such a design can thus be viewed as "forced confinement" of the redox species, as opposed to the one achieved from a thermodynamically driven interaction between the products of the redox reaction and the AC electrode.

Therefore, it is suggested that any procedure that allows E_{0V} to shift away from the potential for the DRS to react at the electrode (in this case the positrode) should help prevent current peaks at low cell voltages. This is particularly important for other DRS such as organic redox molecules, e.g.: quinonoids (see Fig. 2.17) and methyl-violet (see Fig. 2.20), which could result in devices displaying current peaks at low cell voltages. As such, the design of optimal bi-electrolyte cells is another important strategy that can be adopted in the use of DRS in general. In line with this, all the investigations that were carried out to design optimal bi-electrolyte cells in this research were

presented in Ch. 9.

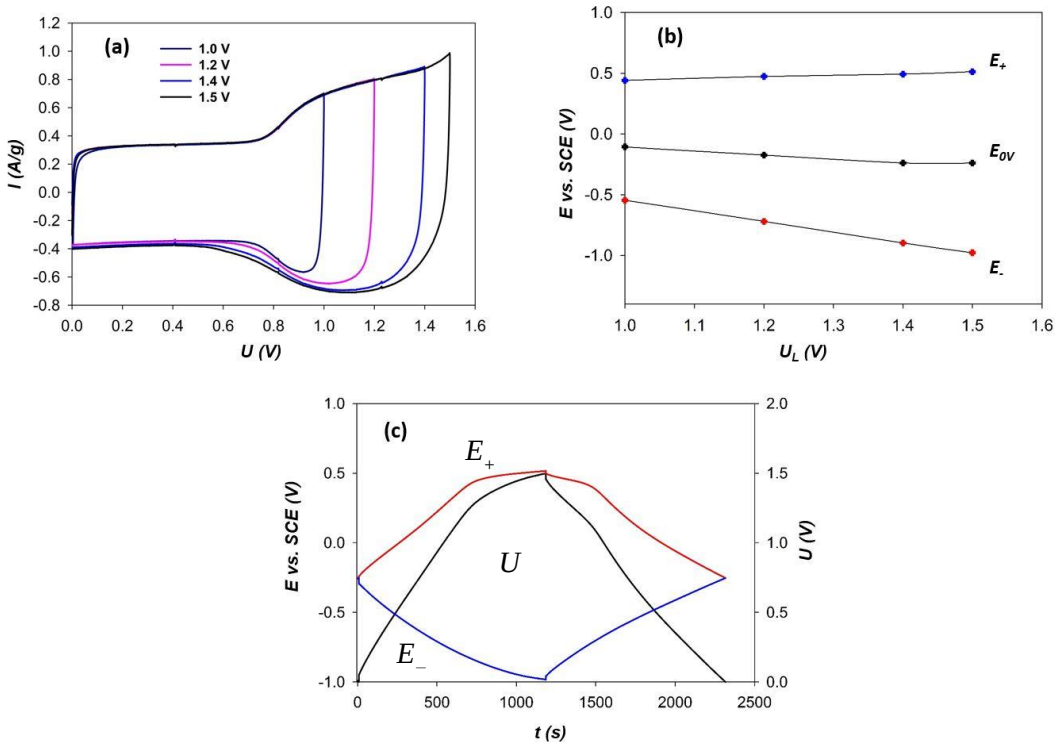

Figure 4.10:Performance of the EEM bi-electrolyte cell, (−) AC | 2.0 mol/L KOH || 1.0 mol/L KI | AC (+): (a) CVs recorded at 5.0 mV/s with different upper limits of cell voltage (U_L), (b) plots of the positrode (E_+), negatrode (E_-) and zero voltage (E_{0V}) potentials vs U_L with data extracted from the GCD plots of U, E_+ and E_-, recorded at I = 0.1 A/g, and (c) GCD plots of U, E_+ and E_-, with U_L = 1.5 V and I = 0.1 A/g.

It is also important to briefly assess the current efficiencies of the bi-electrolyte cell (−) AC | 2.0 mol/L KOH || 1.0 mol/L KI | AC (+) with that of the EEM cell with KBr because both cells display the feature of having the Nernstian contribution at high U_L. Figures 4.11a and 4.11b presents the GCD plots of the EEM bi-electrolyte and 2.0 mol/L KBr cells respectively.

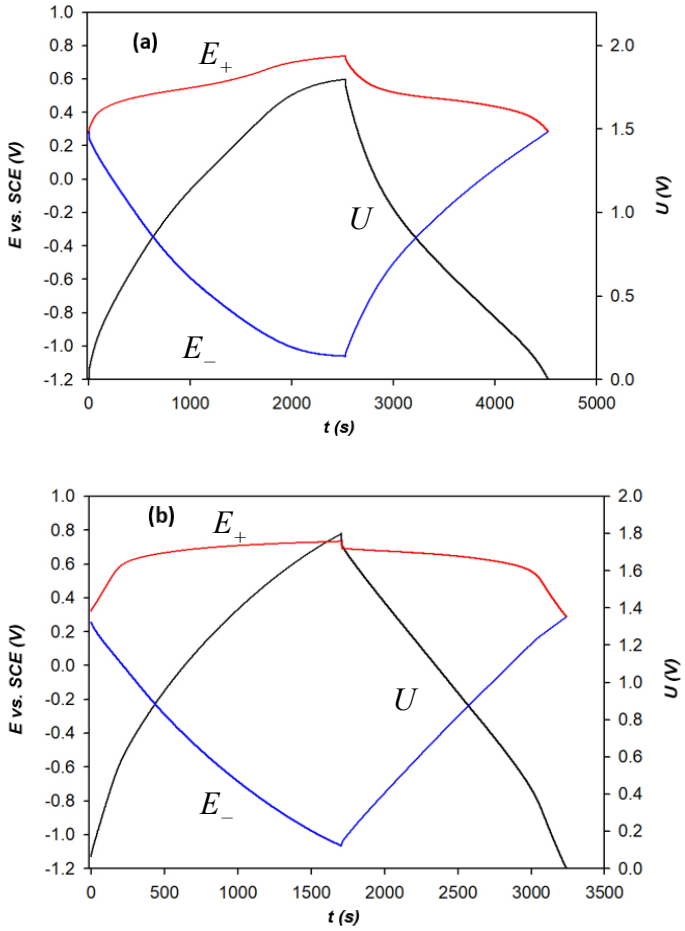

Figure 4.11: GCD plots of U, E_+ and E_-, with U_L = 1.8 V and I = 0.1 A/g for: (a) the EEM bi-electrolyte cell (−) AC | 2.0 mol/L KOH || 1.0 mol/L KI | AC (+) (b) EEM cell (−) AC | 2.0 mol/L KBr | 1.0 mol/L | AC (+).

From these figures, it was observed that the energy and charge efficiencies of both cells reduced from their values at U_L = 1.5 V. For example, the charge efficiency of the bi-electrolyte cell at U_L = 1.5 V reduced from 96.8% (see Fig. 4.10c) to 79.1% (see Fig. 4.11b). Obviously, this significant reduction in charge efficiency can be linked to the generation of more I_2 + I_3^- at higher positive potentials which were not fully recoverable during the succeeding discharging process in the positrode.

Moreover, an interesting feature of this bi-electrolyte cell is that despite the high generation of the iodides, there was still no obvious evidence of shuttling of the I^- / I_2 + I_3^- species, since the E_{0V} is still separated from the

peak value of E_p as has been earlier established.

This essentially is one of the most important feature of the bi-electrolyte cell because the "forced confinement" aids in compartmentalising the reactions at the positrode. With regards to the EEM cell with KBr, its feature at U_L = 1.8 V deviates only slightly from that observed at U_L = 1.5 V (cf. Fig. 4.8c). The charge efficiency at U_L = 1.5 V reduced from 94.2% to 85.3%, at U_L = 1.8 V (Fig. 4.11b). Although this was quite marked, still, it was not as significant as that displayed by the bi-electrolyte cell. Indeed, as was observed from the CV in Fig. 4.4b and was demonstrated in Fig. 4.9c, the thermodynamics of the bromide species at the carbon | KBr interface was such that the cell could be operated up to 2.0 V. These and other related properties of these bi-electrolyte cells were further addressed in Ch. 9.

4.6 Chapter Summary

The shuttling of the products of redox reaction between the positrode and the negatrode in an activated carbon EEM cell with KI as DRS has been conclusively confirmed. Accordingly, the detailed role of the redox reaction thermodynamics and its effects on the features and charge efficiencies of supercapatteries with KI and KBr as redox electrolytes were critically described.

The role of the electrode polarisation in conjunction with the thermodynamics of the redox reaction was studied, in line with this a simple empirical relationship for predicting the onset of the Nernstian contribution to the supercapattery with KBr as electrolyte has been proposed. Accordingly, this detailed fundamental characterisation of the AC electrodes in either KI or KBr could serve as a significant reference for the practical use of these halides as DRS. More so, this is the first rigorous assessment of the role of the combined EDL and Nernstian mechanisms in bromides as practical energy enhancing DRS for applications with AC electrodes.

Additionally, the bi-electrolyte cell was used to explain the difference between "thermodynamic confinement" and "forced confinement" of supercapatteries with redox electrolytes. Accordingly it was used to demonstrate the procedure of shifting the peak electrode potential of the redox interface away from the potential of zero voltage (E_{0V}). As was demonstrated for the case of the bi-electrolyte with KI as posilyte, forced confinement enabled this supercapattery to store the Nernstian contributed charge at higher U_L.

CHAPTER 5: CAPACITANCE UNEQUALISATION AND THE PERFORMANCE OF SUPERCAPATTERIES WITH REDOX ELECTROLYTES

5.1 Introduction

In Ch. 4, the concept of inherent capacitance unequalisation was used to explain the conjoined effects of the polarisation of the AC electrodes and thermodynamics of the DRS, as exemplified by an EEM supercapattery with KBr as DRS.

In this chapter, the electrode polarisation and its effect on the optimal utilisation of the charge generated from the redox process would be analysed. This was done by assessing the charge and energy efficiencies, together with the specific energy of cells with unequal mass of electrodes.

5.2 Capacitance unequalisation of EDL electrodes

Figure 5.1 presents both experimental and schematic representations of the polarisation of EDL electrodes. Generally, from the capacitor equation, it is known that the higher the capacitance of the electrode, the lower its relative polarisation (Eq. 4.1). The electrode polarisation of AC-1 in 1.0 mol/L KBr has been used to describe this concept in Ch.4, and this is reproduced in Fig. 5.1a. From Fig. 5.1(a1), it was noticed that the AC electrode is inherently asymmetric, and this has been used to elucidate the features of the cell using KBr, for example, deriving the voltage U_{redox} at which the redox reaction of KBr would commence in a cell.

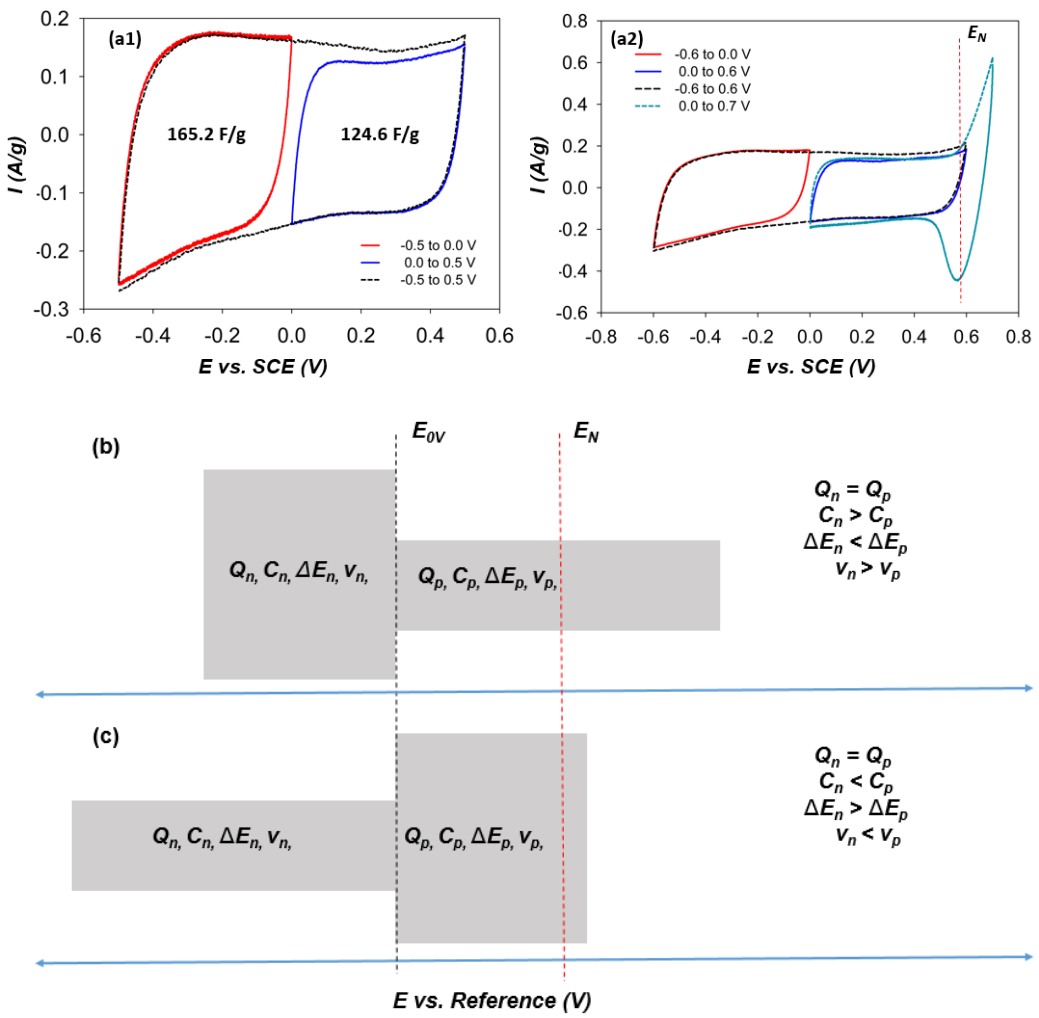

Figure 5.1: Electrode capacitance unequalisation and the relative polarisation of electrodes. CVs of AC-1 electrode in 1.0 mol/L KBr (a1) showing the asymmetry of the capacitance (a2) showing the onset of the oxidation of Br^-. Schematic illustration of the polarisation of electrodes with (b) $m_- > m_+$ (c) $m_- < m_+$.

Note that *Q, C,* and *ΔE* are the charge, capacitance, and electrode potential respectively, with the subscripts n and p denoting the positrode and negatrode respectively. E_N is the redox potential of the DRS, and E_{0V} is the potential of zero voltage (PZV). Note that the position of the PZV as located in Fig. 5.1 (b and c) is arbitrary. All these parameters have been described in Ch.4. Herein, v_n and v_p refers to the rate of change of the polarisation of the positrode and negatrode respectively.

Fundamentally for a carbon electrode, $C \propto A$ (specific surface area). Accordingly, the areal capacitance (with respect to the internal SSA of the carbon) of two identical electrodes made from the same carbon material, can be varied by increasing the mass of one electrode relative to the other. Thus, assuming that the configuration is as given in Fig. 5.1b, with a larger negatrode capacitance the positrode can be effectively polarised to attain E_N which is the onset of the redox reaction of the DRS. Conversely, in the case of a larger positrode capacitance, the polarisation of the positrode would be stunted, resulting in a reduced utilisation of the charge from the DRS.

Understanding this relative polarisation of the carbon electrodes used with DRS is important because of the following reasons:

1. Depending on the electrolyte used, the electrode capacitances of the positrode and negatrode could be unequal (e.g. the case of AC-1 in KBr demonstrated in Ch.4, and reproduced in Fig. 5.1(a1)). This inherent unequal electrode capacitances have been generally described to be due to the relative difference in properties such as the mobility, solvation/de-solvation mechanism of the ions, steric hindrances within the carbon matrix, etc. [17]. In certain situations, for example: activated carbon in some protic ionic liquids with N-chloroalkyl functionalized cations with the $[TFSI]^-$ anion, the equipotential electrode capacitance of the positrode may be greater than that of the negatrode, or the difference between their capacitances may not be too different [197]. Accordingly, in such a situation, except the electrodes are properly matched through a rigorous understanding of the capacitance unequalisation, the DRS would not be effectively utilised.
2. As was stated in Ch. 4, it is usually desirable for the redox potential of the DRS to be as close as possible to the stability limit of the supporting electrolyte. Accordingly, if the relative polarisations of

the electrodes are not clearly understood, some otherwise useful DRS, but with extreme positive/negative potentials might also not be effectively used, or might be considered unsuitable. In fact such claims of unsuitability have been made for the use of bromides in EEM cells [137, 195, 198] because of a poor understanding of the role of the electrode polarisation in the utilisation of the DRS.

Thus, in this chapter, capacitance unequalisation, and effective utilisation of the DRS for Nernstian storage would be assessed from a device engineering perspective.

5.2.1 Relative polarisations of electrodes and the optimal utilisation of DRS for Nernstian storage

In this section, the properties of UEM cells each containing the same volume of 1.0 mol/L KBr electrolyte, with negatrode to positrode AC-1 mass ratios of (3:4) and (4:3), (1:2) and (2:1), (1:2.7) and (2.7:1), would be appraised.

Table. 5.1 shows the electrode mass of a representative series of cells used for the analysis carried out in this chapter.

Onwards, these cells would be referred to by the mass ratio of the negatrode to positrode. As shown in Figs 5.2 (a, b and c), it was observed that cells with higher negatrode to positrode mass ratios offered smaller capacitive currents at lower cell voltages, but larger faradaic currents at higher cell voltages, which means more effective utilisation of the additional charge from the DRS reactions. The reverse was the case for cells with $m_+ > m_-$. That is high EDL at low voltages and little Nernstian contribution at high voltages. Generally, the Nernstian charge stored at higher U for the cells $m_- > m_+$, was in the order (2.7:1) > (2:1) > (4:3).

Table 5.1: Representative mass of AC-1 electrode active materials used in the fabrication of cells described in this chapter.

$m_- : m_+$	m_- (mg)	m_+ (mg)	m_t (mg)
1:1	15.05	15.03	**30.08**
4:3	20.13	15.07	**35.20**
2:1	30.15	15.05	**45.20**
2.7:1	40.55	15.05	**55.60**
3:1	44.97	15.07	**60.04**
4:1	60.21	15.07	**75.28**

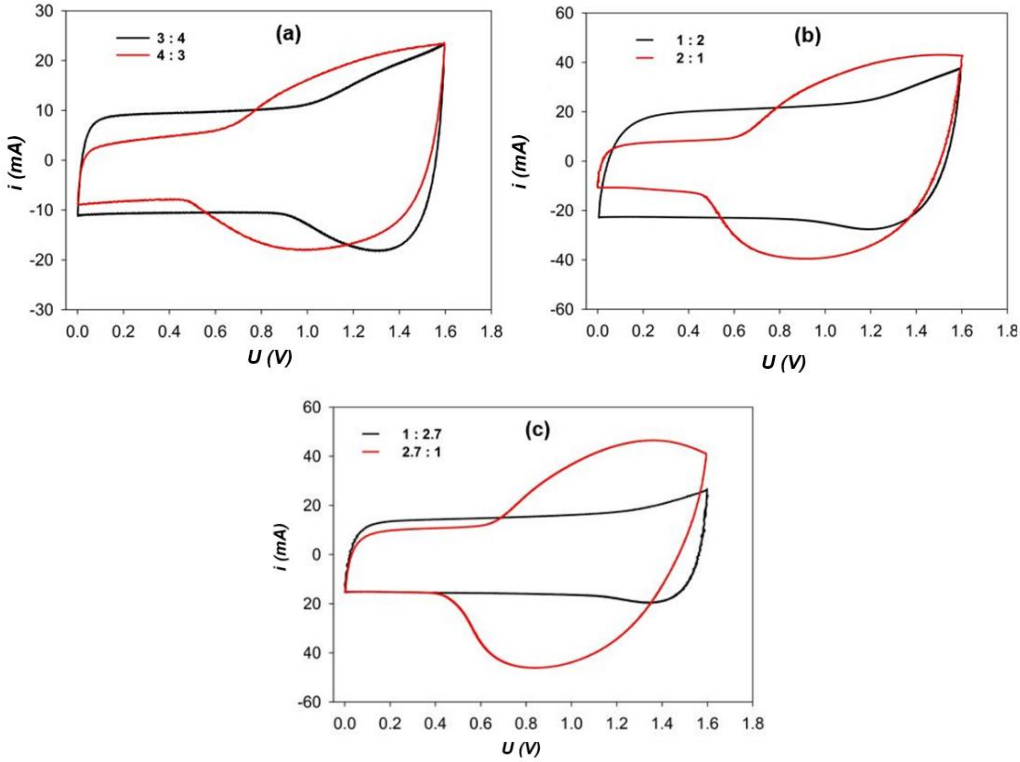

Figure 5.2: UEM cells with different negatrode to positrode mass ratios (note that the total electrode mass on each category of cells are equal), (**a**) (3:4) and (4:3), (**b**) (1:2) and (2:1), and (**c**) (1:2.7) and (2.7:1). Overlay of (4:3), (2:1), and (2.7:1). Scan rate: 10 mV/s.

This observation is expected because, according to Eq. (4.1), and the schematic illustration in Fig. 5.1 (b and c), higher positrode capacitance would

result in lesser polarisation, which consequently limits the utilisation of the DRS for charge storage. Figure 5.4 shows the CVs at different U_L for the cells. It was observed that the cells with $m_- > m_+$ generally showed relative stability up to U_L = 2.0 V. Moreover, the increase in the Nernstian contribution to the charge storage only increased very slightly with increase in U_L, making the capacitive contributions to these cells more marked.

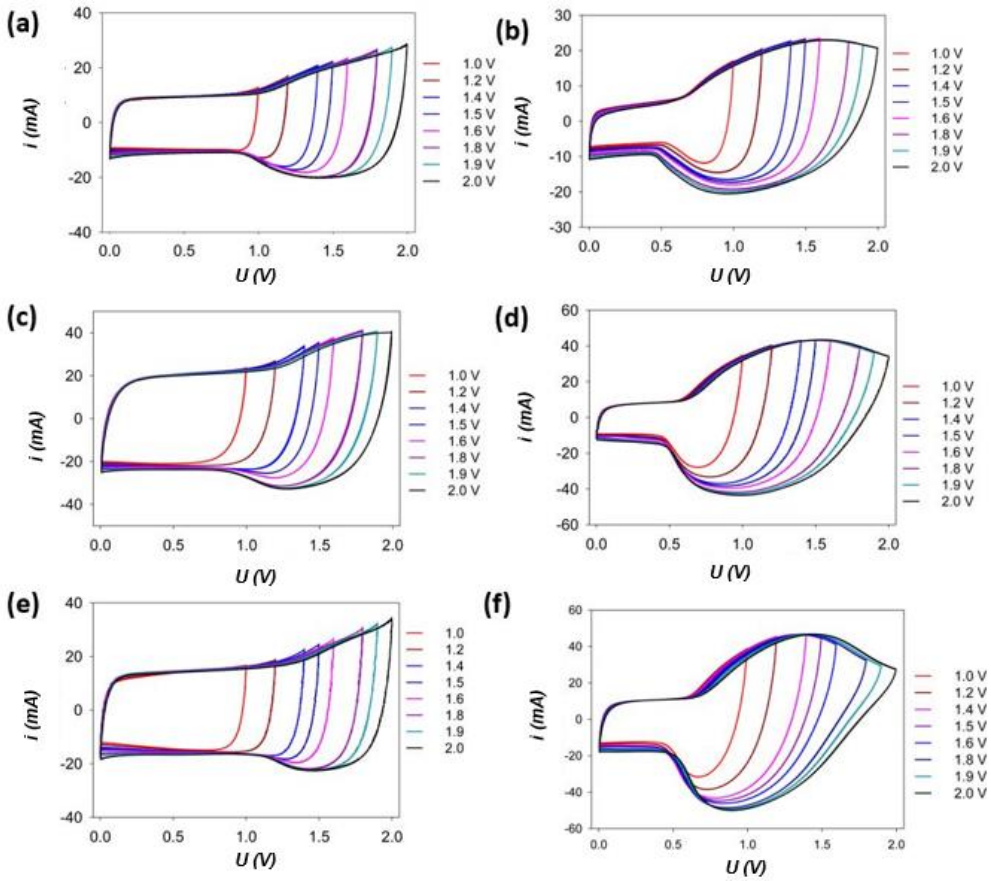

Figure 5.3: CVs at different values of U_L for the UEM cells: (a) (3:4) and (b) (4:3), (c) (1:2) and (d) (2:1), (e) (1:2.7) and (f) (2.7:1). Scan rate: 10 mV/s.

Contrastingly, the cells with $m_- > m_+$ showed marked contributions from the Nernstian storage as U_L is increased. Moreover, the most important features for the cells with $m_- > m_+$ which optimally utilises the contribution from the DRS, were the apparent charge efficiencies displayed by these cells. For example, at U_L = 2.0 for the cell (2.7:1) (see Fig. 5.5f) a sharp tip at the

reverse scan can be noticed.

This is due to the relatively slow discharge/charge of the generated Br^- / (Br_2 + Br_3^-), which are still on the surface of the positrode. This high increase in the generation of redox reaction products, contributed to the enhanced charge capacity, but also affects the displayed charge and energy efficiencies. In line with this, the charge and energy efficiencies of the cells with higher mass of negatrode (m_-) were appraised.

5.2.2 Charge and energy efficiencies of UEM cells with $m_- > m_+$ and the effective utilisation of bromide as DRS

Herein, the mass of the negatrode were further increased. Accordingly, the cells analysed were: (1:1), (4:3), (2:1), (2.7:1), (3:1), and (4:1). Fig. 5.3 presents the GCD curves of the cells. It was observed that the trend in the energy increase (or optimal utilisation of the DRS) for the UEM cells: (2.7:1) > (2:1) > (4:3) which were briefly described with the CVs in Fig. 5.3, was not observed in the cells: (2.7:1), (3:1) and (4:1). Generally, although the cell with mass ratio of (3:1) delivers the highest discharge energy, still its energy efficiency is lower than that of (2.7:1) and (4:1). Table 5.2 shows the performance metrics for the cells presented in Fig. 5.4.

These observations can be explained from the standpoint of the current applied to the electrodes, and the corresponding balancing of the charge by the electrodes. Since the current load applied to the cells was normalised by the total mass of the electrode in each cell as shown in Table 5.2, the current applied to the positrode is different in all cases (red entries in Table 5.2). Accordingly, this would mean that the rate of the electro-conversion between Br^- / Br_2 + Br_3^- would be different in each cell.

In line with this, the rate of recovery of the product of the redox reaction would determine the charge efficiency, whereas the energy efficiency would be mainly defined by the capacity/capacitance balance between the

electrodes. In general, what the data of Table 5.2 shows is that it is important to always take into consideration all the performance metrics, as opposed to simply over-sizing the counter-capacitive electrode arbitrarily.

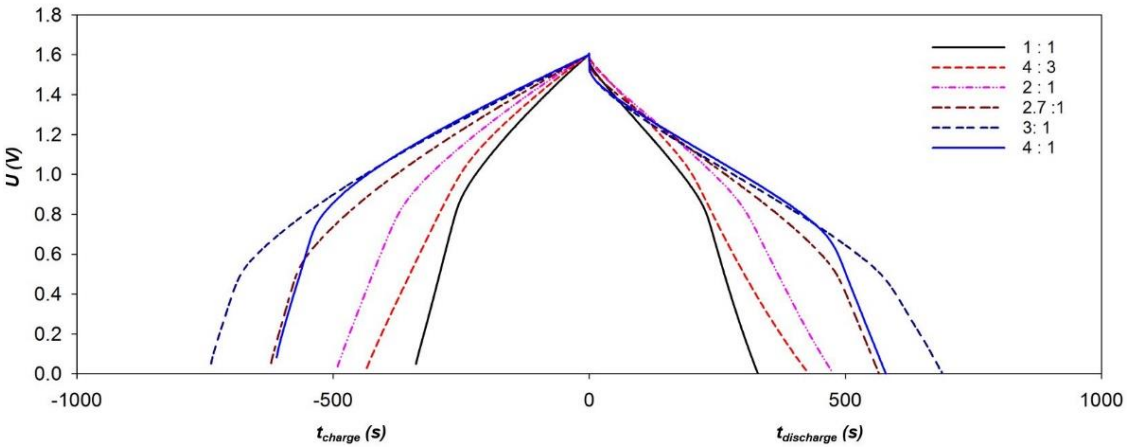

Figure 5.4: GCD plots comparing the EEM cell (1:1) with other UEM cells with the indicated negatrode to positrode mass ratios. Current load: 0.25 A/g (normalised to the total dry mass of active materials on both the positrode and negatrode).

Note that all cells in Fig. 5.4 had an approximately equal volume of 1.0 mol/L KBr electrolyte.

Table 5.2: Cell parameters: η_Q (charge efficiency), η_W (energy efficiency), W_d (specific discharge energy).

$m_- : m_+$	m_t (mg)	η_Q (%)	η_W (%)	W_d (Wh/kg)	$\pm i$ (mA)	$\pm I = \pm i/m_t$ (A/g)
1:1	30.08	97.3	86.0	17.3	7.5	0.25
4:3	35.20	98.6	84.4	20.3	8.8	0.25
2:1	45.20	96.9	83.7	24.1	11.3	0.25
2.7:1	55.60	91.3	78.7	29.0	13.9	0.25
3:1	60.04	93.4	76.6	33.2	15.0	0.25
4:1	75.28	95.1	79.3	30.6	18.8	0.25

Figure 5.5, shows the cycling of the electrode after 1000 cycles each at 50 mV/s between the potential range: 0 to 0.9 V vs SCE. As seen from the CV, there is a gradual decrease in the capacity of the electrode on cycling. This is generally indicative of two general features of cells utilising these DRS. Firstly, the higher the current on the positrode, the higher the degradation of the positrode, secondly successive cycling could also lead to increased oxidation/passivation of the carbon electrode which consequently reduces the general performance.

Figure 5.6 presents SEM images of the fresh carbon, and the carbon that has been cycled from 0 to 0.9 V vs SCE, based on conventional post-mortem analysis of the morphology of cycled carbon electrodes. As seen in Fig. 5.6b, the scales (highlighted by the tip of the arrows) which corresponds to ion adsorption on the carbon shows that Nernstian storage of bromides at the E|E interface with the carbon occur within the nanostructure of the material. This also confirms that the continuous charge/discharge cycles could lead to electrode surface passivation which results to the formation of poorly-conductive surface layers that reduces performance. Thusly, both the duration of cycling and current rate applied would all affect the reduction in performance.

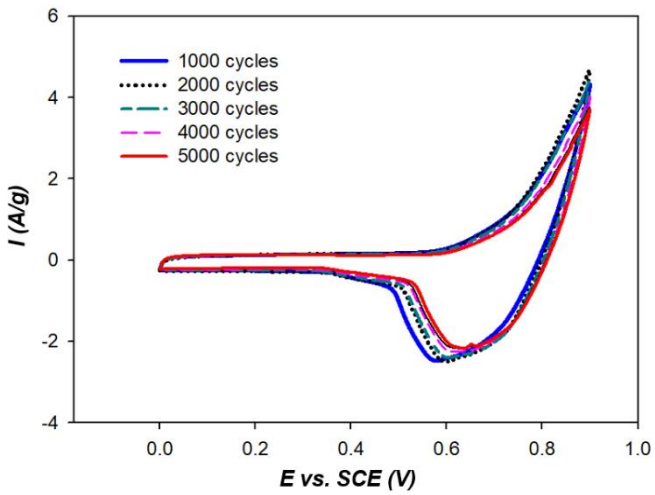

Figure 5.5: CVs at 1.0 mV/s from 0 to 0.9 V vs SCE, for AC-1 electrode after 1,000 successive cycles at 50 mV/s.

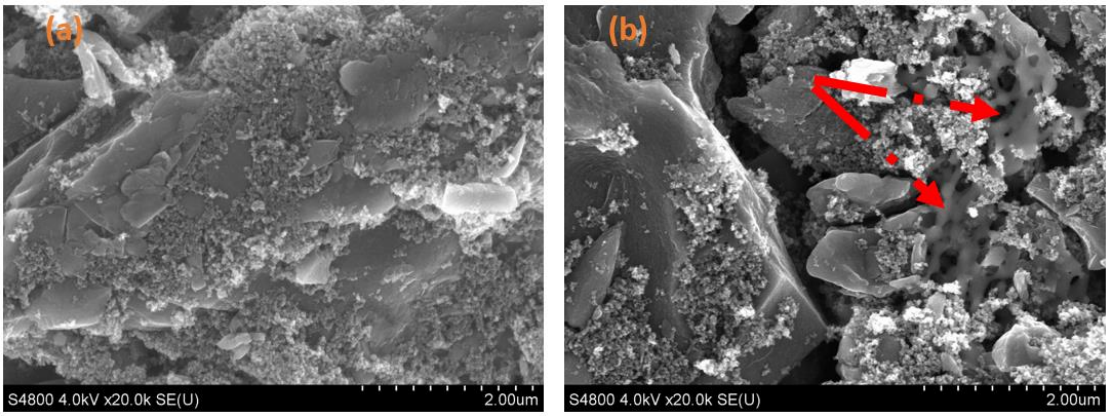

Figure 5.6: SEM micrographs of AC-1 (a) fresh electrode (b) electrode after 5000 cycles from 0 – 0.9 V vs SCE at 50 mV/s.

5.3 Assessing the power performance of UEM cells with DRS

From Table 5.2, it was shown that the cell (3:1) displayed a higher specific energy (W_d) than (4:1). Hence, from a cost standpoint, the cell (3:1) gives a better cost/KWh and cost/weight than (4:1). This finding is very important because in practice, the mass of the electrodes account for about 1/4th the total mass of a packaged cell [178, 199]. In line with this, the general performance of the cell (3:1) is further analysed. Figure 5.7a shows the GCD plots for the cell (3:1) at different current loads, whilst Fig. 5.7b presents the Ragone (energy vs power) plot for the cell.

In general it was observed that at a current load of 0.1 A/g the cell displayed a specific energy and power of 36.78 Wh/kg and 90 W/kg respectively. However, on the other extreme a specific energy and power of 21.31 Wh/kg and 703.82 W/kg was recorded at a current load of 1.0 A/g. It should be pointed out that the applied current corresponding to the current load were labelled on the Ragone plot as shown in Fig. 5.7b. This performance displayed by the UEM cell with bromide as DRS is thus satisfactory. Generally, it has been described that electrodes such as the ones used herein, i.e. areal density greater than 11.3 mg/cm^2, reflect adequately the role in which

tortuosity, interfacial resistance etc. would play in supercapacitors with DRS [179].

This is an important point to note, because it has been shown that thin carbon electrode materials usually equal to or below 100 μm, displays superficially high power performance that are not reflective of practical supercapacitors/supercapatteries.

This is because the average thickness of electrodes used for commercial high energy supercapacitor applications ranges from 200 μm to few hundreds of microns [178]. In line with this, the demonstrated property of this UEM cell, could serve as important benchmark for the potential scale-up of supercapacitors with activated carbon electrodes using KBr as electrolyte.

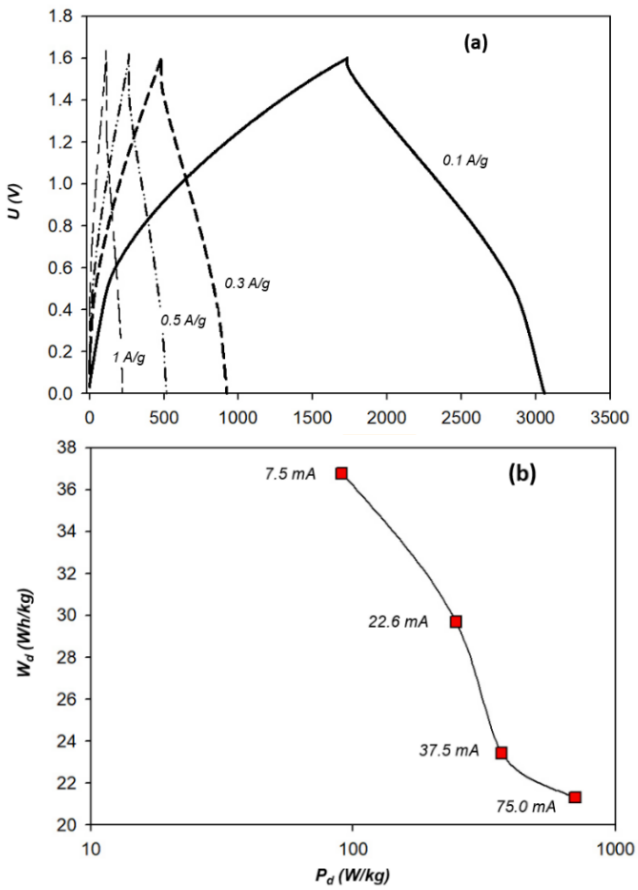

Figure 5.7: GCD plot for the UEM cell with (3:1) negatrode to positrode mass ratio at different current load (b) Ragone plot calculated from (a), labelled with the applied current corresponding to the current load.

In Ch. 4, it was shown that the capacitance unequalisation formula can be used to predict the cell voltage U_{redox} at which the Nernstian contribution from the DRS would be observed. It is important to point out the importance of understanding the cell voltage at which the Nernstian contribution occurs.

1. Knowing the U_{redox} would allow for the utilisation of the DRS to be clearly understood, for example, when the U_{redox} is too high, this might imply that the DRS would be utilised only minimally, as was observed for the cells with $m_+ > m_-$.
2. It should be pointed out that U_{redox} for these DRS with KBr is fundamentally different from $U_{discharge}$ of batteries. Note that $U_{discharge}$ can be thermodynamically linked to $E_p^o - E_n^o$, where E_p^o and E_n^o are the redox potential of the electrode reaction at the positrode and negatrode of the battery respectively. Moreover, these parameters can both be used to describe the energy features of either the supercapattery or battery. Of fundamental importance is the understanding that whilst for the battery $U_{discharge}$ is essentially thermodynamic, U_{redox} for the supercapattery couples both thermodynamic and polarisation properties. This is the basis for the device engineering strategies that can thus be adopted to improve the performance of supercapatteries in general.

Figure 5.8 shows the polarisation of the positrode and negatrode in the (3:1) cell, at different applied current loads, with U_L = 1.6V. It was observed that the positrode was polarised towards more positive values as the applied current is increased. This indeed can be linked to an increase in charge accumulation which is affected by the polarisation resistance of the AC | Br^- interface. Specifically, this determines the charge efficiency of the device. Also, although at higher current loads, the rate of generation of the Br^- / (Br_2 + Br_3^-) is high, still the capacity is expectedly reduced because the charge has a slower rest time at the interface. Furthermore, the overall energy efficiency of this

device, as shown from the GCD plot is determined by the extent of the charge balancing by the counter-capacitive negatrode.

Also, at similar current loads (e.g. 0.1 A/g), the peak positrode potential of the cell (3:1) been 0.78 V compared to 0.72 V for (1:1) (shown in Fig. 4.8c) is due to the increase in the polarisation obtained from these UEM cells with larger negatrode mass, resulting in enhanced capacity which is translated to improved specific energy.

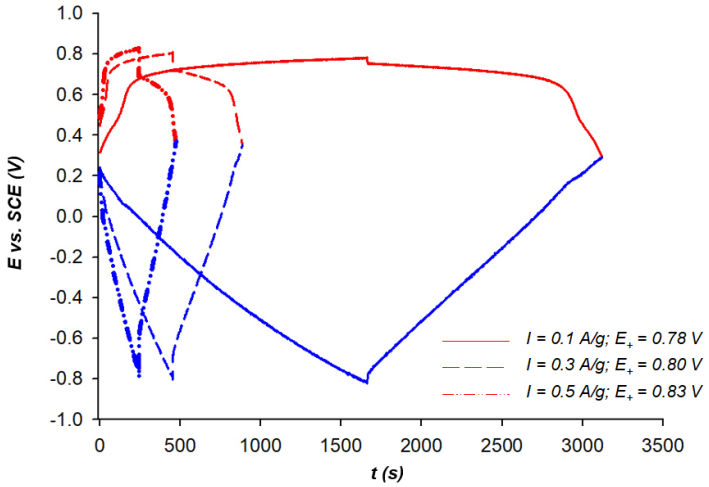

Figure 5.8: GCD plot for the electrodes of the UEM cell with (3:1) negatrode to positrode mass ratio at different current load.

Figure 5.9a shows the CVs of the cell (3:1) at U_L = 1.0 and 1.6 V. It was observed that even at U_L = 1.0 V, there was marked utilisation of the redox species for the cell (3:1) (i.e. low U_{redox} corresponding to increased DRS utilisation). Figure 5.9b shows the CVs of the AC electrode in 1.0 mol/L KBr scanned within the approximate potentials of the positrode and negatrode as displayed in Fig. 5.8.

These variations in the electrode polarisation coupled with a change in capacity per unit electrode potential increase, is thus the fundamental basis to understanding the performance of AC electrodes using DRS. Moreover, understanding these features would also prove important in the improvement

of the volumetric capacity (for example electrode thickness modification [178]) when these EDL electrodes are used with this DRS.

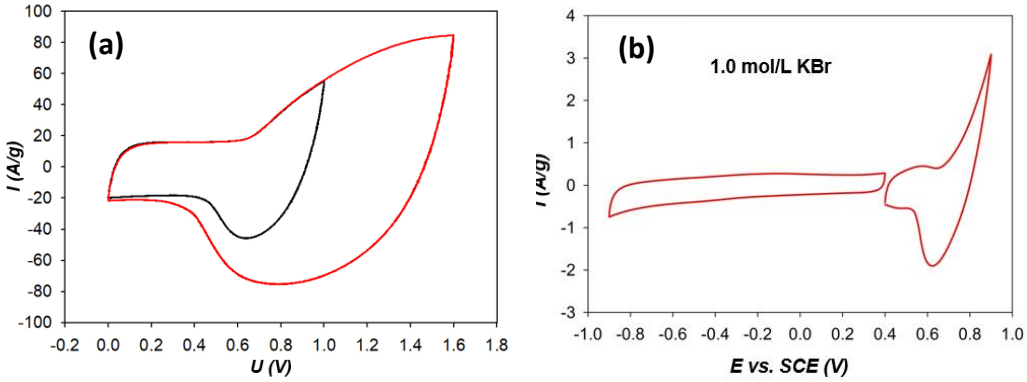

Figure 5.9: (a) CV for the (3:1) UEM cell with 1.0 mol/L KBr, U_L = 1.6 V, scan rate: 5 mV/s (b) AC-1 electrode in 1.0 mol/L KBr scanned at the approximate electrode potential range of the positrode and negatrode at U_L = 1.6V, scan rate: 1 mV/s.

5.4 Chapter Summary

Capacitance unequalisation have been used to increase the energy capacity of UEM cells using 1.0 mol/L KBr as DRS.

Increase in negatrode mass resulted to an increase in specific energy in the order (2.7:1) > (2:1) > (4:3), moreover charge and energy efficiencies reduced. Contrastingly the specific energy displayed by the cell (3:1) is higher than that of (4:1) but with a reduced charge efficiency. The polarisation of the positrode relative to the negatrode when the applied current (under galvanostatic conditions) is increased, has been linked to the power performance of the UEM cell, with the cell still been able to provide an energy of 21.31 Wh/kg with a power of 703.82 W/kg at a current load of 1 A/g (corresponding to an applied current of 76.00 mA).

CHAPTER 6: CARBON ELECTRODE PROPERTIES AND ENERGY CAPACITY OF SUPERCAPATTERIES CONTAINING REDOX ELECTROLYTES

6.1 Introduction

Since ions undergo charging within the porous matrix of carbons used for EDL capacitors, a detailed appraisal of the porosity of the carbons is of utmost importance. In addition to the porosity, the surface physico-chemistry of the carbons also determines the interaction of ions at the electrode | electrolyte (E|E) interface.

Generally, it has been described that for inert electrolytes, the porous volume of the electrode acts as a "dead-volume". This is because, ions are simply withdrawn from the liquid phase, towards the Helmholtz layer. Conversely, with redox electrolytes, this "dead volume", if provided by pores of sizes that can entrap the electro-generated ions, can act as a "functional-volume" [178]. This is because in addition to ions been withdrawn towards the Helmholtz layer for EDL charging, the electrolyte volume itself acts as a source of active species when the redox reaction takes place [15, 178]. This reasoning accentuates the importance of gaining understanding of the role of the electrode's porosity and how it affects charge storage with DRS.

Accordingly, the focus of this chapter is to investigate the performance of devices with redox electrolytes which were fabricated with two different types of carbon electrodes. This was done mainly through understanding the device performance through a correlation between the porous and surface physicochemical characteristics of the electrodes with properties of the redox electrolytes such as the concentration of the active ions, and hydrous sizes of the dissolved ions.

In Ch. 2 (Literature Review) it has been established that there are a large collection of water soluble redox electrolytes. Moreover, as has been

demonstrated in Ch. 4 and 5, bromides generally store their charge at high cell voltages. Accordingly, they were selected as representative dissolved redox species (DRS) in this chapter.

6.2 Overview of carbon electrode material properties and the basis for investigations with redox electrolytes

In Ch. 4, the N_2 physisorption and thermogravimetric properties of the three different carbon electrodes used in this research were described in detail. In this section the properties of these three carbons would be briefly revisited. Table 6.1 is a reproduction of the elemental analysis of these carbons, whilst Fig. 6.1 presents the CVs of these electrodes in inert KCl electrolyte (this had been earlier described in Ch. 4). Herein, two important properties were extracted from Fig. 6.1.

Firstly, the E|E interface of AC-1, with limited surface groups as has been described in Fig. 4.2 and shown in Table 6.1, would be used to describe the property of the polarisations of the alkali metal halides (LiBr, NaBr, and KBr). This would be used to explain the role of the ionisation of these halides with respect to their interaction at the E|E interface of AC-1. In other words, AC-1 is assumed to be a "quintessential" polarisable electrode with negligible contribution from surface groups.

Following this, the closely related EDL properties of AC-2 and GNP in inert KCl electrolyte were further investigated. This was done by critically studying the interaction of DRS from the standpoint of the surface physico-chemistry and physisorption properties of AC-2 and GNP.

Table 6.1: Elemental composition of carbon electrode materials

Carbon	C (%)	O (%)	H (%)	N (%)
AC-1	94.28	4.32	0.52	0.54
AC-2	79.60	18.51	1.52	0.28
GNP	82.75	15.27	1.30	0.65

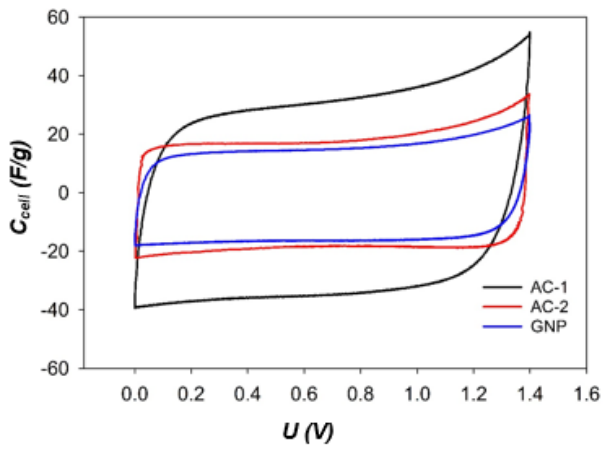

Figure 6.1: CVs of EEM cells fabricated with the three different carbon electrodes using 2.0 mol/L KCl, scan rate: 5 mV/s.

6.3 Electroanalysis of activated carbon electrode with negligible surface oxygen groups (AC-1) in alkali bromides

Figure 6.2 shows the CV of carbon electrode (AC-1) in 1.0 mol/L solutions of LiBr, NaBr and KBr, within the potential range from -1.0 V to 0.9 V vs SCE. As has been described already, electrode polarisation below 0 V vs SCE for iodides and bromides in aqueous solutions displays EDL capacitance. Moreover, in the case of AC-1 with limited surface oxygen groups (SOGs), it could be assumed that the ensuing redox reactions, is due solely to the polarisation at the interface, and the adsorption of the products of the redox reactions (Br_2 + Br_3^-) into its porous matrix.

Referring to Fig. 6.2, from the rectangular shape of the CVs from 0.0 to -1.0 V vs SCE the measured electrode specific capacitance (C_{sp}) within this potential range for the carbon (AC-1) were 204.81, 215.70, and 228.14 F/g (or C/g) for LiBr, NaBr and KBr respectively. (Note that this capacitance value could be equivalently expressed in [C/g] since $C_{sp} = \Delta Q/\Delta E$ and from Fig. 6.2, ΔE = 1.0 V). This trend have been generally ascribed to the inverse correlation between interfacial capacitance (ΔC_M^+) and hydrous cation size (r_M^+) i.e. interfacial capacitance increases ($\Delta C_K^+ > \Delta C_{Na}^+ > \Delta C_{Li}^+$) as the hydrous cation size decreases (r_K^+ (0.331 nm) < r_{Na}^+ (0.358 nm) < r_{Li}^+ (0.382 nm). The average ion

sizes for the components of some electrolytes used in this research are presented in Fig. 6.3.

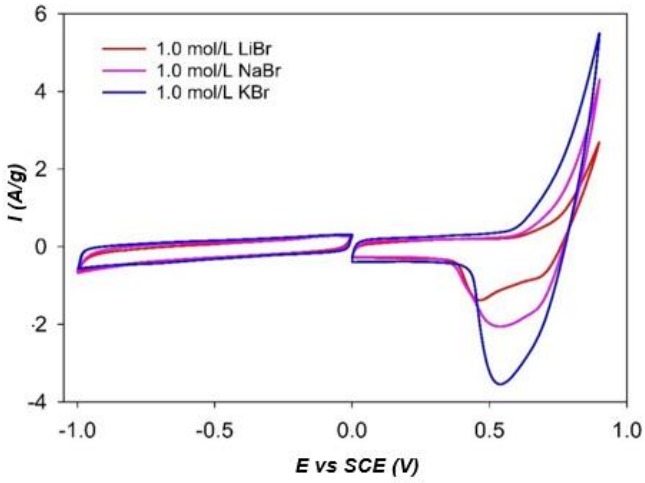

Figure 6.2: CVs of carbon electrode (AC-1) in 1.0 mol/L solutions of LiBr, NaBr and KBr. Scan rate: 1.0 mV/s.

The differences in the redox mechanism of bromides and iodides have been described in Ch. 4. Generally, on polarising the interface towards more positive potentials, the observed Faradaic reactions can be attributed to the Br^- redox reactions. Also, the interfacial charge capacity due to the oxidation of the Br^- still follows similar relationships as the EDL capacitance ($Q_K^+ > Q_{Na}^+ > Q_{Li}^+$), i.e. 668.51 C/g, 409.70 C/g, 265.35 C/g, for KBr, NaBr and LiBr respectively. Since the ionic strength of the salts considered are the same, the difference in interfacial capacity between the bromides can be linked to the effects of the ionic potential [97, 200]. That is the charge capacity would be inversely proportional to the ionic attraction of the cations to the bromides. Accordingly, higher ionic potential would correspond to a reduction in the electrostatic interaction, or any other mechanism of adsorption between the bromides and the positively polarised electrode surface [15, 97, 201].

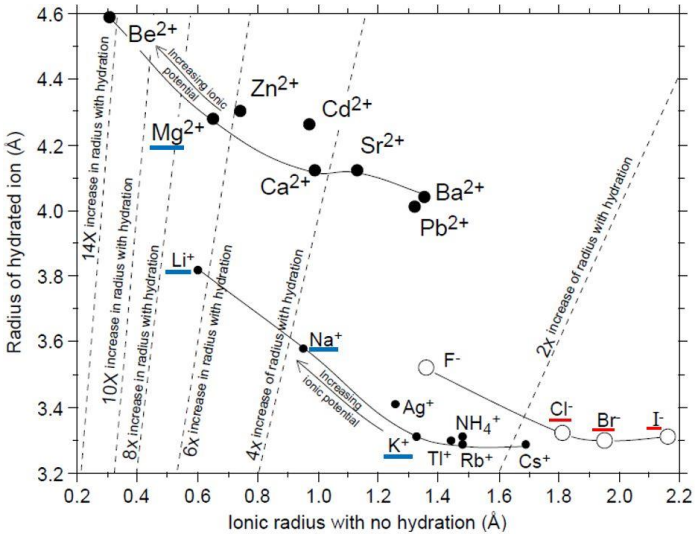

Figure 6.3: Size of the crystal and hydrated radii of some common ions. Cations and anions of some salts used in this work are underlined in blue and red respectively. Adapted from: [202].

Thus, since the attraction between Li^+ and Br^- is larger than that between the K^+ and Br^-, the interaction with the electrode surface from the bromides of the latter ion (i.e. K^+) would be stronger than that obtainable from the Li^+. This relationship between the displayed capacities of different alkali bromides at the E|E interface would be revisited. This is because it is important to the understanding of the dynamics of charge/discharge of different alkali bromides within the porous structures of the carbons.

6.4 Physicochemical properties of micoroporous (AC-2) and mesoporous (GNP) carbons with similar EDL capacitances

From the physisorption analysis described in Ch.4, AC-2 has: BET-SSA = 1487.18 m^2/g, average pore width = 2.23 nm, whilst GNP has BET-SSA = 698.53 m^2/g average pore width = 6.22 nm (refer to Section 4.2.1). From the TGA analysis presented for the carbons (refer to Fig. 4.2), and the elemental analysis briefly summarised in Table 6.1, it was observed that AC-2 and GNP comprises of significant SOGs. In line with this, the surface physico-chemistry and general textural properties of AC-2 and GNP would be further studied, in

order to obtain a basis for understanding the interaction of DRS with these carbons.

Figure 6.4a shows the SEM image of GNP, which appears as a porous agglomerate, moreover, the resolution of the structure with TEM shows the platelet-like microstructure of the crumpled and stacked graphene sheets as shown in Fig. 6.4 (b1 and b2).

The amorphous microstructure of AC-2 is shown by the high resolution SEM image of Fig. 6.5, which is in line with the general features of activated carbons. This displays the fine-grained structure of this carbon electrode material. These micrographs reveal that the two carbons are micro-structurally different. Furthermore, the wettability tests of these carbons (Fig. 6.6), was used to understand the influence of the surface groups of these carbons on their practical use as electrode materials with aqueous electrolytes.

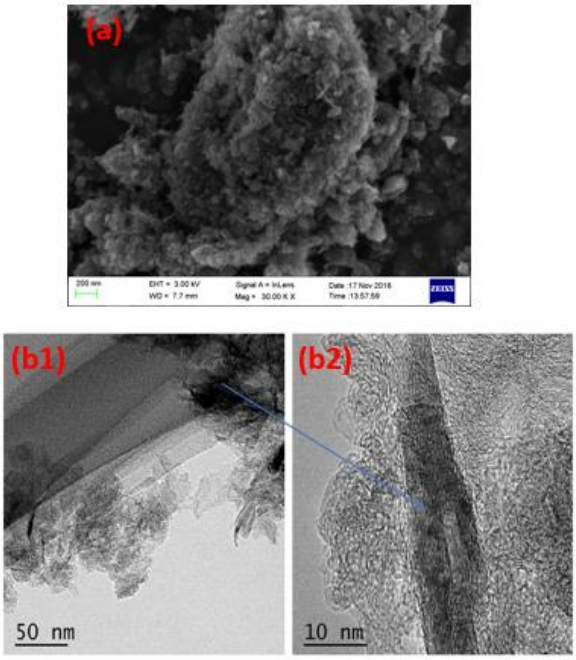

Figure 6.4: SEM image of GNP **(a)** and TEM image of GNP **(b1)** further resolution of b1 **(b2)**

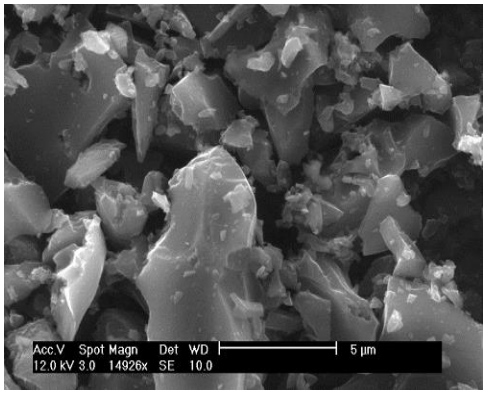

Figure 6.5: High resolution SEM image of AC-2

The wettability tests on AC-2 electrodes show that they are hydrophobic, as exemplified by the meniscus been greater than 90° leading to the formation of a compact liquid droplet of either water or the electrolyte solutions (see Fig. 6.6a). GNP electrode on the other hand, displays high degree of wettability as can be seen from the low contact angle (< 90°), and spreading of both water and electrolyte droplets on its surface. It should also be pointed out that the wettability of both AC-1 and AC-2 are similar.

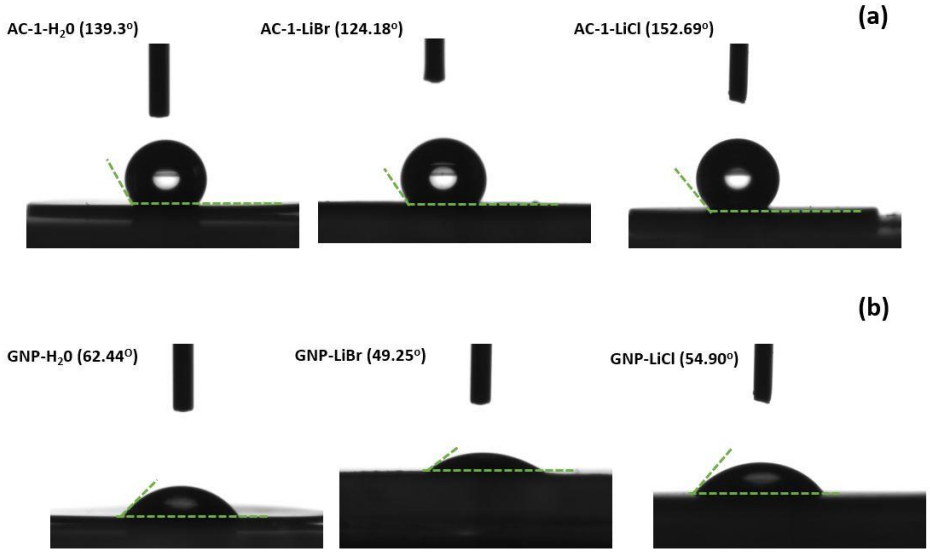

Figure 6.6: Wettability of deionised-water and 2.0 mol/L aqueous solutions of LiBr and LiCl on AC-1 **(a)** and GNP electrodes **(b).**

(Note that in Fig. 6.6, the lines are schematic illustrations, whereas the contact angles presented are the digital read-outs from the device).

When the surface properties are assessed with the aid of the XP spectrograms in Fig. 6.7, it was noticed that although AC-2 comprises of carboxyl groups as is GNP, this might not necessarily help in improving the wettability of the earlier. On the other hand, it has been shown that the carboxyl containing groups in graphene structures, are usually responsible for their improved wettability [203]. Also, the presence of pyridinic nitrogen on graphene-like structures have also been demonstrated to contribute to improved wettability [204].

This means that the hydrophilic properties of the GNP is due to the surface oxygen groups within the graphene sheets of the electrode material, however it is unclear if the limited quantity of nitrogen in GNP aids in the wettability. This is because nitrogen dependent wettability on graphene have only been shown for nitrogen contents greater than at least 2 atomic weight percent, as opposed to less than 0.5% which GNP possesses [204, 205].

From the x-ray photoelectron (XP) spectrographs in Fig. 6.7, it was observed that the C/O ratio for AC-2 is slightly larger than that of GNP. In AC-2, C=O is ca. 62.40% whilst C-O accounts for ca. 37.60%. On the other hand, C=O is ca. 56.28% whilst C-O is ca. 43.72% in GNP. Generally, these surface properties as revealed by the XP spectrographs are consistent with the thermal stability of these carbons as obtained from the thermo-gravimetric analysis in Ch. 4 (see Fig. 4.3).

Furthermore, it was observed that the surface roughness of AC-2 is greater than that of GNP, as shown in Fig. 6.8. Moreover, surface roughness may in certain cases aid in increasing wettability [206, 207], thus it could be concluded that the wettability observed for these carbons can be specifically linked to their surface physico-chemistry, as opposed to the morphology or particulate structure [206, 207]. It is generally well known that the wettability

of the electrodes aids the accessibility of the electrolyte into the porous matrix of the electrodes [31].

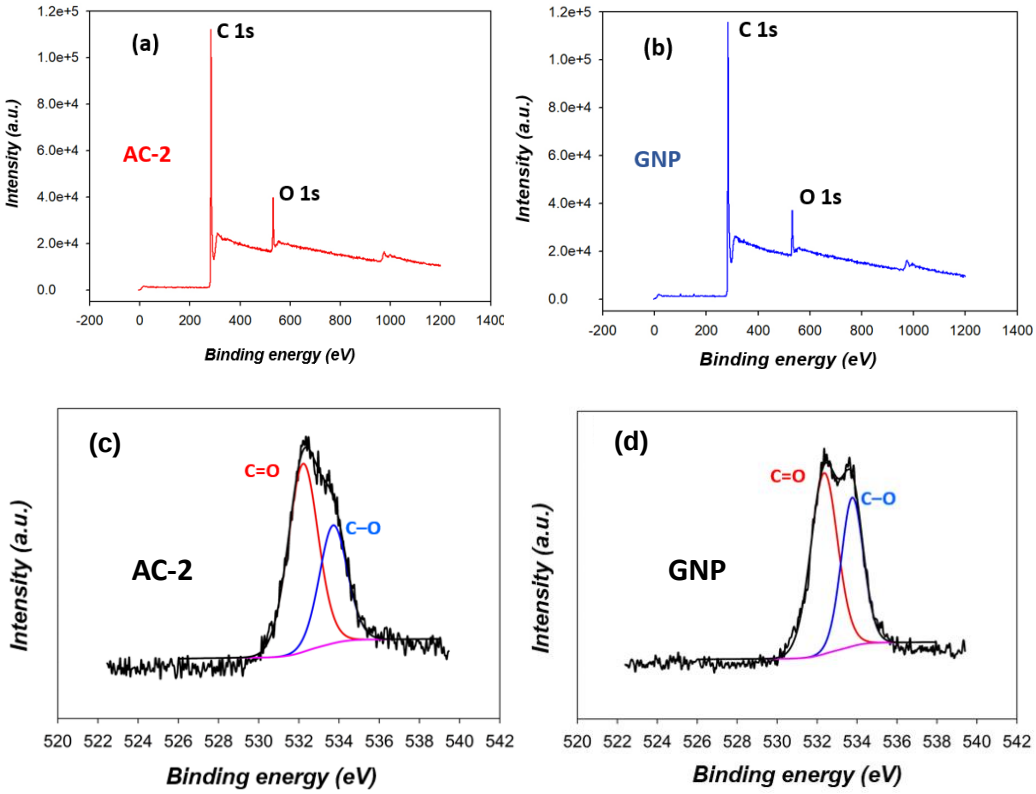

Figure 6.7: X-ray photoelectron spectra for (a) AC-2 (b) GNP; De-convoluted XP spectra for the O 1s core for (c) AC-2 (d) GNP.

Moreover, due to the detailed suction process of electrolyte preparation (as described in Ch. 3: Sections 3.5 and 3.6), it could be assumed that forcing electrolytes into the pores of electrodes, which is a conventional preparation procedure, might reduce the initial disadvantages of the effects of hydrophobicity, although this may not entirely control the disadvantages of in-pore desorption which is significant for hydrophobic materials [31, 205, 208].

Summarily, these two types of carbons with different microstructures i.e. activated carbon (AC-2) and graphene nanoplatelets (GNP) are typical examples of carbon electrode materials with surface oxygen groups (SOGs). In line with this, the interaction of DRS with GNP which is of particular interest in this study would be analysed. Moreover, because AC-2 represents the typical

EDL electrode due to its micoroporous properties, comparisons would always be made between the properties of these two materials in order to gain further insight into the mechanisms of interaction of DRS with different carbons.

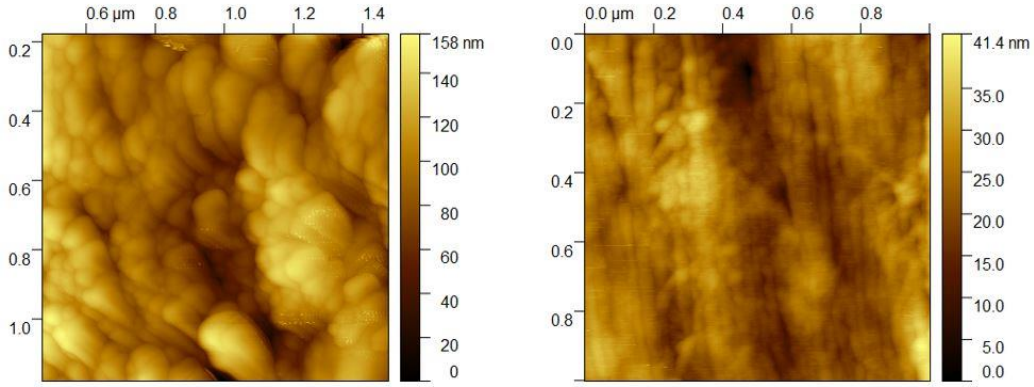

Figure 6.8: Surface profile of AC-1 **(a)** and GNP **(b)**

The remaining part of this chapter would investigate the energy of cells assembled with AC-2 and GNP as electrodes, with redox electrolytes. Moreover, the specific influence of the ionic components of the electrolytes, would be scrupulously investigated in Ch. 7.

The DRS investigated are the bromides LiBr, NaBr, KBr and $MgBr_2$. Herein a detailed and systematic analysis of the device performance as a function of the interactions of the ions with the electrodes at the E|E interface, would be approximately correlated to the porosity and surface physico-chemistry. The properties of the redox electrolyte varied are its concentration and co-ion (in this case the cation, since the anion Br^- is the DRS been investigated). All cells tested are with equal electrode mass (EEM) ($m_+ = m_-$), and comprises of the same volume of electrolyte as was described in the Methodology section (see Ch. 3, Section 3.6).

6.5 Understanding EDL capacitors and supercapatteries assembled with the carbon electrodes AC-2 and GNP

From Fig. 6.1 it was observed that the EDL capacitance of the supercapacitor fabricated with AC-1 and GNP are comparable. This CV for the EEM cells using 2.0 mol/L KCl with either AC-2 (2M-KCl-AC-2) or GNP (2M-KCl-GNP) as electrodes are compared directly in Fig. 6.9a. The cell capacitance for 2M-KCl-AC1 which is 17.1 F/g, is slightly larger than that for 2M-KCl-GNP which is ca. 15.2 F/g. The 12.5% increase in the cell capacitance of 2M-KCl-AC-1 compared to that of 2M-KCl-GNP, may be attributed to the higher surface area of the AC-1 electrode.

With this simple assumption, the high BET-SSA of AC-2 particularly its comparatively higher contents of micropores, may be identified as the reason for this display of a larger specific EDL capacitance, as expressed in Eq. 6.1:

$$\frac{C}{A} = \frac{\varepsilon}{d} \qquad (6.1).$$

Where C (F) is the capacitance, A (m^2) surface area of the carbon, ε permittivity of the electrolyte (F/m), and d (m) is the separation of the ions within the Helmholtz layer of the EDL. Although this might be a fair assumption for the present discussion, still, it should be noted that this correlation between the SSA and the displayed EDL capacitance is at best an approximation. This is because, it has been generally shown that the relationship between the EDL capacitance and SSA of carbons is not necessarily linear [34, 209-211].

Moreover, an interesting finding was that when the cells using 2.0 mol/L KBr was considered (Fig. 6.9b), the difference in charge capacity between GNP and AC-2 was very significant, with the capacity of the earlier been over 50% larger than the latter. More importantly, this charge capacity enhancement was predominant in the Nernstian features of the GNP.

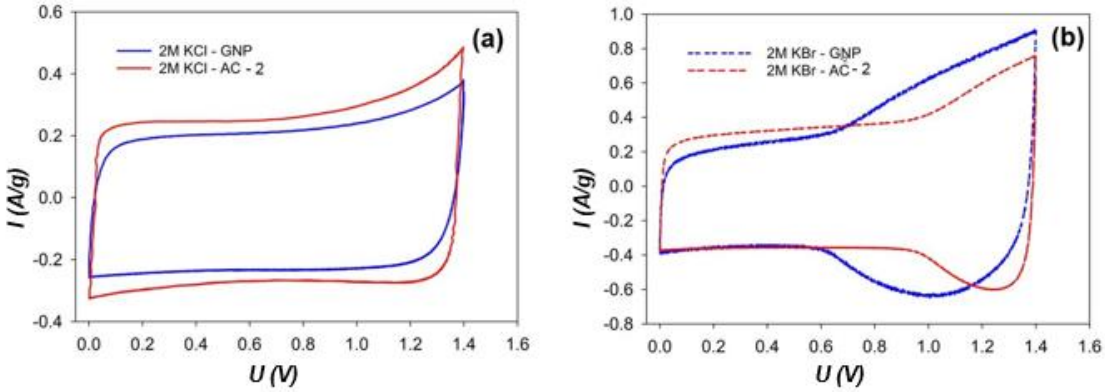

Figure 6.9: CVs of EEM cells with GNP and AC-2 electrodes using inert 2.0 mol/L KCl (a) and active 2.0 mol/L KBr (b) respectively. Scan rate: 5 mV/s.

In this respect, it should be highlighted that Eq. 6.1 cannot be used to explain this observation due to the Nernstian contribution to the observed capacity. This interesting property shows that despite the larger BET-SSA of AC-2 compared to GNP, when redox electrolytes are used, the pore size distribution particularly the presence of mesopores, and possibly the role of the surface reactivity becomes significant. It is important to also highlight that this property was displayed for all redox electrolytes (i.e. LiBr, NaBr and KBr) investigated. This aspect was treated in Ch. 7 (for example see Fig. 7.8).

In addition to the role of the pore size which aids additional entrapment (active volume), this high charge capacity of the GNP using DRS can also be attributed to the effective electrosorption of the products of the Br^- redox reaction within the interlayer of the graphene nanoplatelets. Furthermore, the role of the surface active sites promoting additional surface redox reactions in the GNP cannot be ignored [212-214]. Such improved electrosorption due to the morphology of the surface might not be observed for the AC-2 which is an amorphous carbon [215, 216]. Thus, the charge storage mechanism of the bromides on AC-2 might be attributed mainly to the adsorption and/or

entrapment of the products of the redox reaction, with very little contribution from its surface/textural properties.

To further explore the mechanism of charge capacity enhancement for the AC-2 and GNP electrodes, EQCM measurements were carried out at the (AC-2 or GNP) | 1.0 mol/L KBr interface. The CVs (Fig. 6.10a) and mass change plots (Fig. 6.10b) for the carbons, reflects and agrees with an increase in charge capacity as demonstrated by the CVs measured for the cells which was discussed earlier on (see Fig. 6.9 b). It should be noted that equal mass of GNP and AC-2 powder were drop-casted on the gold substrate of the quartz-crystal. Although, the change in mass as measured from the EQCM is independent of the initial mass of material, moreover, this was done in order to ensure that the volumetric calculations are constant because the active components are in solution. In line with this, it is herein proposed that for testing DRS with the EQCM, the mass of electrode material deposited should always be the same as is the volume of electrolyte in the cell.

Accordingly, considering that the EDL capacitance of AC-2 is actually slightly larger than that of GNP, the larger Q_{sp} (charge capacity) for the GNP electrode compared to AC-2 with the bromides as DRS can thus be linked to the difference in porosity because $Q_{sp} = nFN_0V_{pore}$ (as has been proposed earlier on in Ch. 4: Section 4.4). It should be pointed out that although V_{pore} herein could be linked to the bulk pore volume of the material, i.e. V_{pore} of GNP (1.09 m^3/g) is larger than that of AC-2 (0.80 m^3/g), moreover, the distribution of mesopores in GNP, as was ascertained through the DFT physisorption analysis in Ch. 4 (see Fig. 4.2) is a fundamentally important means of characterising the charge capacity difference of these carbons with regards to porosity.

In line with this, the mesoporous property of the GNP provides improved entrapment or "active-volume storage" of the generated Br_3^- + Br_2 redox species. It is important to state that although this increase in mass may also be linked to enhanced electrosorption due to the surface property of GNP,

the EQCM cannot be used to explicitly ascertain this. However, the cycling stability of the electrodes (demonstrated in Ch. 7, Fig. 7.7) may be used as indirect evidence for this. It is also interesting to note that the onset for the oxidation of the Br^- as shown from the CVs was ca. 0.59 vs. SCE for both carbons, still, the peak mass were at slightly different potentials of 0.69 V and 0.73 V vs SCE for GNP and AC-2 respectively. Although a difference of ca. 40 mV is not markedly significant, still this less positive potential for the peak mass adsorption/desorption of the bromides at the GNP may also be linked to the high proportion of mesopores in, and higher electrosorption of the bromides on, GNP [217].

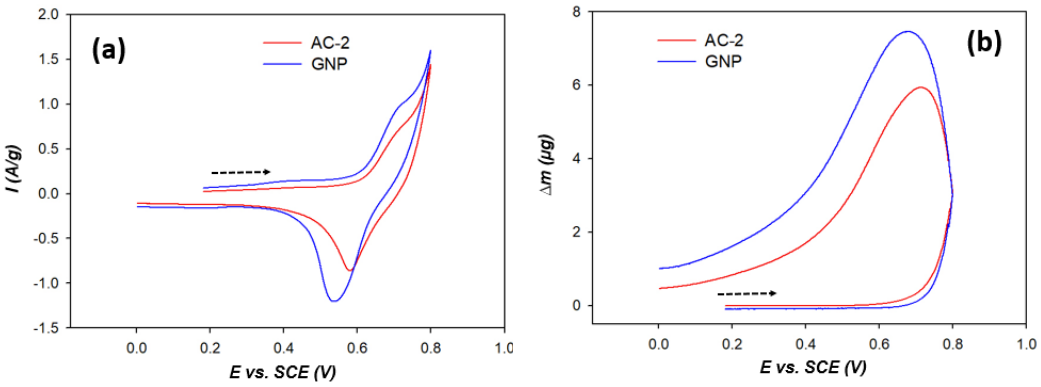

Figure 6.10: CV of AC-1 and GNP in 1.0 mol/L KBr **(a)** corresponding change in mass of redox species with electrode potential for AC-1 and GNP in 1.0 mol/L KBr **(b)**. Scan rate: 5.0 mV/s.

6.6 Correlating the electrode porosity and surface property of AC-2 and GNP to the energy of supercapatteries with dissolved redox species

Due to the strong ionisation power of Li^+ to the Br^-, coupled with its larger hydration radius, its charge dynamics at the carbon | electrolyte interface would be a limiting case. Hence LiBr was selected as the redox electrolyte to investigate the fundamental role of the ionic components in the charge storage properties of supercapacitors with DRS. However, for practical gains in energy capacity, KBr for example would be preferred, and this was

demonstrated in Ch. 7 (Section 7.5) where comparisons were made between the bromides of the common alkali metal cations Li^+, Na^+ and K^+ with either GNP or AC-2 as electrodes.

LiBr was used in the fabrication of EEM cells with AC-2 or GNP as electrodes. The concentration of the DRS used to fabricate the cells were varied. Thus, the cells with varying molarity were denoted as: 1M-LiBr-AC-2, 2M-LiBr-AC-2, and 4M-LiBr-AC-2 for AC-2 electrodes; and 1M-LiBr-GNP, 2M-LiBr-GNP, and 4M-LiBr-GNP for GNP electrodes. Studying the performance of the supercapatteries with different concentrations of redox electrolytes was done for both fundamental understanding and also to inform practical design of cells.

Before the presentation of the observed results, it is pertinent to draw attention to the testing protocol adopted in the analysis of devices throughout this research.

6.6.1 Testing protocols for supercapatteries with DRS

Generally, results from similar devices i.e. with electrodes and electrolyte concentration as was itemised in Section 6.6 were tested in the remaining parts of this chapter, and in most parts of Ch. 7. Moreover, when testing devices with redox electrolytes, it is important to note some of their characteristic features in order to ensure reproducibility of the results.

Firstly, since these cells using bromides possess the capacitive and Nernstian portions, it is important to note that the electrode potential of the electrodes in the devices may shift slightly. This is because there could be minor surface activation of the positrode on charging to higher cell voltages where the Nernstian property has been invoked, a property that is not observed for EDL cells operated within the maximum capacitive voltage. For example when these cells with DRS have been operated to say U_L = 1.6 V, results can no longer be collected for the same cell at say 0.8 V, which is the capacitive range.

Thus, for the test results reported in both this chapter and Ch. 7, multiple cells of similar design i.e. same electrodes and electrolyte concentration were used to carry out different tests. Moreover, to test that these cells were indeed identical, low scan rates at 5.0 mV/s within the EDL range e.g. from 0 to 0.5 V, were used to equilibrate the cells, and since the electrode mass were always the same, the capacitances are ascertained to confirm reproducibility. These careful measures were necessary because the very slight difference in the cell with or without a filled electrolyte volume shown in Fig. 3.22b, becomes quite significant when long duration testing such as EIS or GCD at different U_L are undertaken. It should be pointed out that since the EIS tests undertaken in this research are potentiostatic, it involves a voltage hold at relatively high U_L for example 1.4 V, at which point the redox activity has occurred at the positrode.

Thus, a cell with bromide as DRS that has undergone voltage hold at 1.4 V for slightly over 13 minutes (approximate time to collect the impedance spectra from 100 kHz to 10 mHz at 10 points per decade) might have been activated such that impedance tests on this same cell at 1.6 V, must be reproduced with another similar cell for validity.

In fact, understanding these testing protocols would make one appreciate the difference between a battery and a supercapattery. This is because, for the earlier, the U_{ocv} is usually close to the $U_{discharge}$ (see Fig. 2.12 in Ch.2). Furthermore, the U_{min} for the battery, must always be greater than 0.5 V. However, U_{min} for supercapatteries are usually 0 V, and the difference between U_{redox} and $U_{discharge}$ explained in Ch. 4 and 5, implies that supercapatteries with bromides as DRS have unique voltage ranges for EDL or redox features.

Generally, experimenting with such large number of cells was made possible by the availability of a multichannel workstation that can test multiple cells concurrently (see Fig. 6.11).

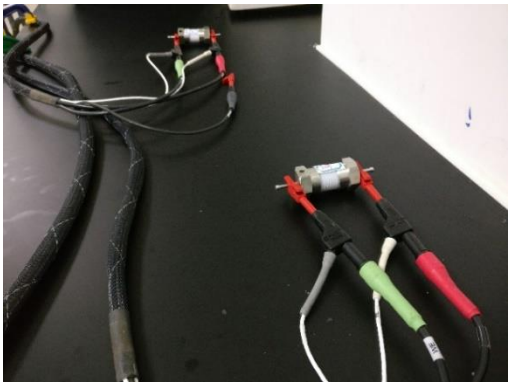

Figure 6.11: Multiple cells under tests with the multichannel electrochemical workstation.

6.6.2 Charge storage properties of supercapatteries with AC-2 or GNP as electrodes, and varying concentration of LiBr as electrolyte

Figures 6.12 and 6.13 shows the cyclic voltammograms and GCD plots at different values of U_L for EEM cells with either AC-2 or GNP as electrodes, with different concentrations of LiBr. These CVs and GCD plots were shown at U_L values from 1.6 to 2.0 V, because for practical reasons, this is the voltage range of interest when the effects of the DRS on the devices are to be appraised. Moreover the broader properties of these cells at U_L within the capacitive range, would be discussed later. Also, note that supercapacitors with DRS are essentially supercapatteries, especially when operated at $U_L \geq U_{redox}$. Moreover, throughout this dissertation these terms would be used interchangeably.

Table 6.2 presents the performance metrics for the cells calculated from the GCD data. These performance metrics are: W_c (specific energy for charging), W_d (specific energy for discharging), W_{eff} (energy efficiency), Q_{eff} (charge efficiency).

From the cyclic voltammograms in Fig. 6.12, it was observed that at different upper limits of cell voltage (U_L), the profiles of the cells with similar

electrodes qualitatively display some slight differences, moreover, cells with different electrodes display markedly different charge storage profiles.

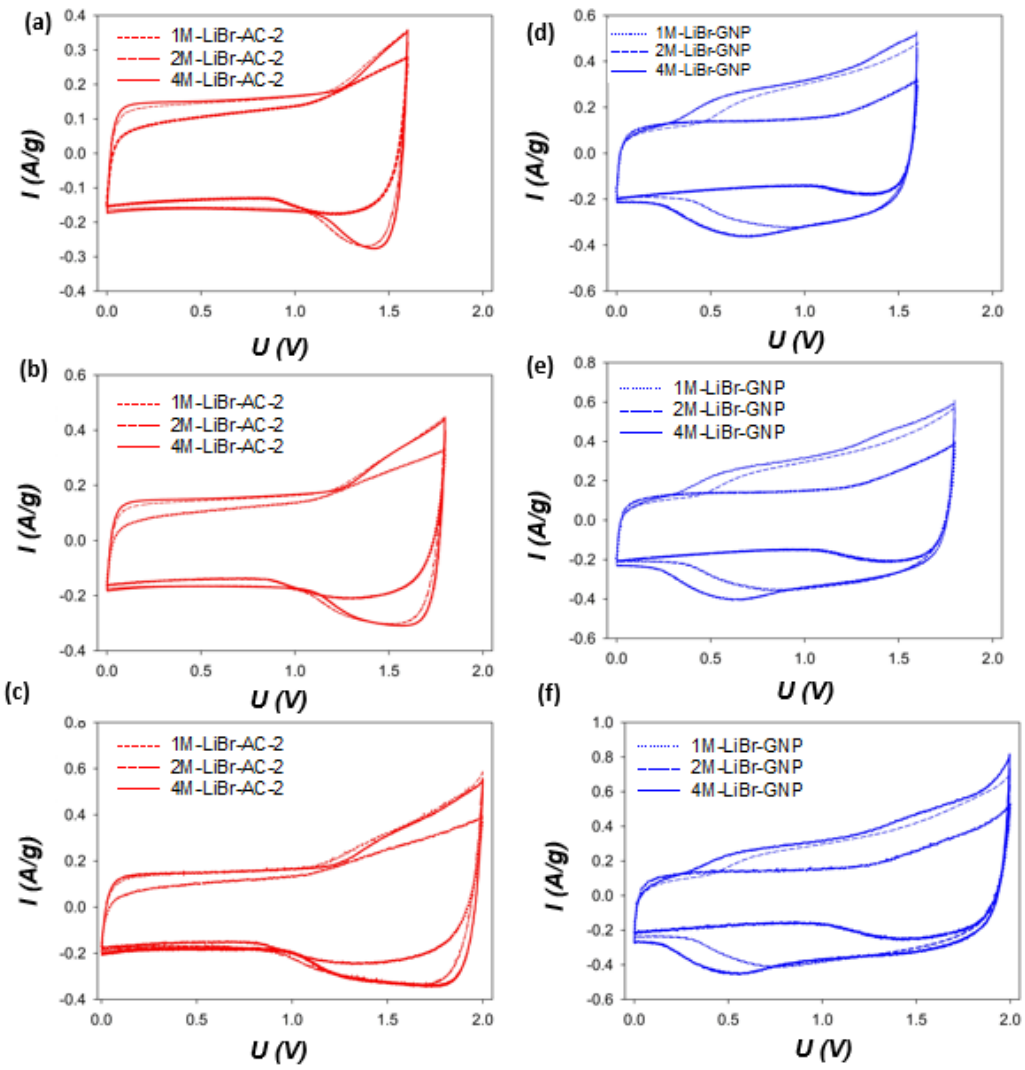

Figure 6.12: CVs at different upper voltage limits for EEM cells with varying concentration of LiBr assembled with: AC-1 U_L = 1.6 V **(a),** 1.8 V **(b)** 2.0 V **(c)** and GNP U_L = 1.6 V **(d)**, 1.8 V **(e)** 2.0 V **(f)**. Scan rate: 10.0 mV/s.

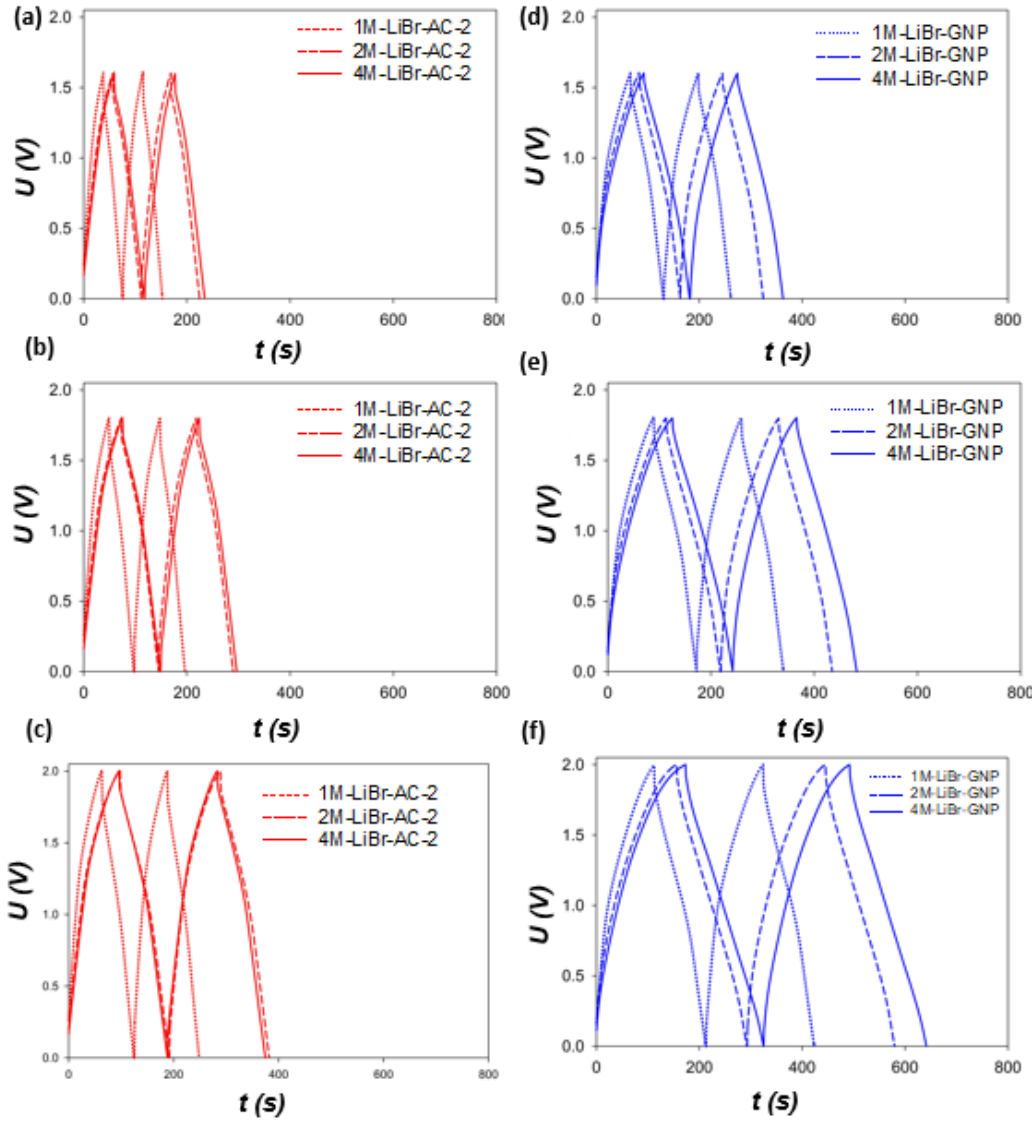

Figure 6.13: GCD plots at different upper voltage limits for EEM cells with varying concentration of LiBr assembled with: AC-1 at U_L = **(a)** 1.6 V **(b)** 1.8 V **(c)** 2.0 V and GNP at U_L = **(d)** 1.6 V **(e)** 1.8 V and **(f)** 2.0 V. Current load: ±0.5 A/g (ca. ± 15 mA of applied current).

Note that the cell performance metrics presented in Table 6.2 were calculated from the GCD plots of the cells in Fig. 6.13 above, i.e. at a current load of ±0.5 A/g (ca. ± 15.0 mA of applied current). These performance metrics are: W_c: specific energy for charging, W_d: specific discharge energy (same as W_{sp} i.e. specific energy of the device), W_{eff}: energy efficiency same as η_W i.e. (W_d/W_c), and Q_{eff}: charge efficiency same as η_Q.

Table 6.2: Device performance metrics at different upper cell voltage limits (U_L) of EEM supercapatteries with different concentration of LiBr for cells with **(a)** AC-2 and **(b)** GNP as electrodes.

(a)

1M-LiBr-AC-2	Wc (Wh/kg)	Wd (Wh/kg)	Weff (%)	Qeff (%)
1.6 V	5.80	3.90	66.38	95.00
1.8 V	8.50	5.80	68.24	94.10
2.0 V	12.10	8.20	67.77	95.30
2M-LiBr-AC-2	**Wc (Wh/kg)**	**Wd (Wh/kg)**	**Weff (%)**	**Qeff (%)**
1.6 V	8.15	6.30	76.69	96.60
1.8 V	12.15	9.20	75.31	97.30
2.0 V	18.60	13.90	74.73	94.90
4M-LiBr-AC-2	**Wc (Wh/kg)**	**Wd (Wh/kg)**	**Weff (%)**	**Qeff (%)**
1.6 V	8.10	6.50	80.25	96.70
1.8 V	12.25	9.60	78.37	96.10
2.0 V	17.70	13.80	77.68	95.80

(b)

1M-LiBr-GNP	Wc (Wh/kg)	Wd (Wh/kg)	Weff (%)	Qeff (%)
1.6 V	9.90	7.35	74.24	95.50
1.8 V	14.82	10.65	71.89	93.20
2.0 V	21.30	13.95	65.50	90.00
2M-LiBr-GNP	**Wc (Wh/kg)**	**Wd (Wh/kg)**	**Weff (%)**	**Qeff (%)**
1.6 V	12.30	9.50	77.23	96.40
1.8 V	18.95	14.45	76.25	92.00
2.0 V	29.15	18.05	61.92	89.95
4M-LiBr-GNP	**Wc (Wh/kg)**	**Wd (Wh/kg)**	**Weff (%)**	**Qeff (%)**
1.6 V	13.40	10.65	79.48	95.70
1.8 V	20.70	15.10	72.95	93.60
2.0 V	31.65	19.55	61.77	89.30

Generally, at all values of voltage and concentration, the discharge or specific energy (W_d) of GNP is greater than that displayed by AC-2. The succeeding paragraphs would discuss these measured performance metrics.

The performance metrics of W_{eff} and Q_{eff} are linked to the charge and mass transfer of the DRS at the E|E interface, thermodynamics and reversibility of the redox reactions, and the electro-sorption/desorption of both active and non-active species inside the porous matrix [31, 56, 141, 218].

These properties are in turn influenced by the porosity and surface physico-chemistry. For example, the generally high Q_{eff} values observed for the cells, particularly at U_L = 1.6 V, can be attributed to the highly reversible reaction of the Br^- / (Br_2 + Br_3^-) redox species at the carbon interface (i.e. at the positrode). The variation in W_{eff} is an important property that can be used to explain the extent of utilisation of the redox species, and also the role of the porous properties and surface physico-chemistry (and possibly morphology) of the carbons. Although, it is not possible to tell which property predominates in the displayed charge storage performance of the GNP electrode. Generally, the larger pores of GNP, might reduce the effects of steric hindrance, and can also accommodate additional product of the redox reaction, even at higher concentration of the ions [205, 212]. On the other hand, the smaller pores of AC-2 may increase confinement of ions which could result to high degree of steric hindrance [219]. Hence, even with increased generation of ions from the redox action they may not contribute to increased storage within the porous matrix of AC-2 [134].

Also, the sensitivity of the Q_{eff} and W_{eff} of the GNP electrode to concentration might further support the claim that in addition to the role of the mesopores been capable of holding more charge, there might be the presence of additional reaction of the generated Br^- / (Br_2 + Br_3^-) with the GNP surface. Such observations have been described as due to possible electro-catalytic effects of the graphitic interlayer/lattice on the activity of some redox ions [212, 214, 220]. This is in contrast to that of AC-2 which is predominantly due to the adsorption or entrapment of the generated species, with strong van-der Waals interaction been responsible for any additional or enhanced adsorption [216, 221].

Broadly speaking, some intuitive illustration of the mechanism of ion-electrosorption as it affects charge compensation mechanisms in porous

carbons may be used to give a general description of the role of ion-packing inside the porous matrix of these carbon electrode materials [209, 222].

6.7 Porosity of carbon electrodes and charge storage of redox electrolytes

The mechanism of EDL charge storage in a porous carbon electrode has been proposed to occur through one or more of the following charge compensation routes: (a) the adsorption of counter-ions outside the pore (ex-pore counter-ions) into the porous matrix of the carbon, (b) the swapping of co-ion inside the pore (in-pore co-ion) for an ex-pore counter-ion, (c) the desorption (or more specifically) the expulsion of in-pore co-ion away from the pores [222]. Figure 6.14 illustrates these mechanisms for a negatively charged pore.

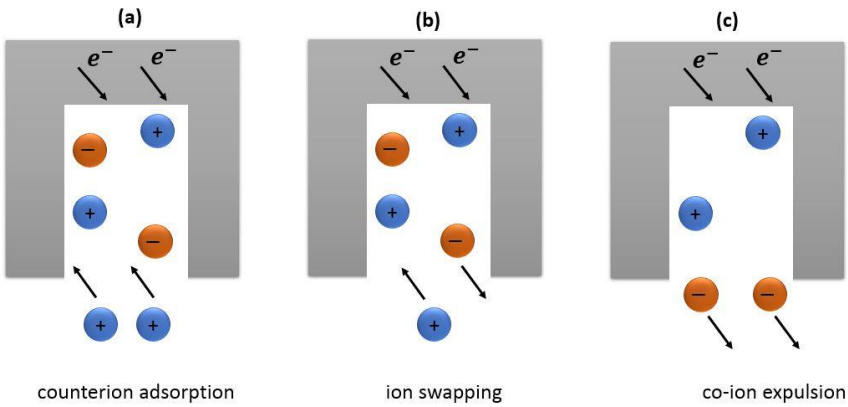

Figure 6.14: Mechanism of charge compensation within the pore of carbons for charge storage showing: counterion adsorption (a) ion swapping (b) co-ion expulsion (c). Adapted from [222].

Furthermore, the actual mechanism of ion adsorption (or entrapment) for different cation-anion combination is quite specific to the types of ions involved, and could also be determined by the nature of the solvation shells around or between the ions i.e. type of contact between the ions [31]. For example, the individual hydration shells of ions could be in contact, ions could share the hydration shells, or ions could be in direct contact with one another

covered by the hydration shell as illustrated in Fig. 6.15 [31]. In line with this, different ion-contact types could result in significantly different ion-electrosorption/charge compensation mechanisms within the porous matrix of the carbon.

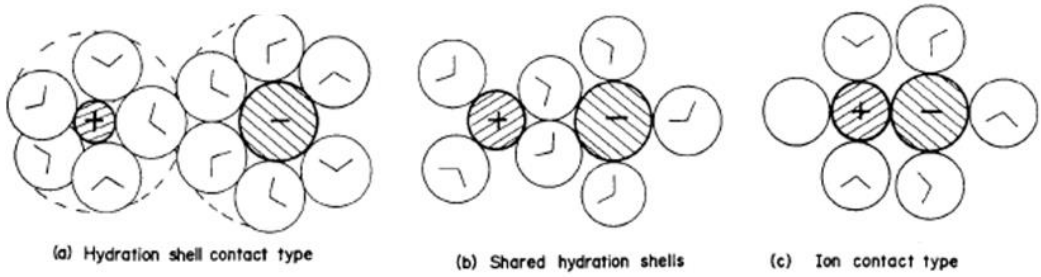

Figure 6.15: Solvation structure of ion-pairs (a) hydration shell contact type (b) shared hydration shells (c) ion contact type [31].

For instance based on the ionisation power of Li^+ on the Br^-, it was shown that depending on the concentration, the ion-contact type could be that of shared hydration shell or direct contact [223]. Accordingly, the entirety of the solvated co-ions may have to enter into the pores to contribute to charge storage.

With this line of thought, any mechanism of storage that involves the hydrated Li^+ be it desorption/adsorption, or ion-exchange, would be kinetically difficult in AC-2, compared to GNP. Thus, the increase in charge and energy efficiency of AC-2 with an increase in concentration from 1.0 to 2.0 mol/L LiBr could imply that a combined diffusion and migration of the electro-generated species into the pores is necessary for AC-2 to effectively store charge. Thus, at high enough concentration such diffusion mechanisms become less important for charge storage in AC-2. Hence, an increase in concentration from 2.0 to 4.0 mol/L LiBr did not result in any significant increase in charge capacity for AC-2.

Contrastingly, for GNP, the concentration of LiBr resulted to an increase in the measured W_d at all values of U_L. This increase in capacity with

concentration, can thus be closely linked to an additional surface reactivity of the GNP which may be aided by the improved electrosorption that has been discussed already.

The presence of low voltage current bumps in the CVs of GNP at high concentration (2.0 or 4.0 mol/L) when U_L = 1.8 or 2.0 V, could be attributed to the combination of the strong ionisation potential of the Li^+ and the existence of a higher diffusion gradient during the charge/discharge of the mesoporous carbon (this aspect would also be re-visited in Ch. 7 where the features of the cells with different cations would be compared). Moreover, this diffusion is confined within the mesoporous carbon, and as such it does not shuttle into the negatrode. In line with this, the migration effects due to localised mass transport of the species within mesopores seems to be significant when LiBr is used with the mesoporous GNP.

Figure 6.16(a1) shows the CV for the cell 1M-LiBr-GNP at different values of U_L. It was observed that at U_L = 1.0 V, the cell was predominantly capacitive, implying that for 1.0 mol/L LiBr with GNP as electrodes, the redox activity of the Br^- has not yet taken effect on the features of the cell.

Figure 6.16(a2) shows the electrode-potential/cell-voltage response vs time corresponding to the cyclic voltammogram of the cell 1M-LiBr-GNP at U_L = 1.0 V and scan rate (v_s) of 10.0 mV/s. Herein, it was noticed that the GNP electrode displayed unequal capacitance as was observed from the positrode been polarised to ca. $\Delta E_p = E_+ - E_{0V}$ = 0.59 – 0.05 = 0.54 V compared to the negatrode which was polarised to $\Delta E_n = E_- - E_{0V}$ = 0.41 – 0.05 = 0.36 V. Thus even with higher polarisation of the positrode which should have shifted the electrode potential to more positive values, the strong ionisation power of Li^+ and the low concentration of bromide species limited the amount of bromides packed within the porous carbon, thus reducing the further polarisation of the positrode.

However, with increase in concentration the U_{redox} for the GNP electrode occurred at less than 0.5 V. Generally, this shift in U_{redox} could be linked to the type of cation (as would be further discussed in Ch. 7). Broadly speaking, with mesoporous carbon, the apparent volume for the entrapment of the ions increases the concentration gradient of the generated redox species, which then makes the migration effects (as explained earlier) within the positrode significant. Accordingly, the current bumps at low cell voltages for GNP with LiBr as DRS, may be linked to the joint effects of the polarisation power of Li^+ and the mesoporous property of the GNP.

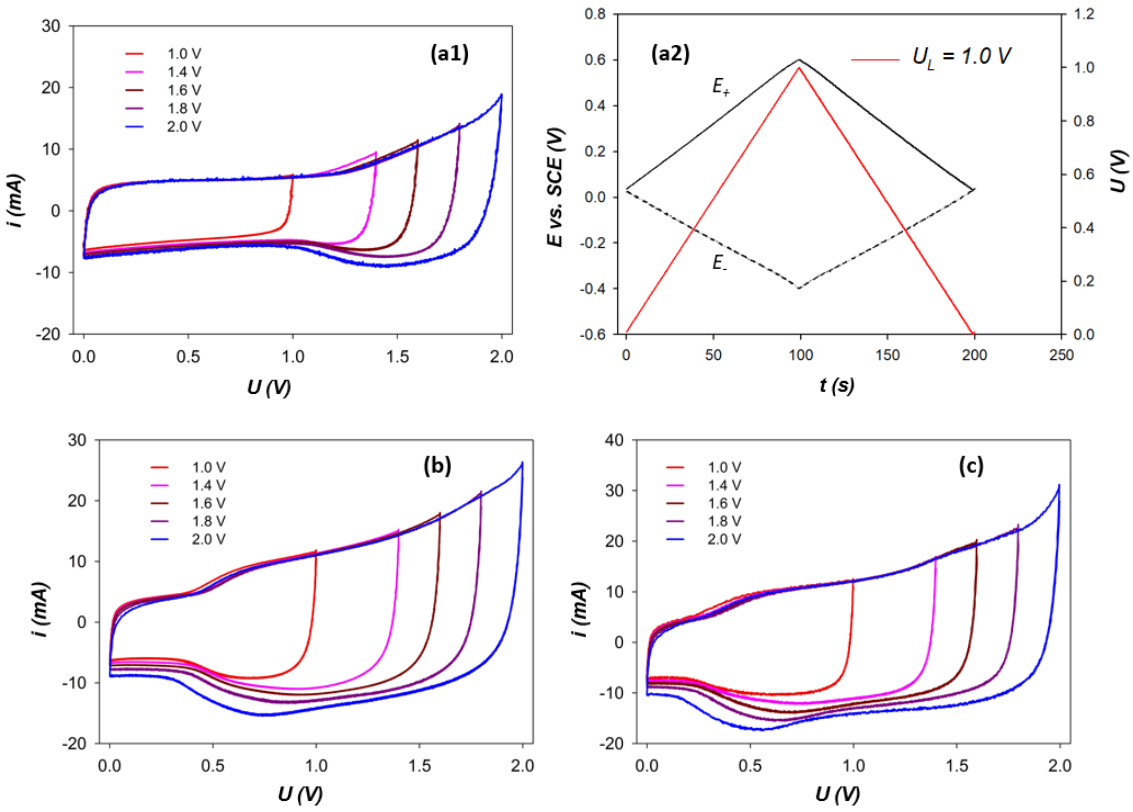

Figure 6.16: (a1) CV at different U_L for 1M-LiBr-GNP (a2) the *U vs.t and E vs. t* response obtained from the CV at U_L = 1.0 V, scan rate: 10 mV/s. CVs for the cell: (b) 2M-LiBr-GNP (c) 4M-LiBr-GNP at different U_L, scan rate: 10 mV/s.

In contrast to GNP, the features of AC-2 displayed no marked contribution from increased mass transport on the positrode, and its charge

storage profile at all concentration of LiBr can be clearly categorised into predominantly EDL region (< 1.0 V) and Nernstian region (> 1.0V) (see Fig. 6.17).

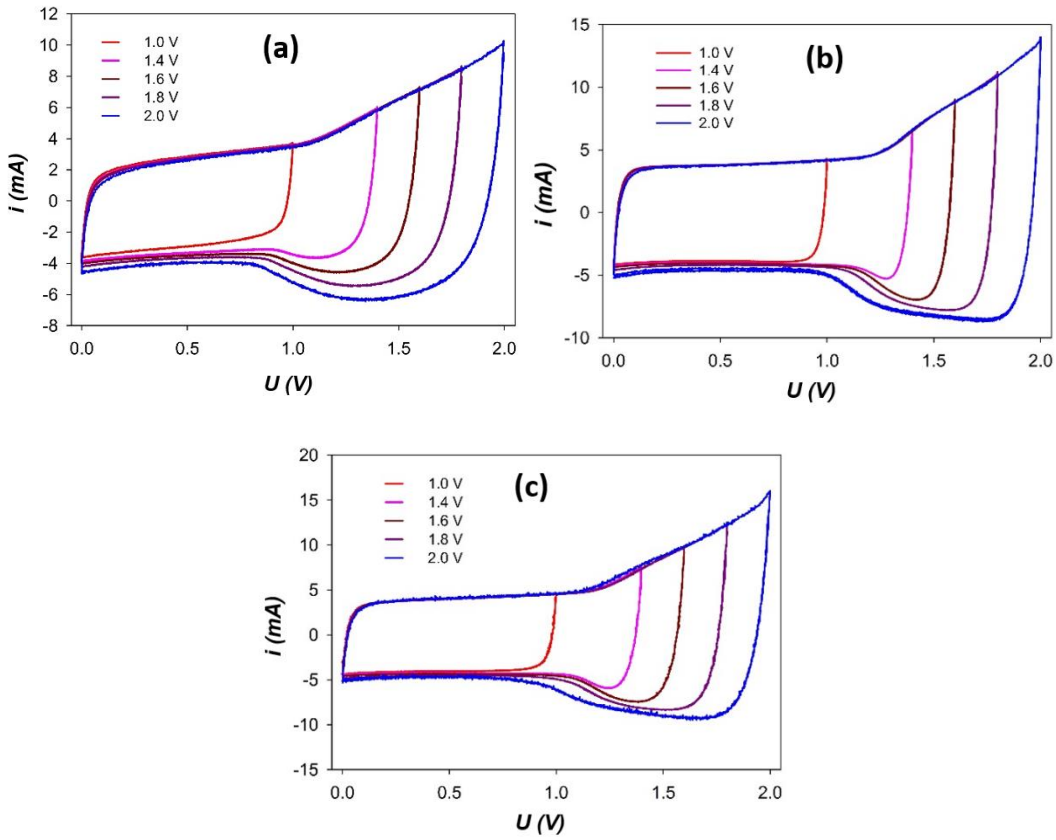

Figure 6.17: CVs for EEM cells with AC-2 as electrodes at different values of U_L (a) 1M-LiBr-AC-2 (b) 2M-LiBr-AC-2 (c) 4M-LiBr-AC-2. Scan rate: 10 mV/s.

This important difference between AC-2 and GNP as summarily illustrated from the GCD plot in Fig. 6.18, demonstrates that the redox charge capacity in GNP is significantly enhanced than that of AC-2, despite the EDL capacitance of AC-2 been slightly larger.

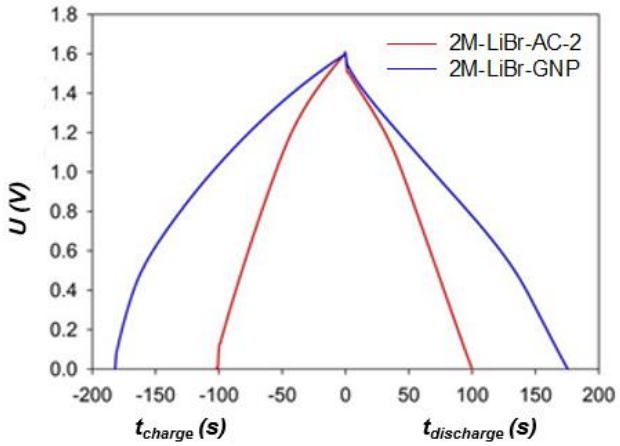

Figure 6.18: GCD of 2M-LiBr-AC-1 and 2M-LiBr-GNP at U_L = 1.6 V and I = 0.25 A/g.

6.8 Chapter Summary

The surface property of the micoroporous activated carbon (AC-2) and mesoporous highly graphitised carbon GNP has been analysed. Both carbons contain significant surface oxygen groups, but AC-1 has a slightly higher C/O ratio. Electrochemical analysis in an inert electrolyte revealed that the EDL capacitance of AC-1 was slightly larger than that of GNP. However, in a redox electrolyte, GNP displayed a markedly enhanced charge capacity compared to AC-2.

The enhanced charge capacity of GNP has been attributed to its mesopores been capable of accommodating more products from the redox reaction, and also to a possible higher surface reactivity due to enhanced electrosorption on its surface.

Generally, whilst the performance metrics of EEM cells with AC-2 as electrodes showed very little sensitivity to change in concentration from 2.0 to 4.0 mol/L LiBr, cells with GNP electrodes displayed a marked improvement in performance with increase in concentration.

In line with these observations, the mesoporous property of GNP coupled with the ionisation power and hydration properties of Li^+ have been correlated to the observed features of the supercapattery with GNP as electrodes. This first report on the use of a highly graphitised and mesoporous carbon in the design of a relatively high voltage supercapattery is thus important in contrasting the performance between the common micoroporous carbons which displays comparatively low "active volume storage". Hence, these performance metrics could act as a benchmark for the selection of electrodes in practice.

CHAPTER 7: ROLE OF CONCENTRATION AND ION DYNAMICS ON THE PERFORMANCE OF SUPERCAPATTERIES WITH REDOX ELECTROLYTES

7.1 Introduction

In Ch. 6, the performance metrics of cells using LiBr as DRS with either GNP or AC-2 as electrodes were investigated. In this chapter, similar cells to the ones investigated in Ch. 6, were further characterised using impedance spectroscopy. The testing protocol described in Section 6.6.1 was adopted in the test of the cells: with GNP or AC-2 with LiBr having concentration of 1.0, 2.0 and 4.0 mol/L.

Generally, there are a large number of bromide salts that may be used as DRS. Accordingly, in this chapter, bromides of Li, Na, K and Mg were rigorously studied to understand their properties either as inherently redox electrolytes, or as additives to inert electrolytes.

7.2 Impedance analysis of supercapatteries fabricated with AC-2 or GNP with LiBr as electrolyte

Electrochemical impedance spectroscopy (EIS) is a versatile technique that can be used to understand the role of the porous properties and the surface physico-chemistry of the electrodes on the device performance. As explained in Ch. 3, Section 3.4.3: data obtained from EIS are usually described based on equivalent electrical circuits in which an element or a specific configuration of some elements in a circuit corresponds to one or more properties of the interface. Generally, the impedance across an E|E interface $Z(\omega)$ can be mathematically expressed as:

$$Z(\omega) = Z'(\omega) + jZ''(\omega) \quad (7.1),$$

where $Z'(\omega)$ and $Z''(\omega)$ are the real and imaginary impedances respectively.

Accordingly, since this impedance value corresponds to the ratio of the input sinusoidal voltage to the (corresponding sinusoidal) current response at a given frequency, it can be related to the frequency dependent capacitance C(ω) as given in Eq. 7.2:

$$Z(\omega) = R_{ESR} + \frac{1}{j\omega C(\omega)} \quad (7.2).$$

Where, R_{ESR} is the high frequency resistance of the interface which is independent of frequency, and is in series with the combination of the other elements that constitutes the interface (see Ch.3, Section 3.4.3). In line with this, *C(ω)* can be expressed in complex notation as:

$$C(\omega) = C'(\omega) - jC''(\omega) \quad (7.3).$$

The real $C'(\omega)$ and complex $C''(\omega)$ components of the frequency dependent capacitance can in turn be expressed by:

$$C'(\omega) = \frac{-Z''(\omega)}{\omega|Z(\omega)|^2} \quad (7.4a),$$

and

$$C''(\omega) = \frac{Z'(\omega)}{\omega|Z(\omega)|^2} \quad (7.4b).$$

From these expressions, $C'(\omega)$ is the measured frequency dependent capacitance of the device, and as $\omega \to 0$, $C'(\omega)$ tends to the capacitance of the interface (or device) measured from say cyclic voltammetry at low scan rates [224, 225]. On the other hand, $C''(\omega)$ describes the dissipative component of the device, and its frequency dependent plot can be used to ascertain the capacitive (or power factor) response of the device. The designation of these parameters in practical devices can be seen from the illustration in Fig. 7.1, which shows the Nyquist (Z′ vs. Z″) plots divided into different regions, based on the frequency.

For example, at the high frequency region, the non-frequency dependent ohmic resistance (R_{ESR} from Eq. 7.2), persists, i.e. the characteristic of the device is resistive. At the medium frequency region, the charge transfer resistance of the cell which describes kinetic parameters in the device can be

observed, this is then followed by the diffusion region which can be used to explain the transient diffusion of the species within the Helmholtz layer [226].

The dispersed capacitance region thus corresponds to the interfacial charge within the porous matrix of the carbon, and broadly reflects the complex contribution of the porous structure of the carbon to the capacitance. The extent of deviation of this dispersed frequency region from ideality (90^0) can also be used to describe the porous property of the electrode, and it also reflects the dissipative features displayed by the device [225, 227]. Thus, if Eq. 7.6 (a and b) is used to describe the features of Fig. 7.1, then, with:

$$\frac{C'(\omega)}{\lim_{\omega \to 0} C'(\omega)} = 0 \qquad (7.6a)$$

the system is mainly resistive, however, when:

$$\frac{C'(\omega)}{\lim_{\omega \to 0} C'(\omega)} = 1 \qquad (7.6b)$$

capacitive properties of the interface would predominate.

In practice, the mathematical limit described in Eq. 7.6 refers to the lowest frequency of the applied AC signal, which in this research was 0.01 Hz. Thus from these descriptions, and from the schematic illustration of the Bode plot (illustrated and described in detail in Ch. 3, Fig. 3.17), it would be observed that the imaginary component of the capacitance i.e. $C''(\omega)$ would attain a maximum value at a specific frequency f_0 which can be correlated with a given time constant (τ): where $\tau = 1/f_0$.

This time constant, is a very important property of supercapacitors, and it is in general related to the time duration for the dielectric relaxation of the electrolyte components within the porous matrix of the carbon. Specifically, the relaxation time or time constant has been described as a "*factor of merit*" in the characterisation of supercapacitors [225, 227]. Generally, this parameter can be used to ascertain the power performance or capacitive response of the supercapacitor. In this research, ascertainment of the time

constant from the impedance measurements was used to further understand the performance of the supercapatteries using DRS.

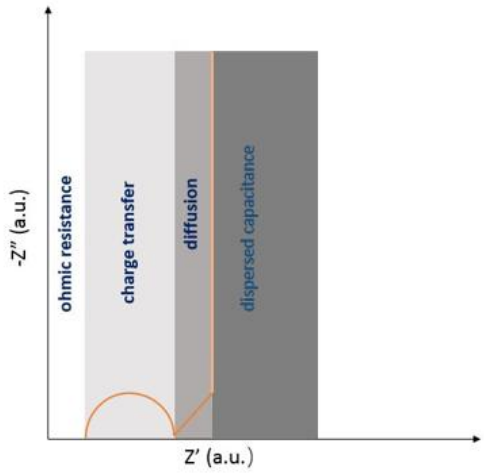

Figure 7.1: Schematic representation of the kinetic properties of the impedance spectra of a representative (ideal) supercapacitor.

It should be highlighted that in practice, the "non-active" device components i.e. the current collectors and separators also contribute to the observed impedance properties. Broadly speaking the role of the earlier on the performance can be linked to the R_{ESR} and the power response whilst the latter might have effects on the R_{CTR} (charge transfer resistance) [225, 226, 228]. Thus the contribution of these so-called non-active components must be taken into account when the performance of the entire device is to be appraised. Moreover, since the current collectors, separators and electrolyte volume used in fabricating the cells in this research are the same, the results obtained can thus be linked to the active components i.e. electrode and electrolyte in the device.

In line with this, one process of using impedance analysis to characterise the cell (together with its components) as shown in Fig. 7.2a, involves designing an electrical analogue of the interface pictured in Fig. 7.2b (but explained and illustrated in more detail as used for this research in Ch. 3, Section 3.4.3, see Fig. 3.16). In Figure 7.2b, the concentration and

potential gradients within the Helmholtz layer formed inside the porous matrix of the carbons are schematically illustrated. The simple illustration in Fig. 7.2b, shows that the transport of the charges either due to the potential gradient (migration) or the concentration gradient (diffusion) are influenced by the size and concentration of the (hydrated) ions, porous structure of the carbon, and in-pore charge compensation mechanisms. In certain cases, equivalent circuits such as the one shown in Fig. 7.2c may be used as analogues to understand the electrical performance of the device.

From Fig 7.2c, it is seen that the distributed capacitance within the porous electrode can be analogised by using a series of resistive and capacitive elements to form a transmission line. This transmission line describes the resistivity of the ions within the porous structure, and the role of the bulk resistivity of the electrode itself.

Accordingly, charge propagation can thus be analysed from such equivalent circuits, or could serve as intuitive guides to understand impedance data. In this research, direct correlation of the data from the EIS was used to critically describe the properties of the devices Fig. 3.16a (Ch. 3, Section: 3.4.3). Simple circuits such as in Fig. 3.16b (Ch. 3, Section: 3.4.3) modelled with the aid of the ZView software were used for confirmation.

In the succeeding paragraphs, detailed analysis of the impedance spectra of the cells fabricated with GNP and AC-2 using varying concentrations of LiBr were analysed.

Figure 7.3 shows the Nyquist plots for cells using AC-2 and GNP with different concentrations of LiBr, taken at U_L = 1.6 V. It should be highlighted that at U_L = 1.6 V the devices are operating as a supercapattery (see Fig. 6.12 and 6.13). Thus, the measured impedance at this cell voltage comprises of the effects from the EDL charging and Nernstian contributions of the DRS.

Figure 7.4 (a and b) shows the plot of the real and imaginary capacitance versus the frequency respectively.

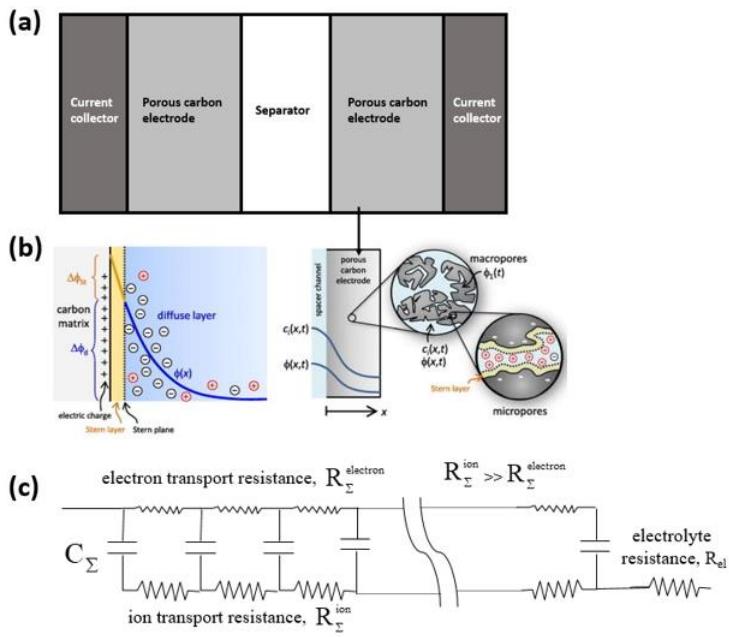

Figure 7.2: Schematic representation of: supercapacitor made of porous electrodes **(a)** inner porous structure of the carbon electrode showing the concentration and potential gradient within the Helmholtz layer of micropores [63] **(b)** equivalent circuit representing the distributed capacitance within the porous-matrix of the carbon as a transmission line **(c)**.

Figure 7.5 presents the plots of some important parameters calculated from this impedance data. These parameters includes: the equivalent series resistance; R_{ESR} (Fig. 7.5a), charge transfer resistance; R_{CTR} (Fig. 7.5b) response time; (τ) (Fig. 7.5c) and surface capacity (C_{surf}) expressed in F/cm^2.

The R_{ESR} of the cell using AC-2 is ca. 8% greater than that of the cell with GNP. However, it is interesting to note that at a concentration of 2.0 and 4.0 mol/L, the R_{ESR} are comparatively similar. Since the sheet resistance of the electrodes are different i.e. 48.45 × 10^{-6} Ω.cm for GNP and 214.24 × 10^{-6} Ω.cm for AC-2, the R_{ESR} measured at any given U_L and electrolyte concentration was influenced only by the resistance of the electrodes.

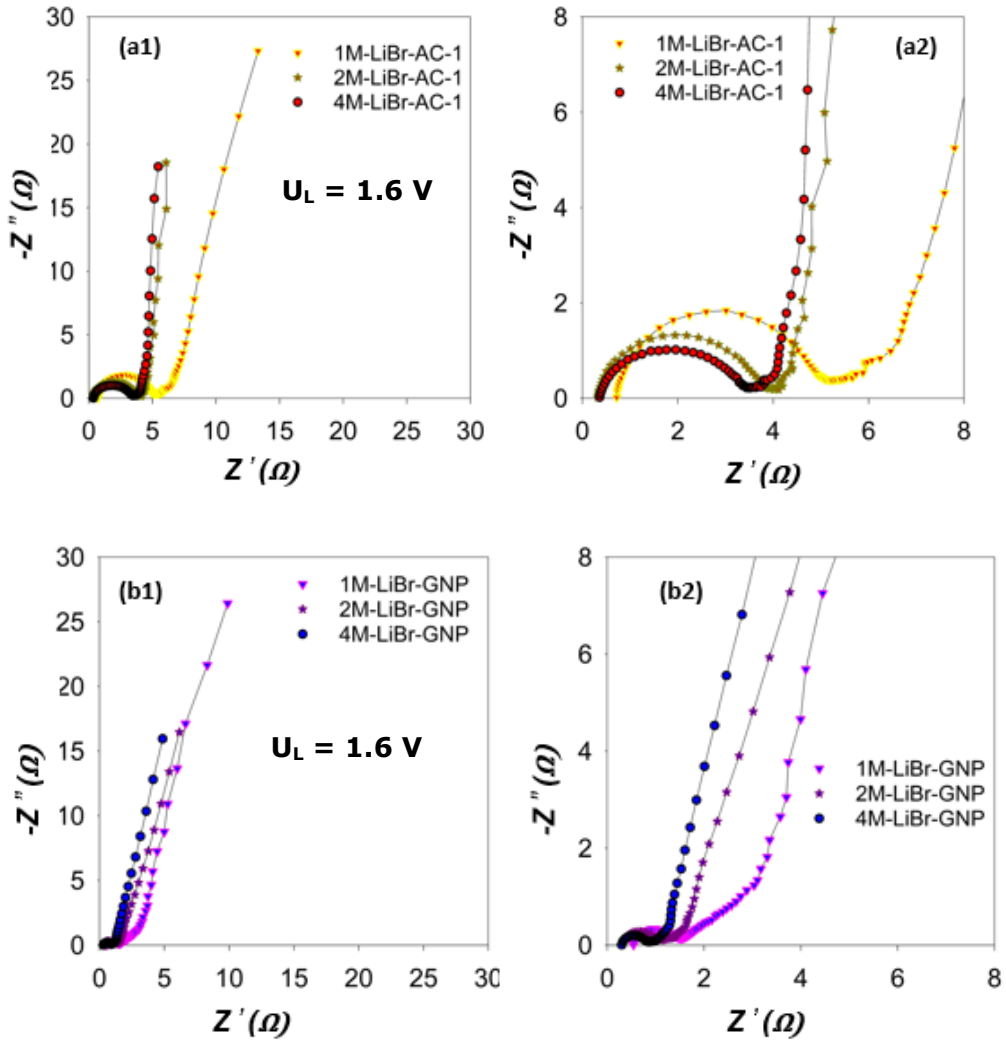

Figure 7.3: Nyquist plots and corresponding expanded view of the high- to mid- frequency regions of supercapatteries with different concentration of LiBr for EEM cells using **(a)** AC-2 **(b)** GNP. (U) i.e. applied upper limit of cell voltage U_L = 1.6 V.

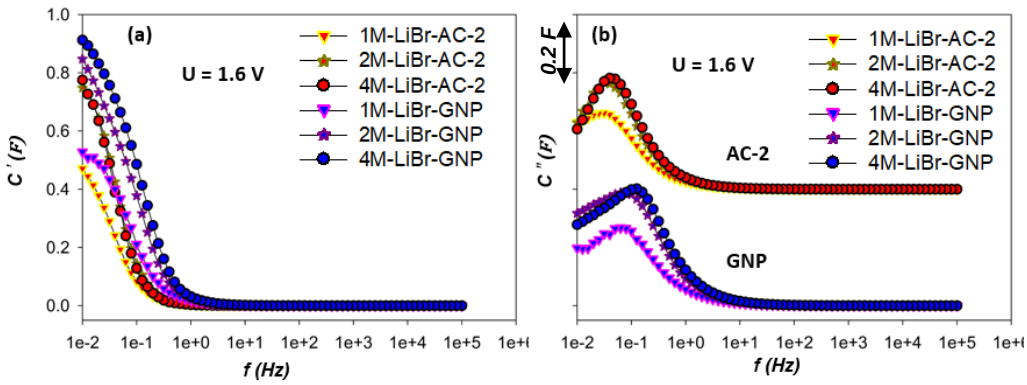

Figure 7.4: Bode plots of supercapatteries with different concentration of LiBr for EEM cells using AC-2 and GNP as electrodes **(a)** real capacitance vs. frequency **(b)** imaginary capacitance vs. frequency. (U) i.e. applied upper limit of cell voltage U_L = 1.6 V.

Another obvious feature of the impedance properties of these cells was the change in R_{CTR} with increase in concentration for all cells, and the markedly lower R_{CTR} for cells with GNP compared to those with AC-2 (see Fig. 7.5b).

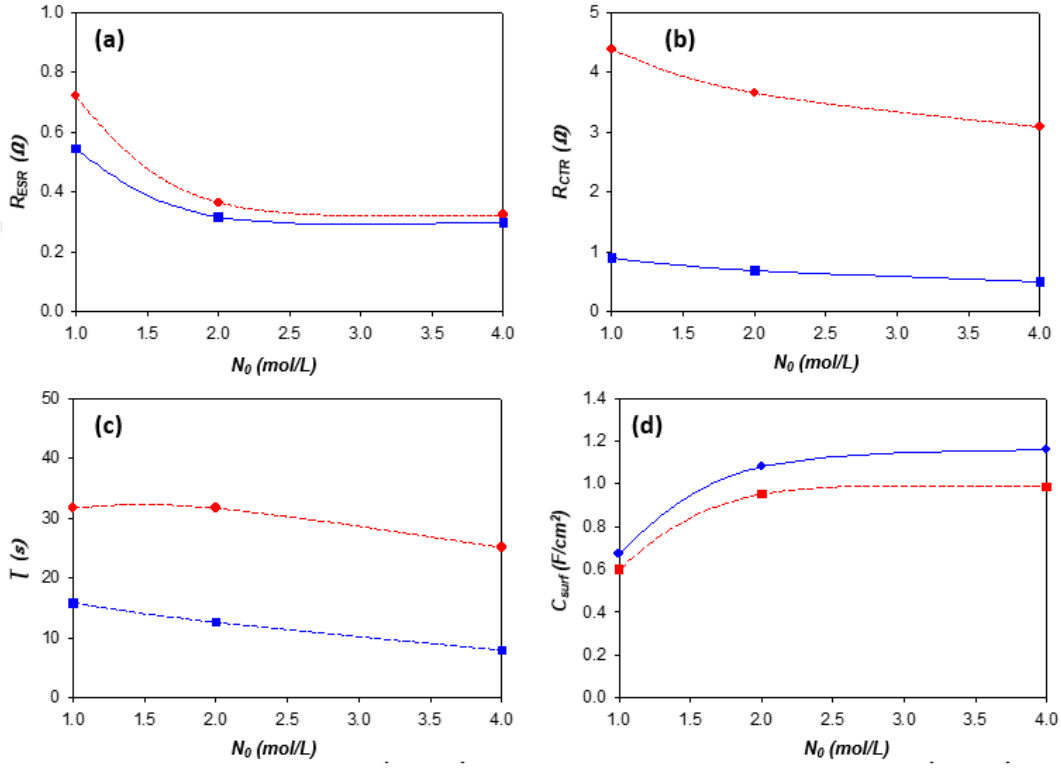

Figure 7.5: Performance metrics obtained from impedance analysis of EEM cells with either AC-1 or GNP electrodes, at varying concentration of LiBr; (a) R_{ESR} (equivalent series resistance) **(b)** R_{CTR} (charge transfer resistance) **(c)** τ (response time) **(d)** C_{surf} (surface capacity expressed in F/cm^2). U_L = 1.6 V.

The reduction in R_{CTR} with increasing concentration could be explained from the standpoint of enhanced activity with increase in concentration. Thus, the difference in R_{CTR} at cell voltage greater than 1.0 V (i.e. when the Nernstian property of the positrode has set in), can be related to the exchange current density (i_0) of the redox reaction since it can be expressed as a function of the net current (i). It should be pointed out that for the bromide DRS as with other reversible redox reactions that can be described with the aid of the Nernst equation, the current density can be expressed by the Butler-Volmer equation:

$$i = i_0 \left[\left(\frac{-\alpha nF\eta}{RT}\right) - \left(\frac{(1-\alpha)nF\eta}{RT}\right)\right] \quad (7.7).$$

In Eq. 7.7, α is the charge-transfer coefficient, n the number of electrons transferred, and η is the overpotential: $E - E_N$ (with E_N been the redox potential), R, T and F are the universal gas constant, absolute temperature and Faraday's constants respectively. Generally $\eta \ll RT/nF$ for highly reversible redox reactions such as that of the Br^-/ (Br^-_3 + Br_2) at the carbon interface [41]. As such Eq. 7.7 can be expressed as the linear equation:

$$i = \frac{nF\eta}{RT} \quad (7.8a).$$

From Eq. 7.8a, the rate of change of the applied overpotential with the current density which corresponds to the kinetically dependent R_{CTR} can thus be expressed as:

$$-\frac{d\eta}{di} = R_{CTR} = \frac{RT}{nFi_0} \quad (7.8b).$$

Since $i_0 \propto k^0 N_0$ where k^0 is the reaction constant and N_0 is the concentration, it follows that an increase in concentration would lead to a corresponding decrease in R_{CTR} as was observed from the Nyquist plots of Fig. 7.3 and graphically presented in Fig. 7.5b. Note that the electrodes used in fabricating all the cells have the same area of ca. 1.33 cm^2, with approximately the same electrode mass and thickness.

The difference in the R_{CTR} at all concentrations for cells using AC-2 was observed to be over three times larger than that of cells using GNP (Fig. 7.5b). This difference in the R_{CTR} can be linked to the surface physicochemical properties of these two electrodes [229, 230] and to the porous property [209]. The high degree of wettability of the GNP which was identified to be due to the presence of the COOH surface group within the graphitic planes of the nanoplatelets [203, 231], also significantly contributed to the reduction of R_{CTR}. This is because, improved wettability results in easy access of the electrolytes to the porous matrix of the electrode. Relatedly, the graphene nanoplatelets have been explained to have improved electrosorption [214, 232], implying that the product of the redox species may easily interact with the surface of

the GNP compared to AC-2. Furthermore, the mesopores in GNP also improves the transport of ions. In other words, more charge are able to pass through the activation barrier within the porous matrix of GNP compared to AC-2.

The response time of the devices which is another important parameter that describes their power performance, also shows that cells with GNP have shorter response times at all concentrations of the DRS.

For example, with 2.0 mol/L of LiBr, the cell with GNP electrodes has a response time of about 12.59 s compared to 31.62 s for the cell with AC-2. This implies that for high power applications in which the capacitive switching time is very important: the cell with GNP would be able to release its energy 2.5 times faster than that of the cell with AC-2 (see Fig. 7.5c).

In general, this comparatively faster capacitive response of GNP can be linked to its mesoporous property, which aids the easy transport of ions within the porous matrix of the electrodes. It has also been shown that the presence of mesopores, improves interfacial percolation, which reduces the capacitive dissipation within the porous matrix of the carbon. This is because a transmission line composed of mesopores would display lower distributed resistance to the flow of the ions (in line with the schematic diagram shown in Fig. 7.2c). Also, this high capacitive response may be linked to the enhanced electrosorption in the GNP electrode because the resistance between the pore walls and the DRS is reduced in the GNP [225, 233, 234].

The change in R_{CTR} with voltage at a concentration of 2.0 mol/L LiBr was also studied to gain further insight into the charge storage characteristics of these two carbons. As presented in Fig. 7.6(a1) the lower R_{CTR} for GNP is also displayed at all upper limit of cell voltages (U_L). An interesting feature of the R_{CTR} vs. U_L plot is that there is an obvious difference in the change of the R_{CTR} profile in the predominantly EDL range (<1.0 V) compared to the region were the redox action for the DRS has set in (>1.0 V). This is understandable because in the EDL region the charge storage is mainly due to electrostatic

interaction at the interface, moreover, at > 1.0 V when the redox activity has commenced, the activation potential of the interface becomes significant due to the transfer of electrons, diffusion of generated species and other surface controlled processes.

Conversely, for the mesoporous carbon, this increase in voltage though contributing to an increase in the rate of reaction, does not necessarily result to more ions been transferred within the porous matrix. Hence, it can be assumed that most of the ions have already accessed the inner porous matrix (within the inner Helmholtz plane of the pore) due to the mesopores acting as conduits for the effective passage of the ions. Furthermore, this insensitivity of the R_{CTR} to increase in the cell voltage (and increase in overpotential of the positrode) for GNP, can be linked to the high degree of electrosorption of the bromides on the GNP electrodes [225, 235]. On the other hand, the R_{CTR} of AC-2 decreases markedly with increasing U_L. This means that the activation resistance for AC-2 is high, which could be due to its hydrophobic properties, and the difficulty of the ions to access its inner porous structure. Thus, the charge transfer for AC-2 is aided by an increase in the electrode polarisation when U_L is increased.

In line with this, the origin of the marked faradaic features of cells with GNP as electrodes and LiBr as electrolyte coupled with the small change in the R_{CTR} with increase in U_L is reflective of a low polarisation resistance which is aided by the mesopores of GNP and the possibility of additional reactions between the GNP and the redox Br^-/ (Br^-_3 + Br_2).

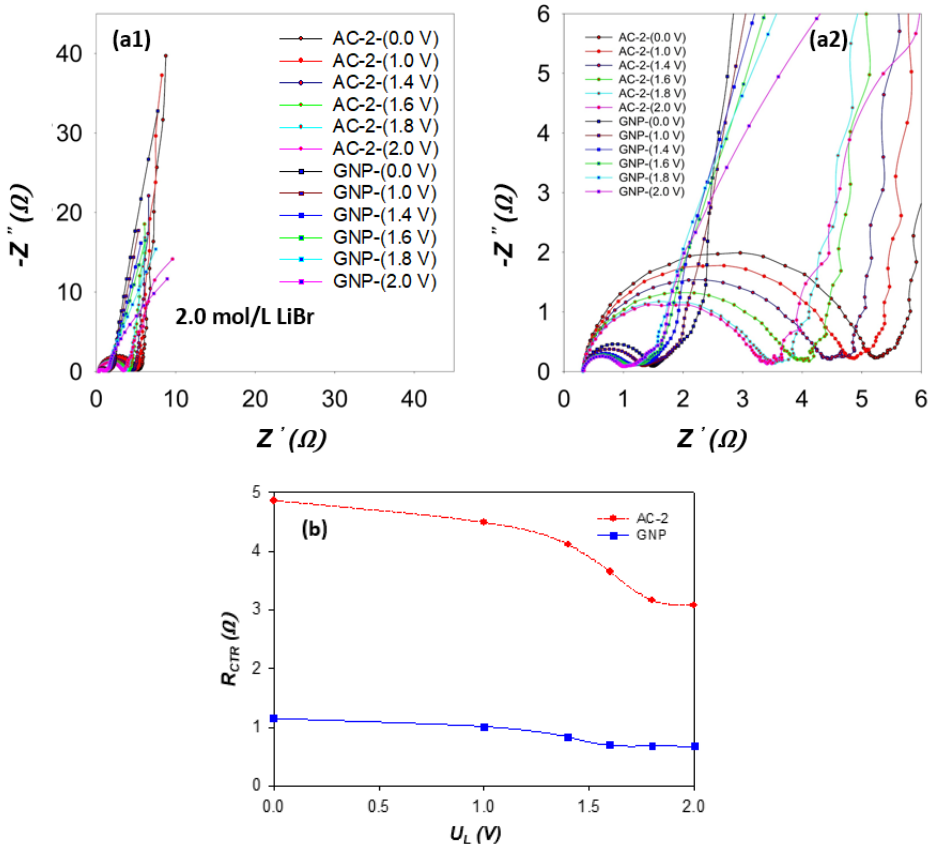

Figure 7.6: Nyquist plots at different values of U_{cell} **(a)** and variation of R_{CTR} (charge transfer resistance) with cell voltage **(b)** for AC-2 and GNP EEM cells using 2.0 mol/L LiBr.

7.3 Cycling stability tests

For the stability tests, six fresh EEM cells were assembled, three of these cells were fabricated with AC-2 electrodes, whilst the remaining three were with GNP electrodes. The electrolyte for all the cells was 2.0 mol/L LiBr. A pair of the cells with different electrodes were each cycled at 0.5 A/g and with U_L values of 1.6, 1.8 and 2.0 V.

As seen from Fig. 7.7a, at 1.6 V both AC-2 and GNP displayed comparatively similar energy retention i.e. 88% and 83% after 10,000 cycles respectively, which is greater than the so-called "end of life criterion" (EoLC). Note that the EoLC has been suggested as a measure of the ultimate stability of supercapacitors, and the cut-off point is 80% of the initial discharge

energy/capacity [236]. However at U_L = 1.8 V, the energy retention of both AC-2 and GNP decreased to ca. 85% and 79% respectively, which is still within the limits of the EoLC.

It should be pointed out that the rate of degradation of the cells at 1.8 V is higher than that at 1.6 V for both cells. However, the rate of degradation of GNP is faster than that of AC-2 at both values of U_L. At 2.0 V for both AC-1 and GNP there is a marked degradation for both cells, with GNP degrading more markedly compared to AC-2. Furthermore, at U_L = 2.0 V, both cells reached their EoLC within the cycling duration, although the degradation of GNP is appreciably worse than that of AC-2.

The degradation in the energy of the cells with cycling can be linked to the irreversibility in the redox reactions which might include decomposition reactions, electrode passivation, etc. [237, 238]. The relatively good stability of both cells at 1.6 V, can be linked to the reversibility of the bromide redox reaction at the positrode, and the relative stability of the negatrode at this applied cell voltage. However, the reduction in stability at U_L = 1.8 V, could be due to the occurrence of irreversible reactions at the negatrode coupled with increased oxidative decomposition and/or passivation on the positrode.

Since the negatrode operates at a much negative potential vs SCE when U_L is increased, it follows that the degradation at 2.0 V is conjointly affected by a faster degradation of both the positrode and the negatrode. Furthermore, the increased rate of degradation of GNP compared to AC-1 at all values of U_L may be linked to the faster rate of passivation of this electrode under cycling. This could also be evidence of its high surface reactivity i.e. the additional interaction between the Br^-/ (Br^-_3 + Br_2) and the surface of the GNP due to enhanced electrosorption. This additional interaction could thus result to the expansion of the interlayer spacing of the graphitic structure of the GNP, since the charge storage mechanism of GNP may also involve the de-/insertion of Br^-/ Br^-_3 [213, 216].

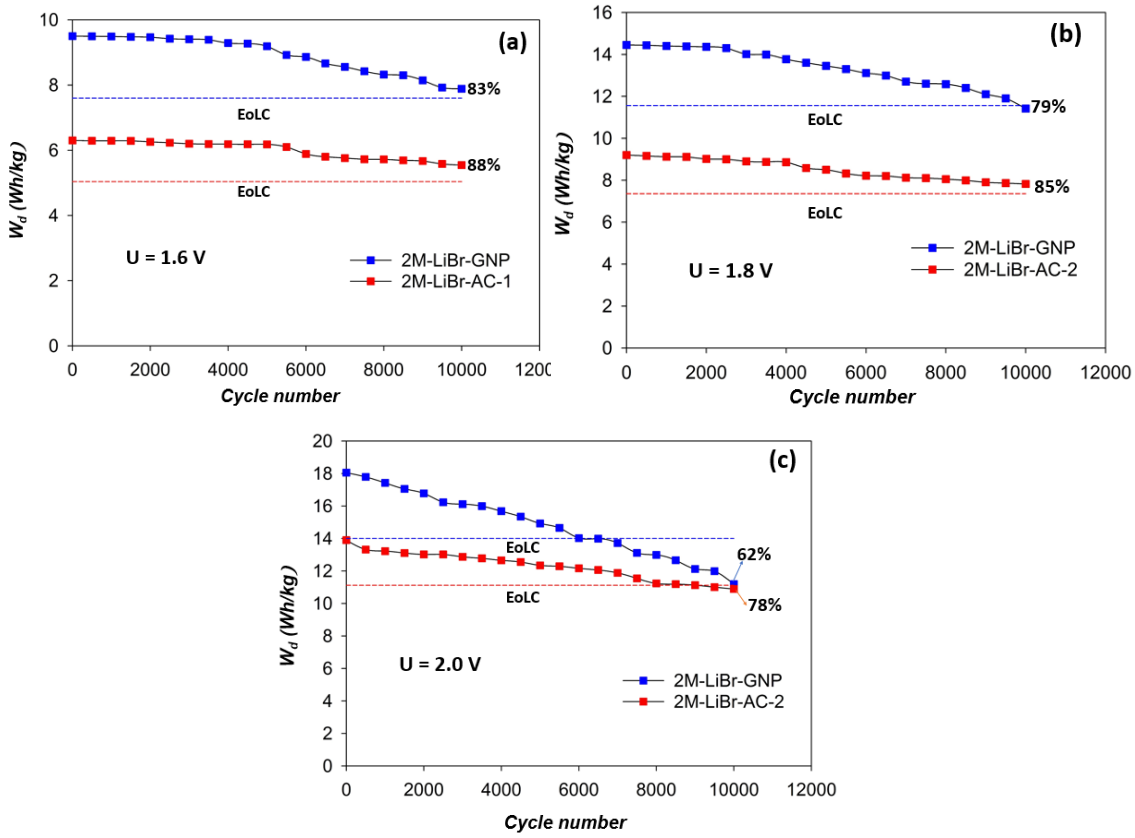

Figure 7.7: Cycling stability of EEM cells using 2.0 mol/L LiBr with AC-2 or GNP electrodes, current load = 0.5 A/g (± 15 mA of applied current) at upper cell voltage limits U_L of: 1.6 V **(a)** 1.8 V **(b)** 2.0 V **(c)**. EoLC: End of Life Criterion.

It can thus be inferred that whilst the surface functionalities and mesoporous property in the GNP electrode is responsible for the observed kinetic properties like reduced R_{CTR}, this surface physciochemistry also plays an important role in the charge storage mechanisms of the GNP electrode i.e. possible increased ion-electrosorption within the graphene layers.

7.4 Correlating the electrode properties with varying cations of dissolved redox species

In this section, the properties of EEM cells with 2.0 mol/L LiBr, NaBr, or KBr with either AC-2 or GNP as electrodes, were analysed. As presented in Fig. 7.8 (a1) the U_{redox} for the GNP cell with LiBr is much lower than that for either NaBr or KBr, cf. Fig. 7.8 (b1 and c1). This observation points out to the role of the ionisation power of the Li^+ in determining the diffusion of the bromides during charging/discharging of the cell with GNP. From Fig. 7.8 (a2, b2, and c2) it is seen that aside from the charge capacity increase, at 10.0 mV/s the features of the cells using AC-2 with all electrolytes were generally identical, with the U_{redox} been comparable. This indicates that the U_{redox} observed for cells is strongly dependent on the polarisation power of the cation together with the nature of the pores.

This finding is important, because in addition to the thermodynamics of the DRS, and polarisation of the carbon electrodes, it has now been conclusively confirmed that the ionisation power of the cation in conjunction with the pore size, also affects the $U_{redox.}$ The significance of this is that, when DRS are been selected for highly graphitised (and mesoporous) carbons which may favourably interact with the products of the redox species, attention must also be paid to the counter-ion in terms of not just the hydrated crystal radius (which is the parameter always scrutinised for EDL research and applications), but also with regards to ionic potential, which has significant effects on the features of the device.

With regards to rate performance, it would be noticed that at 100.0 mV/s all the cells using GNP generally retained the features of the bromide contribution. That is, apart from the expected decrease in charge capacity at high rates, the features of the bromide DRS were still obvious in the cells with GNP electrodes. On the other hand, at 100.0 mV/s, the features of the bromide contribution were generally lost for 2M-LiBr-AC-2, which displayed an almost

rectangular CV, whilst 2M-NaBr-AC-2 showed only a slight contribution from the Nernstian properties of the DRS (cf. Fig 7.8 a2 and b2). On the other hand, relatively good rate performance was observed for 2M-KBr-AC-2 (Fig. 7.8 b3), compared to 2M-LiBr-AC-2 and 2M-NaBr-AC-1.

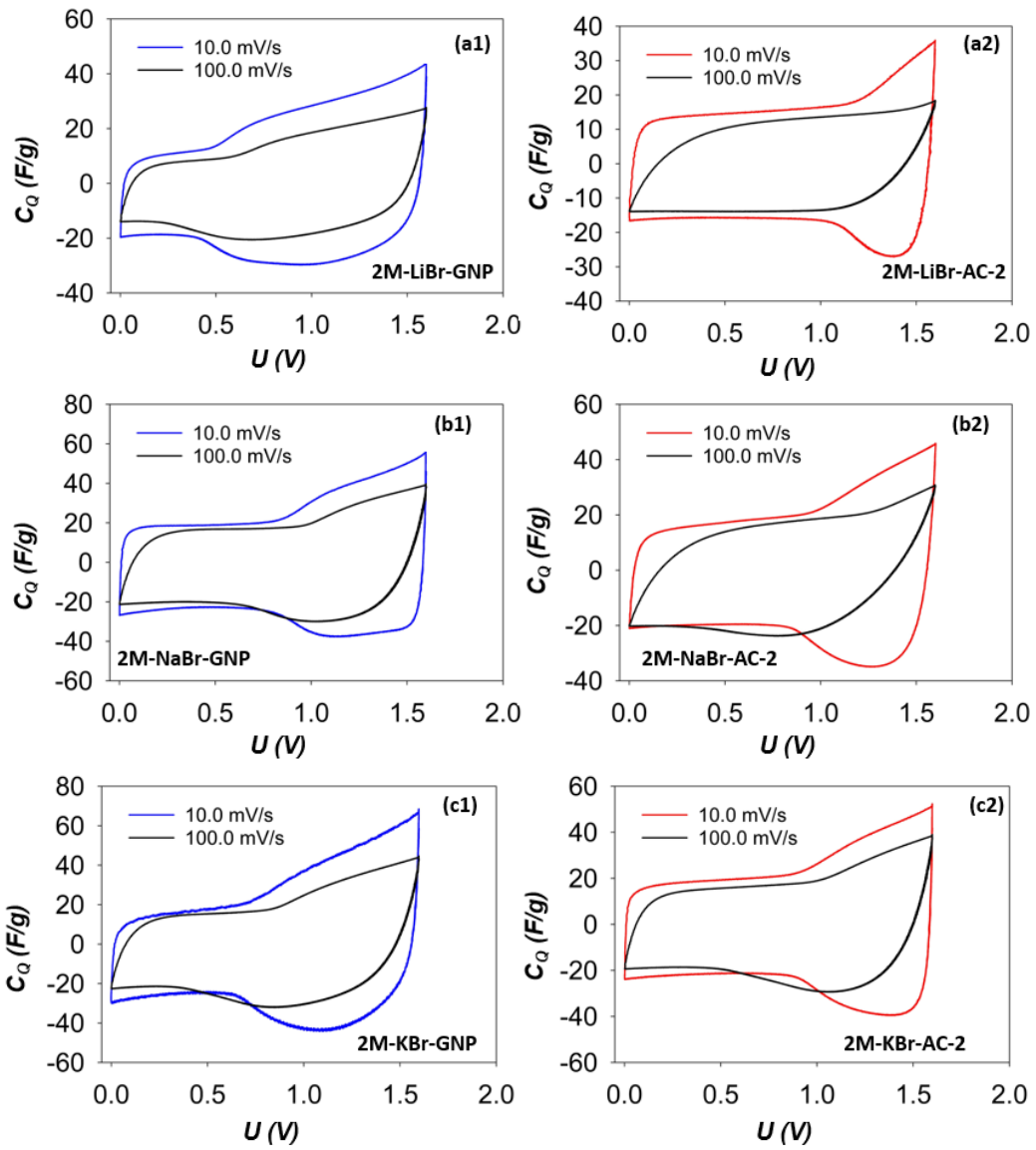

Figure 7.8: CVs of different EEM cells showing the effects of the cations: 2M-LiBr-GNP **(a1)**, 2M-LiBr-AC-2 **(a2)**, 2M-NaBr-GNP **(b1)**, 2M-NaBr-AC-2 **(b2)**, 2M-KBr-GNP **(c1)**, and 2M-KBr-AC-2 **(c2)**.

The most significant property herein is that whilst the highly mesoporous GNP displayed high rate properties i.e. its charge storage profile

is retained at high scan rates irrespective of the cations, AC-2 on the other hand displays a sensitivity to the size of the cations, because only the smaller hydrated K^+ ions were able to retain similar features at higher scan rate (Fig. 7.8 c2).

The specific energy of the cells at different applied current loads are presented in Fig. 7.9. As observed from these figures, GNP electrodes generally showed better rate performance with all the cations. However, only the AC-2 cell with K^+ as cations (see Fig. 7.9c) showed a relatively high rate performance, which is in agreement with the features of the CVs shown in Fig. 7.8.

The charge storage mechanism in carbon EDL electrodes is based on the electrode's porosity and its effects on the migration of ions under the influence of an electric field. The most general albeit approximate description is that: when an electrode material has stratified pores, the mesopores would aid in the transport of the ions, i.e. serving as conduits whilst the EDL layer would be formed within the matrix of the micropores [209, 226].

Moreover, when these species are within the pores, other properties such as surface groups, specific adsorption (e.g. electrosorption on the pore walls), or even the mechanism of charge compensation of the EDL, could also have effects on the redox properties of these DRS. Thusly, charging within the pores of nanostructured carbons have been linked to the conjoined action of steric hindrance and the ability of the charged species (active and non-active) to adsorb within the porous matrix of the carbon [219, 239].

In line with this, it is suggested that the porosity plays a more important role in the observed charge storage features when the cations are changed. Thus, the redox anion Br^- could interact with the surface (insertion or other electrochemical-chemical reaction) of the GNP as shown from increased reactivity with concentration or faster degradation on cycling. Whilst, the porous property of the electrodes determines the dynamics of the charge

compensation mechanism when the hydrated properties of the dissolved ions are considered.

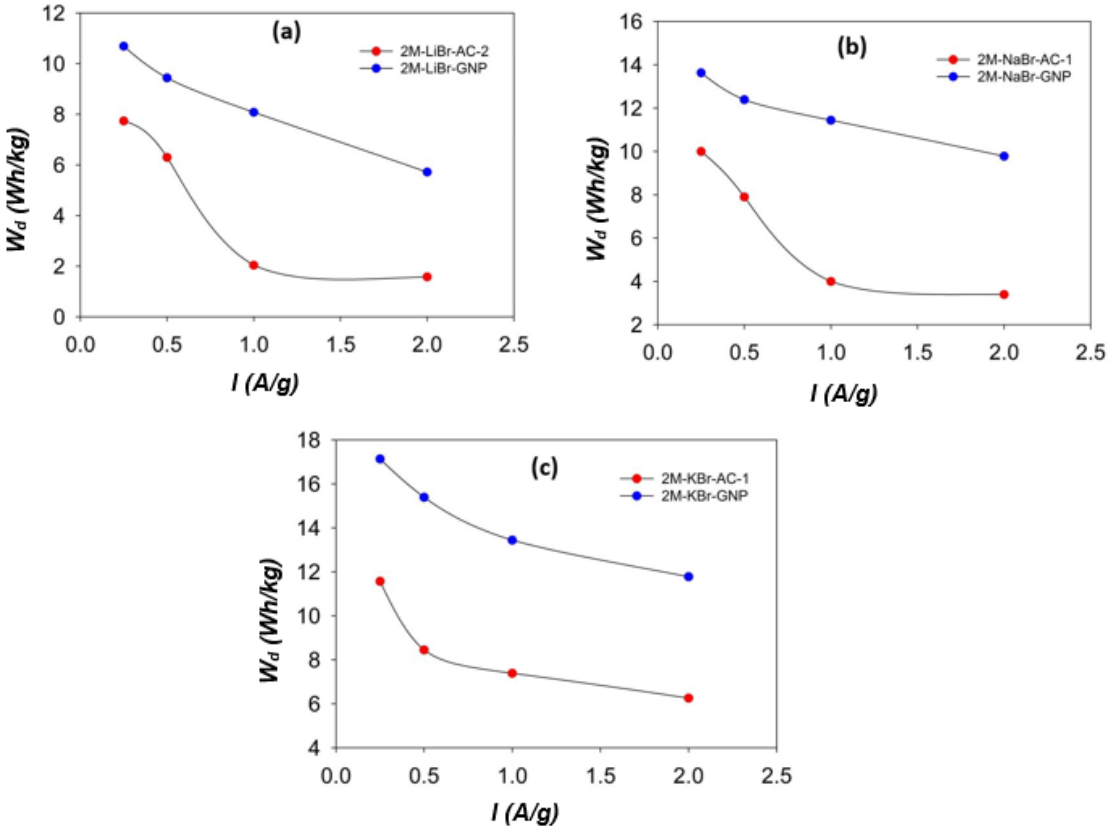

Figure 7.9: Role of cations on the rate performance of EEM cells using different alkali bromides as DRS with AC-2 or GNP as electrodes. Data calculated from GCD plots at different current load ($\pm\boldsymbol{I}$) with U_L = 1.6 V.

7.5 Role of cations in the performance of GNP electrodes with bromides as redox electrolytes or redox additives to inert aqueous electrolytes

Due to the comparatively efficient transport of ions within the porous matrix of the mesoporous GNP, coupled with possible enhanced electrosorption of the Br^-, the correlation between large hydrated cations and the porous property were further investigated. This was done by comparing the properties of EEM cells with GNP as electrode using either Li or Mg bromides as redox electrolytes.

In the cells investigated, the ionic strength of the bromide ion was made to be equal, thus GNP EEM cells with equal volumes of 4.0 mol/L LiBr (called as 4M-LiBr-GNP) and 2.0 mol/L $MgBr_2$ (called as 2M-$MgBr_2$-GNP) were fabricated. It was observed that the charge capacity of 4M-LiBr-GNP is ca. 8.34% more than that of 2M-$MgBr_2$-GNP (see Fig. 7.10a). This can be attributed to the ionisation potential of the Mg^+ ion, and the increased ionic activity of the LiBr.

Moreover, the most striking properties of the cells 4M-LiBr-GNP and 2M-$MgBr_2$-GNP can be observed from the impedance spectra shown in Fig. 7.10b. Herein, it was noticed that although the R_{CTR} of 2M-$MgBr_2$-GNP is at least twice that of 4M-LiBr-GNP, still their capacitive responses are identical with a switching (or relaxation) time of ca. 7.94s (see Fig. 7.10c). This very interesting finding showed that the R_{CTR} of the GNP electrode is strongly affected by the size of the cations, due to the ionising power of the cation to the Br^- in the course of the redox reaction. Moreover, the mesoporous characteristic of GNP, determines the response time of the device, thus allowing it to accommodate larger ions even though their resistance during migration within the pores was high.

This finding also demonstrated that in addition to the diffusion of charged species within the porous matrix of the carbons, mass transfer of the redox species is also important when the power or dielectric relaxation of the cells are considered. Also, the dissipative property of the cell with $MgBr_2$ is lower because C'' is ca. 0.27 F compared to that with LiBr which has a C'' of 0.41 F. This implies that although both cells would deliver similar power, still due to the dielectric properties of the LiBr electrolyte, the cell 2M-LiBr-GNP would lose energy at a slightly faster rate (for example, would generate more heat) during charging [225, 240].

It is well known that in addition to the use of DRS as inherently redox electrolytes, it is also possible to utilise these bromides as additives to inert

electrolytes. Furthermore, Na_2SO_4 [241] and $MgSO_4$ [149] have been shown to be viable aqueous electrolytes for EDL capacitors, both due to the advantageously high CPR which they can provide [241], and also due to the general environment friendliness of these salts [242, 243].

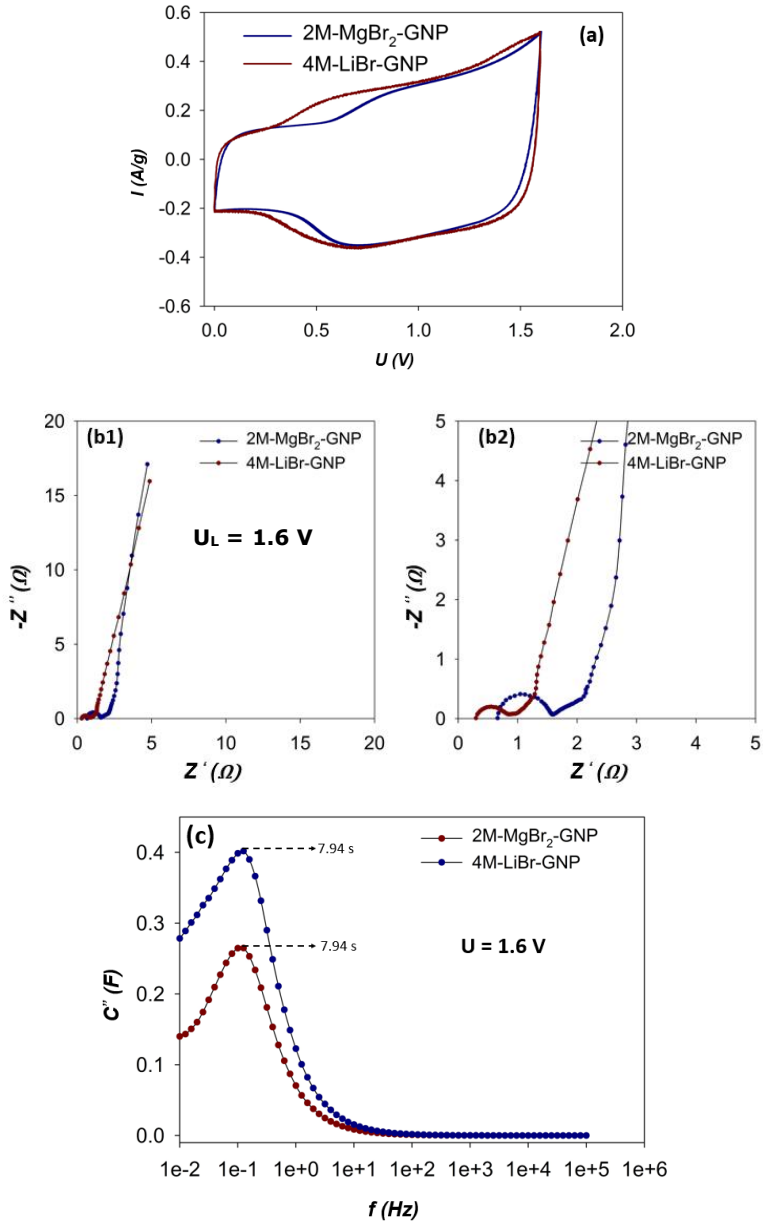

Figure 7.10: Comparison of the performance of 4M-LiBr-GNP and 2M-$MgBr_2$- (a) CV with U_L = 1.6 V and scan rate = 10 mV/s (b) Nyquist plot taken at U_L = 1.6 V (c) Corresponding Bode plot to (b).

To investigate the role of the cations in the inert electrolytes on the redox action of the bromides as additives, 0.15 mol/L of KBr was used as redox additive. GNP electrodes were used in the EEM cells, with either 1.0 mol/L of $MgSO_4$ or Na_2SO_4. The cells without redox additives were denoted as: 1M-$MgSO_4$-GNP and 1M-Na_2SO_4-GNP, whilst those with additives were designated as: 0.15M-KBr-1M-$MgSO_4$-GNP and 0.15M-KBr-1M-Na_2SO_4-GNP.

The CVs of these cells are presented in Fig. 7.11a. From this figure, it was noticed that the capacitance of 1M-Na_2SO_4-GNP (ca. 17.9 F/g) was about 6.5% greater than that of 1M-$MgSO_4$-GNP (ca. 16.8 F/g). The cells with 0.15 mol/L KBr as redox additive showed an increase in charge capacity, and the capacity of the cell 0.15M-KBr-1M-Na_2SO_4-GNP was also slightly larger than that of 0.15M-KBr-1M-$MgSO_4$-GNP.

Considering that the charge capacity of these cells were comparatively similar, the utilisation of either salts for the development of commercial cells would thus be dependent on the availability and safety of the reagents. Since both supporting electrolytes i.e. Na_2SO_4 and $MgSO_4$ are classified as non-hazardous substances [242, 243], it thus follows that the use of any of these reagents for commercial applications are feasible.

In these cells, special attention was paid to the ion dynamics due to the findings of the roles of cations which has already been described in the previous sections. Accordingly, the response time of these devices which gives important information on the role of the dielectric properties of the interacting ions within the porous matrix of the electrodes in the cells were critically studied.

From Fig. 7.11b, it was observed that the response time of 1M-Na_2SO_4-GNP is ca. 2.5 times faster than that of 1M-$MgSO_4$-GNP. This can be explained from the standpoint of the dielectric properties of the $MgSO_4$ and Na_2SO_4 electrolytes, and more importantly the ionisation potential of the cations, i.e. ionisation potential of Mg^{2+} is greater than that of Na^+. This may result in

different ion mobility in $MgSO_4$ electrolyte, which would have effects on its permittivity [201, 244].

Interestingly, with the KBr incorporated as redox additive into these inert electrolytes, it was observed that the response time of the resulting devices became identical. That is, the response time of the Na_2SO_4 cell without DRS (1M-Na_2SO_4-GNP) which was 15.85 s increased to 19.95 s on the addition of KBr. This indicates a slight reduction of the capacitive response on the addition of the DRS. Contrastingly, the response time of the cell with inert ($MgSO_4$) i.e. 1M-$MgSO_4$-GNP which was 39.89 s decreased to 19.95 s in the cell 0.15M-KBr-1M-$MgSO_4$-GNP with redox additive. This means that the use of redox additives actually improved the capacitive response of the cell using $MgSO_4$ electrolyte, but has a reverse effect for the cell with Na_2SO_4 as supporting electrolyte.

This fundamentally important finding, could probably be due to a change in the charge interaction and activity of the ions which may affect the permittivity of the electrolytes containing the hydrated K^+, Mg^{2+} and Br^- ions. For example, it is generally known that the $MgSO_4$ electrolyte could form different ion-ion pairs [245], thus, when the dissolved Br^- interact with this complex, a dual cation-anion pair which could adjust the ionisation of the Mg^{2+} relative to the Br^- could be formed. This possible complex ion pairing mechanism could then result in a reduction of the dielectric relaxation time of the electrolyte at the carbon interface, which then renders the switching properties of the $MgSO_4$ with KBr as additive better than that without the additive.

Such ion-ion interaction may not exist in the solution of the KBr in Na_2SO_4. Accordingly, its properties would become dependent only on the conventional mobility of the ions in the supporting electrolyte resulting in longer dielectric relaxation times. Furthermore, the properties of the GNP electrode, particularly its larger pores which can accommodate larger

hydrated ions or shared hydration shells, implies that such ion-ion pairs and complexes could also be formed within the confines of the porous matrix. This might also support their mobility during charge compensation [239].

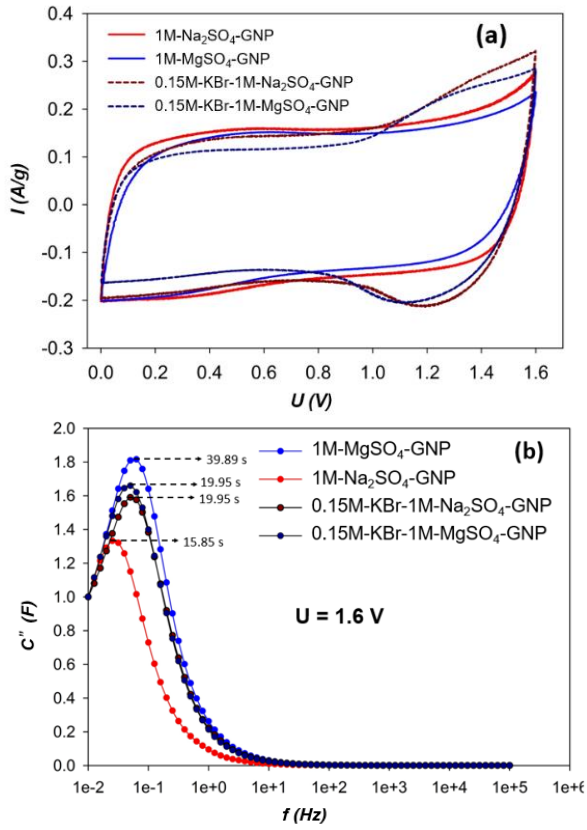

Figure 7.11: Comparisons between EEM cells fabricated with GNP and using the inert electrolytes 1.0 mol/L $MgSO_4$ or Na_2SO_4 with or without 0.15 mol/L KBr as additive (a) CV at U_L = 1.6 V, scan rate: 10 mV/s. (b) C'' *vs* f (Bode plot) at U_L = 1.6 V.

Thus, since the charge capacity of both 0.15M-NaBr-1M-Na_2SO_4-GNP and 0.15M-KBr-1M-$MgSO_4$-GNP are almost similar, it means that in the selection of supporting electrolyte the role of the dielectric properties of these electrolytes must be considered. Accordingly, this important finding might be extended to other combination of additives to critically understand the performance metrics that are actually improved when DRS are used in supercapatteries.

7.6 Chapter Summary

Electrochemical impedance spectroscopy (EIS) has been used to rigorously study the charge storage properties of two types of carbons i.e. GNP (mesoporous and highly-graphitised) and AC-2 (micoroporous and amorphous) which have surface oxygen groups (with similar C/O ratio). It was observed that due to the porous properties of GNP, the polarising power of the Li^+ to the Br^- has strong effects on the observed device features, however, this was not the case for AC-2. GNP displayed lower R_{CTR} when compared with AC-2, and this was attributed to both the surface physicochemical properties and also the presence of mesopores in GNP.

Furthermore, the strong sensitivity of the R_{CTR} of AC-2 with increase in U_L has been linked to the microporous properties of AC-2 which displays a high polarisation resistance. In general, with all electrolytes used, GNP displayed a higher specific capacity and energy coupled with better rate performance than AC-2. The faster degradation of cells with GNP compared to those with AC-2 were also attributed to the strong interaction between the Br^-/ (Br^-_3 + Br_2) and the GNP surface which could result to increased passivation. Moreover, the high rate performance of GNP relative to different cations i.e. Li^+, Na^+, and K^+ has been shown to be mainly due to its mesoporous properties.

From a device design standpoint the effects of KBr as redox additives to inert electrolytes of Na_2SO_4 or $MgSO_4$ with GNP as electrodes have been studied. Herein, it was shown that on the incorporation of the DRS, the response time of the device is reduced for the earlier, and increased for the latter. This observation has been attributed to the effects of ion-ion pairs on the permittivity of the electrolytes.

Summarily, since a possible trend in the early deployment of DRS in commercial cells may be in the areas of using additives. This finding is a

significant contribution to the understanding of the interplay between the solvation properties of the non-active counter-ions relative to the performance of the device.

CHAPTER 8: DISSOLVED QUINONOIDS AS REDOX ADDITIVES IN SUPERCAPATTERIES

8.1 Introduction

As was discussed in Ch. 2 (Literature Review), there are numerous organic molecules that could be used as dissolved redox species (DRS). Accordingly, most investigations in the literatures usually involve the selection of organic molecules and their use for capacity enhancement with little or no insights on their inherent mechanism of charge storage. Of the few fundamental studies that have focused on the mechanism of storage, there have been reports on the role of the carbon structure on the kinetics of redox reactions [246], the effects of the position of the substituent groups [96], and also density functional theoretical studies on the adsorption of some quinonoids on graphitic structures [247].

In this chapter, some fundamental studies relating to the mechanism of charge storage of quinonoids would be reported. Herein, 1,4 benzoquinone (hydroquinone), and its derivative with the methyl substituent i.e. 2-methyl, 1,4 benzoquinone (methyl hydroquinone) were studied as DRS. Although various substituents such as: Cl, Br, NH_2 etc., can be attached to a parent quinonoid, the methyl group as substituent was chosen in order to study any possible influence of the π-π interaction of these quinonoids with the carbons and how this may affect charge storage.

Furthermore, the adsorption of the redox species on the carbon electrode materials were studied using UV-vis spectroscopy, and this was correlated to the charge capacity. Additionally, Raman spectroscopy was employed to probe the mechanism of charge storage in carbons with different structural properties.

8.2 Study of the charge storage properties of activated carbon (AC-1) with quinonoids as redox additives

As was demonstrated in both Chs. 4 and 5, AC-1 is a high surface area, microporous carbon with very small amount of surface oxygen groups. As such it is a typical EDL electrode which can be appraised from the standpoint of capacity enhancement through the use of DRS. Hence, in this section, it was adopted as the electrode to understand some important properties of quinonoids as redox additives to acid (1.0 mol/L H_2SO_4) electrolyte. It should be noted that in this chapter, all the reports on the electrochemical characterisation of the carbon | electrolyte interface (conducted in the 3-electrode configuration) was carried out with a platinum micro-cavity (Pt-MC) electrode. The complete fabrication procedure for the Pt-MC electrode is presented in Section 8.3.2.

Figure 8.1 shows the cyclic voltammograms of AC-1 carbon material (loaded in the Pt-MC electrode) in a solution comprising of 0.1 mol/L of hydroquinone (H_2Q) or methyl-hydroquinone (MH_2Q) dissolved in 1.0 mol/L solution of H_2SO_4. As shown in Fig. 8.1, H_2Q expectedly has a more positive redox potential (ca. 0.42 V vs. SCE) compared to its derivative with the methyl substituent MH_2Q (ca. 0.37 V vs. SCE). This less positive electrode potential of the methyl substituted aromatic is attributed to the tendency of the methyl group to introduce additional electron density into the aromatic ring, resulting to the well-known "inductive effect" [248, 249].

With regards to selection as redox additives, since both molecules have similar solubility, there are some reasons why H_2Q may be preferable. For instance, due to its smaller molar mass (110.11 g/mol) compared to that of MH_2Q (124.14 g/mol) its theoretical charge capacity (Q_t) is ca. 12.0% larger. Furthermore, the slightly more positive electrode potential may be desirable because it could theoretically imply more energy gain from H_2Q. To test this

hypothesis, cells containing 0.25 mol/L of either H_2Q or MH_2Q in 1.0 mol/L H_2SO_4 were assembled with AC-1 electrodes.

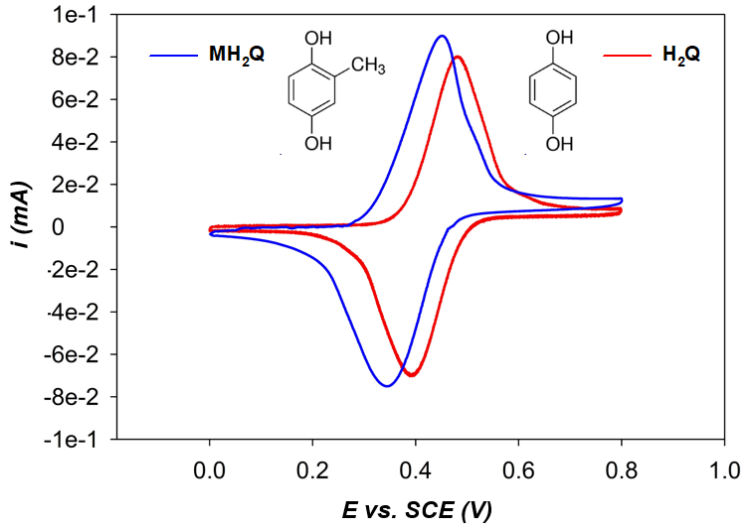

Figure 8.1: CVs of carbon material (AC-1) loaded in a Pt-MC electrode in an electrolyte comprising of 0.1 mol/L MH_2Q or H_2Q in 1.0 mol/L H_2SO_4. Scan rate: 10.0 mV/s.

Figure 8.2 shows the CVs of these two cells. As was observed from this figure, the different electrode potentials or theoretical charge capacity of these DRS did not correlate with the displayed (envisaged) performance features. Firstly, both cells displayed current peaks at low cell voltages. This is obviously linked to the electrode potentials of the DRS (E_N) which is in a narrow range within the stability limit of the supporting electrolyte. Thus, the features of the cells with these quinonoids as DRS were indicative of the redox reaction occurring on both the positrode and negatrode.

Furthermore, it was observed that the cell with MH_2Q displayed a higher charge capacity than that with H_2Q (considering the area of the current peaks at low cell voltage in Fig. 8.2). Note that both cells with DRS comprises of equal volume of electrolytes, and also, the apparent densities of both DRS solutions are similar.

These findings indicate that despite the higher molar mass and less positive E_N of MH_2Q, its normalised experimental charge capacity is still

greater than that of H_2Q. The reasons for this which may be linked to the surface coverage and/or adsorption of the DRS on the carbon would be addressed in Section 8.3.

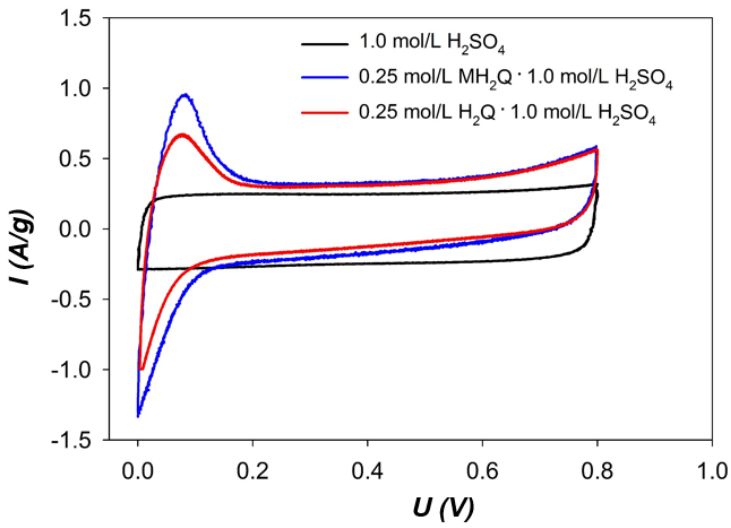

Figure 8.2: CVs of AC-1 EEM cells with equal volumes of inert 1.0 mol/L H_2SO_4 and 1.0 mol/L H_2SO_4 comprising of either 0.25 mol/L H_2Q or MH_2Q. Scan rate: 5.0 mV/s.

The one step de-protonation and two-electron transfer reaction illustrated in Fig. 8.3a has been proposed to be the redox mechanism of quinones in buffered or unbuffered H_2O in which $[H^+] > [Q]$. Where $[H^+]$ denotes the concentration of protons and [Q] is the concentration of quinone in the solution [114, 249]. Also, in unbuffered media with $[H^+] < [Q]$, it was shown that quinone would undergo an overall 2e reaction which would result in the formation of the strongly hydrogen bonded di-anion Q^{2-}. Accordingly, because this di-anion has a high basicity, the various protonation states i.e. Q^{2-}, QH^- and solvated hydroquinone (QH_2) would exist at equilibrium in the mixture [114]. Note that Q refers to the quinone moiety, (see Fig. 8.3b). Also, in aprotic media it was proposed that the reaction would proceed as the two step single electron transfer reaction illustrated in Fig. 8.3c.

It is important to point out that since the parent structure of quinones are generally not changed during electron transfer reactions [249, 250], these

redox mechanisms may also be used to describe the redox reaction of MH_2Q. However, the methyl-substituent would generally introduce differences in rate kinetics, for example, its orientation at the electrode surface would be different [249].

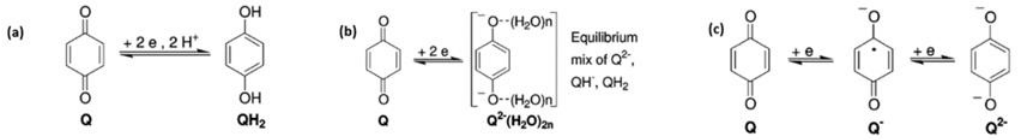

Figure 8.3: Illustration of the reaction mechanism of H_2Q in: (a) buffered or unbuffered H_2O with $[H^+] > [Q]$ (b) unbuffered media with $[H^+] < [Q]$ (c) aprotic media [114].

Generally, factors such as specific adsorption, degree of coverage, etc., which are of importance for charge storage, would be influenced by the stereo-chemical properties of the redox molecule. In line with this, the adsorption of the products from the redox reactions of these two quinonoids were analysed in detail. This analysis was done with the aid of the UV-vis technique, and the products from the redox reactions tested were the stable molecules Q and MQ which are the completely deprotonated (oxidised) derivatives of H_2Q and MH_2Q respectively.

8.3 Adsorption of dissolved redox quinonoids on activated carbon (AC-1) and its effects on device performance

In general, on charging the cells with acid electrolyte in which hydroquinone or methyl-hydroquinone are used as additives, the oxidation reaction at the positrode proceeds as shown in Fig 8.3a for H_2Q, and Fig 8.3b for MH_2Q. The oxidation process which involves the release of two electrons and de-protonation results to the formation of the respective quinone (Q) and methyl quinone (MQ) molecules from the starting dihydroquinone (H_2Q) and methyl dihydroquinone (MH_2Q) additives respectively. Accordingly, it is

possible to use spectroscopic methods to ascertain the adsorption of these species on the carbon.

The spectroscopic approach adopted follows a simple method to quantify the adsorption of various species on carbon, as was demonstrated in [141]. Briefly, the absorption spectrum of the analytes were ascertained before and after adsorption of the DRS by carbon. This was done by measuring the absorption of a known concentration of the analytes ca. 10.00 mM in ultrapure water (H_2O), and also obtaining the absorption of the solution corresponding to the concentration of the analytes remaining after carbon adsorption.

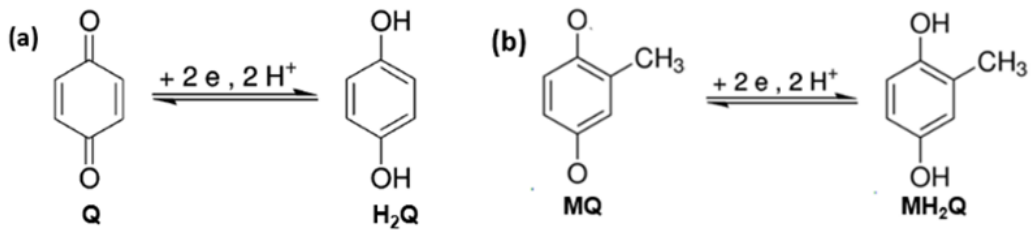

Figure 8.4: Illustration of the reaction mechanism of (a) H_2Q and (b) MH_2Q in unbuffered acid electrolyte.

To test the adsorption of analytes by carbon, 2.00 mL of 10.00 mM solutions of Q, and MQ were prepared in a centrifuge tube of 5.0 mL volume. Following this, the solutions were then degassed with argon (99.8%). Immediately after degassing, 5.00 mg of carbon (AC-1) electrode pellet were each placed in the centrifuge tube containing the solutions and were sealed immediately. After allowing the mixtures to rest for 1 hour, they were agitated for 10 minutes, and further allowed to rest for another 30 minutes. This equal waiting times were undertaken in order to ensure that the equilibration of the analytes are uniform. After this waiting period, the mixtures were then centrifuged for 5 minutes and the supernatant (10.00 μL) was measured from this mixture with the aid of a digital micropipette. This was then transferred into the cuvette for the UV-vis analysis. Note that these

agitation/centrifugation steps were adopted to aid the adsorption of the analytes on the carbon. The supernatant in the cuvette was further diluted (topped up to 2000.00 μL with ultrapure water) and this solution was then used for the absorption test with the UV-vis spectrophotometer. This step was repeated for all the analytes investigated. Also, 2000.00 μL of ultrapure water (equivalent to the total volume of all samples analysed) was used as the background for the UV-vis measurements.

Furthermore, to ascertain the concentration of analytes adsorbed by the carbon, the absorbance of varying concentrations of all the analytes from 2.00 mmol/L to 10.00 mmol/L were calibrated. It should be reiterated that since the protonated species of the analytes i.e. H_2Q and MH_2Q were used as the redox additives, it was assumed that the de-protonated species i.e. Q and MQ respectively, are adsorbed on the electrodes when the cells comprising of these DRS are charged (corresponding to oxidation of the DRS at the positrode in the cell).

Figure 8.5a shows the UV-vis spectra for the charged species (i.e. Q and MQ). Q(10 mM) and MQ(10 mM) corresponds respectively to the spectra for the analyte (Q) and (MQ) before adsorption by carbon, whilst Q(10mM) – Q_{carbon} and MQ(10mM) – MQ_{carbon} are the spectra corresponding to the concentration remaining after carbon adsorption of (Q) and (MQ) respectively. Calibration curves for the absorbance vs. concentration for the Q and MQ species are given in Fig. 8.5 b and c respectively. This curve was used to calculate the concentration corresponding to the measured absorbance.

In Table 8.1 the absorbance presented corresponds to the concentration remaining in the analyte $N_{0(\text{measured})}$ after carbon adsorption. Moreover, $N_{0(\text{adsorbed})}$ is the actual calculated amount of analyte adsorbed by the carbon. Recall that the initial 10.0 mM concentration of the analyte prepared were uniformly diluted (to about 200 times) for all samples analysed. From a reproducibility standpoint, a source of error for these series of experiments

was from the dilution process, however, this was made more accurate by careful solution preparation and sampling (during subsequent repeats of this experiment). Also, the maximum absorbance tested which was below ca. 0.70 but greater than 0.02 implied that the Beer-Lambert Law can be used to accurately ascertain the concentration measured. The accuracy of the parameters obtained was evident from the linearity of the calibration curves in Fig. 8.5 b1 and b2.

The spectra in Fig. 8.4 generally shows the similarities in absorption profile of the Q and its methyl substituent MQ, the slight shift in the wavelength for the MQ, can be linked to the spectroscopic feature of the electron inductive effects [251]. Moreover, for this study, what is of primary concern is the adsorption of these species on the carbon.

Accordingly, as observed from the spectra in Fig. 8.5a and Table 8.1, the MQ species adsorbs more on the carbon than the Q species. This comparatively higher amount of adsorption can be linked to the stereo-chemical properties of the MQ, which could generally favour a slightly stronger pi-pi interaction with the carbon surface. Note that in Section 8.2, the expression provided by Eq. 8.1, was used to argue that the theoretical charge capacity (Q_{sp}) of MH_2Q should be less than that of H_2Q.

$$Q_{sp} = \frac{nF}{M_w} \quad (8.1).$$

However, in practice, when the same concentration of these DRS were used for charge storage, as shown in the voltammogram of the cells presented in Fig. 8.2, it was pointed out that the MH_2Q provides a higher charge capacity than the H_2Q. (As stated earlier, the apparent mass densities of the solutions with these additives were similar, as such, equal volumes correlate to approximately equal mass in practice). In line with these observations, the experimentally observed charge capacity should be directly linked to the surface coverage (Γ). In actuality, this difference in charge capacity as related

to the adsorption by the redox species can actually be described with respect to Fig. 8.1. For example, since Fig. 8.1 obeys Nernst equation (i.e. is a reversible reaction) it follows that the charge capacity (C_q) on the carbon surface can then be expressed as:

$$C_Q = nFA\Gamma_t \qquad (8.4a).$$

Where Γ_t is the total amount of coverage by the active species, which in this respect is considered for the oxidised molecules MQ and Q from the oxidation of MH_2Q and H_2Q respectively. In fact, from Eq. 8.4b, which is the expression for the Nernstian current, it is obvious that the amount of coverage Γ_t has a multiplicative effect on the peak current. This essentially explains the higher peak current for the MH_2Q redox reaction compared to that of H_2Q as observed in Fig. 8.1.

$$i = \frac{n^2F^2A\Gamma_t v \exp\left[\left(E - E^o\right)\frac{nF}{RT}\right]}{RT\left\{1 + \exp\left[\left(E - E^o\right)\frac{nF}{RT}\right]\right\}} \qquad (8.4b).$$

This means that empirically, the surface coverage of the redox species within the porous matrix of the carbon determines the actual capacity. More importantly, this observation demonstrates the fundamental means in which different DRS can be rigorously characterised in practice.

In line with this, the higher charge capacity observed for MH_2Q is because the product of its charging (i.e. MQ) displays a higher surface adsorption/coverage on the carbon electrode (AC-1) in comparison to that of H_2Q (i.e. Q). In other words, MQ occupies more adsorption sites than Q. In general, this may be attributed to the stronger pi-pi interaction aided by orientation effects from the methyl substituent [252].

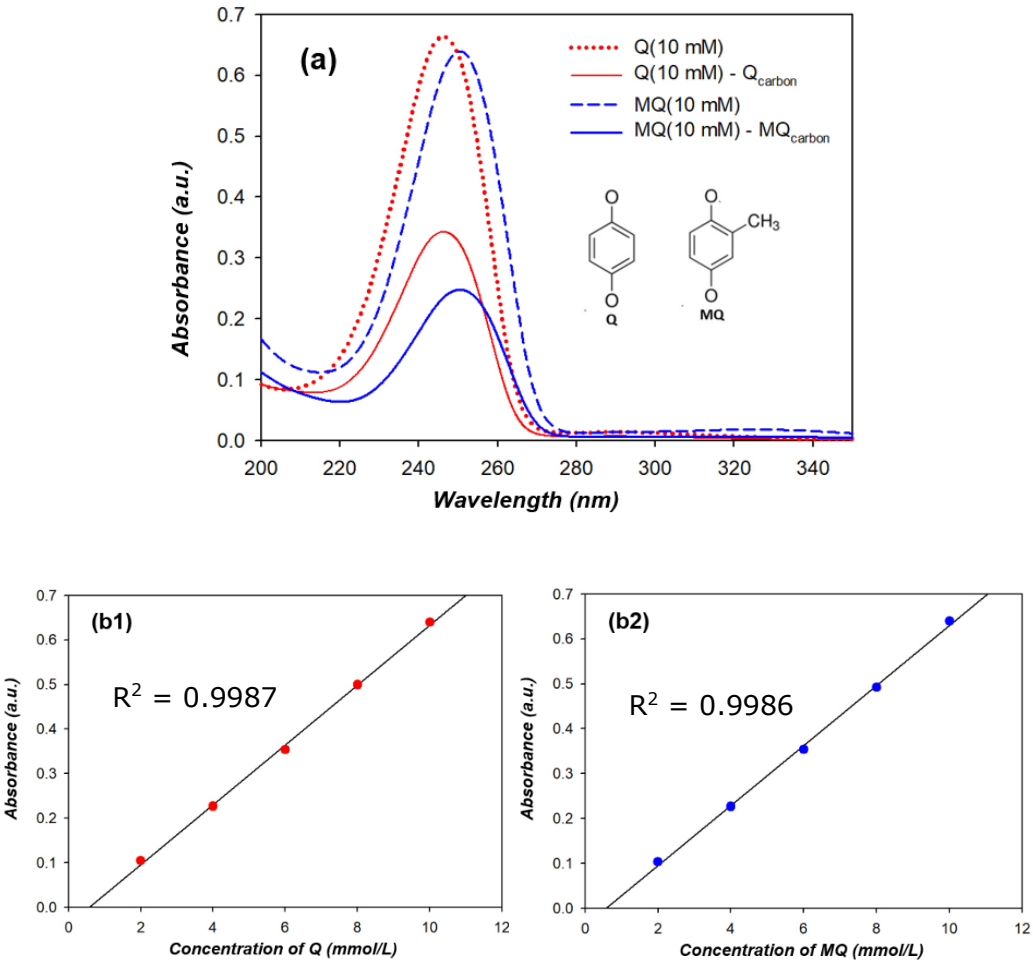

Figure 8.5: (a) UV-vis spectra showing the change in absorbance after the adsorption of Q or MQ from the solution by AC-1 electrode sheet (b) calibration curve for the correlation between the measured absorbance and the concentration of analyte solution for Q and MQ.

Table 8.1: Absorbance and concentration data for the concentration of analytes remaining after adsorption by carbon, from an initial N_0 of 10 mmol/L

Analyte - carbon	Absorbance (a.u.) / Wavelength (nm)	$N_{0(measured)}$ (mmol/L)	$N_{0(adsorbed)}$ (mmol/L)
Q-AC-1	0.34 / 246	5.13	0.0073
MQ-AC-1	0.25 / 250	4.02	0.0090

8.3.1 Performance of supercapatteries with MH_2Q or H_2Q as redox additives in organic electrolyte with AC-1 as electrodes

As was briefly highlighted in Ch. 2 (Literature Review), most commercial supercapacitors/devices adopts organic electrolytes in order to design cells with much higher voltages. Although this research is focused on the use of DRS in aqueous electrolytes, nevertheless, the properties of MH_2Q and H_2Q were further investigated as redox additives to an organic electrolyte of 1.0 mol/L tetraethyl ammonium tetrafluoroborate ($TEABF_4$) dissolved in acetonitrile. Note that these cells were assembled in a glove box with H_2O and O_2 contents of less than 0.5 ppm.

Figure 8.6 shows the CVs of the cells 1M-$TEABF_4$, 0.25M-H_2Q-1M-$TEABF_4$, and 0.25M-MH_2Q-1M-$TEABF_4$. From this figure, it was observed that both redox additives contributed to an increase in the capacity of the supercapattery, as evidenced from the additional contribution to the mass normalised current. For discussion purposes, the cell capacity (C_Q) of the supercapattery would be expressed in F/g. The cell with MH_2Q displayed a slightly higher C_Q of ca. 27.74 F/g compared to the cell with H_2Q which displayed a C_Q of ca. 24.66 F/g. In general this is an obvious increase from the initial C_{cell} with inert electrolyte which was ca. 17.51 F/g.

In the cell with either MH_2Q or H_2Q in organic media, the positrode was also undergoing the redox reaction as evidenced from the presence of small current waves (at low cell voltages). Also, the absence of peaks in the organic electrolyte could be due to the relatively different redox reaction mechanism of the MH_2Q and H_2Q in aprotic organic electrolytes. Generally, most quinonoids in aprotic media theoretically undergo the stepwise electron transfer reaction as illustrated in Fig. 8.2c [249], and this has been shown to result in mixed-Nernstian and capacitive mechanism on the positrode, which generally displays current waves as opposed to marked peaks [114, 250].

Also, the increased charge capacity obtained from MH_2Q further displays the advantage of its strong interaction with the carbon electrodes.

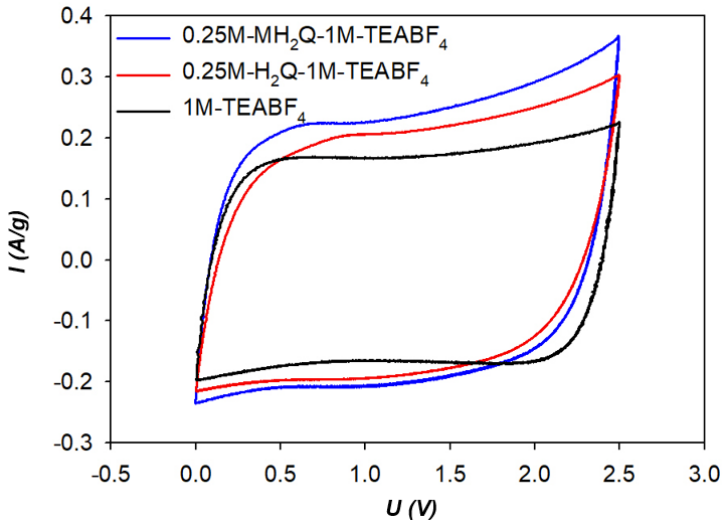

Figure 8.6: CVs of AC-1 EEM cells with equal volumes of inert 1.0 mol/L $TEABF_4$ in acetonitrile (AN) and comprising of either 0.25 mol/L H_2Q or MH_2Q. Scan rate: 10 mV/s.

The main novelty of these investigations is on the appraisal of the characteristics of MH_2Q as a redox additive for the first time, thereby elucidating the role of the methyl substituent on the quinonoid group. Accordingly, the subsequent sections of this chapter would focus on further use of MH_2Q as a redox additive.

It should be noted that the results from all the 3-electrode (E|E interface) characterisation presented in the remainder of this chapter were obtained with Pt-MC electrode which was used in characterising the properties of MH_2Q and H_2Q presented in Fig. 8.1. The detailed fabrication process of the Pt-MC electrodes used in this research would be described in the next section.

8.3.2 Fabrication of the platinum micro-cavity electrode

In the preparation of the Pt micro-cavity (Pt-MC) electrodes for this research, Pt wire of diameter 250 μm, was used. The Pt wire was heat sealed

inside one end of a glass capillary. Following this, the closed tip is polished with abrasive paper (P600, P1000, then P1500) to peel of the covering glass and to expose the microelectrode disc. Smoother abrasives (P3000 and P5000) were then used to polish the exposed microelectrode disc.

After each polishing step with the abrasive paper, the tip is sonicated in ethanol, and then in water for 30 seconds each. The obtained planar electrode is then polished with alumina (1 micron then 0.05 micron), and sonicated for 1 minute in water. To complete the electrode fabrication, graphite powder is added inside the capillary to make contact with the free end of the Pt wire, and then a copper connecting wire was inserted into this graphite powder thus creating a conductive connection. The wire was then sealed shut with quick-set epoxy, and the arrangement is allowed to dry for 24 hours.

Figure 4.1a shows the schematic diagram of the MCE. For the electrochemical calibration, firstly the planar micro-electrode (prior to forming the cavity) is used as the working electrode in a standard three-electrode cell (with Ag/Ag^+ and Pt-spade as reference and counter electrodes respectively). The electrolyte consists of 4.00 mmol/L of ferrocene in 0.30 mol/L of tetrabutyl ammoniumhexafluorophosphate ($TBAPF_6$) in acetonitrile. The cyclic voltammetry data was then used to estimate the real geometric area of the exposed Pt disc [253], by using the equation:

$$I_s = 4nFc_0Dr_e \qquad (8.3).$$

Where, I_s (A) is the steady state current, n the number of electron(s) exchanged in the redox reaction, F is Faraday constant, c_0 is the concentration of dissolved electroactive species ($mol.cm^{-3}$), *D* is the diffusion co-efficient of the DRS (ferrocene) and was taken as 2.3×10^{-9} m^2/s at 298 K [254].

For progressive etching of the tip of the Pt wire to form the cavity, the micro-electrode is dipped in *aqua-regia* (2 mL of conc. HNO_3 (68%) + 8 mL of conc. HCl (36%)) for 1 hour at 80 ^{0}C. After the etching procedure, further

electroanalysis is then utilised to estimate the recessed length of the cavity, through the use of the following expression:

$$I_s = \frac{4\pi F c_0 D r_e^2}{4L_0 + \pi r_e} \quad (8.4).$$

Herein, L_o is the estimated recessed length, and r_e is the radius of the cavity obtained from the electroanalysis with the planar microelectrode [253]. Fig. 8.8: (a) shows the schematic illustration of the cavity, (b and c) is its optical image, d is the geometric descriptions of the cavity used for the mathematical derivation of its dimensions. Figure 8.8e shows the SEM image of the cavity with the apparent diameter of the cavity calculated, the apparent depth of the recessed cavity and the lustrous surface of the Pt wire are obvious.

It should be pointed out that although the dimension of exposed Pt measured as shown from the SEM images gave the diameter of the etched cavity to be ca. 250.00 μm (Fig. 8.8e), the average diameter obtained from electroanalysis is ca. 230.25 μm (which is slightly less than the actual diameter). This may be attributed to the concavity of the exposed tip of the cavity as illustrated in Fig. 8.8d, and the general irregularity of the etched surface. Figure 8.9 shows a representative data of the bare Pt-MC electrode in 4 mmol/L ferrocene dissolved in acetonitrile containing 0.3 mol/L of $TBABF_6$.

To load the Pt-MC electrode with electrode material powders, it was gently pressed on a mound of the powder for several times, and the tip is then gently wiped with lint-free wipes to remove stray powders. In this research, the mass of the loaded materials in the cavity was also ascertained by a direct measurement of the loaded cavity with the aid of a microbalance (see Fig. 8.9).

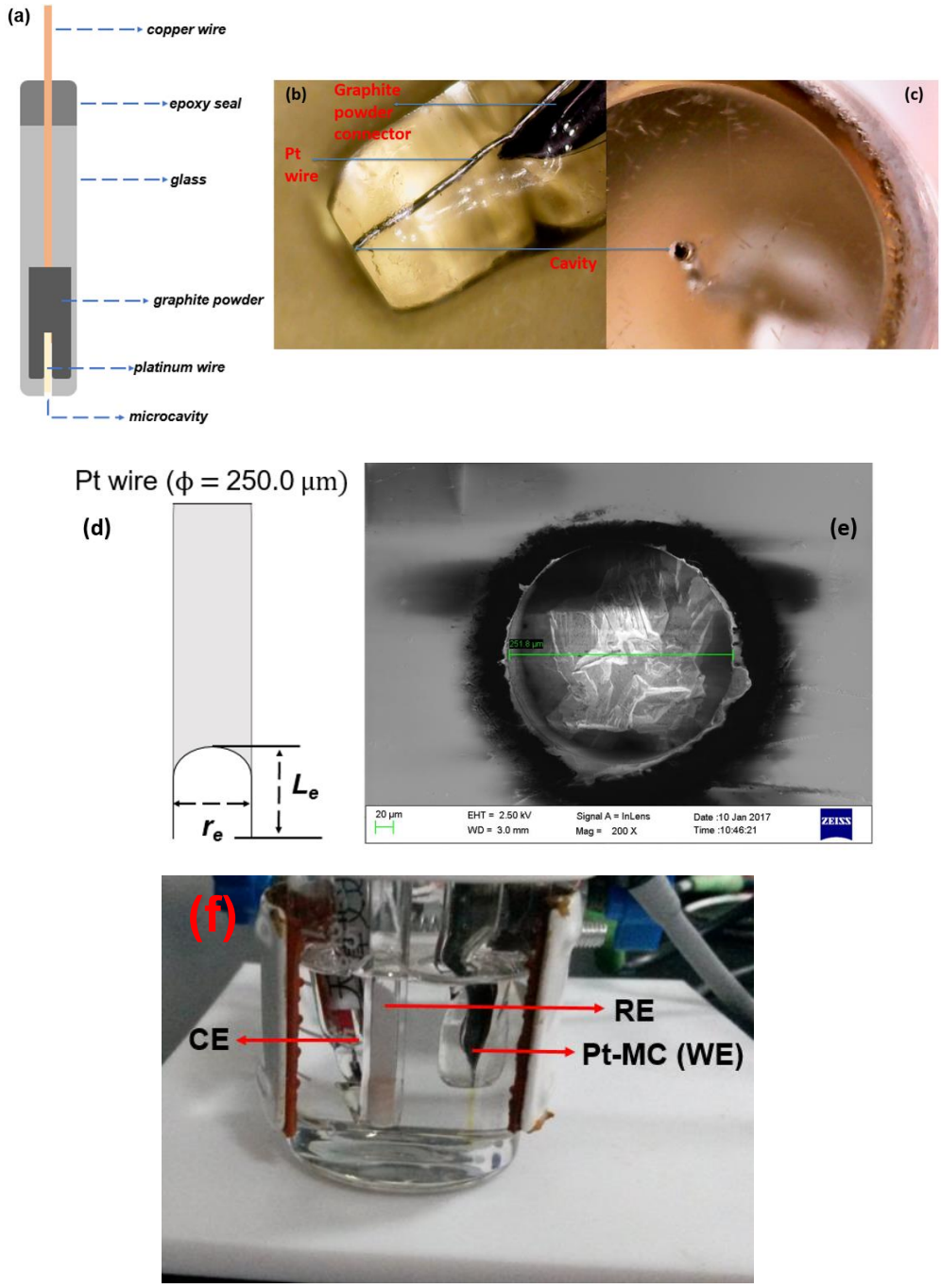

Figure 8.7: Pt-micro-cavity (Pt-MC) electrode (a) schematic illustration (b) and (c) optical micrograph (d) geometric description (e) scanning electron micrograph of the insides of the cavity (f) Pt-MC as the working electrode (WE), SCE as reference electrode (RE) and Pt foil as counter electrode (CE) in a 3-electrode cell which was pictured during electroanalysis as can be seen from the generation of species from the Pt-MC electrode.

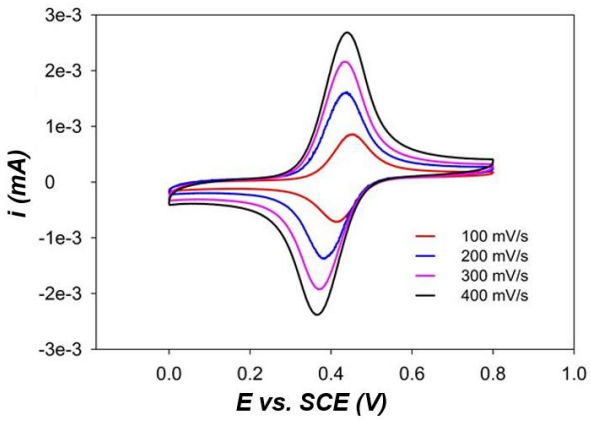

Figure 8.8: Representative CV at different scan rates of the bare Pt-MC electrode in 4 mmol/L ferrocene dissolved in acetonitrile containing 0.3 mol/L of $TBABF_4$.

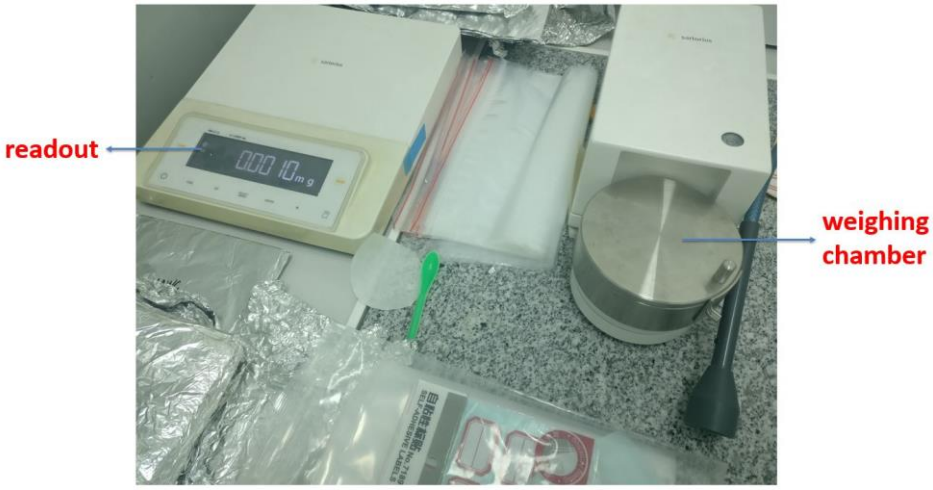

Figure 8.9: Microbalance (with a measuring range from 1.0 to 2000.0 µg) for direct weighing of the loaded MCE.

Moreover, the electrochemical analysis carried out to calibrate the dimensions of the cavity, were also used to indirectly ascertain the mass of the electrode materials. This approach was also important, because it further aids the accuracy of the gravimetric information obtained, and it is very useful when rapid analysis is to be carried out.

This indirect gravimetric method uses the geometric information of the cavity to ascertain the mass. Herein, the volume of the cavity (V_{cavity}) can be

obtained from the expression $\pi r_e^2 L_0$, where L_0 is derived from Eq. 8.4. As such, the mass of the loaded electrode material m_e can be obtained from:

$$m_{MCE} = \rho_T \times V_{cavity} \quad (8.5),$$

where ρ_T is the tapping density of the electrode material.

Table 8.2 shows representative values of loaded mass of materials obtained when the carbon electrode materials (in this case AC-1) were weighed directly, and ascertained from either indirect capacitance measurements or from the geometric information (tapping density and volume of cavity).

Sources of error for the indirect measurement may be linked to the tapping density measurement of the powder, coupled with the irregular surface of the base of the recessed cavity.

Table 8.2: Mass of loaded powder in the MCE obtained from different methods.

Method	**Mass loaded (µg)**
Direct measurement	507.5
Geometric calculation	532.1

Fig. 8.10 shows the CV of a loaded cavity in 1.0 mol/L solution of Na_2SO_4. The ideal rectangular shape of this CV at a high scan rate of 1000.0 mV/s can be attributed to the low *iR* drop of the Pt-MC electrode, making it a versatile tool for rapid and accurate electroanalysis.

Based on these rigorous attempts at improving the quantitative properties of the Pt-MC electrode, results for the detailed electroanalysis of MH_2Q as a DRS with the carbons employed in this research, are presented forthwith.

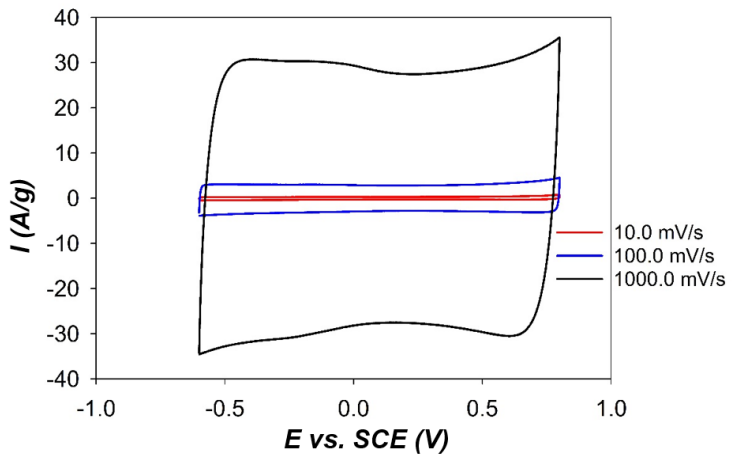

Figure 8.10: CVs at different scan rates of a Pt-MC electrode loaded with AC-1 powder in 1.0 mol/L Na_2SO_4.

8.4 Studies of MH_2Q as redox additives in aqueous electrolytes

Generally the stronger adsorption of the product of the MH_2Q redox reaction i.e. MQ, have been shown to proffer it with some desirable properties such as a larger charge capacity because it has more active sites. Moreover, it is necessary to understand the use of this quinonoid as redox additive to a neutral aqueous electrolyte, in order to further probe its fundamental properties.

Figure 8.11a presents the CVs of AC-1 powder loaded in the Pt-MC electrode in an inert unbuffered 1.0 mol/L Na_2SO_4 electrolyte with or without 0.25 mol/L of MH_2Q as additive. Figure 8.11 b and c presents the CVs and GCDs of the carbon | redox-electrolyte interface respectively.

The fundamental redox mechanism of the quinonoid group (i.e. hydroquinone) in unbuffered neutral aqueous media was illustrated in Fig. 8.2b. Although Fig. 8.2b provides this description for H_2Q, it should be pointed out that the quinonoid groups generally do not change their structure during redox reactions [249]. This is because the electron withdrawal/insertion simply occurs within the parent moiety, which in this instance was benzoquinone. Accordingly, this same description (Fig. 8.2b) can be applied to the redox mechanism of the methyl substituted quinone (MH_2Q) in unbuffered Na_2SO_4.

Of interest to this present discussion is the effects of the fundamental redox property of this quinonoid (MH_2Q) on the displayed charge storage property of the electrode. Accordingly, the broad waves exhibited in the CV for the solution with MH_2Q is reflective of this redox mechanism. That is, the overall 2e reaction results in different protonation states: MQ^{2-}, MQH^-, and MH_2Q which are all at equilibrium. Thus, it is the presence of these additional redox ionic states that contributes to the marked increase in the charge at the interface and also the current waves. Hence, this charge storage profile by the MH_2Q DRS in unbuffered neutral media is a combination of surface confined redox, and EDL-capacitance, mechanisms as reflected by both Fig. 8.11 b and c. It is also important to compare this with the storage mechanism of the MH_2Q in acid.

As seen from Fig. 8.12 a, due to the 2-electron transfer and de-protonation reaction of MH_2Q in acid media, the CVs corresponds to the peak shape already described in Section 8.2, and reviewed in Ch. 2. Hence the MH_2Q clearly displays a localised electron transfer around the electrode potential (band energy) of ca. E_N = 0.37 V vs SCE as might be inferred from either Fig. 8.12 a or b.

This difference in the redox mechanisms of the quinonoids in unbuffered neutral or acid electrolytes is of fundamental importance to the design of practical devices with this DRS. Figure 8.13 a and b shows the CVs of EEM cells (prototype devices) with MH_2Q additive in neutral and acid electrolytes respectively.

Therein, it was observed that the electrode charge storage features strongly affects the performance characteristics of the devices. For example the CV of Fig. 8.13a is semi-rectangular which demonstrates a predominance of the capacitive mechanism, whilst Fig. 8.13b clearly shows a contribution from both the Nernstian mechanism and the EDL-capacitive mechanism.

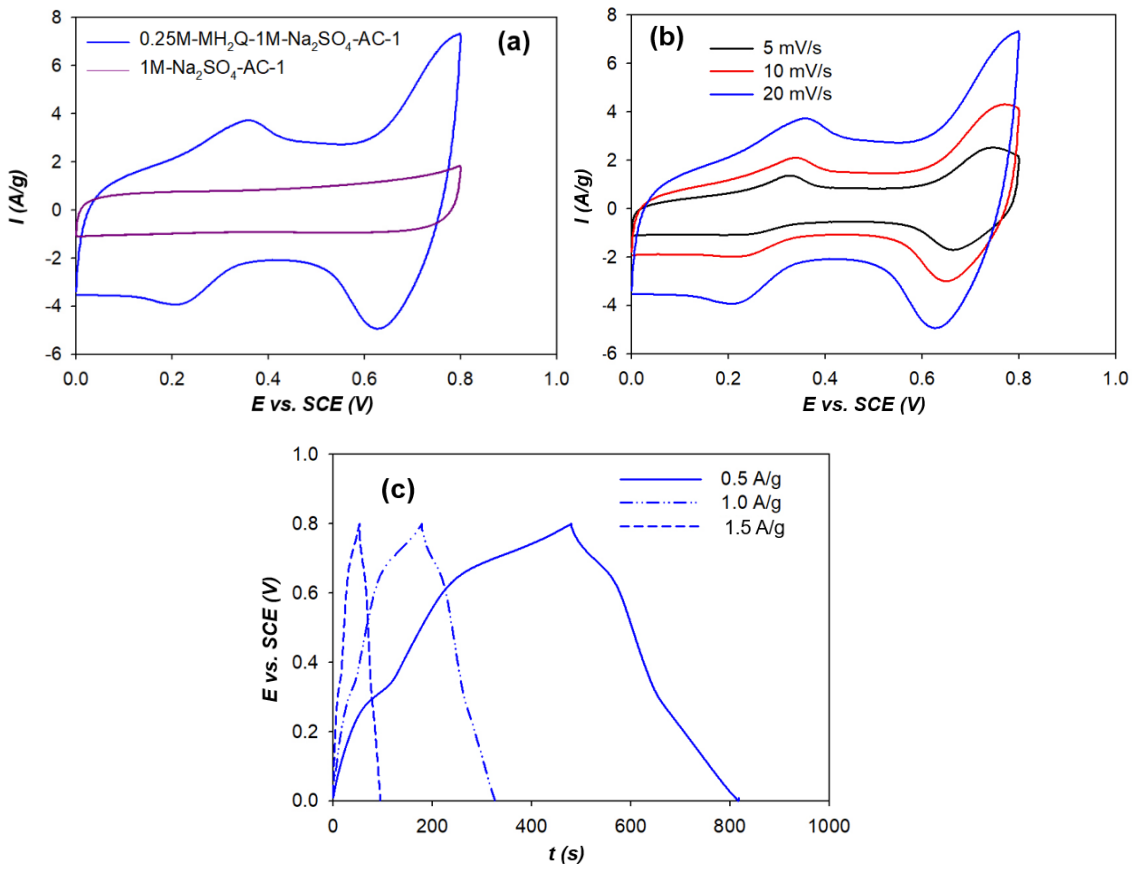

Figure 8.11: Pt-MC electrode loaded with AC-1 (a) CV in 1.0 mol/L Na_2SO_4 with or without 0.25 mol/L MH_2Q scan rate: 20 mV/s. (b) CV and (c) GCD in 0.25 mol/L MH_2Q in 1.0 mol/L Na_2SO_4.

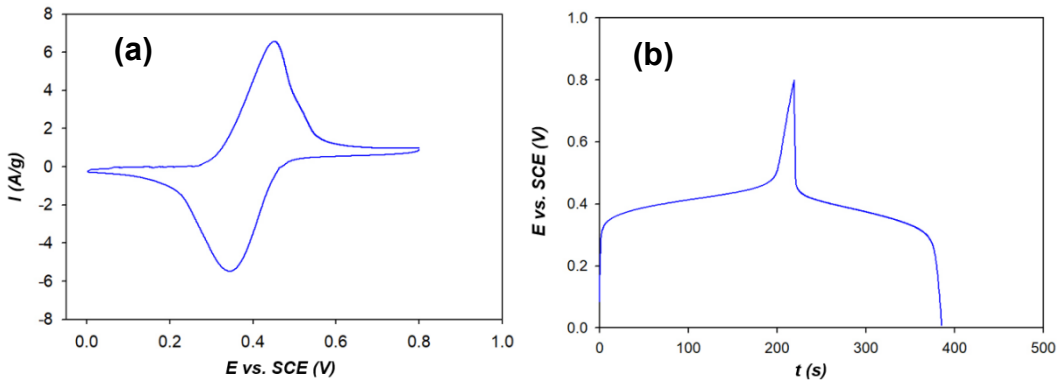

Figure 8.12: Pt-MC electrode loaded with AC-1 in 0.25 mol/L MH_2Q · 1.0 mol/L H_2SO_4 (a) CV, scan rate: 10 mV/s (b) GCD plot, I = 1.0 A/g.

It should also be pointed out that the charge capacity of the mixed faradaic and EDL-capacitance mechanisms of Fig. 8.11c or 8.12b cannot be described by the capacitance equation: $Q = C\Delta E$. Accordingly, this highlights

the significance of the term supercapattery as introduced to describe the resulting cells obtained from these electrodes (Fig. 8.13). And as has been discussed already (Ch. 4), the presence of the current peaks at low cell voltage for Fig. 8.13b is linked to the predominance of the Nernstian mechanism in the positrode (see Fig. 8.12b) conjoined with shuttling which results in the redox reaction occurring at both the positrode and negatrode.

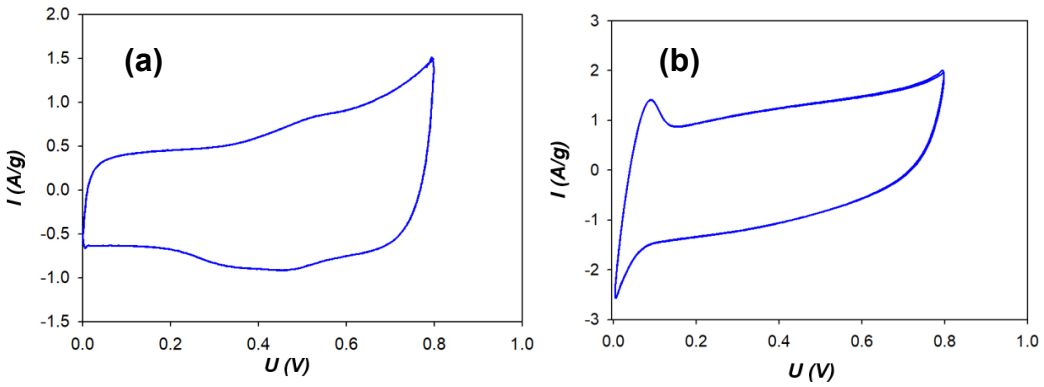

Figure 8.13: CVs of EEM cells containing 0.25 mol/L MH_2Q in (a) 1.0 mol/L Na_2SO_4 (b) 1.0 mol/L H_2SO_4. Scan rate: 10 mV/s.

In Ch. 9, a device engineering procedure to further enhance the charge capacity of the supercapattery with MH_2Q as DRS would be briefly introduced.

8.5 Correlating the redox reaction of MH_2Q with the structural properties of amorphous (AC-2) and highly graphitized (GNP) carbon electrode materials

Since the D and G bands of carbonaceous materials can be used to describe their electronic properties from the standpoint of their lattice structure, the interaction of the MH_2Q on the carbons i.e. AC-2 (amorphous) and GNP (highly graphitised) were further studied with the aid of Raman spectroscopy. Moreover, prior to the descriptions from the structural analysis, electrochemical studies of the redox mechanism of MH_2Q on the two carbons would be presented. It should be re-emphasized that the adoption of spectroscopic techniques in this research was based on the fundamental

principle that the redox mechanisms of these DRS occur in the adsorbed states on the electrode as has been described in Ch.2. Thus, the difference between the use of Raman spectroscopy and UV-vis for these analysis are:

(i) The UV-vis technique was used to ascertain the amount of DRS adsorbed by the carbon.

(ii) Raman spectroscopy was used to further probe the structural interaction between the adsorbed DRS and the carbon.

For the Raman spectroscopy investigations, two different types of adsorption were appraised. Firstly, GNP or AC-2 which have adsorbed MQ (product of the reaction of MH_2Q) as obtained from the procedure described for the UV-vis experiments were analysed. Secondly, GNP and AC-2 electrodes which have been polarised (0.4 V vs. SCE) in an electrolyte solution containing MH_2Q were also assessed.

The sheet resistances of the GNP and AC-2 were ascertained to be 48.45×10^{-6} Ω.cm and 214.24×10^{-6} Ω.cm respectively. Generally, the main reason for employing the Pt-MC electrode in this research was because it allows electroanalysis with inherently small *iR* drops as shown in Fig. 8.14c which presents the CV before and after *iR* correction. Fig. 8.14 a and b shows the CVs of the bare Pt-MC electrode and comparison of the loaded Pt-MC electrode with the unloaded one respectively.

Figure 8.15 a1 and b1 presents the CVs at different scan rates of the Pt-MC electrode loaded with GNP and AC-2 respectively. As was confirmed from the Randles-Sevcik (I vs $v^{1/2}$) plot from both CVs (Fig. 8.15 a2 and b2 for GNP and AC-2 respectively), it was observed that the redox reaction of MH_2Q at both carbons was surface controlled. These plots also showed the effects of the diffusion of the species to and from the electrode. This can be inferred from the symmetry of the anodic and cathodic peak currents as shown in Fig. 8.15 a2 and b2. In general, the effects of the resistivity of the AC-2 electrode can

also be observed from the CV (Fig. 8.15 b1). Furthermore, since the effects of the *iR* drop is negligible for the Pt-MC electrode, the apparent difference in the peak-to-peak separation could give a general insight as to the kinetics of the MH_2Q/MQ reaction at the surface of the carbons. In general, a faster apparent rate kinetics was observed for the GNP carbon material.

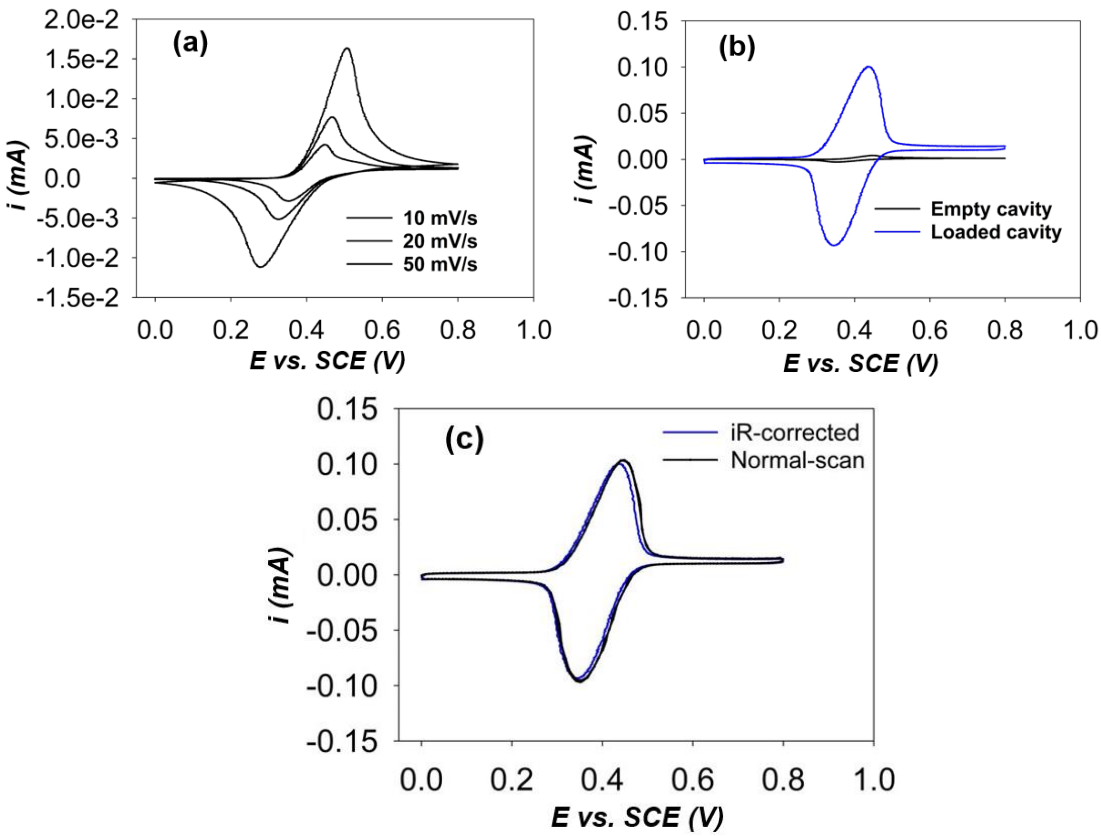

Figure 8.14: CVs showing the *iR* correction procedures of the Pt-MC electrode (a) bare Pt-MC electrode (b) loaded (GNP) and bare Pt-MC electrode and (c) *iR* correction of loaded Pt-MC electrode (scan rate: 10 mV/s). Electrolyte is 0.25 mol/L MH_2Q in 1.0 mol/L H_2SO_4.

Further confirmation of this could be observed from the comparison between the CVs at 50 mV/s and the impedance spectra for the carbons as presented in Fig. 8.16. Due to the surface confined redox reaction and low *iR* attributed to a negligibly small background current, the R_{ESR} (equivalent series resistance) for both carbons are similar. Moreover, the comparatively higher R_{CTR} (charge transfer resistance) for the reaction of MH_2Q at AC-2 carbon material could be linked to the slower rate kinetics at this carbon material.

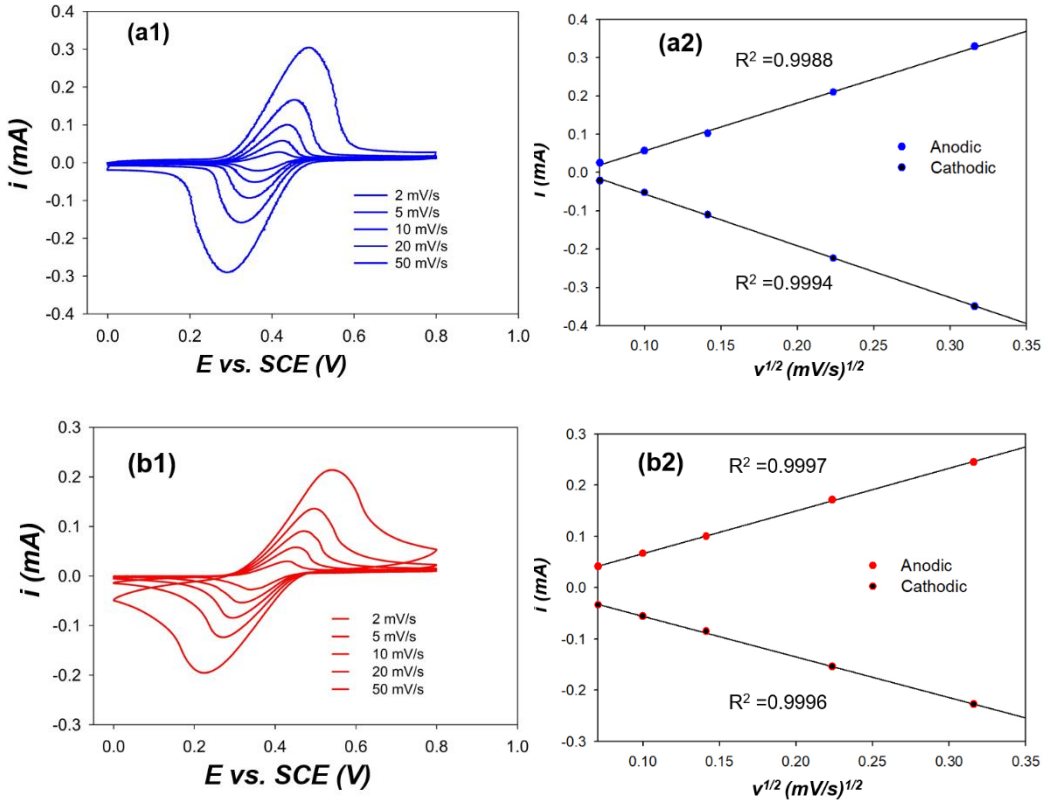

Figure 8.15: CVs of Pt-MC electrode loaded with (a1) GNP (b1) AC-2 and the corresponding i_p vs $v^{1/2}$ plots (a2) GNP (b2).

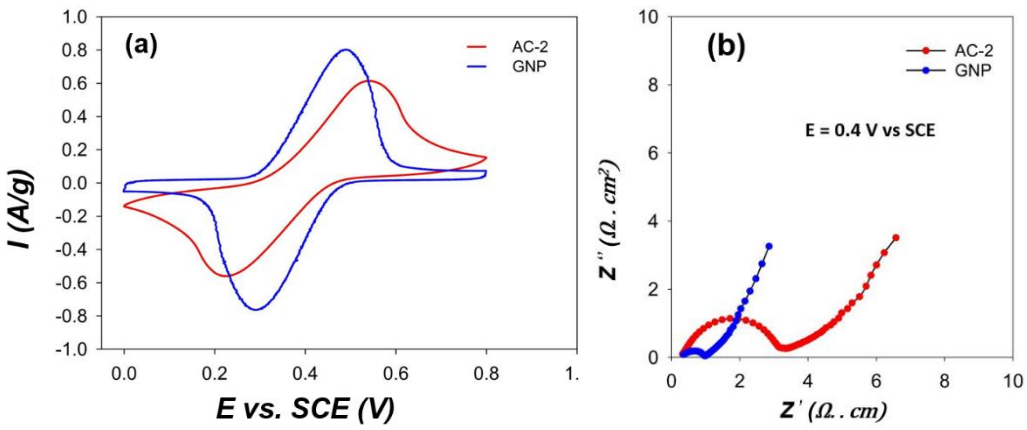

Figure 8.16: Comparison of the loaded Pt-MC electrodes (a) CV at 50 mV/s (b) Nyquist plot at 0.4 V vs SCE.

In line with this electroanalysis, the main reason for the investigation of the novel MH_2Q with a highly graphitized carbon (i.e. GNP), is to observe the structural basis of the reaction of this dissolved redox species with carbon.

Figure 8.19 a and b presents the Raman spectra for GNP and AC-2 respectively. Each figure comprises of the spectra of the as-received carbon, and carbons that have been polarised in a solution of MH_2Q to oxidise the DRS, and also carbon that has adsorbed the oxidised product (MQ) following similar process as was described in Section 8.3. Figure 8.19c plots the I_D/I_G ratio measured for the carbons.

The most dominant features from the Raman spectrum of graphitic materials are the D (around ca. 1357 cm^{-1}), G (around ca. 1580 cm^{-1}) and the 2D or (G^*) (between ca. 2700 cm^{-1} and 2900 cm^{-1}) bands, with the approximate position of the intensities given at a laser energy of 2.54 eV [255]. Generally, the D and G band can be used to obtain the relative crystalinity (or degree of graphitization) of carbon materials. This is because, the G band can be linked to the stretching of the C-C bond within the graphitic hexagonal lattice of carbons, and the D band corresponds to defects in the sp^2 structure of the carbon. Relatedly, the 2D band is an overtone of the D band which could be linked to phonon scattering within the interstitial layers of the graphitic structures of the carbon material. From fundamental considerations, pristine graphene would not display the D band, however, for stacked sheets of graphene i.e. graphite, soot, amorphous carbons, etc. the D band is marked due to the introduction of structural defects [255-257]. Thus, the D and G bands was observed for both as received GNP (black curve in Fig. 8.17a) and AC-2 (black curve in Fig. 8.17b).

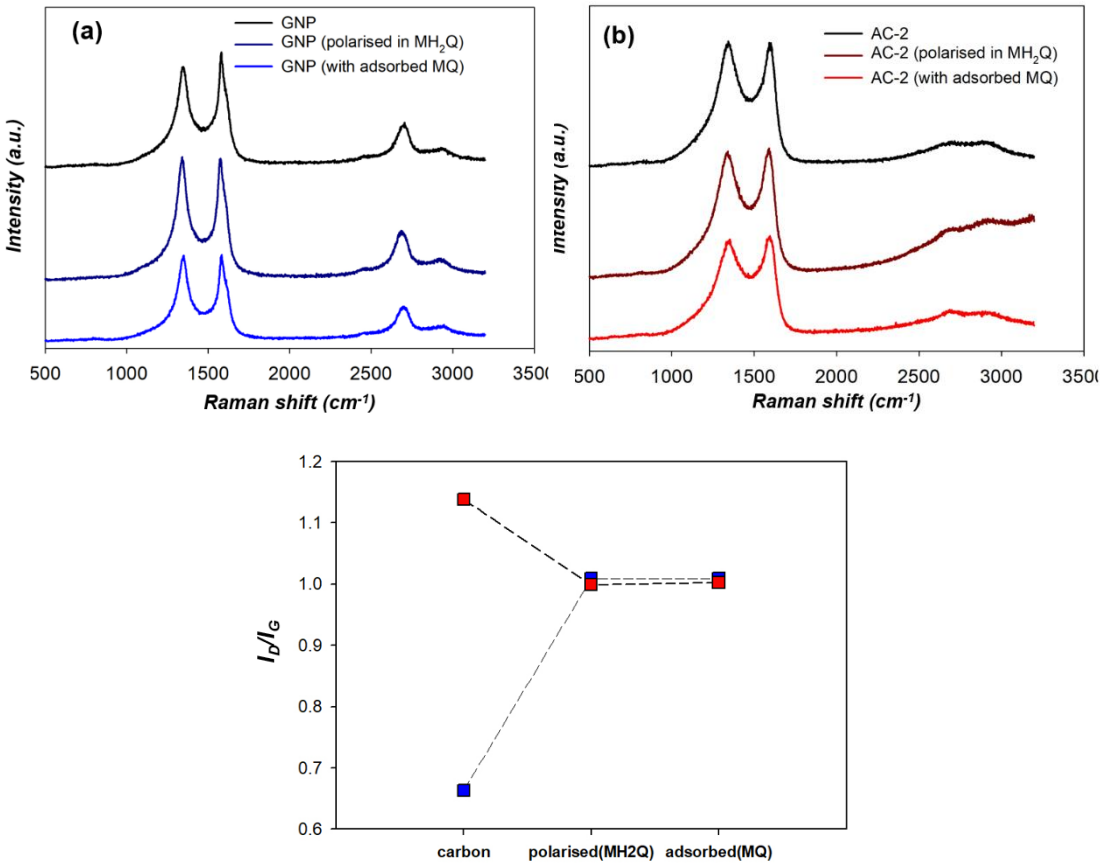

Figure 8.17: Raman spectra for: GNP (a) and AC-2 (b). Comparison of the I_D/I_G ratio for both GNP and AC-2 (c).

However, as observed from Fig. 8.17a, the D band of as received GNP is significantly lower than its G band, and its displayed 2D band features which is broad and right-shifted is indicative of stacked layers of graphene sheets [256], whilst the larger broadening of the 2D band in AC-2 is indicative of highly defective interstitial lattices as expected for amorphous carbons [255].

Notice also, that AC-2 displays a slight broadening of both the D, G and 2D bands compared to GNP, which in addition to its much relatively higher D band, implies that the structural defects of AC-2 is higher than that of GNP. In general, GNP displays the features of multilayer graphene characterised by highly ordered sp^2 bonded hexagonal graphite structures stacked together with the aid of Van der Waals forces but still defective around the edges and through in-plane stacking mechanisms [256, 258].

Moreover, for the sake of discussions when comparing such carbon materials, the I_D/I_G ratio is of utmost significance as it describes the degree of disorder of carbon materials, and this degree of disorder can thus be linked to a combined role of defects, interaction of heteroatoms and general change in the electronic properties of these materials. From the Raman spectra it was observed that the I_D/I_G ratio for both carbons polarised in an electrolyte solution containing MH_2Q and with MQ adsorbed on it are similar (cf. the dark red and red curves in Fig. 8.17a) and (cf. the dark blue and blue curves in Fig. 8.17b). This confirms that the charged species generated as a result of the redox reaction is the MQ species. Moreover, the most significant finding from the spectra is the increase in the disorder of the GNP compared to what was observed for the AC-2 as seen in Fig. 8.19c. This confirms that the redox mechanism of the MH_2Q at the GNP surface is aided by the electron transfer within the interstices of the GNP material possibly due to electroactive edge-planes [259, 260].

This is consistent with experimental investigations of the redox activity of graphene which has shown that both the basal and edge planes display acute electrochemical activity, and that the local microscopic condition (oxygenation, structure etc.) has marked influences on the observed electrochemical properties [261].

Thusly the higher surface area of AC-2 in comparison to GNP does not aid in increased charge storage property with redox electrolytes, because the electrosorption properties confirmed here is also dependent on the morphologically determined electronic structure of the layered-graphenic structure of GNP. Evidently, this finding would aid in the selection and effective coupling of such quinonoids with highly graphitized carbons.

8.6 Chapter summary

H_2Q (hydroquinone) and MH_2Q (methyl-hydroquinone) were used as organic redox molecules. It was observed that a possible stronger interaction of the MH_2Q leading to improved adsorption on the carbon is influential in its comparatively higher charge capacity increase in both aqueous and organic electrolytes.

Also, by designing a Pt micro-cavity (Pt-MC) electrode, detailed electroanalysis of MH_2Q has been carried out. Accordingly, the charge storage mechanism of this DRS in acid or neutral supporting electrolytes, and its redox properties with an amorphous (AC-2) and highly graphitised (GNP) carbons have been characterised.

It was also revealed that the electronic structure as determined by the morphology and presence of oxygen heteroatoms on the GNP electrode strongly affects its interaction with MH_2Q. Accordingly, for the first time a molecular basis to the increased rate kinetics of quinones on graphenic surfaces have been demonstrated through basic Raman spectroscopic studies.

CHAPTER 9: DESIGN OF HIGH PERFORMANCE BI-ELECTROLYTE SUPERCAPATTERIES

9.1 Introduction

In Ch. 4, the bi-electrolyte cell with configuration (-)AC | 2.0 mol/L KOH || 2.0 mol/L KI | AC(+) was used to demonstrate what we termed as "forced confinement" of the redox activity. Therein, redox shuttling was eliminated and the charge due to the Nernstian contribution was stored at higher cell voltages. This was shown to be in contrast to the conventional KI cells which were characterised by current peaks at low cell voltages. In this chapter, a detailed investigation of the properties of bi-electrolyte cells would be presented.

In line with this, a novel immiscible bi-electrolyte cell which displayed high maximum charging voltage (MCV) and slow rate of self-discharge would be demonstrated.

9.2 Fundamental design of bi-electrolyte cells

With respect to EDL capacitors, a bi-electrolyte cell is one in which the full capacitive potential range (CPR) of both the positrode and negatrode are attained due to the compartmentalization of the negatrode | negalyte (N|N) and positrode | posilyte (P|P) interfaces. Note that the negalyte and posilyte are the electrolytes in contact with, or incorporated in, the active materials of the negatrode and positrode respectively. This compartmentalisation can be achieved with the aid of porous membrane(s) or ion conductors which physically separates the two interfaces. The general cell assembly procedure used throughout this research was described in Ch.3 (see Section 3.6, Figs. 3.21 [a and d] and 3.22).

The most important feature of the bi-electrolyte cell is the use of two GF/D membranes soaked in another electrolyte called the membrane

electrolyte (ME). As illustrated in Fig. 3.21a, the bi-electrolyte cell can also be assembled with a reference electrode which is used to monitor the potential variation of the positrode and negatrode when the cell is under operation. When required, an Ag wire coated with Ag/Cl was used as a pseudo reference-electrode, and this was calibrated as 0.06 V vs. a commercial standard calomel electrode (SCE).

Before describing the properties of these bi-electrolyte cells, a brief synopsis of the CPR of activated carbon (AC) electrode in different aqueous electrolytes would be given. Also, it should be noted that the activated carbon electrode used throughout this chapter and herein known as AC is AC-1 which has low surface oxygen content, and is highly micoroporous with a large surface area (see Ch. 4).

Figure 9.1 shows the CPR_{max} (maximum capacitive potential range) of AC electrode in 2.0 mol/L KOH, 1.0 mol/L Na_2SO_4, and 1.0 mol/L H_2SO_4, alkaline, acidic and neutral solutions respectively. The comparison between the CVs of AC in these electrolytes can be used to ascertain the maximum capacitive voltage (MCV) which these conventional aqueous electrolytes may exhibit when used in EDL capacitors. With respect to selection for use in a bi-electrolyte cell, the CVs of Fig. 9.1 shows that AC in KOH can be shifted towards more negative potentials. This has been attributed to the possibility of storing so-called "nascent hydrogen" which is generated during the onset of the cathodic decomposition of water [241, 262].

Also, the choice of 2.0 mol/L KOH is because the concentration of posilytes which may be used usually range from 1.0 to 4.0 mol/L, and as such 2.0 mol/L KOH could ensure that the concentration difference between the compartments is not too high.

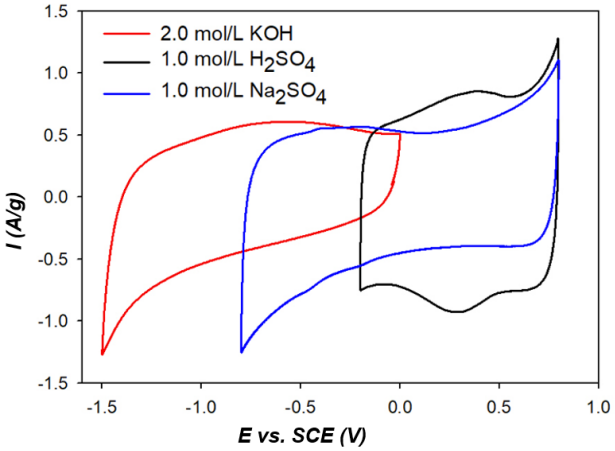

Figure 9.1: CVs showing the maximum possible capacitive potential range of AC electrode in common aqueous electrolytes of different pH. Scan rate: 5 mV/s.

Note that in practice, the CVs in Fig. 9.1 also includes potential regions that may not be reversibly capacitive or involves reversible non-EDL type redox storage e.g. chemisorption (for example, consider the behaviour of the electrode in KOH [red curve] at more negative potentials). Accordingly, these CVs essentially shows the absolute range that could contribute to the capacitive properties of EDL capacitors. In line with this, factors such as the physicochemistry of the electrode's surface, variation of pH (if the solutions are buffered), etc., would become significant in defining the capacitive properties of the electrode/electrolyte combination.

Furthermore, although there are other salts which could exemplify these capacitive potential ranges in aqueous electrolytes, still, some general constraints may limit the adoption of some common choices. For instance, AC in a solution of K_2SO_4 would display a higher EDL capacitance compared to a similar concentration of Na_2SO_4. This could be attributed to the smaller radius of the hydrated K^+ ion [263]. However, the lower solubility of K_2SO_4 in water may preclude its use.

Additionally, the adoption of KNO_3 which actually displays a relatively high CPR is discouraged owing to the strong oxidation power of the NO_3^- anion

[264] which could result in fast degradation of the carbon electrode and spurious interactions especially at high U_L when the electrodes are assembled in a cell. Accordingly, from the foregoing descriptions the solutions of Na_2SO_4 and H_2SO_4 could be used as posilytes, whilst KOH is an appropriate negalyte.

9.3 Bi-electrolyte supercapattery coupling inert negalyte with redox posilyte

Figure 9.2 shows the CVs of the AC electrode in the KOH and KI negalyte and posilyte respectively. As expected the KOH displayed EDL properties whilst the KI is Nernstian. Accordingly these two components can then be used to assemble the bi-electrolyte cell with the configuration: (-)AC | 2.0 mol/L KOH || 1.0 mol/L KI | AC(+).

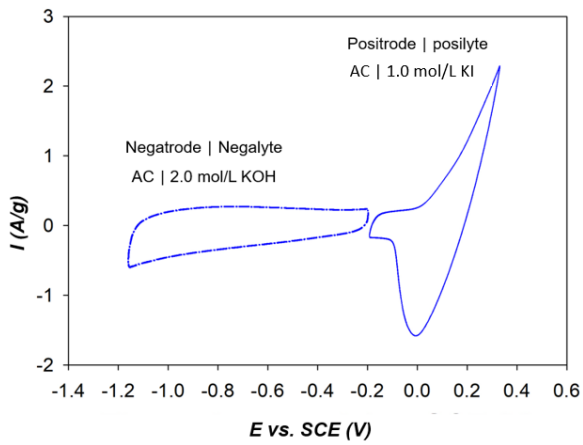

Figure 9.2: CVs of the AC electrode in 2.0 mol/L KOH negalyte and 1.0 mol/L KI posilyte. Scan rate: 1 mV/s.

In the bi-electrolyte cell, it is important to note that the electrolyte solution in which the membranes are soaked i.e. the membrane electrolyte (ME) should possess high conductivity, and the diffusivities of its constituent ions must be similar. The latter characteristic is very important because it is necessary that the ME do not introduce any detrimental liquid junction potential.

KCl was mainly investigated as a ME, and in order to understand the role of the ME in the device performance, it was also compared with Na_2SO_4 as ME. Figure 9.3 shows the CVs of the bi-electrolyte cell (-)AC | 2.0 mol/L KOH || 1.0 mol/L KI | AC(+) assembled with either 1.0, 3.0 mol/L KCl or 1.0 mol/L Na_2SO_4 as the membrane electrolyte (ME).

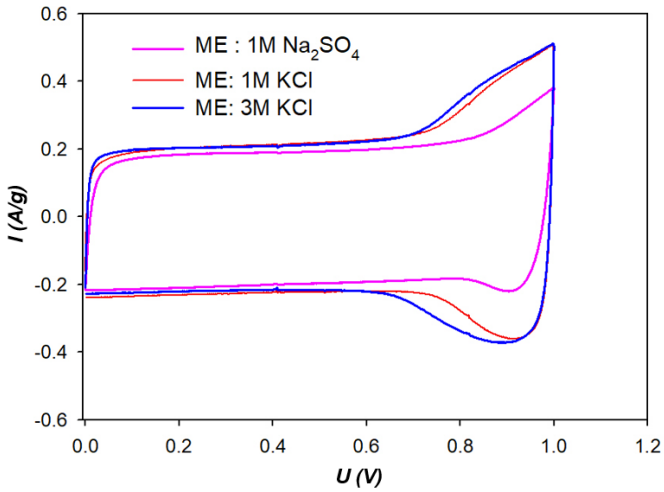

Figure 9.3: CVs of (-)AC | 2.0 mol/L KOH || 1.0 mol/L KI | AC(+) bi-electrolyte supercapatteries with different membrane electrolytes. U_L = 1.0 V, scan rate: 5 mV/s.

As presented in Fig. 9.3, the cell with 1.0 mol/L Na_2SO_4 as ME displayed the least capacity whilst the capacity of the cell with 3.0 mol/L KCl as ME is the largest. Noticeably, the faradaic contribution from the cell with 1.0 mol/L Na_2SO_4 ME is actually very small, and this can be explained from the standpoint of the different single ion conductivities of Na^+ and SO_4^{2-} i.e. 50 and 158 $cm^2/mol.\Omega$ respectively [265]. This reduces the effectiveness of diffusion and possible migration (during dis-/charging) of dissolved ions which is necessary for optimal operation of the cell. On the other hand, the adequately comparable single ion conductivities of K^+ and Cl^- i.e. 74 and 76 $cm^2/mol.\Omega$ [265] respectively, can be identified as the reason for the better performance of the cells with KCl as ME. The rate performance of the cells with 1.0 and 3.0 mol/L KCl as ME are presented in Fig. 9.4. It was observed that the bi-electrolyte cell

with 3.0 mol/L KCl as ME displayed a better rate performance compared to the cell with 1.0 mol/L KCl. This was expected as the preceding descriptions showed. In line with these displayed characteristics, 3.0 mol/L KCl was used as the membrane electrolyte in all the bi-electrolyte cells reported in this research.

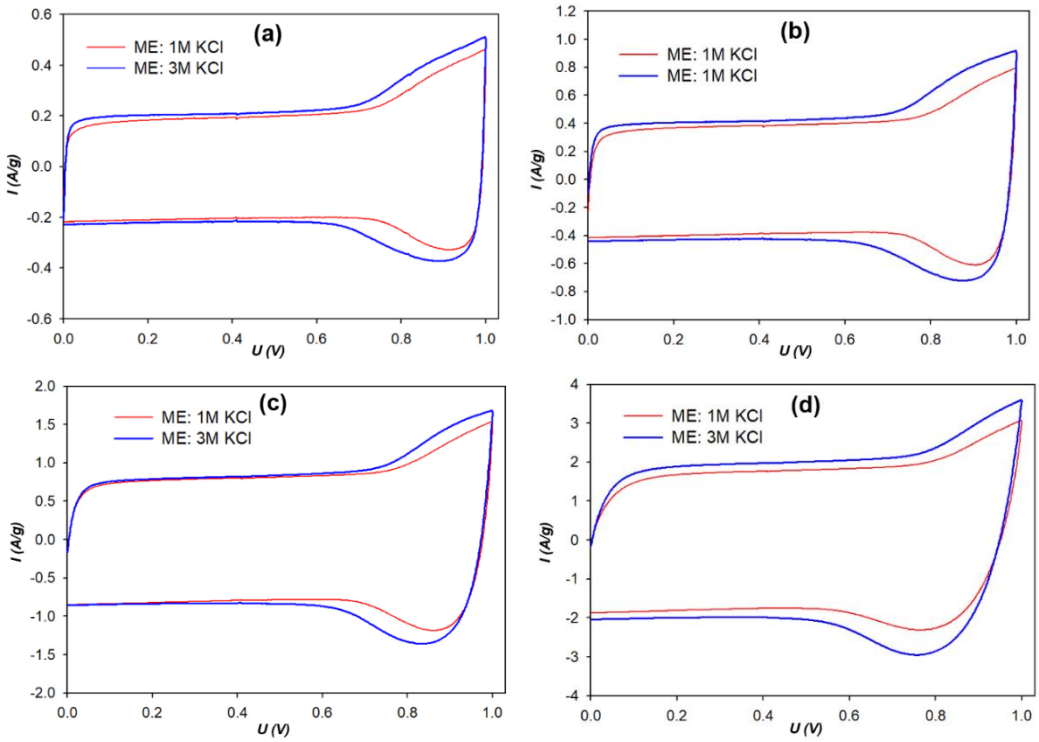

Figure 9.4: CVs showing rate performance for (-)AC | 2.0 mol/L KOH || 1.0 mol/L KI | AC(+) with either 1.0 or 3.0 mol/L KCl as membrane electrolyte: (a) 5 mV/s (b) 10 mV/s (c) 20 mV/s (d) 50 mV/s.

9.3.1 Effects of redox posilyte concentration on the performance of bi-electrolyte cells

The charge capacity (Q) resulting from the Nernstian charging of electrodes with redox electrolytes could be given as: $Q = nFV_0N_0$ (where n, F, V_0, and N_0 are the number of electrons, Faraday's constant, volume of solution, and concentration respectively). Accordingly, the effect of changing the

concentration of the posilyte was investigated by preparing three different bi-electrolyte cells (-)AC | 2.0 mol/L KOH || x mol/L KI | AC(+), where x = 1.0, 2.0, or 3.0 mol/L KI. Figure 9.5 presents the CVs of these cells.

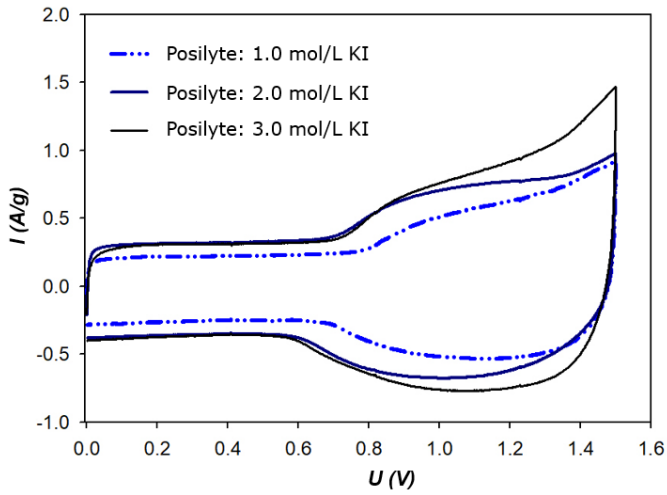

Figure 9.5: CVs for the bi-electrolyte cells (-)AC | 2.0 mol/L KOH || 1.0, 2.0 or 3.0 mol/L KI | AC(+). U_L = 1.5 V, scan rate: 5 mV/s.

From the CVs in Fig. 9.5, the contribution from the redox activity of I^- / (I_2 + I_3^-) was observed to increase with increase in the concentration of the posilyte. Note that since these cells were designed without excess electrolyte, the volume of electrolyte absorbed by the similar positrodes were approximately the same. Accordingly, the increase in capacity of the Nernstian portion of the cell (U_L > 0.8 V) can be attributed to the direct proportionality of the current generated with increase in concentration of the DRS which is in agreement with expectations.

However, whilst the EDL dis-/charging portion of the cells (U_L < 0.8 V) with 2.0 and 3.0 mol/L KI posilyte were similar, that for the cell with 1.0 mol/L KI posilyte is lower. This is linked to the difference in the polarisation of the electrodes and conductivity of the posilyte, because the P|P interface also contributed to the EDL features of these cells (for instance, see Fig. 9.7b). Furthermore, the sharp current rise at U_L > 1.4 V which was obvious for the

cell with 3.0 mol/L KI as posilyte, and less so for the cell with 2.0 or 1.0 mol/L KI posilyte, was as a result of the increase in the redox activity of the I^- / (I_2 + I_3^-). This is indicative of a change in the polarisation of the electrodes, and could have adverse effects on the charge and energy efficiency of the devices (this would be addressed later).

In terms of the rate of self-discharge (SD), the cell with 3.0 mol/L KI posilyte displayed a faster rate of SD compared to the other two cells (see Fig. 9.6).

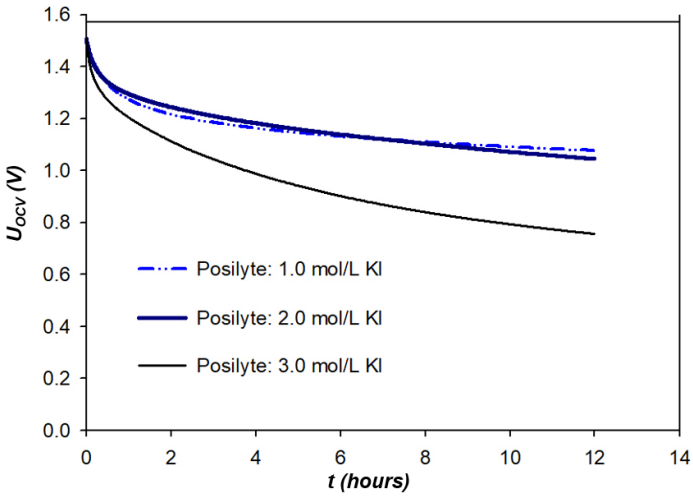

Figure 9.6: Self-discharge properties of the bi-electrolyte cells (-)AC | 2.0 mol/L KOH || 1.0, 2.0 or 3.0 mol/L KI | AC(+). U_L = 1.5 V.

Thus, the SD features observed in Fig. 9.6 also confirms the increased activity of the DRS accompanied by increased diffusion of the species due to the very high concentration gradient at the (+)AC | 3.0 mol/L KI interface. Moreover, it should be noted that the variation in concentration for all cells resulted in a gain in energy, and the CVs for the cells shown in Fig. 9.5 displayed no evidence of redox shuttling at all concentration of posilyte. Furthermore, the relatively high charge capacity and slow rate of SD displayed by the cell with 2.0 mol/L KI posilyte, makes it an optimised configuration of this cell design. It is important to point out that this optimisation procedure

for these cells was instrumental in understanding the concept of "forced confinement" as was introduced and demonstrated in Ch. 4.

9.3.2 Redox reaction of the I^- dissolved redox species and the performance of the bi-electrolyte cells

The effects of the polarisation of the positrode relative to U_L would now be appraised for the optimised cell (-)AC | 2.0 mol/L KOH || 2.0 mol/L KI | AC(+). Figure 9.7a shows the CV for AC in KI electrolyte. Also, this CV was highlighted to approximately indicate the peak electrode potential (E_p), corresponding to the approximate upper limit of the positrode at the cell voltage (U_L = 1.5 V). The GCD plots showing the variation of the positrode and negatrode potentials at different values of U_L ranging from 1.5 V to 1.8 is presented in Fig. 9.7(b1), whilst the GCD plots of the cell at U = 1.5 to 1.8 V, is shown in Fig. 9.7(b2).

From Fig. 9.7(b2), as the value of U_L was increased from 1.5 V to 1.8 V, there was a decrease in the charge and energy efficiency of the cell. In general, this drastic reduction of the charge and energy efficiency with corresponding increase in U_L was observed to be mainly affected by E_p which displayed a marked reduction in the charge efficiency especially at U_L = 1.7 and 1.8 V.

Interestingly, even at such high polarisation of the positrode, there was no evidence for the shuttling of the redox species, hence, forced confinement can be achieved at high values of U_L. Another important observation was that although the full faradaic feature of the KI electrolyte can be observed within the window ca. 0.03 to 0.9 V vs SCE (Fig. 9.7 a), there seem to be a constrain on efficiency of the positrode at E_P > 0.61 V vs SCE (which corresponds to the cell operating at U_L = 1.6 V).

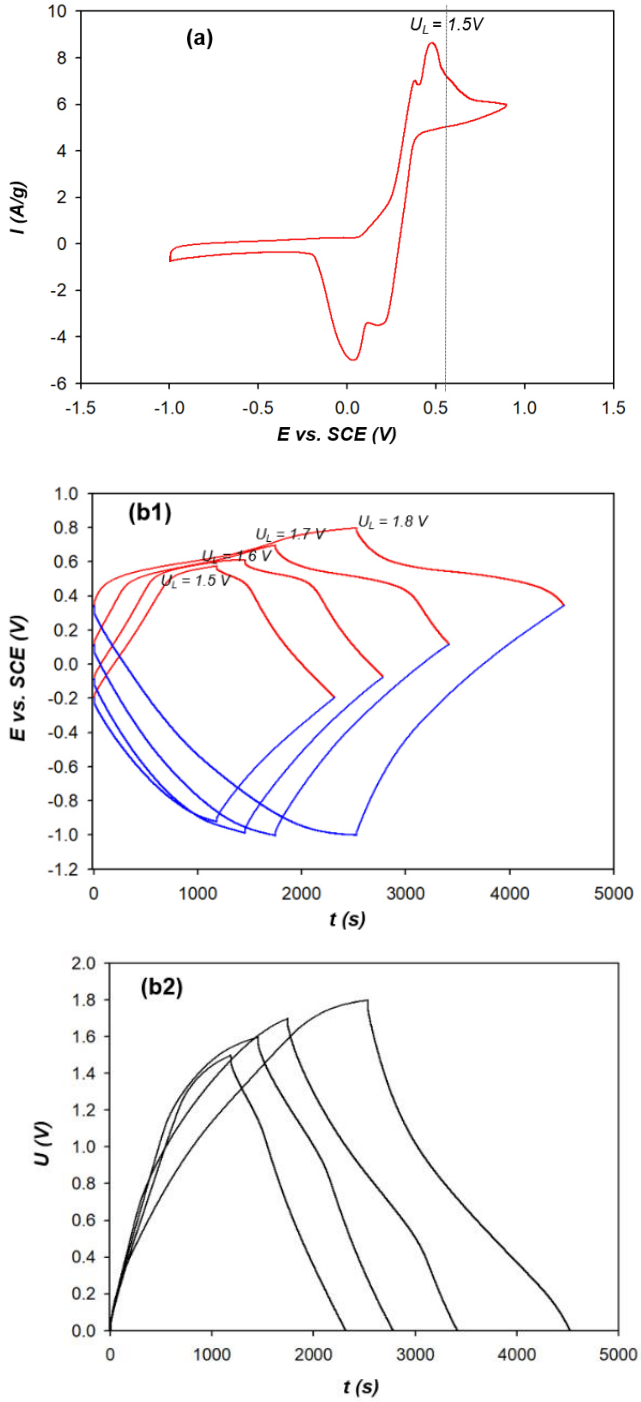

Figure 9.7: Correlating the electrode potential from the CV of the AC in KI (a) with the GCD plots showing the polarisation of the positrode and negatrode (b1) of the bi-electrolyte supercapattery: (-)AC | 2.0 mol/L KOH || 2.0 mol/L KI | AC(+) (b) U_L = 1.5 to 2.0 V, $\pm I$ = 0.1 A/g.

This implies that the maximum optimal cell voltage for the bi-electrolyte cell with KI posilyte is 1.6 V, as determined by the charge and energy efficiency which is affected by the redox reaction at the P|P interface.

This charge and energy efficiency values of ca. 91.2% and 87.9% respectively at U_L = 1.6 V for the bi-electrolyte cell with KI posilyte, is still a greater improvement from the conventional KI cell which cannot be satisfactorily operated at 1.6 V. This is because, as was demonstrated in Ch. 4, the maximum cell voltage was ca. 1.5 V, with a low charge and energy efficiency of ca. 74.2 and less than 70.0 % respectively.

This finding thus conclusively confirms that the membrane kinetically adjusts the E_{0V} of the electrodes in the bi-electrolyte cell, allowing the dis-/charging of the negatrode to be de-coupled from the redox reaction of the I^- / (I_2 + I_3^-) species. Furthermore, it shows that the limitation in the optimal cell voltage (and hence charge and energy efficiency) of the bi-electrolyte cell is mainly affected by the kinetics of the I^- / (I_2 + I_3^-) redox reaction at high peak values of the electrode potential of the positrode E_p. In general, an upper limit of ca. 0.61 V vs. SCE is the maximum electrode potential for the AC positrode to display a fairly acceptable rate kinetics for the I^- / (I_2 + I_3^-) redox reaction, even though it is thermodynamically feasible for this redox reaction to be observed at potentials more positive than 0.61 V vs. SCE.

9.4 Bi-electrolyte supercapattery coupling inert negalyte with immiscible redox posilyte

In this section, a novel strategy for the design of a bi-electrolyte cell in which the negalyte and posilyte are immiscible was introduced. As has been demonstrated already, the preceding bi-electrolyte cells with aqueous electrolytes displayed good performance. Moreover, it was envisaged that the interface between the immiscible electrolytes could result in enhanced performance. For instance, although intermixing is limited between the aqueous electrolytes (e.g.: between the membrane-electrolyte and either the posilyte/negalyte) in the bi-electrolyte cell, still, it cannot be entirely eliminated. The water-immiscible solvent selected was dichloromethane

(CH_2Cl_2), and as seen in Fig. 9.9, the CPR of the CH_2Cl_2 solvent (with inert 0.5 mol/L $TBABF_6$) ranged from ca. -0.82 to 1.07 V vs SCE. Accordingly, it could be used as the solvent for a posilyte to couple with an aqueous negalyte.

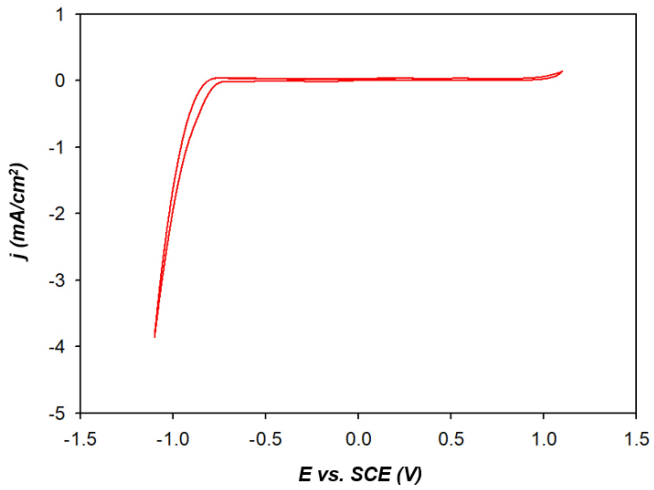

Figure 9.8: CV of Pt disc electrode (ϕ = 3.0 mm) in 0.5 mol/L $TBAPF_6$ dissolved in CH_2Cl_2. Scan rate: 10 mV/s.

CH_2Cl_2 was selected as a water-immiscible solvent because its polar properties imply that a large number of organic solutes can be dissolved in it, also, its electric permittivity is relatively appropriate for an electrolyte solvent [31]. Due to the favourable thermodynamic properties of the Br^- / (Br_2 + Br_3^-) species, bromides was chosen as the DRS. In line with this, a solution of 1.0 mol/L tetrabutyl ammonium bromide (TBABr) dissolved in the CH_2Cl_2 was tested as redox posilyte. Figure 9.10 shows the CVs for the AC electrode in the KOH negalyte, and water-immiscible TBABr posilyte. From Fig. 9.10 the expected EDL property of the KOH electrolyte was displayed, whilst the oxidation of the Br^- to Br_2 + Br_3^- was observed to commence from ca. 0.61 vs SCE. This confirms that the TBABr in CH_2Cl_2 is a viable posilyte for the AC positrode.

The role of the interlayer or "liquid-junction" which may be created due to partition effects is an important property that must be considered when charge transport is expected between two immiscible electrolytes.

Fundamentally, the nature of this interlayer would determine if charge transport, which is necessary for effective charge storage, would be possible.

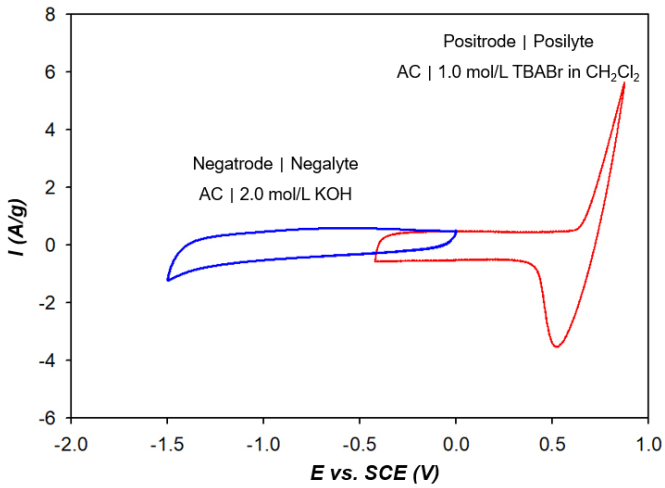

Figure 9.9: CVs of the AC electrode in 2.0 mol/L KOH negalyte and 1.0 mol/L TBABr in CH_2Cl_2 water-immiscible posilyte. Scan rate: 5.0 mV/s.

To test for the properties of the membrane-electrolyte | immiscible-electrolyte interface, the experimental set-up illustrated in Fig. 9.10a, and pictured in Fig. 9.10b was employed.

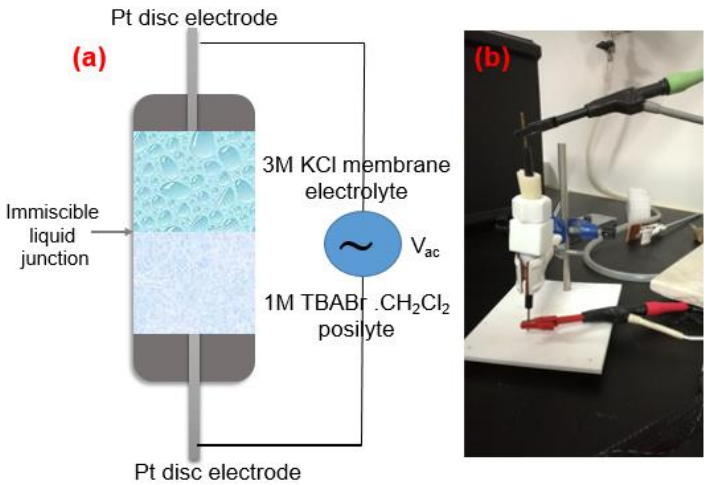

Figure 9.10: Set-up for testing the polarisation of the immiscible electrolyte junction (a) schematic (b) actual experimental layout.

In the cell described in Fig. 9.10, a specific volume of the 1.0 mol/L TBABr in CH_2Cl_2 posilyte was first poured inside the cell, followed by the same

volume of the membrane electrolyte (3.0 mol/L KCl). Note that the apparent density of the 1.0 mol/L TBABr in CH_2Cl_2 solution (ca. 1.43 g/mL) is higher than that of 3.0 mol/L KCl (ca. 1.08 g/L). The cell was then sealed (as pictured in Fig. 9.10 b), and allowed to equilibrate for one hour, after which potentiostatic electrochemical impedance test at the OCV (open circuit voltage U_{OCV}) was taken. The experiment was conducted thrice at intervals of 15 minutes.

Figure 9.11 shows a typical impedance spectra collected across the membrane-electrolyte | posilyte interlayer. From Fig. 9.11, it was observed that the interlayer between the ME and the immiscible electrolyte was polarizable. With knowledge of the polarisability of the immiscible electrolyte junction, the bi-electrolyte cell with immiscible electrolyte was then assembled.

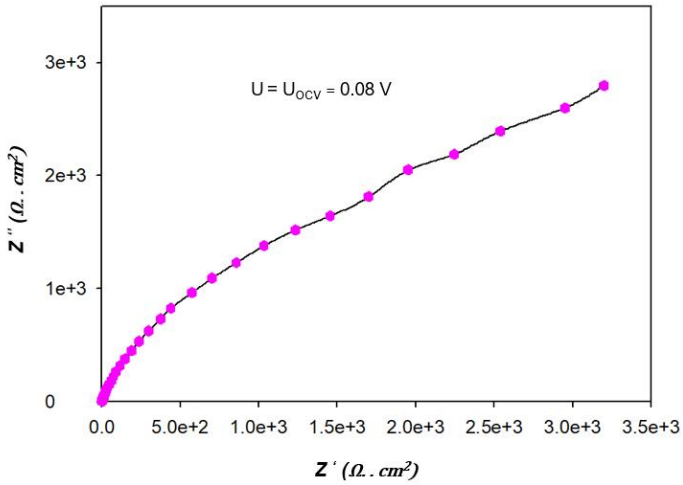

Figure 9.11: Impedance spectra across the (3.0 mol/L KCl)-(1.0 mol/L TBABr in CH_2Cl_2) junction.

In order to mitigate against the volatility of CH_2Cl_2, immediately after the preparation of the electrolyte in the fume-hood, a specific volume was transferred into a tube containing the electrode, and this was hermetically sealed for 30 minutes. After this soaking procedure, the electrode was used immediately to assemble the cell. Since excess electrolytes are not required in the design of bi-electrolyte cells, the saturated electrode comprising of the

CH_2Cl_2 based posilyte is always tightly sealed and contained inside the assembled cell. Accordingly, immiscible bi-electrolyte cells assembled in this research were still operable after several weeks.

Furthermore, as shown in the Fig. 9.12c, the cell arrangement displayed relatively good cycle stability, because it retained ca. 60% of its energy after cycling at 1.0 A/g ($\pm$30.0 mA) for 6000 cycles. It should be pointed out that compared to other reported bi-electrolyte cells with iodide posilyte [100, 111, 149, 192], this displayed cycle stability, are relatively satisfactory. This is because the maximum cell voltage reported and the applied current are actually amongst the highest that have been tested for such class of cells. Also, it is important to highlight that the novel concept of an immiscible bi-electrolyte cell demonstrated herein was also the first to adopt a bromide as posilyte in any bi-electrolyte cell configuration. Thus, the high power performance displayed by the GCD plots of Fig. 9.12 is consistent with the polarisability of the liquid junction between the membrane-electrolyte and the immiscible posilyte as observed from Fig. 9.11.

In line with this, Fig. 9.13a could be used to describe the distribution of ions at the KCl-(TBABr in CH_2Cl_2) interface. On the other hand, if the liquid junction interface was not polarizable their mixed solvent layer would resemble the illustration of Fig. 9.13b. Such a distribution of ions at the immiscible electrolyte interface as described by Fig. 9.13b cannot be used for charge storage because charge transport across such an interlayer is practically impossible.

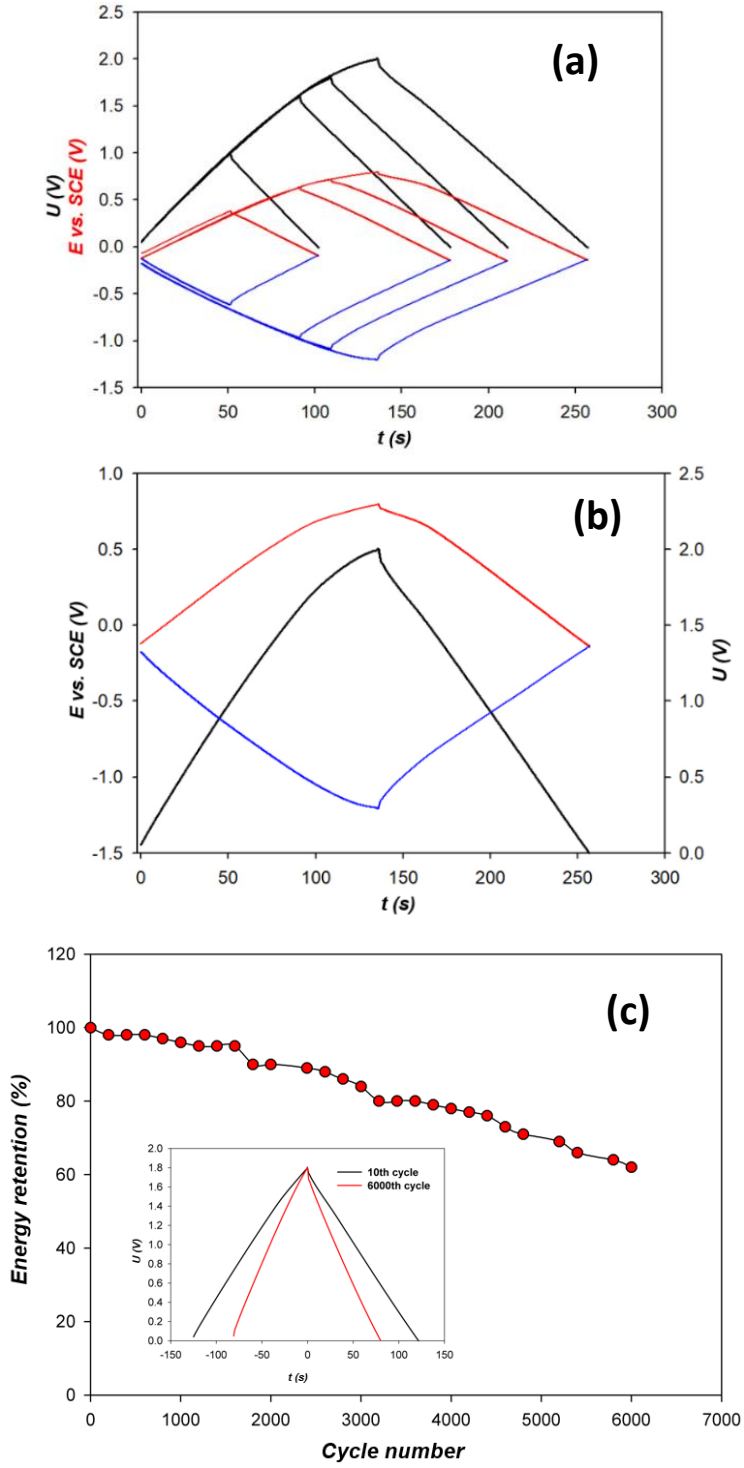

Figure 9.12: GCD plot of the immiscible bi-electrolyte cell: (-)AC | 2.0 mol/L KOH || 1.0 mol/L TBABr in CH_2Cl_2 | AC(+) (a) variation of electrode potential with U (b) variation of electrode potential and cell voltage at U_L = 2.0 V. $\pm I$ = 1.0 A/g. (c) Cycle number vs. Energy retention on GCD cycling at $\pm I$ = 1.0 A/g and U_L = 1.8 V (Inset) GCD plot at 10th and 6000th cycle.

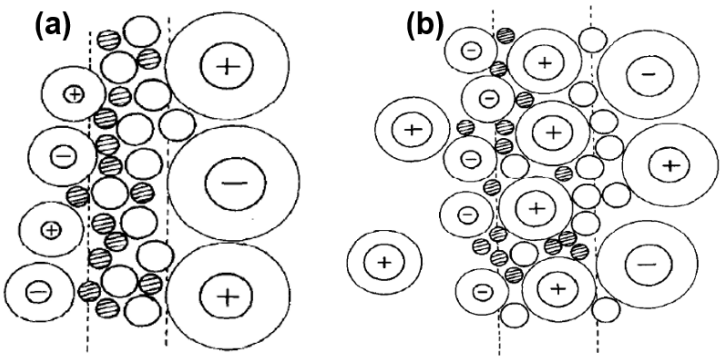

Figure 9.13: Illustration of the liquid interface at the junction of two immiscible electrolytes (a) polarisable interface e.g. (KCl in water)-(TBABr in CH_2Cl_2) (b) non-polarisable interface e.g. (TBABr in water)-($TBABF_4$ in CH_2Cl_2) [266, 267].

Based on these descriptions, the polarisable interface between the KCl membrane-electrolyte and the posilyte (TBABr in CH_2Cl_2) would allow the effective transport of charge. Thusly, when the novel immiscible bi-electrolyte cell was charged, the membrane-negalyte interface would operate as expected through the effective transport of charge across the aqueous electrolyte interface which comprises of the already described membrane-electrolyte ions with adequate molar conductivities.

Relatedly, a combination of diffusion and migration across the membrane-immiscible posilyte interface is responsible for the equally fast transport of charge exhibited across this interface (or interlayer). These effective charge transport across the membrane, was ultimately reflected in the good performance of the cell as shown in Fig. 9.12 a and b.

Moreover, this fast charge transport across the immiscible-electrolyte layer may also be accompanied or probably aided by capillary effects of the membrane. Accordingly, this could promote the transference and subsequent hydration of the $TBA^+.Br^-$ in the surrounding water molecules at the interface [268]. This proposed mechanism might be possible because the polarisable immiscible-electrolyte interface (illustrated in Fig. 9.13a) has a thickness of

around 3.0 angstroms (30.0 nm) [266] which is within range of the hydration shell.

Accordingly, during the dis-/charging process, the interlayer might be characterised by the possible formation of an aqueous complex of the hydrated [$TBA^+.Br^-$] which has been described as a packing of the tetrabutylammonium (TBA^+) cations clustered by the hydrated bromide anions and hydrogen-bonded water molecules [269]. The existence of this complex at the interlayer, may subsequently retard the diffusion of the Br^- / (Br^2 + Br_3^-) generated at the P|P interface.

For an EDL capacitor with DRS, the adsorption of the redox species on the electrode and the rate of diffusion of the generated species away from the E|E interface, are two major factors that affects the rate of self-discharge of the cells. Along these lines, the possible stabilisation effects at the membrane-immiscible posilyte interface which could potentially slow down the rate of diffusion at the P|P interface was further probed to confirm the extent of its effects on the rate of self-discharge.

Figure 9.14 shows the U_{OCP} measured from the initial U_L of 1.8 V in the course of 12 hours resting time, this figure also shows the open circuit potential of the positrode and the negatrode during this rest duration. It was observed that from 0 to 2000 s, the rate of self-discharge (SD) of the cell was mainly driven by the faster rate of SD from the P|P as well as the N|N interfaces. This faster rate of SD from the positrode is due to a higher rate of diffusion of the generated species accumulated during charging. Afterwards, the rate of SD of the P|P interface appears to slow down with only a small change in the positrode potential throughout the remaining open circuit duration. Hence, the stabilisation effects appears to have reduced the rate of SD at the P|P interface.

In this vein, after 12 hours of SD, the cell retained ca. 55% of its initial energy. With respect to the literature, a U_L of 1.8 V, and the subsequent retention of 55% of the energy, are amongst the highest values that has been

reported for cells with DRS [100, 111, 149, 192]. Note that this higher U_L (1.8 V) which is usually not tested for the literature cells owing to rapidly fast degradation [112], was deliberately selected herein to increase the rate of diffusion of the redox species at the P|P interface. This was in order to effectively test the role of the membrane electrolyte-immiscible posilyte layer/interface in reducing the rate of SD of the cell.

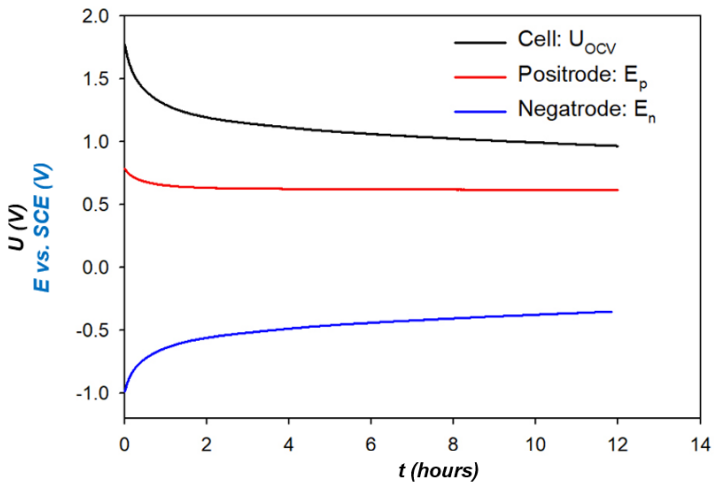

Figure 9.14: Self-discharge of the cell: (-)AC | 2.0 mol/L KOH ||• 1.0 mol/L TBABr in CH_2Cl_2 | AC(+), showing the variation of potential of the positrode and negatrode from a U_L of 1.8 V.

As has been demonstrated in this research (Ch. 4), the thermodynamic properties of bromides as DRS enabled the conventional cell (-)AC | KBr | AC(+) to operate at high cell voltages (up to 2.0 V). Also, there was no evidence of shuttling, and the Nernstian contribution stored charge at higher cell voltages, which is in contrast to iodides. Moreover, the similarly good performance of the immiscible bi-electrolyte cell as observed from the GCD in Fig. 9.12 a and b, warrants further comparison with the conventional KBr cell in order to confirm if this modification of the cell design is practically desirable.

Along these lines, the rate of SD of two different cells using bromides as DRS were compared with the immiscible bi-electrolyte cell: (-)AC | 2.0 mol/L KOH || 1.0 mol/L TBABr in CH_2Cl_2 | AC(+). These cells were the

Conventional cell (-)AC | KBr | AC(+). (Note that for this test, two GF/D membranes were used as separators in the conventional cell in order to make its physical design comparable with the bi-electrolyte cell). Also, the usual Miscible bi-electrolyte cell design (i.e. with 1.0 mol/L KBr in water as the posilyte): (-)AC | 2.0 mol/L KOH || 1.0 mol/L KBr | AC(+), was assembled through the procedure already described. From Fig. 9.15, it was observed that the rate of SD of the Immiscible bi-electrolyte cell which was analysed in Fig. 9.14, was markedly slower than that displayed by either the miscible bi-electrolyte cell with aqueous KBr posilyte, or the conventional KBr cell.

This confirms that the bi-electrolyte cells in general could aid in reducing the SD of supercapatteries with DRS, because the Miscible bi-electrolyte cell displayed a comparably lower rate of SD than the conventional KBr cell with double membranes. Furthermore, this comparison conclusively showed that the modified interlayer obtained from the (membrane-electrolyte) | (immiscible-redox-posilyte) is of practical application to these bi-electrolyte supercapatteries.

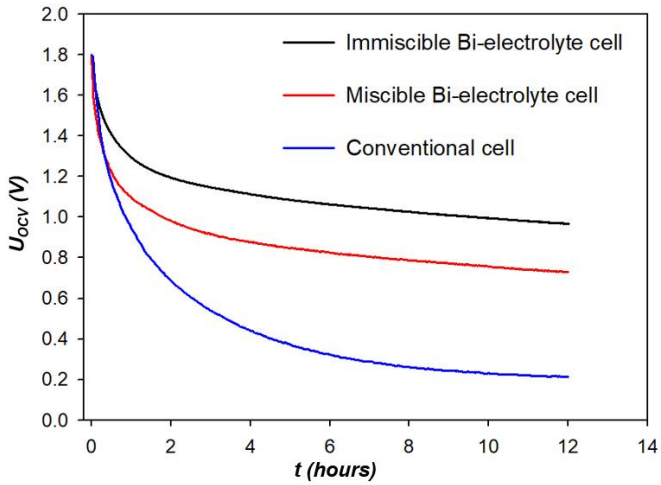

Figure 9.15: Comparing the rate of SD of the conventional KBr cell, and bi-electrolyte cells with KBr as posilyte, with or without immiscible electrolytes.

The energy displayed by this immiscible bi-electrolyte supercapattery was also compared with the conventional KBr supercapattery as shown in the GCD plot of Fig. 9.16.

From Fig. 9.16, it was observed that the Immiscible bi-electrolyte cell displayed a higher specific energy (ca. 35.83 Wh/kg) compared to the conventional supercapattery (29.27 Wh/Kg) at 0.5 A/g current load, with the cells charged to U_L = 2.0 V. This impressive performance from the immiscible bi-electrolyte cell can be attributed to the de-coupling of the charging mechanism of the positrode from the negatrode. That is, the forced confinement allowed the change in polarisation of the positrode i.e. (E_p - E_N) to be slightly higher in the bi-electrolyte cell, which could result to an enhancement in charge capacity.

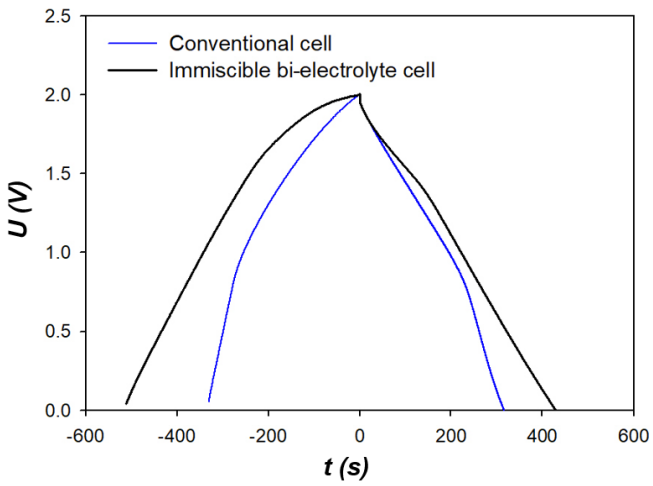

Figure 9.16: GCD plot of the conventional cell with KBr redox electrolyte and the immiscible electrolyte cell with (TBABr in CH_2Cl_2) as posilyte. U_L = 2.0 V, $\pm I$ = 0.5 A/g.

From the preceding discussions and analysis, the immiscible electrolyte cell has been confirmed as a novel and practical addition to the few categories of bi-electrolyte cell designs that are currently available. The principal novelty in this configuration of bi-electrolyte cell is the demonstration for the first time that an appropriate polar immiscible solvent can be used as

the electrolyte to improve the self-discharge and specific energy of supercapatteries.

Furthermore, since CH_2Cl_2 is not ozone depleting [270, 271], it is the most easily accessible and more environment friendly water-immiscible solvent especially from the standpoint of the regulatory controls of industrial chemicals [271]. Nevertheless, due to its potential health hazards [272], safer alternatives are encouraged in order to further enhance the deployment of this novel cell design for commercial applications.

9.5 Novel device engineering to improve the performance of methyl-hydroquinone as redox additive

In this section, the knowledge of the properties of MH_2Q (methyl hydroquinone) which was rigorously studied in Ch. 8 were integrated with an understanding of device engineering principles which has been put to practice throughout this chapter. In Ch.8, it was ascertained that MH_2Q generally displays strong adsorption at the carbon interface. Moreover, as was also demonstrated, due to the thermodynamics of this redox quinonoid, current peaks still exists at low cell voltages, i.e. a large proportion of the Nernstian charge is stored at low cell voltages.

In line with this, attempts were made to devise a simple but effective means of enhancing the charge storage properties of supercapatteries with this redox quinonoid. However, in this situation, Nafion cation-exchange membrane was chosen as a separator (i.e. solid-electrolyte or electrolyte-membrane). This was because though the H_2SO_4 inert electrolyte was shown to be a good posilyte (see Fig. 9.1), coupling this electrolyte incorporated with the MH_2Q/MQ redox species with the KOH negalyte to build a bi-electrolyte supercapattery would not be effective. This is because, the redox potential of the MH_2Q/MQ couple is too narrow within the CPR. In line with this, a modified cell design protocol was developed.

Before the Nafion membrane was used as the separator/solid electrolyte, it was activated by heating in 3 wt% H_2O_2 at 80 ^{0}C for 30 minutes, followed by heating in deionised (DI) water at 80 ^{0}C for another 30 minutes. Finally it was heated in 1.0 mol/L H_2SO_4 for 30 minutes. After allowing to cool in this solution until room temperature, it was then soaked in a de-gassed and air-tight solution of 1.0 mol/L H_2SO_4 for at least 3 days before use.

Before assembling the novel cell using the activated Nafion membrane, the active carbon materials of the electrodes were subjected to 20 cyclic voltammetry cycles at 5.0 mV/s from 0 to 0.8 V in a conventional cell comprising of 0.05 mol/L MH_2Q in 1.0 mol/L HSO_4. After the cycling step, this cell was then disassembled and the positrode and negatrode were first soaked in a solution of 0.25 mol/L MH_2Q for 30 minutes in vacuum (following the normal procedure for cell design already described). After soaking, these same electrodes were still used as the positrode and the negatrode in the modified cell. The novel cell design is illustrated in Fig. 9.17, shows that the separator used was the activated Nafion membrane that was soaked only in the inert electrolyte

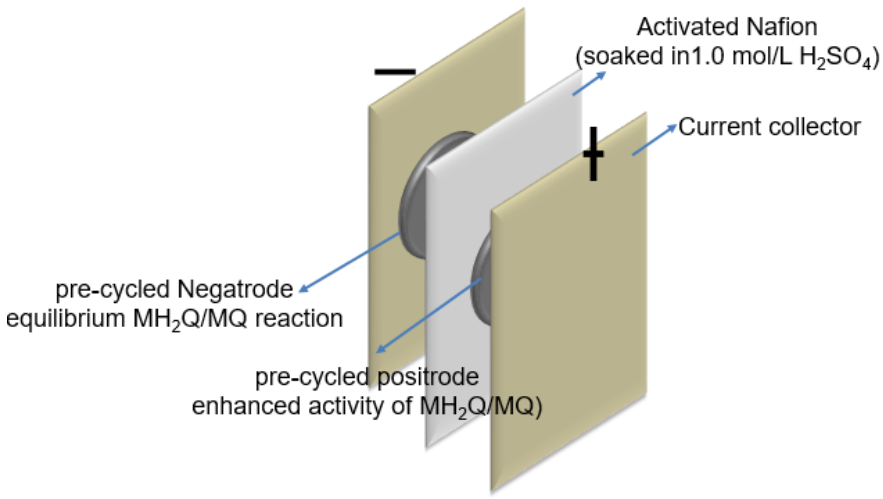

Figure 9.17: Schematic illustration of the modified supercapattery with MH_2Q as DRS, CV from this design is shown in Fig. 9.18b.

Figure 9.18a shows the CV for the conventional cell whilst Fig. 9.18b presents the CV of the modified supercapattery. As was observed from these CVs, the modified cell resulted in enhanced charge capacity and storage of charge at higher cell voltages. The low current peaks in the novel cell design, can be attributed to the intersection of the E_{0V} with the redox potential of the DRS. However, the increased charge capacity at higher cell voltages can be linked to forced confinement on the pre-cycled positrode, and the generally strong adsorption of the MH_2Q/MQ DRS.

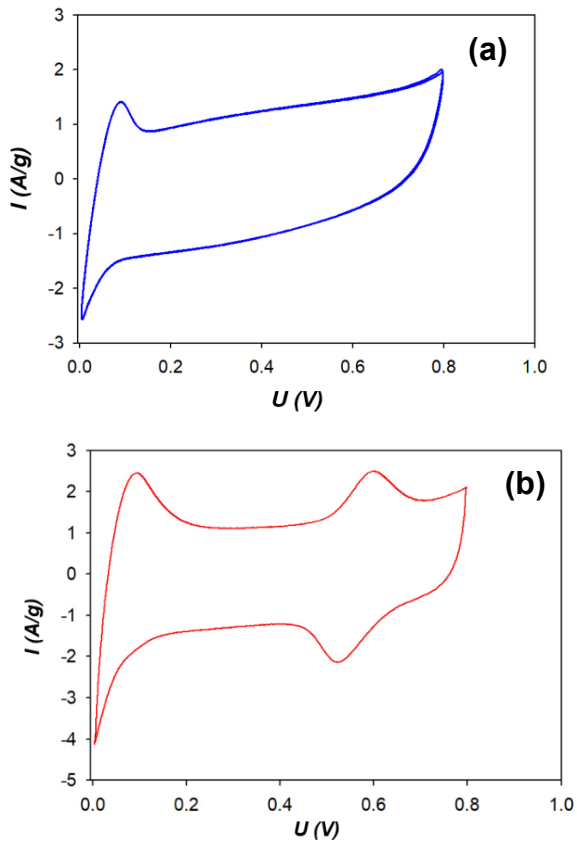

Figure 9.18: CVs of cells with 0.25 MH_2Q in 1.0 mol/L H_2SO_4 (a) conventional design of cells (b) novel design utilising pre-cycled positrode and negatrode, with Nafion membrane soaked in 1.0 mol/L H_2SO_4. Scan rate: 10 mV/s.

Generally, it should be noted that Nafion membrane as adopted herein, may also be replaced with other cheaper ion-selective alternatives. Also, there are other preparation protocols based on this novel cell design strategy that may still be adopted to improve the performance of these cells. For example,

only the positrode may be cycled, or the pre-cycling duration may be increased, etc. (these are all future investigations that may be carried out). As such, this brief proof of concept was simply to demonstrate how the strong adsorption of the products of the MH_2Q redox molecule, could be exploited in designing novel cell configurations with improved performance.

9.6 Chapter Summary

The bi-electrolyte cell comprising of inexpensive glassy-paper membranes soaked in an adequate membrane electrolyte which compartmentalises an EDL and a Nernstian interface has been demonstrated to be an optimal device engineering strategy.

In line with this, the I^- DRS which has a narrow redox potential, can be utilised as the posilyte of a bi-electrolyte cell to assemble supercapatteries with high specific energy.

Furthermore, the Br^- DRS with more positive redox potentials and hence optimal source of thermodynamically effective Nernstian charging of the electrode in a conventional cell, were also found to benefit from a novel immiscible bi-electrolyte cell. This supercapattery was demonstrated to display high specific energy, slow rate of self-discharge, and acceptable cycle stability.

Knowledge of the fundamental properties of methyl hydroquinone such as its high adsorption to the carbon surface has informed the preliminary design of a novel pre-cycled electrode cell with Nafion separator. The assembled cell displayed improved charge capacity and higher energy compared to the conventional supercapattery with the redox MH_2Q as DRS.

Accordingly, the detailed properties of what we have termed as "forced confinement" has been used to explain effective charge capacity enhancement, slow rate of self-discharge, and a general kinetic modification of the redox action of supercapatteries with DRS.

CHAPTER 10: GENERAL CONCLUSIONS AND RECOMMENDATIONS FOR FUTURE WORK

10.1 General Conclusions

As was discussed in the Literature Review (Ch. 2), organic molecules mostly quinonoids, iodides, $Fe(CN)_6^{3-}/Fe(CN)_6^{4-}$, viologens, and few transition metal cations have been tested as dissolved redox species (DRS). However, only few studies have described the use of bromides as DRS. In fact, findings from this PhD research published in [273], were the first to conclusively describe the role of the inherent unequalisation of electrode capacitance which enables bromides to be viable DRS even in equal electrode mass (EEM) cells.

It should be stated that since the focus of this PhD research was on fundamental device engineering, we had earlier identified halides (specifically (I^- / I_3^- and Br^- / Br_3^-) as potential DRS that would be used to fundamentally understand the engineering of supercapacitors with DRS [15]. This was the main reason for the focus on, and major findings regarding, halides, been the principal aspects of this research. The significance of the results obtained from this research can also be further appreciated in view of recent publications on the use of DRS in supercapacitors. For example, it was claimed in [195] that bromides would require ion-exchange membranes in order to operate favourably as DRS. However, the GCD plots of a cell with ion-exchange membranes in which KBr was used as additive to Na_2SO_4 displayed low voltage plateaus which was evident of shuttling of the bromide species (see Ch. 2, Fig. 2.28). From such a performance feature, the function of the ion-exchange membrane is thus unclear. With regards to our research, which used a common porous separator to demonstrate optimal charge storage with bromides, it can thus be opined that these assumptions for the need of membranes were probably due to a misconception of the role of adsorption and thermodynamics of the DRS.

In a more recent publication, it was also claimed that bromides cannot be operated in aqueous electrolytes because the more positive electrode potential of the DRS would not be accommodated in water [198]. However, in light of our findings on the role of unequal electrode capacitances in the utilisation of DRS, it is obvious that this misconception was only possible because the inherent asymmetry in the EDL capacitance of electrodes, which is a fundamental property of ion adsorption at carbons, has not been considered in research into DRS. Furthermore, the use of appropriate electrode geometries (areal density of at least 11. 3 mg/cm^2) which accurately simulates the tortuosity, interfacial resistance, and sorption properties of commercial high-energy supercapacitor electrodes, was also instrumental in further making the engineering principles described in this research applicable in practice. Accordingly, the limited "active volume" of DRS in thin electrodes (usually less than 100.0 micron) which would give exaggerated power as has been identified by [179], but would also display poor utilisation of the DRS as exemplified in [137] (see Ch. 2, Fig. 2.27), were issues that the basic engineering principles adopted and further optimised in this research were able to mitigate.

Accordingly, findings from this research has demonstrated that bromides (e.g. KBr) can actually become viable DRS for supercapatteries. Such that its adoption in practice would become similar to the widespread applications of inert electrolytes such as sulphates (e.g. Na_2SO_4), nitrates (e.g. KNO_3), hydroxides (e.g. KOH), and chlorides (e.g. KCl), which are common for supercapacitors and related hybrids in general (i.e. devices with EDL capacitive and/or pseudocapacitive electrodes).

With respect to the electrodes, majority of the research on redox electrolytes usually utilise activated carbons with negligible surface groups, and only few works have critically investigated the conjoined effects of porosity and surface properties on the action of the DRS. Also, in a couple of

investigations were this has been considered for KI [134] or for $VOSO_4$ [100], attention was only paid to the apparent charge capacity increase, with only little attempts at critically describing the ion-dynamics which is of fundamental importance to the understanding of the performance of these cells.

Accordingly, in this research, commercial graphene nanoplatelets (i.e. surface activated and porous few-layer graphene stacks) (GNP) was selected as a highly graphitised and porous electrode material to be studied with DRS. In this vein, the interaction of bromides with mesoporous graphene-like carbon reported throughout this research was the first of its kind in this research area.

Also the bromides of Li, Na, K and Mg have been tested with both the amorphous carbons (AC-2) and the highly graphitised carbon (GNP). In general, it has been demonstrated that the capacity displayed by supercapatteries using these redox electrolytes are affected by:

1. Ionisation potential of the cation which when correlated with the porous property of the carbon affects the displayed U_{redox}, appearance of current bumps corresponding to confined diffusion, etc. This was exemplified by cells with LiBr as redox electrolytes and GNP as electrodes. Also, it is important to point out that the properties of the alkaline bromides as characterised in this research was reflective of similar experiments carried out for alkaline iodides (cf. Fig. 2.24 [Ch.2] and Fig. 6.2 [Ch. 6]). However, bromide contribute to additional EDL-capacitance which is fundamentally significant. This characteristics, coupled with its thermodynamic property that allows for high voltage operation of at least 1.6 to 1.8 V compared to 0.8 or 1.0 V for most literature KI cells, implied that the role of cations as revealed from this research are actually of fundamental importance in addition to been able to aid in the practical selection of DRS.
2. Porosity and surface properties of the mesoporous and highly graphitised GNP contributes to its enhanced charge storage. The porous property

mostly affects the bromide entrapment in the "active volume", moreover, evidence of surface reactivity contributing to charge storage was observed for GNP.

3. General rate properties of supercapatteries with different alkali bromides as redox electrolytes, demonstrated that mesoporous GNP electrodes have a high rate with the cations of Li^+, Na^+ and K^+. However, AC-2 only displayed good rate properties with the KBr which has the smallest hydrated cation.
4. The capacitive response properties of redox additives of bromides and inert electrolytes have been linked to the interaction of the different cations with the bromides, through the possible formation of ion-ion pairs, which in turn adjusts the dielectric properties within the porous matrix of the mesoporous GNP which can accommodate larger hydrated ions.

Two simple quinonoids i.e. hydroquinone and its derivative methyl-hydroquinone were rigorously studied as DRS. It was revealed that MH_2Q interacts more strongly with the carbon surface compared to H_2Q. In line with this, the charge capacity of MH_2Q was explained from the standpoint of its comparatively stronger surface interaction. Additionally, the fundamental charge storage property of MH_2Q as a DRS has been critically explored wherein it was revealed that this DRS electronically modifies the properties of carbons when it interacts with them.

Novel device design strategies were introduced to increase the specific energy and reduce the rate of self-discharge of supercapatteries. The optimisation of the membrane electrolytes for these cells and its use with either conventional aqueous electrolytes or immiscible electrolytes have been extensively demonstrated. In fact, another important finding from this research, was to demonstrate that the inexpensive paper membranes can actually be used to replace ion-selective membranes which have been used in most cases for DRS applications [100, 148]. Also, knowledge of the properties

displayed by MH_2Q coupled with innovative device procedures, was the basis of a new cell design proposal, in which ion-exchange membranes can be adopted. In line with this, such a finding demonstrates that whilst simple porous separators can be used to achieve many of the design functions which ion-exchange membranes has been used for, still, more innovative strategies may still gain from the use of ion-exchange membranes.

As stated already, the main motivation for studying the application of DRS in supercapacitors is because of the facile approach which it promises. Thus, Fig. 10.1 shows a simplified production line for a commercial supercapacitor, with points P1 and P2 denoting production-line components which some findings from this study may be relevant to.

Based on the results from this research, bromides as DRS with the commercial carbons such as AC-1 or GNP could be applicable to P1. Thus, the gain in energy from the use of unequal electrode capacitances which was demonstrated in this research, can be seamlessly integrated into existing supercapacitor manufacturing plants.

On the other hand, the use of novel cell designs such as bi-electrolyte cells, would require significant adjustments to currently existing manufacturing technologies for supercapacitors [111]. With respect to our research, the GF/D membranes used to design the bi-electrolyte cells are good analogues of some fibre separators used commercially. In line with this, the adoption of bi-electrolyte cells would not be limited by material requirements, but by the complexity of the requisite modification of the manufacturing process. For example, rather than inject the electrolyte directly into the rolled capacitor as in the usual cylindrical or prismatic designs, separate soaking procedures or adjustments to the internal design of the cells needs to be devised.

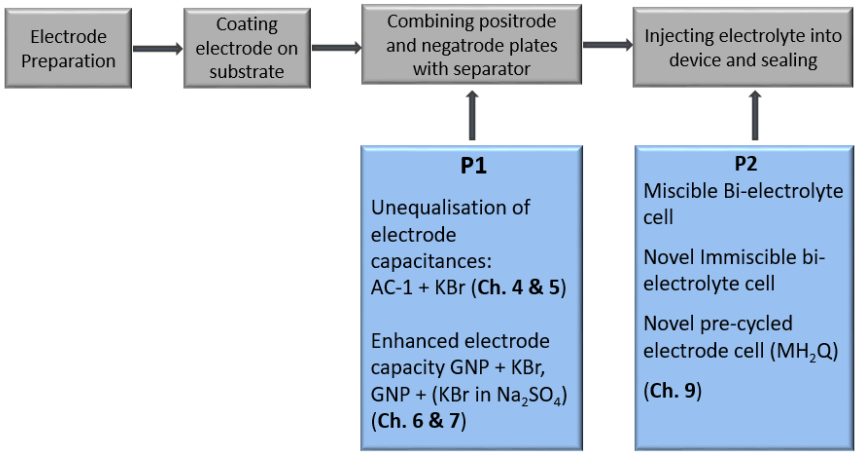

Figure 10.1: Schematic illustration of industrial production-line of commercial supercapacitors (grey boxes), point where findings from this research as presented in various chapters of this thesis could be applied in practice (blue boxes).

It is important to point out that the grafting of these redox species into carbon electrode materials [274] or electronically conducting polymers [146] is another important research area, although these methods also face a number of challenges such as passivation after long cycles [146], instability/solubility of the electrodes [274] etc.

In certain cases, the slow self-discharge rates of some of these devices with grafted redox species compared to when the redox species are dissolved in solution [275] implies that grafting of these species into the electrode is also promising. However, it is important to point out that grafting redox components to the electrode structure is not aimed at replacing, and cannot actually substitute for, the use of DRS in practice. This is because the targets of these two research aspects are different. For example, whilst at its most basics, the use of DRS targets P1 (i.e. simple modification of the existing electrolytes using current technology which can be done in-house on the factory floor), the use of electrode grafting would have to affect the supply side of the carbon (or other electrode) materials. Moreover, most SC manufacturers obtain their activated carbon electrode materials from vendors [276]. Thus,

electrode grafting would have a more challenging commercial entry-point compared to the simple modification of electrolytes for improved charge storage which the use of DRS promises.

10.2 Recommendations for Future Work

As with all research, there is always room for further improvements, innovations and hopefully inventions. With respect to the research on the use of redox electrolytes in supercapacitors, four broad areas which generally stems from some of the findings of this current study could be of importance to furthering this intriguing research area.

10.2.1 Porosity matching with solvated geometries of dissolved redox species

It would be necessary to further match the porosity of selected carbonaceous electrode materials with the dissolved redox species. For example, knowledge of the pore size distribution of the carbons can be used to inform the direct selection of the DRS (including the non-active counter-ion). Accordingly, preparing simple carbon composites for instance mixing of carbon onions with graphene-nanoplatelets could help in modulating the pore volume which could in turn enhance the already good performance of this material.

10.2.2 Investigations of modulated electrolyte permittivity

The results from the mixed electrolyte interaction has shown that the dielectric properties of these dissolved redox species are very important. Moreover, there are still numerous supporting-electrolyte/redox-electrolyte combinations that could be studied to further understand the fundamental principles of coupling the ionic compositions of both the inert and redox electrolytes.

10.2.3 Fundamental studies of the molecular basis of redox reactions at the carbon lattice

In the investigations of quinonoids, it would be important to further probe the stereo-chemical basis of the interaction of redox organic molecules within the carbons. Furthermore, investigating the fundamental basis of the electronic structure interaction of the carbons with these DRS which was carried out from a basic perspective herein, could also be extended to include in-situ Raman spectroscopic studies in order to acquire further understanding of these interactions.

10.2.4 Life cycle analysis for the environmental impact of dissolved redox species

One important factor that would facilitate the adoption of DRS for commercial applications would be a detailed understanding of the environmental impact of the DRS used. For example, the resource availability and disposal of bromides, quinonoids and other DRS needs to be assessed for their environmental impacts. Accordingly, it would be necessary to undertake detailed life cycle analysis of the wide variety of DRS that could be utilised.

10.2.5 Theoretical simulations of the transport properties of dissolved redox species in carbons

Since the adsorption on, and diffusion away from the porous matrix of the carbon electrodes determines the utilisation of DRS for effective charge storage, it would be necessary to undertake fundamental modelling of the transport properties of the DRS within the porous matrix of carbons. This modelling of the transport properties of the DRS should also be correlated to the pore size distribution of the carbon materials.

10.2.6 Device engineering modifications and improvements

Rigorous manufacturing process analysis and material modification procedures should be further studied in order to devise optimal methods that would enable the integration of the device engineering strategies developed in this work into existing manufacturing processes.

REFERENCES

[1] Y. Atwa, E. El-Saadany, M. Salama, and R. Seethapathy, "Optimal renewable resources mix for distribution system energy loss minimization," *IEEE Transactions on Power Systems,* vol. 25, pp. 360-370, 2010.

[2] J. P. Barton and D. G. Infield, "Energy storage and its use with intermittent renewable energy," *IEEE transactions on energy conversion,* vol. 19, pp. 441-448, 2004.

[3] J. O'M. Bockris, "The origin of ideas on a hydrogen economy and its solution to the decay of the environment," *International journal of hydrogen energy,* vol. 27, pp. 731-740, 2002.

[4] World Nuclear Association, World Energy Needs and Nuclear Power [Online]. Available: http://www.world-nuclear.org/information-library/current-and-future-generation/world-energy-needs-and-nuclear-power.aspx

[5] Ineternational Energy Agency, International Energy Outlook Executive Summary, 2018. Available: https://www.eia.gov/outlooks/ieo/pdf/exec_summ.pdf

[6] C. A. Hill, M. C. Such, D. Chen, J. Gonzalez, and W. M. Grady, "Battery energy storage for enabling integration of distributed solar power generation," *IEEE Transactions on smart grid,* vol. 3, pp. 850-857, 2012.

[7] C.-J. Yang, "Pumped hydroelectric storage," in *Storing Energy*, ed: Elsevier, pp. 25-38, 2016.

[8] G. J. May, A. Davidson, and B. Monahov, "Lead batteries for utility energy storage: A review," *Journal of Energy Storage,* vol. 15, pp. 145-157, 2018.

[9] B. Dunn, H. Kamath, and J.-M. Tarascon, "Electrical energy storage for the grid: a battery of choices," *Science,* vol. 334, pp. 928-935, 2011.

[10] A. S. Subburaj, B. N. Pushpakaran, and S. B. Bayne, "Overview of grid connected renewable energy based battery projects in USA," *Renewable and Sustainable Energy Reviews,* vol. 45, pp. 219-234, 2015.

[11] H. Chen, T. N. Cong, W. Yang, C. Tan, Y. Li, and Y. Ding, "Progress in electrical energy storage system: A critical review," *Progress in natural science,* vol. 19, pp. 291-312, 2009.

[12] K. B. Hueso, M. Armand, and T. Rojo, "High temperature sodium batteries: status, challenges and future trends," *Energy & Environmental Science,* vol. 6, pp. 734-749, 2013.

[13] E. Barbour. (2, October). *Energy Storage Sense*. Available: http://energystoragesense.com/energy-storage-technologies/

[14] C. Klumpner, G. Asher, and G. Z. Chen, "Selecting the power electronic interface for a supercapattery based energy storage system," in *2009 IEEE Bucharest PowerTech*, 2009, pp. 1-7.

[15] B. Akinwolemiwa, C. Peng, and G. Z. Chen, "Redox electrolytes in supercapacitors," *Journal of The Electrochemical Society,* vol. 162, pp. A5054-A5059, 2015.

[16] G. Z. Chen, "Supercapacitor and supercapattery as emerging electrochemical energy stores," *International Materials Reviews,* vol. 62, pp. 173-202, 2017.

[17] B. Akinwolemiwa, C. Wei, and G. Z. Chen, "Mechanisms and Designs of Asymmetrical Electrochemical Capacitors," *Electrochimica Acta,* vol. 247, pp. 344-357, 2017.

[18] B. Akinwolemiwa and G. Z. Chen, "Fundamental consideration for electrochemical engineering of supercapattery," *Journal of the Brazilian Chemical Society,* vol. 29, pp. 960-972, 2018.

[19] X. Ning, S. Phadke, B. Chung, H. Yin, P. Burke, and D. R. Sadoway, "Self-healing Li–Bi liquid metal battery for grid-scale energy storage," *Journal of Power Sources,* vol. 275, pp. 370-376, 2015.

[20] Y. Wang and W. H. Zhong, "Development of Electrolytes towards Achieving Safe and High ‐ Performance Energy ‐ Storage Devices: A Review," *ChemElectroChem,* vol. 2, pp. 22-36, 2015.

[21] V. Barsukov, V. Khomenko, S. Chivikov, I. Barsukov, and T. Motronyuk, "On the faradaic and non-faradaic mechanisms of electrochemical processes in conducting polymers and some other reversible systems with solid-phase reagents," *Electrochimica acta,* vol. 46, pp. 4083-4094, 2001.

[22] C. D. Wessells, S. V. Peddada, and M. T. McDowell, "R. a. Huggins and Y. Cui," *Nat. Commun,* vol. 2, p. 550, 2011.

[23] B. Conway and W. Pell, "Double-layer and pseudocapacitance types of electrochemical capacitors and their applications to the development of hybrid devices," *Journal of Solid State Electrochemistry,* vol. 7, pp. 637-644, 2003.

[24] L.-Q. Mai, A. Minhas-Khan, X. Tian, K. M. Hercule, Y.-L. Zhao, X. Lin*, et al.*, "Synergistic interaction between redox-active electrolyte and binder-free functionalized carbon for ultrahigh supercapacitor performance," *Nature communications,* vol. 4, 2013.

[25] L. Su, L. Gong, and Y. Zhao, "A new strategy to enhance low-temperature capacitance: combination of two charge-storage mechanisms," *Physical Chemistry Chemical Physics,* vol. 16, pp. 681-684, 2014.

[26] L. Guan, L. Yu, and G. Z. Chen, "Capacitive and non-capacitive faradaic charge storage," *Electrochimica Acta,* vol. 206, pp. 464-478, 2016.

[27] J. M. Bockris, M. Devanathan, and K. Müller, "On the structure of charged interfaces," in *Electrochemistry*, ed: Elsevier, 1965, pp. 832-863.

[28] L. L. Zhang and X. Zhao, "Carbon-based materials as supercapacitor electrodes," *Chemical Society Reviews,* vol. 38, pp. 2520-2531, 2009.

[29] S. Yiacoumi and C. Tien, *Kinetics of metal ion adsorption from aqueous solutions: models, algorithms, and applications*: Springer Science & Business Media, 2013.

[30] G. Torrie and J. Valleau, "Electrical double layers. 4. Limitations of the Gouy-Chapman theory," *The Journal of Physical Chemistry,* vol. 86, pp. 3251-3257, 1982.

[31] B. E. Conway, *Electrochemical Supercapacitors: Scientific fundamentals and technological applications*. New York: Kluwer-Plenum, 1999.

[32] J. O'M. Bockris, B. E. Conway, E. Yeager, and R. E. White, "Comprehensive treatise of electrochemistry," 1980.

[33] M. Z. Bazant, K. Thornton, and A. Ajdari, "Diffuse-charge dynamics in electrochemical systems," *Physical review E,* vol. 70, p. 021506, 2004.

[34] J. Chmiola, C. Largeot, P. L. Taberna, P. Simon, and Y. Gogotsi, "Desolvation of ions in subnanometer pores and its effect on capacitance and double‐layer theory," *Angewandte Chemie International Edition,* vol. 47, pp. 3392-3395, 2008.

[35] G. Z. Chen, "Understanding supercapacitors based on nano-hybrid materials with interfacial conjugation," *Progress in Natural Science: Materials International,* vol. 23, pp. 245-255, 2013.

[36] T. Chen and L. Dai, "Carbon nanomaterials for high-performance supercapacitors," *Materials Today,* vol. 16, pp. 272-280, 2013.

[37] W. Gu and G. Yushin, "Review of nanostructured carbon materials for electrochemical capacitor applications: advantages and limitations of activated carbon, carbide-derived carbon, zeolite-templated carbon, carbon aerogels, carbon nanotubes, onion-like carbon, and graphene," *Wiley Interdisciplinary Reviews: Energy and Environment,* vol. 3, pp. 424-473, 2014.

[38] T. Brousse, D. Bélanger, and J. W. Long, "To be or not to be pseudocapacitive?," *Journal of The Electrochemical Society,* vol. 162, pp. A5185-A5189, 2015.

[39] J. Wang and M. M. Collinson, "Electrochemical characterization of inorganic│organic hybrid films prepared from ferrocene modified silanes," *Journal of Electroanalytical Chemistry,* vol. 455, pp. 127-137, 1998.

[40] W. Xiao, D. Hu, C. Peng, and G. Z. Chen, "Interfacial synthesis: amphiphilic monomers assisted ultrarefining of mesoporous manganese oxide nanoparticles and the electrochemical implications," *ACS applied materials & interfaces,* vol. 3, pp. 3120-3129, 2011.

[41] A. J. Bard and L. R. Faulkner, "Fundamentals and applications," *Electrochemical Methods,* vol. 2, 2001.

[42] A. Singh and A. Chandra, "Significant performance enhancement in asymmetric supercapacitors based on metal oxides, carbon nanotubes and neutral aqueous electrolyte," *Scientific reports,* vol. 5, 2015.

[43] X. Jin, W. Zhou, S. Zhang, and G. Z. Chen, "Nanoscale microelectrochemical cells on carbon nanotubes," *Small,* vol. 3, pp. 1513-1517, 2007.

[44] J. Zhang, J. Jiang, H. Li, and X. Zhao, "A high-performance asymmetric supercapacitor fabricated with graphene-based electrodes," *Energy & Environmental Science,* vol. 4, pp. 4009-4015, 2011.

[45] N. Wu, C. Han, and S. Kuo, "Enhanced performance of SnO 2 xerogel electrochemical capacitor prepared by novel crystallization process," *Journal of power sources,* vol. 109, pp. 418-421, 2002.

[46] D. Jewell and G. Z. Chen, "Carbon nanotube and conducting polymer composites for supercapacitors," *Progress in Natural Science,* vol. 7, p. 002, 2008.

[47] G. A. Snook, P. Kao, and A. S. Best, "Conducting-polymer-based supercapacitor devices and electrodes," *Journal of Power Sources,* vol. 196, pp. 1-12, 2011.

[48] L. Yu and G. Z. Chen, "Redox electrode materials for supercapatteries," *Journal of Power Sources,* vol. 326, pp. 604-612, 2016.

[49] M. J. Bleda-Martínez, C. Peng, S. Zhang, G. Z. Chen, E. Morallón, and D. Cazorla-Amorós, "Electrochemical methods to enhance the capacitance in activated carbon/polyaniline composites," *Journal of the Electrochemical Society,* vol. 155, pp. A672-A678, 2008.

[50] M. A. Bissett, S. D. Worrall, I. A. Kinloch, and R. A. W. Dryfe, "Comparison of Two-Dimensional Transition Metal Dichalcogenides for Electrochemical Supercapacitors," *Electrochimica Acta,* vol. 201, pp. 30-37, 5/20/ 2016.

[51] C. Peng, D. Hu, and G. Z. Chen, "Theoretical specific capacitance based on charge storage mechanisms of conducting polymers: Comment on 'Vertically oriented arrays of polyaniline nanorods and their super electrochemical properties'," *Chemical Communications,* vol. 47, pp. 4105-4107, 2011.

[52] B. Zhang, X. Ji, K. Xu, C. Chen, X. Xiong, J. Xiong*, et al.*, "Unraveling the different charge storage mechanism in T and H phases of MoS2," *Electrochimica Acta,* vol. 217, pp. 1-8, 2016.

[53] X. Ji, K. Xu, C. Chen, B. Zhang, H. Wan, Y. Ruan*, et al.*, "Different charge-storage mechanisms in disulfide vanadium and vanadium carbide monolayer," *Journal of Materials Chemistry A,* vol. 3, pp. 9909-9914, 2015.

[54] X. Ji, K. Xu, C. Chen, B. Zhang, Y. Ruan, J. Liu*, et al.*, "Probing the electrochemical capacitance of MXene nanosheets for high-performance pseudocapacitors," *Physical Chemistry Chemical Physics,* vol. 18, pp. 4460-4467, 2016.

[55] J. H. Chae and G. Z. Chen, "1.9 V aqueous carbon-carbon supercapacitors with unequal electrode capacitances," *Electrochimica Acta,* vol. 86, pp. 248-254, 2012.

[56] W. G. Pell and B. E. Conway, "Peculiarities and requirements of asymmetric capacitor devices based on combination of capacitor and battery-type electrodes," *Journal of Power Sources,* vol. 136, pp. 334-345, 2004.

[57] C. Peng, S. Zhang, X. Zhou, and G. Z. Chen, "Unequalisation of electrode capacitances for enhanced energy capacity in asymmetrical supercapacitors," *Energy & Environmental Science,* vol. 3, pp. 1499-1502, 2010 2010.

[58] Z. Dai, C. Peng, J. H. Chae, K. C. Ng, and G. Z. Chen, "Cell voltage versus electrode potential range in aqueous supercapacitors," *Scientific reports,* vol. 5, p. 9854, 2015.

[59] J. W. Long, D. Bélanger, T. Brousse, W. Sugimoto, M. B. Sassin, and O. Crosnier, "Asymmetric electrochemical capacitors—Stretching the limits of aqueous electrolytes," *Mrs Bulletin,* vol. 36, pp. 513-522, 2011.

[60] D. Cericola and R. Kötz, "Hybridization of rechargeable batteries and electrochemical capacitors: Principles and limits," *Electrochimica Acta,* vol. 72, pp. 1-17, 2012.

[61] H. Shao, N. Padmanathan, D. McNulty, C. O′ Dwyer, and K. M. Razeeb, "Supercapattery Based on Binder-Free Co3(PO4)2 • 8H2O Multilayer Nano/Microflakes on Nickel Foam," *ACS Applied Materials & Interfaces,* vol. 8, pp. 28592-28598, 2016.

[62] E. Zhang and Y. Ni, "3D reticulate Co x Ni 3− x S 2 nanostructure on nickel foam as a new type of electroactive material for high-performance supercapacitors," *RSC Advances,* vol. 6, pp. 106465-106472, 2016.

[63] K. K. Lee, W. S. Chin, and C. H. Sow, "Cobalt-based compounds and composites as electrode materials for high-performance electrochemical capacitors," *Journal of Materials Chemistry A,* vol. 2, pp. 17212-17248, 2014.

[64] J. Lee, S. Choudhury, D. Weingarth, D. Kim, and V. Presser, "High Performance Hybrid Energy Storage with Potassium Ferricyanide Redox Electrolyte," *ACS Applied Materials & Interfaces,* vol. 8, pp. 23676-23687, 2016.

[65] S. Roldan, D. Barreda, M. Granda, R. Menendez, R. Santamaria, and C. Blanco, "An approach to classification and capacitance expressions in electrochemical capacitors technology," *Physical Chemistry Chemical Physics,* vol. 17, pp. 1084-1092, 2015.

[66] H. Wang, H. S. Casalongue, Y. Liang, and H. Dai, "Ni (OH) 2 nanoplates grown on graphene as advanced electrochemical pseudocapacitor materials," *arXiv preprint arXiv:1005.0853,* 2010.

[67] H. Li, M. Yu, F. Wang, P. Liu, Y. Liang, J. Xiao*, et al.*, "Amorphous nickel hydroxide nanospheres with ultrahigh capacitance and energy density as electrochemical pseudocapacitor materials," *Nature communications,* vol. 4, p. 1894, 2013.

[68] H. Y. Lee, S. Kim, and H. Y. Lee, "Expansion of active site area and improvement of kinetic reversibility in electrochemical pseudocapacitor electrode," *Electrochemical and Solid-State Letters,* vol. 4, pp. A19-A22, 2001.

[69] X.-H. Xia, J.-P. Tu, X.-L. Wang, C.-D. Gu, and X.-B. Zhao, "Mesoporous Co3O4 monolayer hollow-sphere array as electrochemical pseudocapacitor material," *Chemical Communications,* vol. 47, pp. 5786-5788, 2011.

[70] K.-H. Chang, C.-C. Hu, C.-M. Huang, Y.-L. Liu, and C.-I. Chang, "Microwave-assisted hydrothermal synthesis of crystalline WO 3–WO 3· 0.5 H 2 O mixtures for pseudocapacitors of the asymmetric type," *Journal of Power Sources,* vol. 196, pp. 2387-2392, 2011.

[71] J. Duay, E. Gillette, R. Liu, and S. B. Lee, "Highly flexible pseudocapacitor based on freestanding heterogeneous MnO 2/conductive polymer nanowire arrays," *Physical Chemistry Chemical Physics,* vol. 14, pp. 3329-3337, 2012.

[72] D. Sarkar, G. G. Khan, A. K. Singh, and K. Mandal, "High-performance pseudocapacitor electrodes based on α-Fe2O3/MnO2 core–shell

nanowire heterostructure arrays," *The Journal of Physical Chemistry C,* vol. 117, pp. 15523-15531, 2013.

[73] H.-Y. Hsu, K.-H. Chang, R. R. Salunkhe, C.-T. Hsu, and C.-C. Hu, "Synthesis and characterization of mesoporous Ni–Co oxy-hydroxides for pseudocapacitor application," *Electrochimica Acta,* vol. 94, pp. 104-112, 2013.

[74] T. Brezesinski, J. Wang, S. H. Tolbert, and B. Dunn, "Ordered mesoporous [alpha]-MoO3 with iso-oriented nanocrystalline walls for thin-film pseudocapacitors," *Nature materials,* vol. 9, pp. 146-151, 2010.

[75] M. Liu, J. Chang, J. Sun, and L. Gao, "A facile preparation of NiO/Ni composites as high-performance pseudocapacitor materials," *RSC Advances,* vol. 3, pp. 8003-8008, 2013.

[76] Z. Jian, V. Raju, Z. Li, Z. Xing, Y. S. Hu, and X. Ji, "A High‐Power Symmetric Na‐Ion Pseudocapacitor," *Advanced Functional Materials,* vol. 25, pp. 5778-5785, 2015.

[77] W.-j. Huang, T. Chang-Hsien, and Y.-J. Liou, "Supercapattery and method for controlling charge/discharge of the supercapattery by using a magnetic force," ed: Google Patents, 2015.

[78] M. W.-S. Zhao L-P, Wang H-Y, Qi L., "MoS2-C Composite as Negative Electrode Material for Sodium-Ion Supercapattery," *Acta Physico-Chimica Sinica,* vol. 33, pp. 787-794, 2017.

[79] A. A. Alguail, A. H. Al-Eggiely, and B. N. Grgur, "Polyaniline–lead sulfate based cell with supercapattery behavior," *Journal of Saudi Chemical Society*.

[80] S. Vijayakumar, S. Nagamuthu, and K.-S. Ryu, "CuCo2O4 flowers/Ni-foam architecture as a battery type positive electrode for high performance hybrid supercapacitor applications," *Electrochimica Acta,* vol. 238, pp. 99-106, 2017.

[81] Y. F. Huang, W. H. Ruan, D. L. Lin, and M. Q. Zhang, "Bridging Redox Species-Coated Graphene Oxide Sheets to Electrode for Extending Battery Life Using Nanocomposite Electrolyte," *ACS Applied Materials & Interfaces,* vol. 9, pp. 909-918, 2017.

[82] S. Vijayakumar, S. Nagamuthu, S.-H. Lee, and K.-S. Ryu, "Porous thin layered nanosheets assembled ZnCo2O4 grown on Ni-foam as an efficient electrode material for hybrid supercapacitor applications," *International Journal of Hydrogen Energy,* vol. 42, pp. 3122-3129, 2017.

[83] N. Padmanathan, H. Shao, D. McNulty, C. O'Dwyer, and K. M. Razeeb, "Hierarchical NiO–In 2 O 3 microflower (3D)/nanorod (1D) hetero-architecture as a supercapattery electrode with excellent cyclic stability," *Journal of Materials Chemistry A,* vol. 4, pp. 4820-4830, 2016.

[84] X. Liang, W. Pan, K. Chen, D. Xue, "Advance in Research and Development of Novel Supercapacitors," *Chinese Journal of Applied Chemistry,* vol. 33, pp. 867-875, 2016.

[85] K. Chen and D. Xue, "Materials chemistry toward electrochemical energy storage," *Journal of Materials Chemistry A,* vol. 4, pp. 7522-7537, 2016.

[86] D. G. Gromadskyi, "Characterization of Ag/Ag2SO4 system as reference electrode for in-situ electrochemical studies of advanced aqueous

supercapacitors," *Journal of Chemical Sciences,* vol. 128, pp. 1011-1017, 2016// 2016.

[87] G. Hatui, G. Chandra Nayak, G. Udayabhanu, Y. K. Mishra, and D. D. Pathak, "Template-free single pot synthesis of SnS2@Cu2O/reduced graphene oxide (rGO) nanoflowers for high performance supercapacitors," *New Journal of Chemistry,* vol. 41, pp. 2702-2716, 2017.

[88] F. N. Ajjan, N. Casado, T. Rebis, A. Elfwing, N. Solin, D. Mecerreyes*, et al.*, "High performance PEDOT/lignin biopolymer composites for electrochemical supercapacitors," *Journal of Materials Chemistry A,* vol. 4, pp. 1838-1847, 2016.

[89] M. Zeiger, N. Jackel, V. N. Mochalin, and V. Presser, "Review: carbon onions for electrochemical energy storage," *Journal of Materials Chemistry A,* vol. 4, pp. 3172-3196, 2016.

[90] S. Admassie, F. N. Ajjan, A. Elfwing, and O. Inganas, "Biopolymer hybrid electrodes for scalable electricity storage," *Materials Horizons,* vol. 3, pp. 174-185, 2016.

[91] R. N. O'brien, "Battery charging method using supercapacitors at two stages," ed: Google Patents, 2004.

[92] H. Zhou, X. Wang, E. Sheridan, H. Gao, J. Du, J. Yang*, et al.*, "Boosting the Energy Density of 3D Dual-Manganese Oxides-Based Li-Ion Supercabattery by Controlled Mass Ratio and Charge Injection," *Journal of The Electrochemical Society,* vol. 163, pp. A2618-A2622, 2016.

[93] L. Yu and G. Z. Chen, "High energy supercapattery with an ionic liquid solution of LiClO4," *Faraday discussions,* vol. 190, pp. 231-240, 2016.

[94] S. Makino, Y. Shinohara, T. Ban, W. Shimizu, K. Takahashi, N. Imanishi*, et al.*, "4 V class aqueous hybrid electrochemical capacitor with battery-like capacity," *RSC Advances,* vol. 2, pp. 12144-12147, 2012.

[95] D. Cericola, P. Novák, A. Wokaun, and R. Kötz, "Hybridization of electrochemical capacitors and rechargeable batteries: An experimental analysis of the different possible approaches utilizing activated carbon, Li 4 Ti 5 O 12 and LiMn 2 O 4," *Journal of Power Sources,* vol. 196, pp. 10305-10313, 2011.

[96] E. Frackowiak, M. Meller, J. Menzel, D. Gastol, and K. Fic, "Redox-active electrolyte for supercapacitor application," *Faraday discussions,* vol. 172, pp. 179-198, 2014.

[97] G. Lota, K. Fic, and E. Frackowiak, "Alkali metal iodide/carbon interface as a source of pseudocapacitance," *Electrochemistry Communications,* vol. 13, pp. 38-41, 2011.

[98] S. Roldan, M. Granda, R. Menendez, R. Santamaria, and C. Blanco, "Mechanisms of Energy Storage in Carbon-Based Supercapacitors Modified with a Quinoid Redox-Active Electrolyte," *J. Phys. Chem.,* vol. 115, p. 17606, 2011.

[99] Q. Li, K. Li, C. Sun, and Y. Li, "An investigation of Cu2+ and Fe2+ ions as active materials for electrochemical redox supercapacitors," *Journal of Electroanalytical Chemistry,* vol. 611, pp. 43-50, 2007.

[100] E. Frackowiak, K. Fic, M. Meller, and G. Lota, "Electrochemistry Serving People and Nature: High - Energy Ecocapacitors based on Redox - Active Electrolytes," *ChemSusChem,* vol. 5, pp. 1181-1185, 2012.
[101] L. Su, L. Gong, H. Lu, and Q. Xu, "Enhanced low-temperature capacitance of MnO2 nanorods in a redox-active electrolyte," *J. Power Sources,* vol. 248, p. 212, 2014.
[102] C. Zhao, W. Zheng, X. Wang, H. Zhang, X. Cui, and H. Wang, "Ultrahigh capacitive performance from both Co (OH) 2/graphene electrode and K3Fe (CN) 6 electrolyte," *Scientific reports,* vol. 3, p. 2986, 2013.
[103] K. Fic, G. Lota, M. Meller, and E. Frackowiak, "Novel insight into neutral medium as electrolyte for high-voltage supercapacitors," *Energy & Environmental Science,* vol. 5, pp. 5842-5850, 2012.
[104] W. Chen, C. Xia, R. Rakhi, and H. N. Alshareef, "A general approach toward enhancement of pseudocapacitive performance of conducting polymers by redox-active electrolytes," *Journal of Power Sources,* vol. 267, pp. 521-526, 2014.
[105] P. Díaz, Z. González, R. Santamaría, M. Granda, R. Menéndez, and C. Blanco, "Enhanced energy density of carbon-based supercapacitors using Cerium (III) sulphate as inorganic redox electrolyte," *Electrochimica Acta,* vol. 168, pp. 277-284, 2015.
[106] H. Yu, L. Fan, J. Wu, Y. Lin, M. Huang, J. Lin*, et al.*, "Redox-active alkaline electrolyte for carbon-based supercapacitor with pseudocapacitive performance and excellent cyclability," *RSC Advances,* vol. 2, pp. 6736-6740, 2012.
[107] J. Menzel, K. Fic, M. Meller, and E. Frackowiak, "The effect of halide ion concentration on capacitor performance," *Journal of Applied Electrochemistry,* vol. 44, pp. 439-445, 2014.
[108] Y. Wang, Z. Chang, M. Qian, Z. Zhang, J. Lin, and F. Huang, "Enhanced specific capacitance by a new dual redox-active electrolyte in activated carbon-based supercapacitors," *Carbon,* vol. 143, pp. 300-308, 2019.
[109] S. Roldán, D. Barreda, M. Granda, R. Menéndez, R. Santamaría, and C. Blanco, "An approach to classification and capacitance expressions in electrochemical capacitors technology," *Physical Chemistry Chemical Physics,* vol. 17, pp. 1084-1092, 2015.
[110] Y. Tian, R. Xue, X. Zhou, Z. Liu, and L. Huang, "Double layer capacitor based on active carbon and its improved capacitive properties using redox additive electrolyte of anthraquinonedisulphonate," *Electrochimica Acta,* vol. 152, pp. 135-139, 2015.
[111] K. Fic, M. Meller, J. Menzel, and E. Frackowiak, "Around the thermodynamic limitations of supercapacitors operating in aqueous electrolytes," *Electrochimica Acta,* vol. 206, pp. 496-503, 2016.
[112] B. Evanko, S. J. Yoo, S.-E. Chun, X. Wang, X. Ji, S. W. Boettcher*, et al.*, "Efficient Charge Storage in Dual-Redox Electrochemical Capacitors through Reversible Counterion-Induced Solid Complexation," *Journal of the American Chemical Society,* vol. 138, pp. 9373-9376, 2016.
[113] L. Chen, H. Bai, Z. Huang, and L. Li, "Mechanism investigation and suppression of self-discharge in active electrolyte enhanced

supercapacitors," *Energy & Environmental Science,* vol. 7, pp. 1750-1759, 2014.

[114] M. Quan, D. Sanchez, M. F. Wasylkiw, and D. K. Smith, "Voltammetry of Quinones in Unbuffered Aqueous Solution: Reassessing the Roles of Proton Transfer and Hydrogen Bonding in the Aqueous Electrochemistry of Quinones," *J. Am. Chem. Soc. ,* vol. 129, p. 12847, 2007.

[115] N. Gupta and H. Linschitz, "Hydrogen-bonding and protonation effects in electrochemistry of quinones in aprotic solvents," *Journal of the American Chemical Society,* vol. 119, pp. 6384-6391, 1997.

[116] M. Quan, D. Sanchez, M. F. Wasylkiw, and D. K. Smith, "Voltammetry of quinones in unbuffered aqueous solution: reassessing the roles of proton transfer and hydrogen bonding in the aqueous electrochemistry of quinones," *Journal of the American Chemical Society,* vol. 129, pp. 12847-12856, 2007.

[117] D. Gastol, J. Walkowiak, K. Fic, and E. Frackowiak, "Enhancement of the carbon electrode capacitance by brominated hydroquinones," *Journal of Power Sources,* vol. 326, pp. 587-594, 2016.

[118] W. Chen, R. Rakhi, and H. N. Alshareef, "Capacitance enhancement of polyaniline coated curved-graphene supercapacitors in a redox-active electrolyte," *Nanoscale,* vol. 5, pp. 4134-4138, 2013.

[119] Y. Zhu, E. Liu, Z. Luo, T. Hu, T. Liu, Z. Li*, et al.*, "A hydroquinone redox electrolyte for polyaniline/SnO2 supercapacitors " *Electrochim. Acta,* vol. 118, p. 106, 2014.

[120] J. Wu, H. Yu, L. Fan, G. Luo, J. Lin, and M. Huang, "A simple and high-effective electrolyte mediated with p-phenylenediamine for supercapacitor," *Journal of Materials Chemistry,* vol. 22, pp. 19025-19030, 2012.

[121] Z. J. Zhang, Y. Q. Zhu, X. Y. Chen, and Y. Cao, "Pronounced improvement of supercapacitor capacitance by using redox active electrolyte of p-phenylenediamine," *Electrochim. Acta,* vol. 176, p. 941, 2015.

[122] Y. F. Nie, Q. Wang, H. T. Yi, X. Y. Chen, and Z. J. Zhang, "Remarkable capacitive enhancement of templated carbon materials by the redox additive electrolyte of p-phenylenediamine," *RSC Advances,* vol. 5, pp. 65100-65109, 2015.

[123] A. D. Modestov, J. Gun, I. Savotine, and O. Lev, "On-line electrochemical–mass spectrometry study of the mechanism of oxidation of N,N-dimethyl-p-phenylenediamine in aqueous electrolytes," *J. Electroanal. Chem.,* vol. 565, p. 7, 2004.

[124] J. Stejskal, "Polymers of phenylenediamines," *Prog. Polym. Sci.,* vol. 41, p. 1, 2015.

[125] H. Yu, J. Wu, L. Fan, S. Hao, J. Lin, and M. Huang, "An efficient redox-mediated organic electrolyte for high-energy supercapacitor," *J. Power Sources,* vol. 248, p. 1123, 2015.

[126] H. Yu, J. Wu, J. Lin, L. Fan, M. Huang, Y. Lin*, et al.*, "A Reversible Redox Strategy for SWCNT ‐ Based Supercapacitors Using a High ‐ Performance Electrolyte," *ChemPhysChem,* vol. 14, pp. 394-399, 2013.

[127] S. Roldán, M. Granda, R. Menéndez, R. Santamaría, and C. Blanco, "Supercapacitor modified with methylene blue as redox active electrolyte," *Electrochimica Acta,* vol. 83, pp. 241-246, 2012.

[128] Q. Wang, Y. F. Nie, X. Y. Chen, Z. H. Xiao, and Z. J. Zhang, "Use of pyrocatechol violet as an effective redox additive for highly promoting the supercapacitor performances," *Journal of Power Sources,* vol. 323, pp. 8-16, 2016.

[129] Y. Q. Zhu, L. Zhang, X. Y. Chen, Z. H. Xiao, and Z. J. Zhang, "Notable improvement of capacitive performance of highly nanoporous carbon materials simply by a redox additive electrolyte of p-nitroaniline," *Journal of Power Sources,* vol. 299, pp. 629-639, 2015.

[130] Z. J. Zhang, Q. Wang, Y. Q. Zhu, and X. Y. Chen, "Nanoporous graphitic carbon materials: Systematic incorporation of p-/m-/o-nitroaniline as effective redox additives for largely improving the capacitive performance," *Carbon,* vol. 100, pp. 564-577, 2016.

[131] A. Borenstein, S. Hershkovitz, A. Oz, S. Luski, Y. Tsur, and D. Aurbach, "Use of 1, 10-Phenanthroline as an Additive for High-Performance Supercapacitors," *The Journal of Physical Chemistry C,* vol. 119, pp. 12165-12173, 2015.

[132] A. Singh and A. Chandra, "Enhancing Specific Energy and Power in Asymmetric Supercapacitors-A Synergetic Strategy based on the Use of Redox Additive Electrolytes," *Scientific reports,* vol. 6, 2016.

[133] Q. Abbas and F. Béguin, "Influence of the iodide/iodine redox system on the self-discharge of AC/AC electrochemical capacitors in salt aqueous electrolyte," *Progress in Natural Science: Materials International,* vol. 25, pp. 622-630, 2015.

[134] M. Meller, J. Menzel, K. Fic, D. Gastol, and E. Frackowiak, "Electrochemical capacitors as attractive power sources," *Solid State Ionics,* vol. 265, pp. 61-67, 2014.

[135] T. Shimooka, S. Yamazaki, T. Sugimoto, T. Jyozuka, H. Teraishi, Y. Nagao*, et al.*, "Capacitance enhancement of Aqueous EDLC systems by electrochemical treatment," *Electrochemistry,* vol. 75, pp. 273-279, 2007.

[136] S. Yamazaki, T. Ito, M. Yamagata, and M. Ishikawa, "Non-aqueous electrochemical capacitor utilizing electrolytic redox reactions of bromide species in ionic liquid," *Electrochimica Acta,* vol. 86, pp. 294-297, 2012.

[137] Q. Li, M. Haque, V. Kuzmenko, N. Ramani, P. Lundgren, A. D. Smith*, et al.*, "Redox enhanced energy storage in an aqueous high-voltage electrochemical capacitor with a potassium bromide electrolyte," *Journal of Power Sources,* vol. 348, pp. 219-228, 2017.

[138] X. Tang, Y. H. Lui, B. Chen, and S. Hu, "Functionalized carbon nanotube based hybrid electrochemical capacitors using neutral bromide redox-active electrolyte for enhancing energy density," *Journal of Power Sources,* vol. 352, pp. 118-126, 2017.

[139] K. Chen, F. Liu, D. Xue, and S. Komarneni, "Carbon with ultrahigh capacitance when graphene paper meets K3Fe(CN)6," *Nanoscale,* vol. 7, pp. 432-439, 2015.

[140] R. Narayanan and P. R. Bandaru, "High Rate Capacity through Redox Electrolytes Confined in Macroporous Electrodes," *Journal of The Electrochemical Society,* vol. 162, pp. A86-A91, 2015.

[141] S.-E. Chun, B. Evanko, X. Wang, D. Vonlanthen, X. Ji, G. D. Stucky*, et al.*, "Design of aqueous redox-enhanced electrochemical capacitors with high specific energies and slow self-discharge," *Nature communications,* vol. 6, 2015.

[142] L.-H. Su, X.-G. Zhang, C.-H. Mi, B. Gao, and Y. Liu, "Improvement of the capacitive performances for Co–Al layered double hydroxide by adding hexacyanoferrate into the electrolyte," *Physical Chemistry Chemical Physics,* vol. 11, pp. 2195-2202, 2009.

[143] A. Shanmugavani, S. Kaviselvi, K. V. Sankar, and R. K. Selvan, "Enhanced electrochemical performances of PANI using redox additive of K 4 [Fe (CN) 6] in aqueous electrolyte for symmetric supercapacitors," *Materials Research Bulletin,* vol. 62, pp. 161-167, 2015.

[144] Q. Abbas, P. Ratajczak, and F. Béguin, "Sodium molybdate–an additive of choice for enhancing the performance of AC/AC electrochemical capacitors in a salt aqueous electrolyte," *Faraday discussions,* vol. 172, pp. 199-214, 2014.

[145] T.-t. Liu, Y.-h. Zhu, E.-h. Liu, Z.-y. Luo, T.-t. Hu, Z.-p. Li*, et al.*, "Fe3+/Fe2+ redox electrolyte for high-performance polyaniline/SnO2 supercapacitors," *Transactions of Nonferrous Metals Society of China,* vol. 25, pp. 2661-2665, 2015.

[146] K. Pandey, P. Yadav, and I. Mukhopadhyay, "Elucidating the effect of copper as a redox additive and dopant on the performance of a PANI based supercapacitor," *Physical Chemistry Chemical Physics,* vol. 17, pp. 878-887, 2015.

[147] Y. Zhao, L. Wang, and H. R. Byon, "High-performance rechargeable lithium-iodine batteries using triiodide/iodide redox couples in an aqueous cathode," *Nature communications,* vol. 4, p. 1896, 2013.

[148] J. Lee, B. Krüner, A. Tolosa, S. Sathyamoorthi, D. Kim, S. Choudhury*, et al.*, "Tin/vanadium redox electrolyte for battery-like energy storage capacity combined with supercapacitor-like power handling," *Energy & Environmental Science,* vol. 9, pp. 3392-3398, 2016.

[149] J. Menzel, K. Fic, and E. Frackowiak, "Hybrid aqueous capacitors with improved energy/power performance," *Progress in Natural Science: Materials International,* vol. 25, pp. 642-649, 2015.

[150] S. Senthilkumar, R. K. Selvan, N. Ponpandian, and J. Melo, "Redox additive aqueous polymer gel electrolyte for an electric double layer capacitor," *RSC Advances,* vol. 2, pp. 8937-8940, 2012.

[151] K. Sun, F. Ran, G. Zhao, Y. Zhu, Y. Zheng, M. Ma*, et al.*, "High energy density of quasi-solid-state supercapacitor based on redox-mediated gel polymer electrolyte," *RSC Advances,* vol. 6, pp. 55225-55232, 2016.

[152] H. Yu, J. Wu, L. Fan, K. Xu, X. Zhong, Y. Lin*, et al.*, "Improvement of the performance for quasi-solid-state supercapacitor by using PVA–KOH–KI polymer gel electrolyte," *Electrochimica Acta,* vol. 56, pp. 6881-6886, 2011.

[153] E. Feng, G. Ma, K. Sun, Q. Yang, H. Peng, and Z. Lei, "Toughened redox-active hydrogel as flexible electrolyte and separator applying supercapacitors with superior performance," *RSC Advances,* vol. 6, pp. 75896-75904, 2016.
[154] D. Kim, G. Lee, D. Kim, J. Yun, S.-S. Lee, and J. S. Ha, "High performance flexible double-sided micro-supercapacitors with an organic gel electrolyte containing a redox-active additive," *Nanoscale,* vol. 8, pp. 15611-15620, 2016.
[155] S. Brunauer, P. H. Emmett, and E. Teller, "Adsorption of gases in multimolecular layers," *J. Am. Chem. Soc.,* vol. 60, pp. 309-319, 1938.
[156] M. Thommes, K. Kaneko, A. V. Neimark, J. P. Olivier, F. Rodriguez-Reinoso, J. Rouquerol*, et al.*, "Physisorption of gases, with special reference to the evaluation of surface area and pore size distribution (IUPAC Technical Report)," *Pure and Applied Chemistry,* vol. 87, pp. 1051-1069, 2015.
[157] K. S. Sing, "Reporting physisorption data for gas/solid systems with special reference to the determination of surface area and porosity (Recommendations 1984)," *Pure and applied chemistry,* vol. 57, pp. 603-619, 1985.
[158] S. Gaisford, V. Kett, and P. Haines, *Principles of thermal analysis and calorimetry*: Royal society of chemistry, 2016.
[159] P. Gabbott, *Principles and applications of thermal analysis*: John Wiley & Sons, 2008.
[160] S. Solomon, R. Sanders, M. Carroll, and A. Schmeltekopf, "Visible and near ‐ ultraviolet spectroscopy at McMurdo Station, Antarctica: 5. Observations of the diurnal variations of BrO and OClO," *Journal of Geophysical Research: Atmospheres,* vol. 94, pp. 11393-11403, 1989.
[161] H.-H. Perkampus, *UV-VIS Spectroscopy and its Applications*: Springer Science & Business Media, 2013.
[162] R. Van Grieken and A. Markowicz, *Handbook of X-ray Spectrometry*: CRC press, 2001.
[163] R. Karazija, *Introduction to the Theory of X-ray and Electronic Spectra of Free Atoms*: Springer Science & Business Media, 2013.
[164] R. L. McCreery, *Raman spectroscopy for chemical analysis* vol. 225: John Wiley & Sons, 2005.
[165] N. Colthup, *Introduction to infrared and Raman spectroscopy*: Elsevier, 2012.
[166] C. L. Haynes, A. D. McFarland, and R. P. Van Duyne, "Surface-enhanced Raman spectroscopy," ed: ACS Publications, 2005.
[167] R. F. Egerton, *Physical principles of electron microscopy*: Springer, 2005.
[168] A. Clarke, C. N. Eberhardt, and C. Eberhardt, *Microscopy techniques for materials science*: Woodhead Publishing, 2002.
[169] L. Reimer, *Transmission electron microscopy: physics of image formation and microanalysis* vol. 36: Springer, 2013.
[170] G. A. Mabbott, "An introduction to cyclic voltammetry," *Journal of Chemical education,* vol. 60, p. 697, 1983.
[171] D. Adrienko, 2008, Cyclic Voltammetry. Available: http://www2.mpip-mainz.mpg.de/~andrienk/journal_club/cyclic_voltammetry.pdf

[172] F. Scholz, *Electroanalytical methods* vol. 1: Springer, 2010.
[173] D. D. Macdonald, "Reflections on the history of electrochemical impedance spectroscopy," *Electrochimica Acta,* vol. 51, pp. 1376-1388, 2006.
[174] R. Martin, J. J. Quintana, A. Ramos, and I. Nuez. 2008, Modeling Electrochemical Double Layer Capacitor, from Classical to Fractional Impedance. Available: http://ieeexplore.ieee.org/stamp/stamp.jsp?arnumber=04618411
[175] R. Kotz, M. Hahn, and R. Gallay, "Temperature behavior and impedance fundamentals of supercapacitors," *J. Power Sources,* pp. 550-555, 2005.
[176] B.-Y. Chang and S.-M. Park, "Electrochemical Impedance Spectrscopy," *Annu. Anal. Chem.,* vol. 3, pp. 207-229, 2010.
[177] CH Instruments. 2018, *Electrochemical Quartz Crystal Microbalance*. Available: http://www.chinstruments.com/chi400.shtml
[178] M. D. Stoller and R. S. Ruoff, "Best practice methods for determining an electrode material's performance for ultracapacitors," *Energy & Environmental Science,* vol. 3, pp. 1294-1301, 2010.
[179] B. Evanko, S. W. Boettcher, S. J. Yoo, and G. D. Stucky, "Redox-Enhanced Electrochemical Capacitors: Status, Opportunity, and Best Practices for Performance Evaluation," *ACS Energy Letters,* vol. 2, pp. 2581-2590, 2017.
[180] Y. Song, T. Liu, B. Yao, M. Li, T. Kou, Z.-H. Huang*, et al.*, "Ostwald Ripening Improves Rate Capability of High Mass Loading Manganese Oxide for Supercapacitors," *ACS Energy Letters,* vol. 2, pp. 1752-1759, 2017/08/11 2017.
[181] X. Li, J. Shen, W. Sun, X. Hong, R. Wang, X. Zhao*, et al.*, "A super-high energy density asymmetric supercapacitor based on 3D core–shell structured NiCo-layered double hydroxide@ carbon nanotube and activated polyaniline-derived carbon electrodes with commercial level mass loading," *Journal of Materials Chemistry A,* vol. 3, pp. 13244-13253, 2015.
[182] K. A. Cychosz and M. Thommes, "Progress in the Physisorption Characterization of Nanoporous Gas Storage Materials," *Engineering,* 2018.
[183] K. A. Cychosz, X. Guo, W. Fan, R. Cimino, G. Y. Gor, M. Tsapatsis*, et al.*, "Characterization of the pore structure of three-dimensionally ordered mesoporous carbons using high resolution gas sorption," *Langmuir,* vol. 28, pp. 12647-12654, 2012.
[184] A. V. Neimark, Y. Lin, P. I. Ravikovitch, and M. Thommes, "Quenched solid density functional theory and pore size analysis of micro-mesoporous carbons," *Carbon,* vol. 47, pp. 1617-1628, 2009.
[185] J. Rouquerol, F. Rouquerol, P. Llewellyn, G. Maurin, and K. S. Sing, *Adsorption by powders and porous solids: principles, methodology and applications*: Academic press, 2013.
[186] S. Storck, H. Bretinger, and W. F. Maier, "Characterization of micro-and mesoporous solids by physisorption methods and pore-size analysis," *Applied Catalysis A: General,* vol. 174, pp. 137-146, 1998.

[187] Y. Tian and J. Wu, "A Comprehensive Analysis of the BET Area for Nanoporous Materials," *AIChE Journal,* 2018.
[188] P. Kleszyk, P. Ratajczak, P. Skowron, J. Jagiello, Q. Abbas, E. Frąckowiak*, et al.*, "Carbons with narrow pore size distribution prepared by simultaneous carbonization and self-activation of tobacco stems and their application to supercapacitors," *Carbon,* vol. 81, pp. 148-157, 2015.
[189] C. Wu, X. Huang, G. Wang, L. Lv, G. Chen, G. Li*, et al.*, "Highly conductive nanocomposites with three‐dimensional, compactly interconnected graphene networks via a self‐assembly process," *Advanced Functional Materials,* vol. 23, pp. 506-513, 2013.
[190] G. Wang, J. Yang, J. Park, X. Gou, B. Wang, H. Liu*, et al.*, "Facile synthesis and characterization of graphene nanosheets," *The Journal of Physical Chemistry C,* vol. 112, pp. 8192-8195, 2008.
[191] M. S. Shafeeyan, W. M. A. W. Daud, A. Houshmand, and A. Shamiri, "A review on surface modification of activated carbon for carbon dioxide adsorption," *Journal of Analytical and Applied Pyrolysis,* vol. 89, pp. 143-151, 2010.
[192] K. Fic, M. Meller, and E. Frackowiak, "Interfacial redox phenomena for enhanced aqueous supercapacitors," *Journal of The Electrochemical Society,* vol. 162, pp. A5140-A5147, 2015.
[193] B. Akinwolemiwa and G. Chen, "Dissolved redox species for the improvement of the performance of supercapacitors," vol. 19, pp. 47-65, 2017.
[194] O. Chailapakul, M. Amatatongchai, P. Wilairat, K. Grudpan, and D. Nacapricha, "Flow-injection determination of iodide ion in nuclear emergency tablets, using boron-doped diamond thin film electrode," *Talanta,* vol. 64, pp. 1253-1258, 2004.
[195] J. Lee, P. Srimuk, S. Fleischmann, A. Ridder, M. Zeiger, and V. Presser, "Nanoconfinement of redox reactions enables rapid zinc iodide energy storage with high efficiency," *Journal of Materials Chemistry A,* 2017.
[196] P. Przygocki, Q. Abbas, P. Babuchowska, and F. BÚguin, "Confinement of iodides in carbon porosity to prevent from positive electrode oxidation in high voltage aqueous hybrid electrochemical capacitors," *Carbon,* vol. 125, pp. 391-400, 2017.
[197] B. Gorska, J. Pernak, and F. Béguin, "Protic ionic liquids with N-chloroalkyl functionalized cations as electrolytes for carbon-based electrochemical capacitors," *Electrochimica Acta,* vol. 246, pp. 971-980, 2017.
[198] B. Gorska, E. Frąckowiak, and F. Beguin, "Redox active electrolytes in carbon/carbon electrochemical capacitors," *Current Opinion in Electrochemistry,* 2018.
[199] Y. Gogotsi and R. M. Penner, "Energy storage in nanomaterials–capacitive, pseudocapacitive, or battery-like?," ed: ACS Publications, 2018.
[200] S. Koneshan, J. C. Rasaiah, R. Lynden-Bell, and S. Lee, "Solvent structure, dynamics, and ion mobility in aqueous solutions at 25 C," *The Journal of Physical Chemistry B,* vol. 102, pp. 4193-4204, 1998.

[201] P. J. Lenart, A. Jusufi, and A. Z. Panagiotopoulos, "Effective potentials for 1: 1 electrolyte solutions incorporating dielectric saturation and repulsive hydration," *The Journal of chemical physics,* vol. 126, p. 044509, 2007.
[202] B. E. Conway, *Ionic hydration in chemistry and biophysics* vol. 12: Elsevier Science Ltd, 1981.
[203] R. Rasuli, Z. Mokarian, R. Karimi, H. Shabanzadeh, and Y. Abedini, "Wettability modification of graphene oxide by removal of carboxyl functional groups using non-thermal effects of microwave," *Thin Solid Films,* vol. 589, pp. 364-368, 2015.
[204] Z. Gao, X. Liu, J. Chang, D. Wu, F. Xu, L. Zhang*, et al.*, "Graphene incorporated, N doped activated carbon as catalytic electrode in redox active electrolyte mediated supercapacitor," *Journal of Power Sources,* vol. 337, pp. 25-35, 2017.
[205] T. Lin, I.-W. Chen, F. Liu, C. Yang, H. Bi, F. Xu*, et al.*, "Nitrogen-doped mesoporous carbon of extraordinary capacitance for electrochemical energy storage," *Science,* vol. 350, pp. 1508-1513, 2015.
[206] H. Nakae, R. Inui, Y. Hirata, and H. Saito, "Effects of surface roughness on wettability," *Acta materialia,* vol. 46, pp. 2313-2318, 1998.
[207] S. Herminghaus, "Roughness-induced non-wetting," *EPL (Europhysics Letters),* vol. 52, p. 165, 2000.
[208] Y. Huang, J. Liang, and Y. Chen, "An overview of the applications of graphene - based materials in supercapacitors," *Small,* vol. 8, pp. 1805-1834, 2012.
[209] S. Kondrat, C. Perez, V. Presser, Y. Gogotsi, and A. Kornyshev, "Effect of pore size and its dispersity on the energy storage in nanoporous supercapacitors," *Energy & Environmental Science,* vol. 5, pp. 6474-6479, 2012.
[210] C. Largeot, C. Portet, J. Chmiola, P.-L. Taberna, Y. Gogotsi, and P. Simon, "Relation between the ion size and pore size for an electric double-layer capacitor," *Journal of the American Chemical Society,* vol. 130, pp. 2730-2731, 2008.
[211] D. Qu and H. Shi, "Studies of activated carbons used in double-layer capacitors," *Journal of Power Sources,* vol. 74, pp. 99-107, 1998.
[212] Y. Munaiah, P. Ragupathy, and V. K. Pillai, "Single-Step Synthesis of Halogenated Graphene through Electrochemical Exfoliation and Its Utilization as Electrodes for Zinc Bromine Redox Flow Battery," *Journal of The Electrochemical Society,* vol. 163, pp. A2899-A2910, 2016.
[213] J. R. Gaier, N. F. Ditmars, and A. R. Dillon, "Aqueous electrochemical intercalation of bromine into graphite fibers," *Carbon,* vol. 43, pp. 189-193, 2005.
[214] J. Xu, I. Y. Jeon, J. M. Seo, S. Dou, L. Dai, and J. B. Baek, "Edge - selectively halogenated graphene nanoplatelets (XGnPs, X= Cl, Br, or I) prepared by ball - milling and used as anode materials for lithium - ion batteries," *Advanced materials,* vol. 26, pp. 7317-7323, 2014.
[215] E. D. Grayfer, V. G. Makotchenko, A. S. Nazarov, S.-J. Kim, and V. E. Fedorov, "Graphene: chemical approaches to the synthesis and modification," *Russian Chemical Reviews,* vol. 80, pp. 751-770, 2011.

[216] H. Zhou, H. Zhang, P. Zhao, and B. Yi, "A comparative study of carbon felt and activated carbon based electrodes for sodium polysulfide/bromine redox flow battery," *Electrochimica Acta,* vol. 51, pp. 6304-6312, 2006.
[217] M. R. Deakin, T. T. Li, and O. R. Melroy, "A study of the electrosorption of bromide and iodide ions on gold using the quartz crystal microbalance," *Journal of electroanalytical chemistry and interfacial electrochemistry,* vol. 243, pp. 343-351, 1988.
[218] S. J. Yoo, B. Evanko, X. Wang, M. Romelczyk, A. Taylor, X. Ji*, et al.*, "Fundamentally Addressing Bromine Storage through Reversible Solid-State Confinement in Porous Carbon Electrodes: Design of a High-Performance Dual-Redox Electrochemical Capacitor," *Journal of the American Chemical Society,* 2017.
[219] D. M. Ford and E. D. Glandt, "Steric hindrance at the entrances to small pores," *Journal of membrane science,* vol. 107, pp. 47-57, 1995.
[220] W. Eeles and J. Turnbull, "The crystal structure of graphite-bromine compounds," *Proc. R. Soc. Lond. A,* vol. 283, pp. 179-193, 1965.
[221] B. R. Puri and R. Bansal, "Studies in surface chemistry of carbon blacks part III. Interaction of carbon blacks and aqueous bromine," *Carbon,* vol. 3, pp. 533-539, 1966.
[222] J. M. Griffin, A. C. Forse, H. Wang, N. M. Trease, P.-L. Taberna, P. Simon*, et al.*, "Ion counting in supercapacitor electrodes using NMR spectroscopy," *Faraday discussions,* vol. 176, pp. 49-68, 2015.
[223] L. Gordeeva, G. Restuccia, A. Freni, and Y. I. Aristov, "Water sorption on composites “LiBr in a porous carbon”," *Fuel processing technology,* vol. 79, pp. 225-231, 2002.
[224] W. J. Albery, Z. Chen, B. R. Horrocks, A. R. Mount, P. J. Wilson, D. Bloor*, et al.*, "Spectroscopic and electrochemical studies of charge transfer in modified electrodes," *Faraday Discussions of the Chemical Society,* vol. 88, pp. 247-259, 1989.
[225] P. Taberna, P. Simon, and J.-F. Fauvarque, "Electrochemical characteristics and impedance spectroscopy studies of carbon-carbon supercapacitors," *Journal of The Electrochemical Society,* vol. 150, pp. A292-A300, 2003.
[226] S. Porada, R. Zhao, A. Van Der Wal, V. Presser, and P. Biesheuvel, "Review on the science and technology of water desalination by capacitive deionization," *Progress in Materials Science,* vol. 58, pp. 1388-1442, 2013.
[227] J. Gamby, P. Taberna, P. Simon, J. Fauvarque, and M. Chesneau, "Studies and characterisations of various activated carbons used for carbon/carbon supercapacitors," *Journal of power sources,* vol. 101, pp. 109-116, 2001.
[228] J. R. Macdonald and W. B. Johnson, "Fundamentals of impedance spectroscopy," *Impedance spectroscopy: theory, experiment, and applications,* pp. 1-20, 2018.
[229] E. Frackowiak, Q. Abbas, and F. Béguin, "Carbon/carbon supercapacitors," *Journal of Energy Chemistry,* vol. 22, pp. 226-240, 2013.
[230] D. Aurbach, J. Gnanaraj, M. Levi, E. Levi, J. Fischer, and A. Claye, "On the correlation among surface chemistry, 3D structure, morphology,

electrochemical and impedance behavior of various lithiated carbon electrodes," *Journal of Power Sources,* vol. 97, pp. 92-96, 2001.

[231] M. Yi, W. Zhang, Z. Shen, X. Zhang, X. Zhao, Y. Zheng*, et al.*, "Controllable functionalization and wettability transition of graphene-based films by an atomic oxygen strategy," *Journal of Nanoparticle Research,* vol. 15, p. 1811, 2013.

[232] B. Jia and L. Zou, "Graphene nanosheets reduced by a multi-step process as high-performance electrode material for capacitive deionisation," *Carbon,* vol. 50, pp. 2315-2321, 2012.

[233] D.-W. Wang, F. Li, H.-T. Fang, M. Liu, G.-Q. Lu, and H.-M. Cheng, "Effect of pore packing defects in 2-D ordered mesoporous carbons on ionic transport," *The Journal of Physical Chemistry B,* vol. 110, pp. 8570-8575, 2006.

[234] S. Prabaharan, R. Vimala, and Z. Zainal, "Nanostructured mesoporous carbon as electrodes for supercapacitors," *Journal of Power Sources,* vol. 161, pp. 730-736, 2006.

[235] W. Sugimoto, H. Iwata, K. Yokoshima, Y. Murakami, and Y. Takasu, "Proton and electron conductivity in hydrous ruthenium oxides evaluated by electrochemical impedance spectroscopy: the origin of large capacitance," *The Journal of Physical Chemistry B,* vol. 109, pp. 7330-7338, 2005.

[236] A. Burke and M. Miller, "Testing of electrochemical capacitors: Capacitance, resistance, energy density, and power capability," *Electrochimica Acta,* vol. 55, pp. 7538-7548, 2010.

[237] J. R. Gaier, "A comparison of the bromination dynamics of various carbon and graphite fibers," *Synthetic metals,* vol. 22, pp. 15-22, 1987.

[238] L. Demarconnay, E. Raymundo-Pinero, and F. Béguin, "Adjustment of electrodes potential window in an asymmetric carbon/MnO 2 supercapacitor," *Journal of Power Sources,* vol. 196, pp. 580-586, 2011.

[239] J. Segalini, E. Iwama, P.-L. Taberna, Y. Gogotsi, and P. Simon, "Steric effects in adsorption of ions from mixed electrolytes into microporous carbon," *Electrochemistry Communications,* vol. 15, pp. 63-65, 2012.

[240] M. E. Orazem and B. Tribollet, *Electrochemical impedance spectroscopy* vol. 48: John Wiley & Sons, 2011.

[241] L. Demarconnay, E. Raymundo-Piñero, and F. Béguin, "A symmetric carbon/carbon supercapacitor operating at 1.6 V by using a neutral aqueous solution," *Electrochemistry Communications,* vol. 12, pp. 1275-1278, 2010.

[242] Sigma Aldrich, Sodium Sulphate Safety Data Sheet. Available: https://www.sigmaaldrich.com/MSDS/MSDS/DisplayMSDSPage.do?country=US&language=en&productNumber=239313&brand=SIGALD&PageToGoToURL=https%3A%2F%2Fwww.sigmaaldrich.com%2Fcatalog%2Fsearch%3Fterm%3Dsodium%2Bsulphates%26interface%3DAll%26N%3D0%26mode%3Dmatch%2520partialmax%26lang%3Den%26region%3DUS%26focus%3Dproduct

[243] Sigma Aldrich, Magnesium Sulphate Safety Data Sheet. Available: https://www.sigmaaldrich.com/MSDS/MSDS/DisplayMSDSPage.do?cou

ntry=US&language=en&productNumber=M7506&brand=SIGALD&PageToGoToURL=https%3A%2F%2Fwww.sigmaaldrich.com%2Fcatalog%2Fsearch%3Finterface%3DAll%26term%3Dmagnesium%2520sulphate%26N%3D0%26mode%3Dmatch%2520partialmax%26focus%3Dproduct%26lang%3Den%26region%3DUS%26cm_re%3DDid%2520You%2520Mean-_-magnesium%2520sulphate-_-magnessium%2520sulphate

[244] J. Barthel, H. Hetzenauer, and R. Buchner, "Dielectric relaxation of aqueous electrolyte solutions. I. Solvent relaxation of 1: 2, 2: 1, and 2: 2 electrolyte solutions," *Berichte der Bunsengesellschaft für physikalische Chemie,* vol. 96, pp. 988-997, 1992.

[245] R. Buchner, T. Chen, and G. Hefter, "Complexity in “simple” electrolyte solutions: ion pairing in MgSO4 (aq)," *The Journal of Physical Chemistry B,* vol. 108, pp. 2365-2375, 2004.

[246] J. Park, V. Kumar, X. Wang, P. S. Lee, and W. Kim, "Investigation of charge transfer kinetics at carbon/hydroquinone interfaces for redox-active-electrolyte supercapacitors," *ACS applied materials & interfaces,* vol. 9, pp. 33728-33734, 2017.

[247] H.-J. Kim and Y.-K. Han, "How can we describe the adsorption of quinones on activated carbon surfaces?," *Current Applied Physics,* vol. 16, pp. 1437-1441, 2016.

[248] F. Mirkhalaf, K. Tammeveski, and D. J. Schiffrin, "Substituent effects on the electrocatalytic reduction of oxygen on quinone-modified glassy carbon electrodes," *Physical Chemistry Chemical Physics,* vol. 6, pp. 1321-1327, 2004.

[249] J. Q. Chambers, "Electrochemistry of quinones," *The Quinonoid Compounds (1988) Part 1,* vol. 1, pp. 719-757, 1988.

[250] P. S. Guin, S. Das, and P. C. Mandal, "Electrochemical Reduction of Quinones in Different Media: A Review," *Int. J. Electrochem. ,* p. 816202, 2011.

[251] L. Tong, Q. Chen, A. A. Wong, R. Gómez-Bombarelli, A. Aspuru-Guzik, R. G. Gordon*, et al.*, "UV-Vis spectrophotometry of quinone flow battery electrolyte for in situ monitoring and improved electrochemical modeling of potential and quinhydrone formation," *Physical Chemistry Chemical Physics,* vol. 19, pp. 31684-31691, 2017.

[252] M. Nishio and M. Hirota, "CH/π interaction: Implications in organic chemistry," *Tetrahedron,* vol. 45, pp. 7201-7245, 1989.

[253] C. Cachet-Vivier, V. Vivier, C. Cha, J.-Y. Nedelec, and L. Yu, "Electrochemistry of powder material studied by means of the cavity microelectrode (CME)," *Electrochimica Acta,* vol. 47, pp. 181-189, 2001.

[254] T. L. Broder, D. S. Silvester, L. Aldous, C. Hardacre, A. Crossley, and R. G. Compton, "The electrochemical oxidation and reduction of nitrate ions in the room temperature ionic liquid [C2mim][NTf2]; the latter behaves as a 'melt' rather than an 'organic solvent'," *New Journal of Chemistry,* vol. 31, pp. 966-972, 2007.

[255] L. Malard, M. Pimenta, G. Dresselhaus, and M. Dresselhaus, "Raman spectroscopy in graphene," *Physics Reports,* vol. 473, pp. 51-87, 2009.

[256] J. Park, A. Reina, R. Saito, J. Kong, G. Dresselhaus, and M. Dresselhaus, "G′ band Raman spectra of single, double and triple layer graphene," *Carbon,* vol. 47, pp. 1303-1310, 2009.
[257] R. Beams, L. G. Cançado, and L. Novotny, "Raman characterization of defects and dopants in graphene," *Journal of Physics: Condensed Matter,* vol. 27, p. 083002, 2015.
[258] M. Pimenta, G. Dresselhaus, M. S. Dresselhaus, L. Cancado, A. Jorio, and R. Saito, "Studying disorder in graphite-based systems by Raman spectroscopy," *Physical chemistry chemical physics,* vol. 9, pp. 1276-1290, 2007.
[259] A. Ambrosi, C. K. Chua, A. Bonanni, and M. Pumera, "Electrochemistry of graphene and related materials," *Chemical reviews,* vol. 114, pp. 7150-7188, 2014.
[260] A. N. Patel, K. McKelvey, and P. R. Unwin, "Nanoscale electrochemical patterning reveals the active sites for catechol oxidation at graphite surfaces," *Journal of the American Chemical Society,* vol. 134, pp. 20246-20249, 2012.
[261] M. Velicky, D. F. Bradley, A. J. Cooper, E. W. Hill, I. A. Kinloch, A. Mischenko*, et al.*, *ACS Nano,* vol. 8, p. 10089, 2014.
[262] K. Fic, E. Frackowiak, and F. Béguin, "Unusual energy enhancement in carbon-based electrochemical capacitors," *Journal of Materials Chemistry,* vol. 22, pp. 24213-24223, 2012.
[263] J. H. Chae and G. Z. Chen, "1.9 V aqueous carbon–carbon supercapacitors with unequal electrode capacitances," *Electrochimica Acta,* vol. 86, pp. 248-254, 2012.
[264] K. Fic, M. He, E. J. Berg, P. Novák, and E. Frackowiak, "Comparative operando study of degradation mechanisms in carbon-based electrochemical capacitors with Li2SO4 and LiNO3 electrolytes," *Carbon,* vol. 120, pp. 281-293, 2017.
[265] R. G. Compton and G. H. Sanders, *Electrode potentials*, 1998.
[266] H. Girault, "Electrochemistry at the interface between two immiscible electrolyte solutions," *Electrochimica acta,* vol. 32, pp. 383-385, 1987.
[267] M. H. Abraham and J. Liszi, "Calculations on ionic solvation—V the calculation of partition coefficients of ions," *Journal of Inorganic and Nuclear Chemistry,* vol. 43, pp. 143-151, 1981.
[268] H. Girault and D. Schiffrin, "Thermodynamic surface excess of water and ionic solvation at the interface between immiscible liquids," *Journal of Electroanalytical Chemistry and Interfacial Electrochemistry,* vol. 150, pp. 43-49, 1983.
[269] J. Lipkowski, V. Y. Komarov, T. V. Rodionova, Y. A. Dyadin, and L. S. Aladko, "The structure of tetrabutylammonium bromide hydrate (C4H9) 4NBr· 21/3H2O," *Journal of Supramolecular Chemistry,* vol. 2, pp. 435-439, 2002.
[270] L. J. Carpenter, S. Reimann, J. B. Burkholder, C. Clerbaux, B. D. Hall, R. Hossaini*, et al.*, "Update on ozone-depleting substances (ODSs) and other gases of interest to the Montreal protocol," *Scientific assessment of ozone depletion: 2014,* pp. 1.1-1.101, 2014.

[271] United States Environmental Protection Agency, [Online]. Available: https://www.epa.gov/ozone-layer-protection/ozone-depleting-substances

[272] P. M. Schlosser, A. S. Bale, C. F. Gibbons, A. Wilkins, and G. S. Cooper, "Human health effects of dichloromethane: key findings and scientific issues," *Environmental health perspectives,* vol. 123, pp. 114-119, 2014.

[273] B. Akinwolemiwa, C. Wei, Q. Yang, L. Yu, L. Xia, D. Hu*, et al.*, "Optimal Utilization of Combined Double Layer and Nernstian Charging of Activated Carbon Electrodes in Aqueous Halide Supercapattery through Capacitance Unequalization," *Journal of The Electrochemical Society,* vol. 165, pp. A4067-A4076, 2018.

[274] T. Tomai, S. Mitani, D. Komatsu, Y. Kawaguchi, and I. Honma, "Metal-free aqueous redox capacitor via proton rocking-chair system in an organic-based couple," *Scientific reports,* vol. 4, p. 3591, 2014.

[275] G. Shul and D. Bélanger, "Self-discharge of electrochemical capacitors based on soluble or grafted quinone," *Physical Chemistry Chemical Physics,* vol. 18, pp. 19137-19145, 2016.

[276] L. Weinstein and R. Dash, "Supercapacitor carbons," *Materials Today,* vol. 10, pp. 356-357, 2013.